UNIVERSITY OF OKLAHOMA

GRADUATE COLLEGE

THEORY AND OBSERVATIONS OF BORES IN THE NOCTURNAL ENVIRONMENT OF THE GREAT PLAINS

A DISSERTATION

SUBMITTED TO THE GRADUATE FACULTY

in partial fulfillment of the requirements for the

Degree of

DOCTOR OF PHILOSOPHY

By

KEVIN REZA HAGHI
Norman, Oklahoma
2017

THEORY AND OBSERVATIONS OF BORES IN THE NOCTURNAL ENVIRONMENT OF THE GREAT PLAINS

A DISSERTATION APPROVED FOR THE
SCHOOL OF METEOROLOGY

BY

Dr. David D. Parsons, Chair

Dr. Alan A. Shapiro

Dr. Steven. E. Koch

Dr. Howard. B. Bluestein

Dr. Jonathan R. Kujawa

To my parents, Ali and Kerri Haghi: I have only succeeded because you let me fail; to my friends here and then: you are the color on my canvas; and to the ones who follow:

Ain't about how fast I get there
Ain't about what's waiting on the other side
It's the climb.
$\sim$ Miley Cyrus

Acknowledgements

I want to first thank my committee for assisting me throughout this process. To Dave, I can not thank you enough for all of the advice, encouragement and direction you provided. I have come to think of you more and more as a friend. I hope that we will have many more opportunities to open a bottle of champagne. To Alan, you are the reason I have had any success understanding the dynamics of the atmosphere. I will never forget the large amount of time you selflessly set aside for me. You are the scientist I hope to become one day. Steven, you have provided this research with great context and applicability. Every time we would spend hours talking about bores, I felt as if we were solving the problems of the world. For your help during PECAN, I can never thank you enough. I am not sure the bore tools and analysis would have been so thorough without you. To Howie, you are an inspiration to me. Your passion for every facet of meteorology reminds me why I am in this field-to appreciate and love mother nature. I hope that in the future we can find ourselves gawking together over a bore or a storm somewhere and simply embracing the unknown. To Jonathan, I know our involvement has been limited to Abstract Linear Algebra, but that way you teach re-inspired me to fall back in love with math.

To Larisa, you are the only reason I was able to master coding. You are also the reason I am able to graduate today. But more than anything, you have been the friend who navigated through graduate school by my side. I couldn't have picked a better mate. To Manda, you are the laughter that fills my heart. I can say PECAN would easily not have been as fun and as fulfilling without your comic relief and friendship. I hope to see you soon making a big difference in the world. To Robert, your strength and encouragement made my general exam and the graduate process manageable.

You talked me down off of many mental ledges and I am grateful for your friendship. To Hristo, your selfless interest in my research and your commitment to pushing the bounds of my understanding is invaluable. For your work, dedication, and genuine friendship, I thank you dearly. I know I'll hear great things about you in the future. Thank you to Kelton, specifically for the CAPE/CIN/LFC plots you made for me, but also for being a beacon of joy and excitement. I hope to hear good things about you coming out of Wisconsin.

To Becky, I can not explain how much you have been a calming soul to me. I hope you continue to help others along their way as you did for me. Christie, I would also not be graduating today if you had not stepped in at every oversight and got my butt in order! Thank you for always being so pleasant about it too. To Nancy, for dealing with Concur for me and always putting a smile on my face. I always know where to go for a piece of bubble gum. To Marcia, our time was cut short. But you are and will always be my favorite person in the whole world. To Debbie, I know we just got to know one another, but you're funny, you're quick witted; I wish we had more time. To Shelby, thank you for letting me scare you. That always brought an ironic calm to my day. I really am so lucky to have had you six.

To my friends and family, new and old, this is for you.

Table of Contents

List of Tables

List of Figures

Abstract

Accurate representation of bores in forecast models is a challenge. This challenge is of considerable interest to both the operational and the research communities because bores are capable of producing vertical displacements of air sufficient for initiating convection. While the research presented here does not offer improvements to forecast models, it lays a foundation for future numerical studies focused on the life cycle of nocturnal thunderstorms and the development of forecast tools designed to predict the onset of bore-initiated convection. Although the current research may be relevant to similar nocturnal convection systems in other regions of the world, the scope of this research is limited to the Southern Great Plains of the United States, where the forecast skill for nocturnal thunderstorms is relatively poor.

The datasets for the current study are predominantly from two field projects over the Great Plains. The first dataset is from the International H_20 Project (IHOP_2002), and the dataset is used to characterize the origin of radar fine lines in reflectivity as density currents, bores or other nocturnal phenomena. Subsequently, the frequency of bores observed in IHOP_2002 data is compared with a statistical model applied to hydraulic theory. The longevity of the observed bores and their preferred direction is compared with environmental winds and wave ducting properties using linear wave theory. Next, using the Plains Elevated Convection At Night (PECAN) dataset, a method for forecasting the generation of a bore and subsequent bore-initiated convection is proposed and tested on a 3 June 2015 case study. Two techniques based on hydraulic and linear wave theory are used as part of the method to forecast the vertical displacement of parcels.

The results indicate that density currents often generated bores in the nocturnal

environment observed during IHOP_2002. This result is consistent with hydraulic theory which characterizes the interaction between a density current and the observed environment as partially blocked, leading to the generation of a bore. Of the parameters used to evaluate the flow regime, the inversion properties had the most influence over changes in the flow regime with time. Once a bore developed, the maintenance of a wave duct is diagnosed with a two-layer model based on the Scorer parameter. The curvature of the horizontal wind with height is a component of the Scorer parameter and the curvature associated with the nocturnal low level jet was found to be the primary mechanism for maintaining a wave duct.

Convective instability parameters calculated from pre- and post-bore environment soundings are compared to gauge if a bore would initiate convection. The post bore soundings are generated with one of two techniques that mimic the parcel displacement through a bore. The technique based on hydraulic theory overestimates the displacement while the technique based on linear wave theory severely underestimates the displacement. These findings are part of a new line of investigation into the development of reliable tools to predict bore-initiated and bore-maintained convection.

Chapter 1

Introduction

1.1 Overview

The Southern Great Plains warm-season environment is relatively unique in that it exhibits a nocturnal maximum in convective precipitation (Kincer 1916; Wallace 1975; Maddox 1980; Heideman and Fritsch 1988; Dai et al. 1999; Dai 2001). A large portion of this rainfall occurs under weak synoptic forcing. This rainfall is attributed to envelopes of organized convection that develop over the eastern extent of the Rocky Mountains, grow upscale and propagate eastward over the Great Plains during the night (Maddox 1980, 1983; Carbone et al. 2002; Carbone and Tuttle 2008). The envelop of convection exhibits this life cycle frequently during the warm season months (Carbone et al. 2002; Carbone and Tuttle 2008). Studies have indicated that large-scale mechanisms inherent to the Great Plains environment may modulate this envelope of organized convection (Trier et al. 2010; Li and Smith 2010).

Large-scale mechanisms that assist the development of nocturnal convection are not capable on their own of producing the observed amount of rainfall. In conjunction with larger-scale mechanisms, a study by Heideman and Fritsch (1988) demonstrated that mesoscale mechanisms and convective feedbacks account for a significant portion of the observed rainfall (however Heideman and Fritsch 1988 did not specify which mechanisms are responsible for the rainfall). Various mesoscale mechanisms and convective feedbacks have been proposed in studies to account for a portion of the

observed rainfall from convective systems, but unable to account for all of it. (Geerts et al. 2016). An effort to quantify the range of influences on the nocturnal convective life cycle is currently ongoing within the research community. This problem is of great importance to the research community because numerical model products reach their lowest skill during the warm summer season (Carbone et al. 2002), and can in part be attributed to the limitation of parameterization schemes to depict the life cycle of the propagating systems (Davis et al. 2003; Clark et al. 2007; Surcel et al. 2010) and representation of the nocturnal boundary layer (Holtslag et al. 2013).

The convective feedback mechanism examined in the current study is a bore. A bore is one consequence of an obstruction that blocks stable fluid from ascending over the obstacle's crest. When some or all of the fluid is unable to ascend over the obstacle, a sudden jump arises in the stable fluid depth (Long 1954; Houghton and Kasahara 1968; Rottman and Simpson 1989; Baines 1984). An obstruction to the fluid can be a solid object such as a mountain or another more dense fluid. Bores are observed in various fluids over the globe: within rivers (Cummins et al. 2010), oceans (Kobbé 1899; Lynch 1982), and the atmosphere (Nagpal 1979; Clarke 1984). In the atmosphere, bores are frequently generated from density currents, such as cold fronts (Tepper 1950; Koch and Clark 1999), katabatic flows (Clarke 1972; Clarke et al. 1981; Smith et al. 1986), and convective outflows (Koch et al. 2008a,b; Coleman and Knupp 2011). Over the Southern Great Plains, convective outflows are a known catalyst for bore formation during the night (Wilson and Roberts 2006; Geerts et al. 2016).

The presence of a bore implies a rapid change to the depth of the stable layer accompanied by appreciable vertical motions. These vertical motions have been documented to destabilize the nocturnal environment (Koch and Clark 1999; Coleman and Knupp 2011). In two benchmark idealized numerical simulations, bores appear to develop from convective outflows that are generated by a squall line under conditions akin to the Great Plains nocturnal environment (Parker 2008; French and Parker

2010). These simulations have implications for the present study because the simulated bores appear to assist in the maintenance of the ongoing squall lines (Parker 2008; French and Parker 2010). Recently, a WRF-ARW simulation of an observed MCS demonstrated the development of a bore along the extent of its convective outflow (Blake et al. 2017). In their study, the bore aided ongoing convection by increasing the convective instability through adiabatically lifting parcels (Blake et al. 2017). This study by Blake et al. (2017) was the first simulated MCS based on observed conditions to demonstrate a process for bores to maintain a nocturnal system, previously only documented in observational studies (Tepper 1950; Koch and Clark 1999; Wilson and Roberts 2006) and the two benchmark idealized studies (Parker 2008; French and Parker 2010). While it appears that the potential for bores to positively contribute to the production of rainfall at night through convective initiation and maintenance, there are some questions yet to be addressed:

1. At what frequency does a density current generate a bore over the Southern Great Plains?

2. Once a bore forms, are they long-lived and, if so, how are they commonly maintained in the nocturnal environment?

3. Can a prognostic tool be developed to predict bore generation?

4. Does this prognostic tool accurately describe vertical displacement of air?

5. Can this tool help distinguish between environments that are and are not conducive for bore-initiated convection?

These questions will be addressed by the following research using well known theoretical models adapted from hydraulic and linear wave theory and compared against observations of bores and their environment. The work herein is different from other studies because (i) observations of bores are addressed in a systematic

approach, which allows generalizations to be made about the frequency of bores in the nocturnal environment; (ii) theoretical parameters are resampled by applying a bootstrap to determine how likely a bore is to form and be maintained in the observed nocturnal environments; (iii) it is the first time theory is used in a case study for prognostic determination of bore-initiated convection. The dataset used for the first part of this study is from the International H_20 Project (IHOP_2002), which is suitable for studying bores because it includes the Oklahoma Mesonet surface network (Brock et al. 1995), Automated Surface Observing Systems (ASOS), and special soundings launched from 5 different sites at 3 hour intervals (Weckwerth and Parsons 2006). The dataset for the second part of this study comes from the Plains Elevated Convection at Night (PECAN) (Geerts et al. 2016). This dataset will be used to test a proposed methodology that predicts bore-initiated convection.

The dissertation is organized into sections discussing the following topics: (1) An introduction to the unique conditions of the nocturnal environment and the possible mechanisms that produce nocturnal convection; (2) The derivations of hydraulic and linear wave theory; (3) The methods describing the application of theories to observations; (4) A systematic study of atmospheric bores during IHOP_2002; (5) A case study using the bore-initiated convection tools; (6) Conclusions.

1.2 Southern Great Plains nocturnal convection

1.2.1 Environmental conditions

To the west of the Southern Great Plains lies the Rocky Mountains, oriented nearly north-south. The slope of the Rocky Mountains induces vertical motion that generates clusters of storms. These storms can eventually grow upscale into convective systems (Jiang et al. 2006; Carbone and Tuttle 2008; Pritchard et al. 2011). Additionally, the terrain along the mountain can act as an elevated heat source, producing potential

temperature anomalies in the mid-level flow (Li and Smith 2010). These temperature anomalies have been proposed to favorably interact with deep shear over the Great Plains and induce positive vertical motions (Li and Smith 2010). These mechanisms either assist the development of new convection or work in concert with the preexisting storms. These convective cells organize into convective systems and propagate eastward over the Great Plains.

As the convective systems move eastward, they encounter warm, relatively moist parcels that are transported during the night by the nocturnal low-level jet (NLLJ) northward (Bonner 1968; Stensrud 1996; Arritt et al. 1997; Jiang et al. 2007). The NLLJ may interact favorably with frontal boundaries or the storms themselves to generate new or maintain existing nocturnal convection (Tuttle and Davis 2006). Over the Great Plains, this source of moist warm air is the Gulf of Mexico.

The NLLJ develops over the Great Plains due to two conditions. First, the slope along the western extent of the Great Plains (where the gradient of terrain points towards the Rocky Mountains) is appreciable enough to induce horizontal temperature gradients, as discussed in Holton (1967) and Parish et al. (2010). In Parish et al. (2010), it is shown that the generally warmer air to the west along the slope induces a northerly thermal wind at 850mb, reaching its peak in the afternoon, strengthening the southerly component of the geostrophic wind below 850mb. Second, the boundary layer decouples from the surface layer during the transition from afternoon to night due to the decrease in turbulent kinetic energy through the development of a stable boundary layer (Blackadar 1957). Blackadar (1957) demonstrated that the response to the reduction of friction is an ageostrophic flow, which causes the low-level horizontal flow to undergo a process of geostrophic adjustment. The adjustment manifests as a clockwise inertial oscillation of the horizontal winds (Blackadar 1957). Recently, these two mechanisms have been theoretically unified to produce the Great Plains NLLJ with qualitatively good agreement with observations (Shapiro et al. 2016).

1.2.2 Nocturnal maximum in precipitation

The Great Plains region offers a scientific challenge to meteorologists because of its relatively unique cycle of convection and associated rainfall (figure 1.1). Unlike most regions of the United States, the Southern Great Plains' maximum in convection and precipitation occurs after nightfall during the warm seasons of summer (Kincer 1916; Wallace 1975). The nocturnal maximum in precipitation is argued in part to be the result of a specific, yet frequent set of conditions over the Great Plains: a weak synoptic environment, with northwesterly flow at mid-levels and southerly low-level flow (Trier et al. 2010). This large-scale environment is in contrast to the synoptically-driven weather of spring (Heideman and Fritsch 1988; Augustine and Howard 1991). During the daytime under weak synoptic forcing, gentle upslope flow develops in the lee of the Rocky Mountains due to a mountain-valley circulation (Toth and Johnson 1985; Trier et al. 2010). The upslope flow leads to convective development along the Rocky Mountain range (Jiang et al. 2006; Carbone and Tuttle 2008; Pritchard et al. 2011). As nighttime sets in, the conditions of upslope flow reverse and a drainage flow develops (Toth and Johnson 1985; Trier et al. 2010). An envelope of convection moves eastward towards the Great Plains as part of the large-scale mountain-valley circulation (Bleeker and Andre 1951; Wetzel et al. 1983; Bonner 1968; Cotton et al. 1983; Carbone et al. 2002; Hane et al. 2003; Carbone and Tuttle 2008; Trier et al. 2010, etc.; figure 1.2), transitioning to an organized convective system, such as a Mesoscale Convective System (MCS), over the Great Plains region (Easterling and Robinson 1985). MCSs account for 30% to 70% of this nocturnal rainfall, with an even higher contribution from MCSs during drought years (Fritsch et al. 1986). Studies by Carbone et al. (2002) and Carbone and Tuttle (2008) have used the National Center for Environmental Prediction (NCEP) North American Regional Reanalysis (NARR) radar composites to support the claims that this cycle of convection is in-

deed responsible for a large portion of the nocturnal maximum.

Accurate predictions of MCSs over the United States Great Plains are of great importance to the weather and regional climate communities and to the public. MCSs create dangerous flooding events causing fatalities, destruction to property, and erosion (Stensrud et al. 2009). From a 10-year average, flooding claims 75 lives (http://www.nws.noaa.gov/om/hazstats.shtml) annually with nearly 4 Billion dollars in damage (https://www.floodsmart.gov/floodsmart/pages/flood_facts.jsp). However, MCSs also provide beneficial, necessary rainfall for agriculture and livestock. Prediction of nocturnal precipitation is not of just national importance- Laing and Fritsch (1993a,b); Laing and Michael Fritsch (1997) and Miller and Fritsch (1991) identified particularly similar MCS development over various parts of the world, specifically South Africa (Farquharson 1939), South America (Vera et al. 2006) and South China (He et al. 2016).

Studies using numerical weather prediction models to recreate the nocturnal maximum in precipitation have produced mixed results. Davis et al. (2003) attempted to recreate the observed nocturnal maximum in precipitation, and indeed captured the afternoon maximum over the lee of the Rockies that transitioned eastward at night. However, the convection tended to initiate too early, often out of phase with the observed diurnal cycle. This failure was attributed to the inability of the convective scheme to capture the observed mode of convective system propagation. As with regional numerical weather predication models, Surcel et al. (2010) tested the Global Environmental Multiscale (GEM) model's ability to reproduce the nocturnal maximum in precipitation and found that the nocturnal maximum is out of phase with diurnal circulation in insolation (their study also illustrated how the warm-season mechanisms for convective propagation are dynamically different from the spring). But convective parameterizations in coarse grid models are not the only source of error. Clark et al. (2007) compared convective resolving models with non-convective

resolving models and found both had issues, but for different reasons. While the convective resolving model more accurately represented the nocturnal maximum, it also over-predicted the amount of rainfall. The non-convective model in the Clark et al. (2007) study was similar to the results of Davis et al. (2003), as the model struggled with timing of the diurnal cycle of precipitation.

Large-scale models also struggle with accurate representation of the stable boundary layer. In contrast to the well-modeled daytime boundary layer, the nocturnal boundary layer is "typically too deep, the nocturnal jet maximum is too weak and the turning of the wind with height is too little" (Holtslag et al. 2013). The errors are magnified during the warm summer months (Davis et al. 2003). Even if the nocturnal boundary layer is accurately modeled, it is unclear if reducing these shortcomings would significantly improve the life cycle of an organized nocturnal system. Because an accurate representation of nocturnal convection in forecast models has yet to be achieved, it is imperative to improve the understanding of physical mechanisms behind convective initiation and maintenance of nocturnal convection. This knowledge is a foundation for future scientific explorations-whether they be theoretical, observational or numerical-and a path towards improving the representation of nocturnal convection in numerical models.

1.2.3 Proposed mechanisms of nocturnal convection

The research community has keyed in on several mechanisms proposed to explain nocturnal convection over the Great Plains. For example, the mountain-plains solenoid is evidenced with multiple observational and numerical platforms: satellite, surface, and analyzed synoptic maps (Wetzel et al. 1983); the Colorado State University's South Park Area Cumulus Experiment (Cotton et al. 1983); sounding and the Colorado State University Regional Atmospheric Modeling System (Wolyn and Mckee 1994); and the North American Regional Reanalysis (NARR) data (Li and

Smith 2010). The mountain-plains solenoid exhibits a positive correlation with derived nocturnal rainfall from composited radar data (Carbone and Tuttle 2008). Other research has explored how the elevated heating along the Rocky Mountains during the daytime causes potential vorticity (PV) anomalies that drift eastward (Li and Smith 2010). These PV anomalies are hypothesized to generate lift by deforming theta surfaces in an environment with variations in vertical wind shear, leading to vertical motions within the lower troposphere and the triggering of convection Li and Smith (2010). However, the authors admittedly state that any one mechanism is insufficient for reproducing the observed nocturnal maximum of convection.

To the east of the Rockies, a NLLJ transports high theta-e[1] air over the Great Plains from the Gulf of Mexico. (Higgins et al. 1997). In the absence of a frontal boundary, the MCS maintenance appears to be highly correlated with the NLLJ, often at its terminus (Tuttle and Davis 2006; Arritt et al. 1997). When a quasi-stationary E-W oriented front is present, at times generated from the convective outflows of the previous day's convection, the NLLJ will ride over the front and vertically transport relatively unstable parcels for ingestion into ongoing convective systems (Trier and Parsons 1993; Trier et al. 2010). As a result, NLLJ is frequently is observed on days that generate nocturnal convection (Carbone and Tuttle 2008). [2]

Once convection has organized, various convective feedbacks may cause more localized ascent to assist convective maintenance. Past studies have argued that a gravity wave mechanism, called wave-CISK, is capable of maintaining an organized convective system (Lindzen and Tung 1976a; Raymond 1984; Emanuel 1983; Xu and Clark 1984; Carbone et al. 2002). In an updraft of a thunderstorm, the vertical gradient of diabatic heat release and vertical velocity can fall out of phase with one another due to the presence of vertical wind shear. This phenomenon is a favorable condition

[1] theta-e is the equivalent potential temperature, defined in section 7

[2] For a historical review of jets, see Stensrud (1996)

for generating tropospheric gravity waves with positive growth rates (Emanuel 1983). These gravity waves are often observed to move on the order of 15-20 ms^{-1} and with wavelengths on an order of 100s of kilometers. Some wave-CISK modes move 2 to 5 times faster in analytical models than the propagation speeds of observed nocturnal systems (Emanuel 1983; Nehrkorn 1986). For this reason, wave-CISK acting alone to generate convection has been generally discounted; yet the principal still remains. For example, Houze (2004) attributed the slantwise ascent ahead of tropical MCSs as a byproduct of diabatic heating-induced gravity wave responses, a similar finding to other tropical MCS research studies (Mapes 1993). However, the results of tropical studies are often difficult to verify because direct observations are a challenge to obtain.

Within a similar branch of research, Fovell et al. (2006) has used the concept of discrete propagation as a framework for explaining some observations of convective systems being fed by gravity wave-induced convective cells riding along surface inversion. These gravity waves consist of a long and short period gravity wave mode. The long period gravity wave is a subsidence wave, propagating outwards first and creating sinking motion (Raymond 1983). The short period gravity wave induces rising motion within the lower half of the troposphere and downward motion within the upper half of the troposphere (Raymond 1983). These gravity waves are argued to be the result of an interaction between a critical layer embedded within the convective anvil and the surface inversion (Fovell 2002; Fovell et al. 2006). [3] Propagation modes, which expand according to their internal gravity wave speeds (Tripoli and Cotton 1989), can be maintained through the continuation of latent heat release within the updraft (Tripoli and Cotton 1989; Fovell 2002; Fovell et al. 2006).

Conventional approaches to convective maintenance during the day (Rotunno-

[3] While Fovell et al. (2006) does not explicitly mention wave-CISK, the gravity waves discussed within Fovell et al. (2006) are analogous to the propagation modes of wave-CISK.

Klemp-Weisman framework-RKW, Rotunno et al. 1988; Weisman and Rotunno 2004; Bryan and Rotunno 2014b) have been applied to nocturnal case studies. Convective maintenance during the day often requires a balance of forcing between the baroclinic vorticity generated along a density current front and the environmental shear (Rotunno et al. 1988). While RKW theory has shown promise to explain convective maintenance during the day, as the nocturnal boundary layer stabilizes the density difference between the density current and its environment diminish. As the CAPE vanishes in the nocturnal boundary layer, simulations show that the convection transitions to an elevated state (Parker 2008). As a result, the RKW balance diminishes through the night. However, the development of a bore in French and Parker (2010) simulations lead to a new shear balance between the bore and the shear above the jet. As in Parker (2008), French and Parker (2010) simulated squall line remained locked onto the bore. It is unsure, based on these simulations alone, how often a convective outflow develops an atmospheric bore and how often this bore assists in driving the convective system. These questions will be addressed in this dissertation.

1.2.4 Current understanding of bore-initiated convection

While (Parker 2008; French and Parker 2010) are some of the first numerical models to elucidate the process of bore-assisted convection, the maintenance of convection by bores was observed in earlier observational work. Tepper (1950) was one of the first studies to observe a cold front produce a "pressure jump line." This pressure jump line is now widely referred to as a bore in the subsequent literature (Smith 1988; Rottman and Simpson 1989; Houze 2004; Knupp 2006; Coleman and Knupp 2011). Other studies provide credible observations that bores favorably destabilize parcels through upward vertical displacement and subsequently those parcels were ingested into the updraft of ongoing convection (Koch and Clark 1999; Koch et al. 2008b). While Koch and Clark (1999) also demonstrated that a bore may provide upwards displacements

that alone are not capable of maintaining a storm, the destabilized air can be lifted by a trailing density current into the convective system. Together, the bore and the density current can maintain a convective system. Koch and Clark (1999) also recognized that the shear in the NLLJ interacted with the leading wave in the bore to enhance lifting. More recently, Blake et al. (2017) modeled a nocturnal MCS using the WRF-ARW that developed a bore along its convectively active portion, and demonstrated that parcels had their LFC heights reduced as they passed through the bore. This behavior was noticed as well in observations by Coleman and Knupp (2011).

Convective initiation episodes also contribute to the nocturnal maximum in precipitation. A systematic study using radar fine lines in reflectivity observed during IHOP_2002 identified boundaries which initiated convection and eventually grew upscale into an organized system (Wilson and Roberts 2006). The study delineated the initiation episodes into either surface based or elevated. Outside of frontal boundaries, density currents accounted for the highest frequency of convective initiation (figure 1.3 a). Additionally, density currents were highly correlated with longer-lived organized convection (figure 1.3 b). As the night progressed, elevated convective initiation occurred more frequently (figure 1.3 c).

While Wilson and Roberts (2006) indicated that bores do not play a major role in convective initiation, their study did not include the use of thermodynamic data to examine if a single fine line in radar reflectivity deemed to be a density current did indeed have traces of a bore in surface observations. If Parker (2008) and French and Parker (2010) are correct, the maintenance of a convective system along its outflow may be assisted by bores that develop along the convective outflow. Consequently, the Wilson and Roberts (2006) finding that nocturnal systems, which develop a gust front persist longer in the night, may then be partially attributable to the presence of an atmospheric bore. This lifting may also provide a mechanism for convective systems to be maintained when the density difference between the convective out-

flow and the environment become small and the convective outflow dissipates, as in Parker (2008) and French and Parker (2010). An reexamination of the convergence boundaries studied in Wilson and Roberts (2006) that include surface data for categorizing boundaries could reveal that bores are ubiquitous to the nocturnal environment. Most importantly, if bores are supported frequently by the nocturnal environment, then there need to be more studies that examine the role of bores in the initiation and maintenance of nocturnal convection.

As mentioned before, the lift experienced behind the leading edge of a bore destabilizes the nocturnal stable layer (Coleman and Knupp 2011; Koch and Clark 1999). Koch and Clark (1999) was able to take advantage of vertical profilers to reconstruct the expected parcel displacements, but only used theory as a diagnostic tool. If prognostic tools were developed for forecasters , then decisions about whether convection will or will not occur along a bore could be made. The most viable tool for operational nowcasting should only depend on observational measurements or model output that are readily accessible to a forecaster.

The duration of gravity waves associated with a bore is typically explained by the presence of a wave duct (Crook and Miller 1984; Crook 1988; Koch et al. 1991; Koch and Clark 1999; Goler and Reeder 2004; Zimmerman and Rees 2004; Koch et al. 2008a; Martin and Johnson 2008). Specific to the Great Plains, studies have illustrated that the NLLJ may play a discriminating role in determining wave trapping through the curvature term (Koch and Clark 1999; Martin and Johnson 2008), but it is unclear if the curvature is the dominant mechanism for trapping low-tropospheric gravity waves. Understanding the dominant mechanism for wave trapping is an important frontier to explore since the volume of vertically displaced air is partially dependent on the longevity of a bore. Additionally, because the NLLJ is closely linked to nocturnal convection, the interplay between a bore and the NLLJ may provide useful insight into convective maintenance.

Another mechanism proposed to be associated with the maintenance of gravity wave modes is a critical level wave reflection. A critical level is where the wind speed and direction are equal to a supposed gravity wave mode. If this critical level appears in a sheared layer where the Richardson number < 0.25, Lindzen and Tung (1976a) have shown that the wave over-reflects, extracting energy from the background flow. In this case, positive growth rates are theorized to maintain and amplify the gravity wave modes. These mechanisms should be explored to identify the dominant modes of wave trapping.

1.3 Goals of current research

(i) Assess the frequency of bores over the Southern Great Plains.

To extend the work of Wilson and Roberts (2006), the current research incorporates thermodynamic surface observations into the categorization of the 152 observed boundaries in radar reflectivity. This approach provides a more accurate determination of bore frequency. The frequency of bores observed within IHOP_2002 will serve as a proxy for determining how often the environment is favorable for the development of a bore.

(ii) Relate the frequency to the environmental flow regime.

The purpose of evaluating the flow regime is two-fold. First, there is a desire to examine how well a commonly used variation of hydraulic theory reproduces the frequency of bores observed in the systematic study. Second, if the variation of hydraulic theory appears to agree with observations, then an analysis of the distribution of observed flow regimes will reveal information about some factors that are favorable for bore generation. Typically, the generation of a bore is studied through hydraulic theory using a two-layer variation (Rottman and Simpson 1989). Rather than using proximity soundings ahead of a bore to diagnose an individual case, this approach uses 5 differ-

ent locations within the IHOP_2002 domain to determine the tendency of outflows to produce bores during the entire field campaign. This approach employs a statistical model to sample observations and reproduce the theoretical distribution of the flow regime. This statistical model is a bootstrap resampling. The highest values in the 2D density estimate of the bootstrap resamplings are interpreted as the preferred flow regime.

(iii) Identify the maintenance mechanism for bores.

There are two mechanisms that are hypothesized to maintain gravity waves in the nocturnal environment. They are the curvature of the horizontal wind with height associated with the NLLJ and a critical level embedded in a heavily sheared layer. A comparison between the direction of bores and various bulk shear vectors of the environmental winds will be shown to exhibit a high correlation. Based on these findings, the curvature (the second derivative of the horizontal wind with height) contained within the Scorer parameter and any critical levels are examined in 13 soundings ahead of bores observed during IHOP_2002. These theoretical constructs will be derived in section 2 and 3.

(iv) Construct sounding profiles that reflect parcel displacement.

A tool has been developed to provide guidance for forecasters to determine if a bore will develop from a density current and if that bore will generate more convection. This tool is tested on a June 3 2015 bore. First the flow regime is examined with the previously mentioned hydraulic theory. If the flow regime is conducive for bore development, then the bore height and bore speed are calculated using hydraulic theory. The calculated bore height and bore speed are used in two techniques adapted from hydraulic and linear wave theory. These techniques theoretically lift parcels to mimic the changes to vertical thermodynamic profiles. These profiles are referred to as "disturbed." The hydraulic theory is applied when a bore has first developed and linear wave theory is applied to a bore that has pulled far away from its density current.

These methods are used for pure heuristic purposes. The methodology is discussed in section 3.

(v) Analyze convective instability parameters to predict bore-initiated convection.

Values of CAPE, CIN, and the vertical distance between a parcel's displaced height and its LFC (LFC-LPL) are calculated from bore-modified soundings.[4] The disturbed profiles are compared with undisturbed soundings to gauge if the destabilization will lead to convective initiation. The results are then compared with radar reflectivity and wind profiler observations to determine if a forecaster would have correctly identified bore-initiated convection. The shortcomings of the methods are then discussed. This study is the first of its kind to use theory for the prediction of bore-initiated convection.

1.4 Background

1.4.1 Density currents

Density currents are flows driven by horizontal differences in density between two fluids. The denser fluid spreads outward at a rate proportional to the force of gravity acting over its depth (Benjamin 1968). As a density current spreads out, it will develop a nose at its leading edge (Craig Goff 1976). Just behind the nose along the interface of the density current and the environmental fluid is an area of enhanced mixing (Simpson 1997). This description works well in environments where the density difference between the cold and warm fluid is small (Prandtl 1952).

Often the convergence of warmer ambient air and colder air at the leading edge of a density current modifies the shape, size and intensity of the density current flow. In the simplest of cases, opposing unidirectional flow will retard the density current speed and deepen the density current head, while the opposite is true for density current aligned with the unidirectional flow (Liu and Moncrieff 1996). Low-level shear

[4] See section 7.1 for explanation of abbreviations of CAPE, CIN, LFC, and LPL

(Liu and Moncrieff 1996; Bryan and Rotunno 2014a) and stratification within the environmental air (Liu and Moncrieff 2000) are two additional documented environmental factors that control the shape of the density current. For example, the fluid within a density current head can vertically elongate if environmental shear whose horizontal vorticity is of an opposite orientation to the baroclinic vorticity within the density current head. However, environmental stratification has a counteractive response. Environmentally lifted stable air over a density current reduces the depth of the density current head (Liu and Moncrieff 2000). Under large stratification the density current head will take on the shape of a wedge (Liu and Moncrieff 2000).

Since convective outflows are assumed to behave as density currents (Simpson 1997), environmental complexities similar to those just described often make accurate prediction of their height and speed difficult. Even more challenging is the lack of dense vertical profiling networks in the Great Plains. Instead, theoretical calculations of the speed and height of density currents must be used that rely on surface observations. For this reason, our research will approximate the properties of a convective outflow by using surface data and assuming the convective outflow depth is well approximated by a hydrostatic equation detailed in the appendix of Koch et al. (1991). The method and shortcomings are discussed in section 3.

1.4.2 Bores

1.4.3 Bore generation

The formation of a bore from a convective outflow is studied in literature with hydraulic theory (Rayleigh 1914; Long 1954; Baines 1984; Rottman and Simpson 1989; Baines 1995; White and Helfrich 2012).[5] When a thunderstorm produces a downdraft that intrudes the stable boundary layer, the downdraft spreads out along the sur-

[5]The analog to a bore in hydraulic theory is a hydraulic jump.

face. The convective outflow can effectively block stable air from rising over its head. Blocked flow is a necessary condition for the generation of atmospheric bores (Long 1954; Houghton and Kasahara 1968; Baines 1984; Rottman and Simpson 1989) determined by two essential flow parameters: the upstream Froude number Fr_o and non-dimensional height H_o [6] (Rottman and Simpson 1989).

A diagram based on two-layer hydraulic theory, originally developed from Davies (1979), is shown in figure 1.5. This plot is useful for diagnosing the nature of gravity wave disturbances whose horizontal extent (horizontal wavelength) is much larger than its vertical extent (Baines 1995). For a gravity wave disturbance in the nocturnal boundary layer over the Great Plains, this is appropriate. The conditions conducive for bore development are when the flow in the stable boundary layer is supercritical and transitions to subcritical before reaching the top of the density current (Long 1954; Rottman and Simpson 1989; Baines 1995). If the flow in the stable layer remains supercritical over the entire depth of the density current ($Fr > 1$), then the flow will not be blocked and the fluid depth will deepen as its passes over the density current (Rottman and Simpson 1989; Baines 1995). The opposite is true of subcritical flow. The response of the fluid to the subcritical flow ($Fr < 1$) is a decrease in the depth of the surface layer dips as it passes over the depth of the density current. (figure 1.5 d regime). Both of these states are considered to be steady states and no fluid is blocked. [7]

For long period gravity waves,[8] the phase velocity is independent of the horizontal wavelength (Lighthill 1978; Pedlosky 1987), i.e. no wave dispersion. When there is no wave dispersion, the group velocity and the phase velocity are aligned in the same direction (Pedlosky 1987). This alignment implies that the energy flux associated

[6] the Froude number Fr and non-dimensional height H are defined in section 7, and the mathematical descriptions are found in section 3.2

[7] see section 2.3.1 for a description of supercritical and subcritical flow

[8] see section 2.3.1 for a description of long period gravity waves

with a gravity wave is positive in the direction of gravity wave propagation (Gossard and Hooke 1975; Baines 1995). In supercritical flow, gravity waves along the fluid interface are unable to propagate upstream and therefore are advected downstream. This implies that any energy associated with gravity waves is transported downstream towards the bore. In the subcritical flow, a gravity wave may propagate upstream and downstream. Gravity waves that propagate upstream will do so until they reach the transition between supercritical and subcritical flow. At the bore head where this transition occurs, there is no possibility for the gravity wave to move through the location where $Fr = 1$. But since the energy cannot disappear, the energy is transferred into potential energy to steepen the waves at bore head. As a result, the depth of the bore head increases. There is a limit to the deepening before dissipation due to turbulence converts the potential energy into heat (Long 1954; Christie et al. 1979; Klemp et al. 1997; White and Helfrich 2012).

The flow regime for the development of the jump occurs in regime b or c (figure 1.5). These regimes are either partially or completely blocked, insinuating that some or all of the stable layer fluid does not ascent over the density current. Fr_o and H_o intuitively make sense as parameters for judging if a bore will form. If the height of an obstruction is raised or the fluid depth decreases, the fluid will have to overcome a deeper vertical distance to rise over the obstruction. To overcome this obstruction, more kinetic energy is required. If the incoming fluid speed is reduced or the density current speed decreases, then less kinetic energy is available for the fluid to rise over the density current. These are a few factors that are important for determining if a bore will form.

When a bore is generated, vertical expansion creates a semi-permanent displacement of the stable boundary layer. This expansion must induce vertical motions that move upstream (Carbone et al. 1990; Wakimoto and Kingsmill 1995; Koch and Clark 1999). Consequently, a bore will act as an impulse traveling away from the convec-

tion and modifying the air flowing towards the associated convective outflow. The conditions under which the jump moves ahead at a speed C_b or moves at the same speed as the density currents are derived in section 2.

1.4.4 Bore maintenance

It has been show that an arbitrary initial disturbance within a wave guide (herein called a wave duct) will evolve into a finite packet of waves (Christie 1989, figure 1.6). The gravity waves can persist indefinitely until the dissipative effects become important and the gravity waves quickly diminish through mixing between the inversion and the fluid along the bore interface (Lindzen and Tung 1976a). The Scorer parameter, a diagnostic tool used to identify wave ducts, has been used by Crook (1986, 1988); Koch and Clark (1999); Koch et al. (2008a,b); Marsham et al. (2011); Coleman and Knupp (2011) to demonstrate how gravity waves associated with a bore can become trapped. The process is one form of internal reflection (Lindzen and Tung 1976a; Clark and Peltier 1984; Alexander et al.; Tutig 1992; Lane. and Clark 2002), where a wave duct selects waves with a given horizontal and vertical wavelength to persist. A large and positive Scorer parameter layer adjacent to the ground topped by a very small or negative Scorer parameter layer is a preferable profile for trapping surface gravity waves. Positive layers of Scorer parameter support vertical wave propagation while negative Scorer parameter layers inhibit vertical wave propagation (Scorer 1949). Given a favorable profile, an infinite packet of waves can be trapped within the wave duct (Baines 1995).

In the atmosphere, the two-layer linear wave concept is limited. First of all, the atmosphere is more complex than two layers, often exhibiting multiple elevated stable layers and vertical wind shear profiles that create multiple couplets of positive and negative Scorer parameter. Second, it has been shown that the growth rate is asymmetric according to a gravity wave's vertical wavelength (Lindzen and Tung 1976a).

Third, the response with the largest wavelength tends to become the dominant mode due to dissipative effects (Lindzen and Tung 1976a). Last, gravity waves within the atmosphere can become nonlinear (Christie et al. 1979). When the nonlinear components of the wave dominate, linear wave theory no longer well describes the observed vertical motions and wave speeds. These nonlinear waves are often attributed to the behavior of a solitary wave (Christie et al. 1979; White and Helfrich 2012; Christie 1989; Koch et al. 2008a,b; Knupp 2006, figure 1.7 c and d).

When gravity waves become more nonlinear, they steepen and move faster than a linear wave of equal horizontal wavelength (Christie 1989). The steepening also implies that the gravity waves behave less as long period gravity waves becomes and the waves become dispersive, with the longest wavelengths traveling the fastest Baines (1995). When the dispersive and nonlinear forces are in balance, a solitary wave structure is well maintained (Christie 1989). This balance is an important concept for observing bores in the atmosphere. If a bore does evolve into a packet of solitary waves, it will move, by definition, faster than the long period gravity waves and therefore be able to move against the supercritical flow. For this reason, solitary waves are observed with no permanent displacement in the inversion layer (Christie et al. 1979; Christie 1989; White and Helfrich 2012). This phenomenon has been observed in the atmosphere (Knupp 2006; Koch et al. 2008b,a), and for this reason this research will attempt to delineate between a bore and a solitary wave. However, this work is limited in our discussion about solitary waves due to our reliance at this point on linear wave theory. These shortcomings will be discussed in section 5 and 6.

Components of the nocturnal environment that are important for wave maintenance are the stable boundary layer and the second derivative of the horizontal wind with height. For this reason, this study will attempt to draw parallels between the presence of the inversion, the NLLJ and the presence of bores in the environment. In this research, there is no attempt to distinguish between what mechanism(s) is/are

producing the NLLJ, but instead define the NLLJ as a layer of winds within and just above stable boundary-layer with a maximum greater than or equal to 10 m/s.

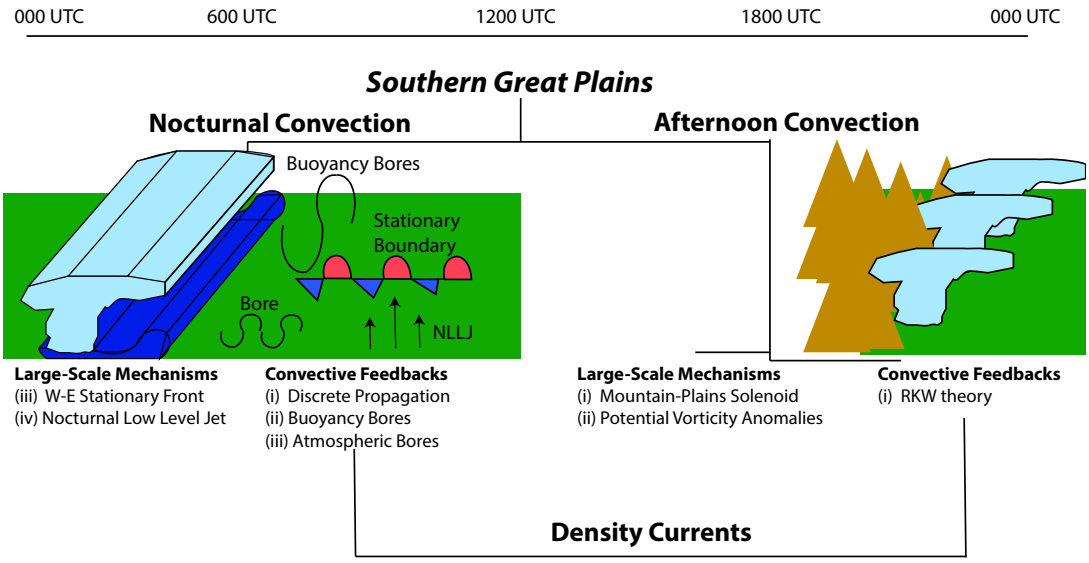

Figure 1.1: A depiction of the life-cycle for warm-season convection over the Southern Great Plains. Illustrations are instructive; not drawn to be visually accurate.

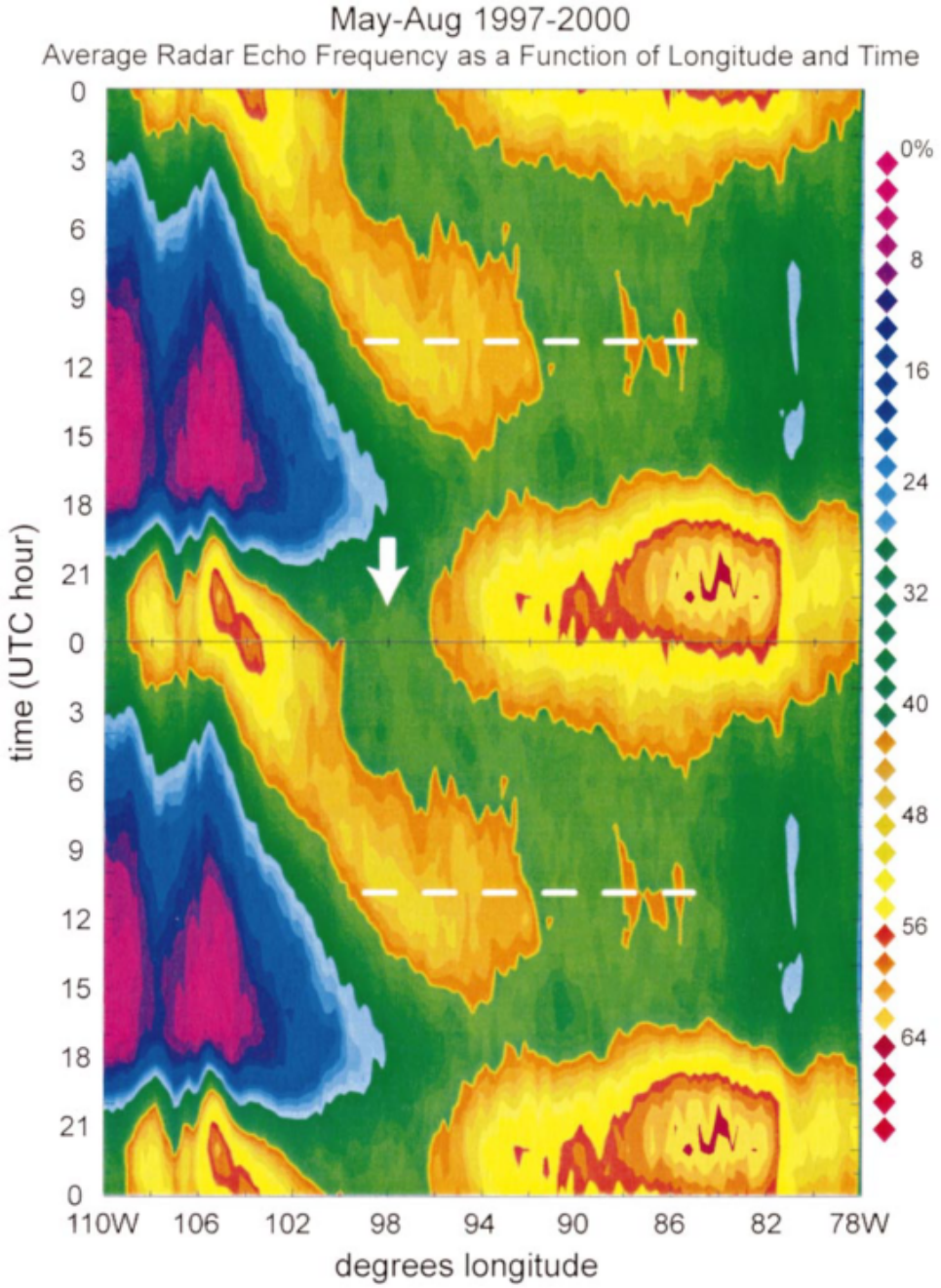

Figure 1.2: Diurnal echo frequency *Hovmoëller* diagram for the entire period of record (1997-2000). The diurnal cycle is repeated twice for clarity across the UTC day boundary. The scale corresponds to the percentage of days during which precipitation echo is present at the given longitude-UTC hour coordinate. Figure from Carbone et al. (2002)

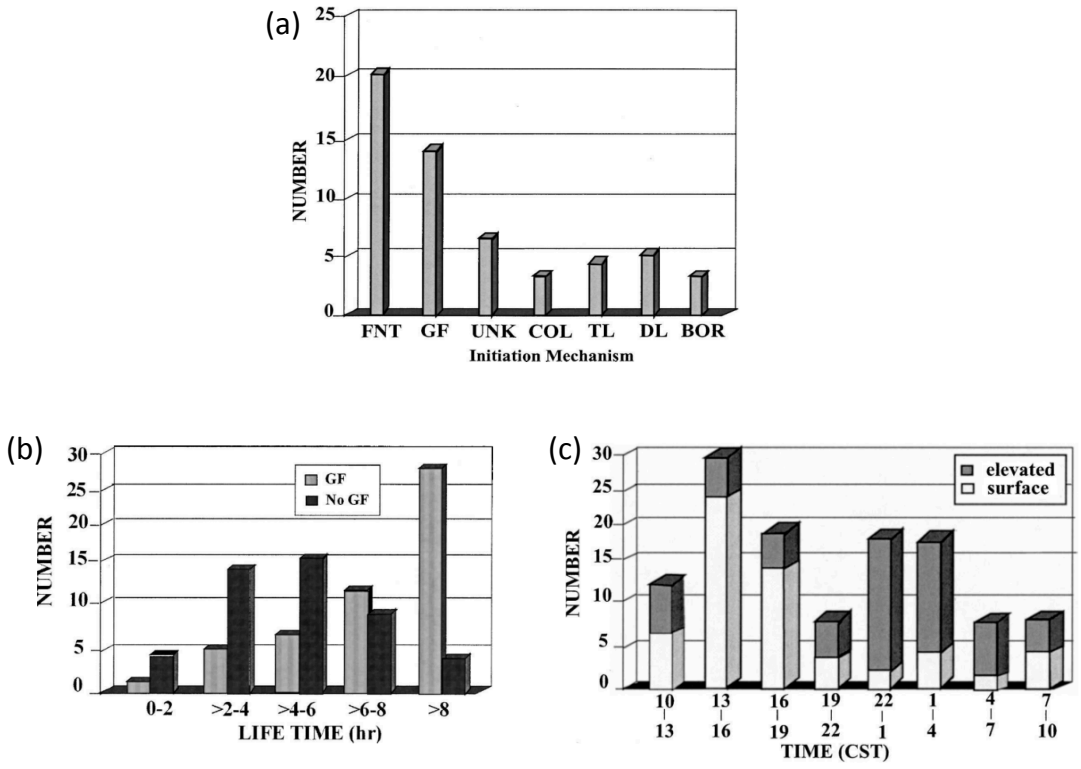

Figure 1.3: Statistics calculated from a systematic study using IHOP_2002 data: a) the chart of the frequency a boundary observed in radar initiated convection that grew upscale (FNT-front,GF-gust front,UNK-unknown,COL-collision,TL-trough,DL-dryline,BOR-bore); b) the lifetime of an organized system that either did or did not developed a mesoscale gust front; c) the difference between elevated and surface based convective initiation as a function of time. Figure found in (Wilson and Roberts 2006).

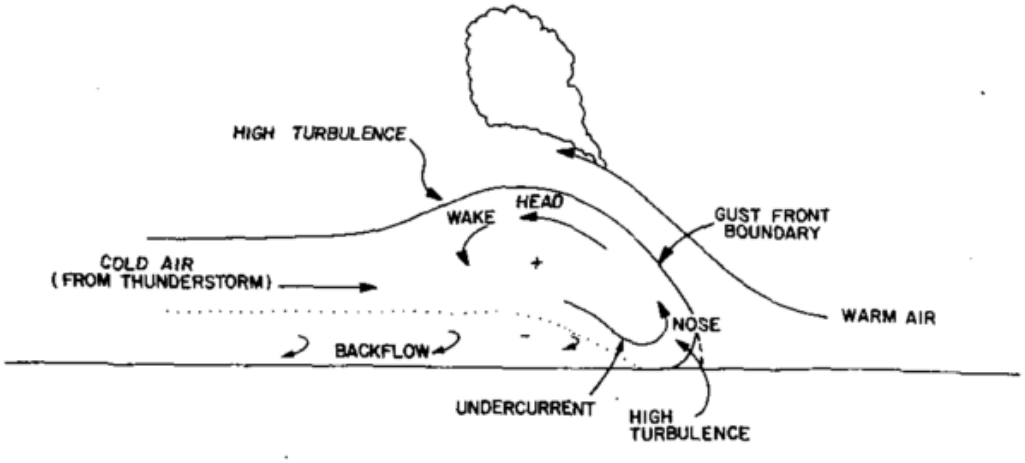

Figure 1.4: Schematic diagram of an outflow's leading edge. Figure found in (Craig Goff 1976)

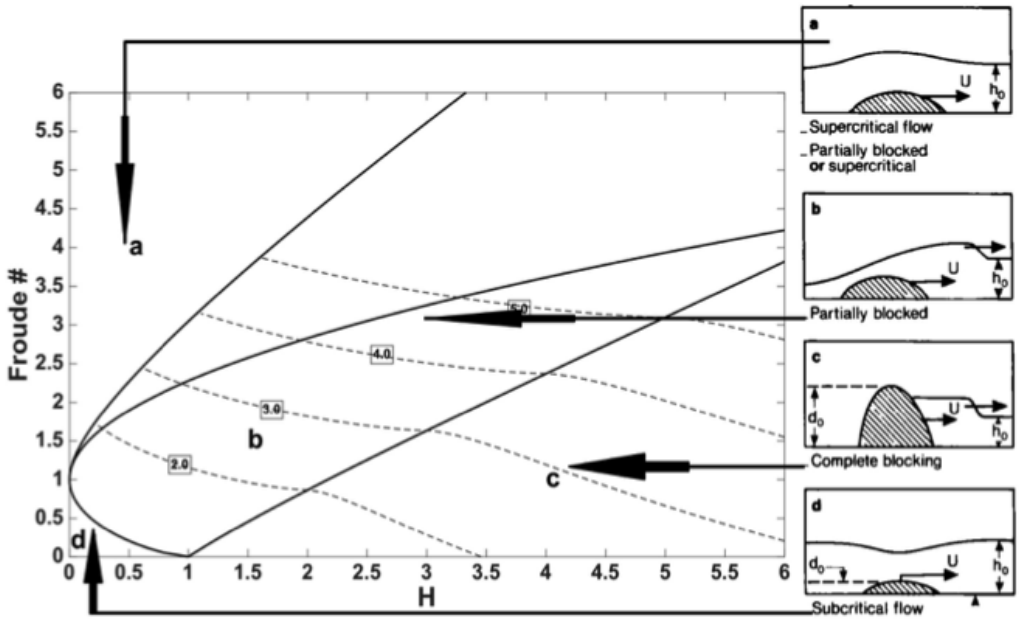

Figure 1.5: Diagram modeled after Rottman and Simpson (1989) that displays the flow regime based on H and the Froude #. Dashed lines are the bore strength. Equations found in 3

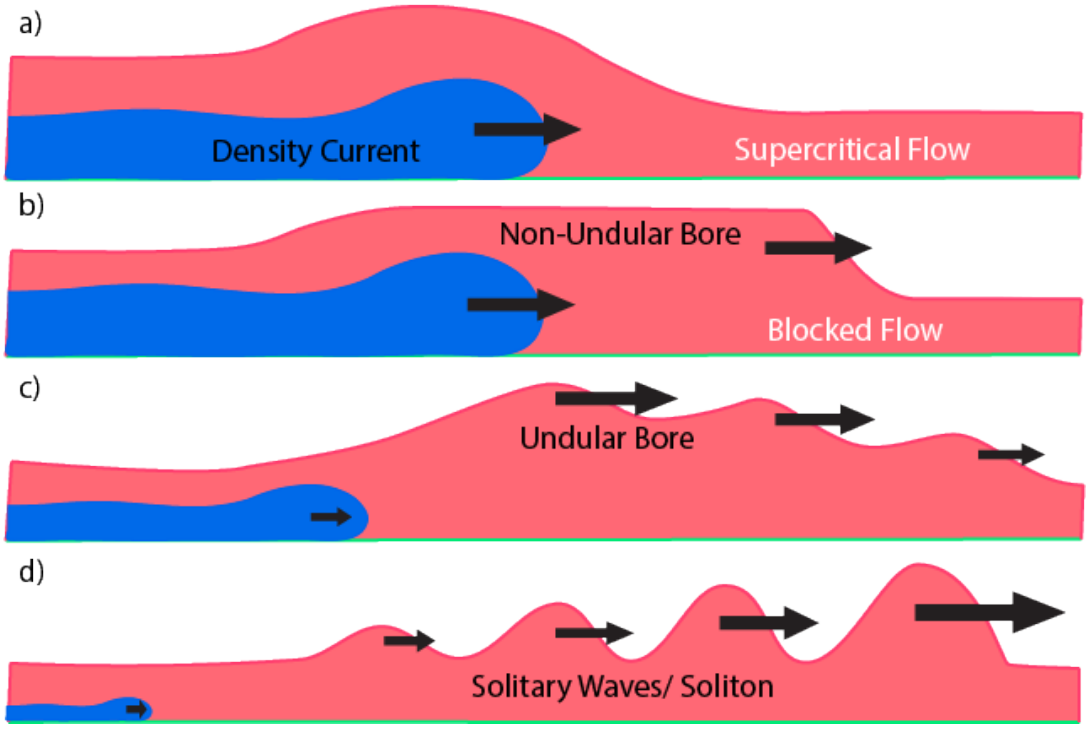

Figure 1.6: Schematic of a density current (a) in supercritical flow that transitions to blocked flow and develops a non-undular bore (b). The non-undular bore may evolve into an undular bore (c), and eventually a solitary wave(s) (d) if the nonlinear components of motion become important. This is similar to the Knupp (2006) description. White and Helfrich (2012) describe variations of this evolution.

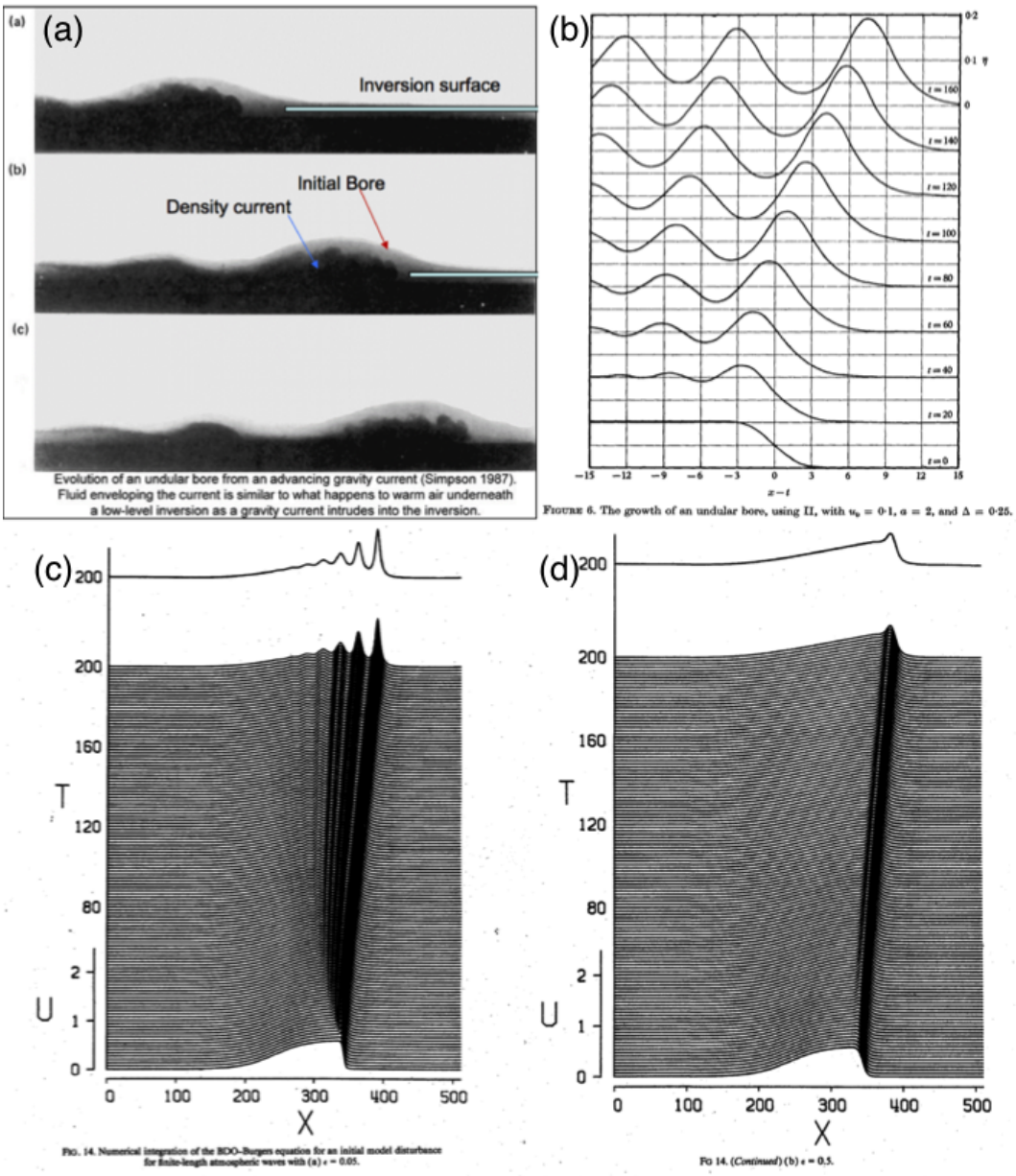

Figure 1.7: Images and illustrations of bores and solitary waves: a) a bore generated in a laboratory setting from Rottman and Simpson (1989); b) The evolution of an undular bore as described by Peregrine (1965); c) the evolution of a solitary wave from a bore with reduced dissipation; d) same as c, but with a higher amount of dissipation Christie (1989).

Chapter 2

Derivations

2.1 Overview

The following chapter includes derivations of hydraulic and linear wave theory used in this study. The derivation of hydraulic theory provides a description for how a one-layer fluid behaves when encountering an obstruction based on two parameters, the upstream Froude number Fr_o and non-dimensional height H_o. Next, a version of two-layer hydraulic theory is derived that is equal to the one-layer system, but with a reduced form of gravity replacing total gravity in the buoyancy term. The derivation is heavily based on Baines (1995) along with supplementary studies and textbooks, such as Stoker (1957); Long (1954); Houghton and Kasahara (1968); Gossard and Hooke (1975); Baines (1984); Pedlosky (1987); Rottman and Simpson (1989); and Kundu (2008).

The second derivation is a variation of linear wave theory which includes constructing the Taylor-Goldstein equation (TGE). Solutions to the TGE are obtained by assuming that the atmosphere is well represented by two layers with differing Scorer parameter values, where the first layer adjacent to the surface exhibits a large and positive Scorer parameter value and is capped by an infinitely deep layer exhibiting a much smaller or negative Scorer parameter value. If the solutions for the perturbation u' and w' winds are wave-like in the x-direction and combining them with the background state flow, then solutions for u and w are obtained. The derivation of linear

wave theory is based on the work explained in Baines (1995) along with supplementary studies and textbooks, such as Scorer (1949); Gossard and Hooke (1975); and Lindzen and Tung (1976a).

Intermediate steps in the derivations are included within section 7.

2.2 One-layer hydraulic theory

The interaction between a density current and its surrounding environment under certain conditions result in the generation of a bore. Historically, the generation of a bore in observations has been diagnosed with a variation of hydraulic theory (Koch and Clark 1999; Koch et al. 2008b,a; Coleman and Knupp 2011). The stable layer inversion is assumed to behave as a single-layer fluid and the density current is assumed to be approximated well by an immalleable obstruction to the flow. While this approach contains some obvious simplifications, the nearly identical two-layer variation of hydraulic theory has shown to provide qualitatively good agreement with observations. For simplicity, the derivations will be derived for the one-layer fluid, while the present work will be analyzed with the two-layer variation of hydraulic theory.

2.2.1 Setup

This derivation begins with the Navier-Stokes equations of motion and the mass continuity equation for a 3D system

$$\frac{Du}{Dt} = -\frac{1}{\rho}\frac{\partial p}{\partial x} + \nu\nabla^2, \tag{2.1}$$

$$\frac{Dv}{Dt} = -\frac{1}{\rho}\frac{\partial p}{\partial y} + \nu\nabla^2, \tag{2.2}$$

$$\frac{Dw}{Dt} = -g - \frac{1}{\rho}\frac{\partial p}{\partial z} + \nu\nabla^2, \tag{2.3}$$

$$\frac{1}{\rho}\frac{D\rho}{Dt} + \nabla \cdot \mathbf{u} = 0. \tag{2.4}$$

The equations of motions are to be applied within a two dimensional (2D) system; therefore the conditions under which the 2D approximation is valid must be established. Imagine that a dome of cold air from a thunderstorm strikes the surface and spreads out and a layer of environmental fluid encounters the convective outflow. The interaction is highly three-dimensional (3D) because the radius of curvature along the leading edge initially is small. From a birds-eye view (looking at the x-y plane and along the z-axis), as the convective outflow continues to spread out, the radius of curvature along the leading edge of the convective outflow increases. Take any point along the curve of the leading edge and draw its tangent. An increase in the radius of curvature implies that the curve along the convective outflow is locally approaching its tangent. Another way to interpret this is that the 3D outflow is approaching a two dimensional (2D) shape. This 2D approximation should be sufficient when the horizontal aspect ratio of the obstruction along the plane ($\frac{normal}{parallel}$) is greater than 10 (Epifanio et al. 2001). This approximation has been empirically shown to successfully diagnose observed bore properties (Koch and Clark 1999; Koch et al. 2008b,a; Coleman and Knupp 2011). Therefore, it is assumed here that a 2D approximation (y-component of wind v = 0) is sufficient to diagnose the bore generation.

Recall that the convective outflow is approximated by a general obstruction intruding into the nocturnal surface inversion (Figure 2.1). Some distance upstream from the obstruction is the undisturbed surface inversion with a depth h_o. The inversion layer is assumed to be a single-layer fluid with a constant density $\rho = \rho_o$. The depth of the obstruction is defined by $d_o(x)$ and reaches its crest at a height d_m. The top of the fluid is considered to be a free surface. Above the inversion layer is an infinite fluid with significantly less density, such that any motion within the above layer does not affect the inversion layer. The displacement of the fluid from h_o is defined by

$\eta = f(x,t)$, such that the maximum fluid inversion height is $h_o + \eta$. The thickness of the single-layer fluid d is defined as

$$d(x,t) = h_o + \eta(x,t) - d_o(x). \tag{2.5}$$

The fluid herein is assumed to be nearly incompressible. According to Pedlosky (1987), when the density differences between adjacent parcels in a fluid are small, then the density terms describing mass balance are negligible relative to the advective terms, the continuity equation (2.4) is well approximated to be

$$\nabla \cdot \mathbf{u} = 0. \tag{2.6}$$

Far upstream from the obstruction, first assume that the horizontal flow is represented by a value u_o and is constant with height, so that $\frac{\partial u_o}{\partial z} = 0$. Second, assume that the vertical velocity in the fluid upstream is 0. The second assumption implies that upstream, $\frac{\partial w_o}{\partial x} = 0$. Therefore, vorticity, defined as $\frac{\partial u_o}{\partial z} - \frac{\partial w_o}{\partial x}$, is 0 within the undisturbed fluid. According to Kelvin's theorem, cited in Stoker (1957), if a fluid begins irrotational, then the fluid remains irrotational. Therefore, $\frac{\partial u}{\partial z}$ will be considered to be 0 throughout the fluid, except through the bore head and along the obstruction. This procedure is congruent with the derivation found in Baines (1995).

Additionally, it is possible to ignore viscosity in the equations of motion in (2.1) because a simple scale analysis demonstrates that the viscosity term is significantly smaller than the horizontal pressure gradient term. Then the x and z-components of the equation of motion become

$$\frac{Du}{Dt} = \frac{\partial u}{\partial t} + u\frac{\partial u}{\partial x} = -\frac{1}{\rho}\frac{\partial p}{\partial x}. \tag{2.7}$$

$$\frac{Dw}{Dt} = -g - \frac{1}{\rho}\frac{\partial p}{\partial z} \tag{2.8}$$

The lower kinematic boundary condition is the impermeability condition:

$$w(x,0,t) = \frac{Dd_o}{Dt} = \cancelto{0}{\frac{\partial d_o}{\partial t}} + u\frac{dd_o}{dx} + w\cancelto{0}{\frac{\partial d_o}{\partial z}} \Rightarrow$$

$$w(x,0,t) = u\frac{dd_o}{dx}. \tag{2.9}$$

Along η, the upper kinematic boundary condition requires that w is determined by

$$w(x,\eta,t) = \frac{D\eta}{Dt} = \frac{\partial \eta}{\partial t} + u\frac{\partial \eta}{\partial x} + w\cancelto{0}{\frac{\partial \eta}{\partial z}} \Rightarrow$$

$$w(x,\eta,t) = \frac{\partial \eta}{\partial t} + u\frac{\partial \eta}{\partial x}. \tag{2.10}$$

The pressure at the top of the fluid is considered to be p_o, and the general equation for pressure is written as

$$p(x,z,t) = p_o + f(x,z,t). \tag{2.11}$$

To solve for $f(x,z,t)$, consider the horizontal and vertical scales of motion in the system. The horizontal motions observed within a stable layer are on the order of 10 ms^{-1}, while the vertical motions are an order less. As stated in (Pedlosky 1987), the horizontal character of the fluid is such that the Archimedean principle for a static fluid is approximately valid. In this case, the total derivative of vertical motion, $\frac{Dw}{Dt}$ may be neglected, and fluid motion can be regarded as hydrostatic. modifying (2.3), the vertical equation of motion, equation (2.3) becomes

$$0 = g - \frac{1}{\rho}\frac{dp}{dz}. \tag{2.12}$$

By integrating equation (2.12) from an arbitrary height z to the top of the fluid $\eta + h_o$

and solving for f(x,z,t) in equation (2.11), a full equation for pressure is obtained:

$$p(x,z,t) = p_o + \rho g(\eta + h_o - z). \tag{2.13}$$

As a review, the assumptions are

(i) 2D flow (x,z plane) appropriately describes a single-layer flow over an convective outflow approximated as an immalleable obstruction;

(ii) the fluid is considered a single layer of constant density;

(iii) the flow is irrotational;

(iv) the motion is hydrostatic.

Transforming equations of motion for a 2D single-layer flow

As it stands, the equations of motion and the continuity equation are

$$\frac{Du}{Dt} = \frac{\partial u}{\partial t} + u\frac{\partial u}{\partial x} = -\frac{1}{\rho}\frac{\partial p}{\partial x}, \tag{2.14}$$

$$0 = -g - \frac{1}{\rho}\frac{dp}{dz}, \tag{2.15}$$

$$\nabla \cdot \mathbf{u} = 0. \tag{2.16}$$

Now that there is an established relationship between pressure p and the displaced height η using equation (2.13), it will be beneficial to replace p with η in the equations of motion. To do so, differentiate equation (2.13) with respect to x. Then, take that result and set it equal to $\frac{\partial p}{\partial x}$ in equation (2.14). The new form of the x-equation of motion is:

$$\frac{\partial u}{\partial t} + u\frac{\partial u}{\partial x} = -g\frac{\partial \eta}{\partial x}. \tag{2.17}$$

Next, integrate (2.16) over the depth of the fluid:

$$\int_{d_o}^{\eta+h_o} (\nabla \cdot \mathbf{u}) dz = \frac{\partial \eta}{\partial t} + \frac{\partial}{\partial x}(ud) = 0, \tag{2.18}$$

where the Leibniz rule has been applied to expand the $\frac{\partial u}{\partial x}$ integrand. To review, the nonlinear equation of motion and the continuity equation for a one-layer flow are:

$$\frac{\partial u}{\partial t} + u\frac{\partial u}{\partial x} = -g\frac{\partial \eta}{\partial x}. \tag{2.19}$$

$$0 = \frac{\partial \eta}{\partial t} + \frac{\partial}{\partial x}(ud). \tag{2.20}$$

2.3 Evaluating the flow over an obstruction

In the following discussion, equations (2.19) and (2.20) are manipulated in order to describe the behavior of the fluid as it traverses an obstruction. The fluid behavior will be referred to as a flow regime. The solutions for the flow regimes are considered to be steady state. Initially, the following analysis will describe subcritical and supercritical flow regimes. Afterwards, the derivation will reconstruct a diagram commonly used in hydraulic theory as shown in figure 2.3. The diagram delineates between flow regime based on the Fr_o and H_o. The diagram is based on Baines and Davies (1980), but the derivations stem from work described in Rayleigh (1914); Long (1954); and Houghton and Kasahara (1968).

2.3.1 No jump criteria

The first part of this derivation addresses the conditions under which flow responses are supercritical (figure 2.3,regime a) and subcritical (figure 2.3, regime d). This current analysis is restricted to descriptions of long period gravity wave disturbances (those which the horizontal wavelength is an order of magnitude greater than its ver-

tical wavelength Lamb 1932; Baines 1995), which are also known as shallow water waves (Kundu 2008), and tidal waves (Lamb 1932; Stoker 1957). Because a steady state flow is assumed, the time derivatives in our equations of motion are set equal to 0 and the equations of motion become

$$u\frac{du}{dx} + g\frac{d\eta}{dx} = 0, \tag{2.21}$$

$$\frac{d}{dx}(ud) = 0. \tag{2.22}$$

Combining equations (2.21) and (2.22), the result is

$$\left(\frac{u^2}{dg} - 1\right)\frac{dd}{dx} = \frac{dd_o}{dx}, \tag{2.23}$$

Where $\frac{u}{\sqrt{gd}}$ is defined to as Fr. As mentioned before, the Fr_o is a parameter used for diagnosing the steady-state solution for a flow regime in this variation of hydraulic theory. Fr is the Froude # along the flow as a function of x, a ratio of the fluid speed to the speed of long period gravity waves. Mathematically, based on equation (2.23), the value of Fr can change the sign of the linear relationship describing the change in thickness of the fluid and the change to the height of the obstruction $d_o(x)$. This situation is discussed in Long (1954).

In the case where Fr is 1, equation (2.23) is insufficient on its own to describe the relationship between $\frac{dd}{dx}$ and $\frac{dd_o}{dx}$. In order to diagnose what happens to the flow regime, it is necessary to take the derivative of equations (2.23) and (2.20) with respect to x. By combining these derivatives of equations (2.23) and (2.20), Long (1954) creates an equation to evaluate the flow regime when $Fr = 1$:

$$-\frac{3u^2}{d^2g}\left(\frac{dd}{dx}\right)^2 + \left(\frac{u^2}{dg} - 1\right)\frac{d^2d}{dx^2} = \frac{d^2d_o}{dx^2}. \tag{2.24}$$

1) Sonic flow condition

Froude # = 1:

A value of $Fr = 1$, referred to as critical or sonic flow, is where the background flow is moving at the same speed, u, as a gravity wave in a fluid of depth d (Baines 1995). According to equation (2.23), a $Fr = 1$ requires the difference $(\frac{u^2}{dg} - 1)$ to be 0, which implies that $\frac{dd_o}{dx}$ must also equal zero. This condition can occur at the crest of the obstruction and along the flat ground. Along the flat ground in the upstream flow, d_o is a constant 0. In a steady state, the initial conditions remain unchanged along the flat ground. The following analysis will focus on how the fluid changes as it traverses over the obstruction.

Just to either side of the obstruction crest, $\frac{dd_o}{dx}$ is nonzero. According to equation (2.23), Fr cannot be 1 along the rise or fall of the obstruction (otherwise this implies that $\frac{dd_o}{dx}$ is 0 and (2.23) would be violated). Also, the condition of a $Fr = 1$ at the crest of the obstruction does not alone provide a unique solution to equation (2.23). Instead, there exist an infinite amount of solutions for $\frac{dd}{dx}$ that satisfy $Fr = 1$ at the crest of the obstruction. In this case, there must be more information provided about the initial conditions in order to determine the behavior of the flow. These cases will be described within the following super- and subcritical condition discussions.

2) Supercritical flow condition

$Fr > 1$:

A $Fr > 1$ is supercritical flow, defined as the condition where the background flow is moving faster than the long period gravity wave speed defined by the depth d. When $Fr > 1$, then $\frac{dd}{dx}$ has a positive linear relationship with $\frac{dd_o}{dx}$, i.e. as height of the obstruction increases, so does the depth of the flow. As the flow reaches the crest of the obstruction, where $\frac{dd_o}{dx} = 0$, the Fr must be ≥ 1, otherwise the supercritical flow

condition over the entire fluid is violated. In pure supercritical flow throughout the entire domain, $Fr \neq 1$ at the crest.

In the case where $Fr = 1$ at the crest and supercritical flow upstream, equation (2.24) determines what happens to the flow regime downstream of the crest (Long 1954). The second term on the left-hand side of equation (2.24) is 0 when $Fr = 1$. Assuming the flow regime is supercritical ahead of the crest, then $\frac{dd}{dx}$ is positive upstream of the crest. At the crest, $\frac{d^2 d_o}{dx^2}$ does not equal 0 and is negative, which, according to equation (2.24), implies that $\frac{dd}{dx}$ cannot equal zero at the crest either. In this case, there are two possibilities: that $\frac{dd}{dx}$ preserves its sign or switches to being negative. If $\frac{dd}{dx}$ becomes negative at the crest, this requires that some Δx upstream from the crest, $\frac{dd}{dx}$ changed sign from positive to negative. This change of sign is an impossible condition, since along the distance Δx where the transition of $\frac{dd}{dx}$ occurs, Fr cannot equal 1 because equation (2.23) requires that $\frac{dd_o}{dx}$ is nonzero and positive. Therefore it is impossible for $\frac{dd}{dx}$ to change signs from positive to negative as the fluid approaches the crest. The only realistic solution is where $\frac{dd}{dx}$ does not change sign. The consequence of this analysis is that the flow regime must transition from supercritical to subcritical flow across the crest (Long 1954). However, in this case there is not an immediately clear steady state, since the flow must also become supercritical far downstream to match its state upstream. Unfortunately, equations (2.23) and (2.24) are not sufficient on their own to describe how the fluid transitions back to supercritical far downstream. Laboratory experiments by Long (1954) demonstrates that the solution a bore develops on the upstream side of the flow, causing the flow to transition to subcritical flow before it reaches the crest. In order for this flow to reach a quasi-steady state, the flow must reach a $Fr = 1$ at the crest again, and transition from subcritical to supercritical flow. Consequently, the flow becomes supercritical far downstream and the flow has reached a quasi-steady state. This quasi-steady state will be described in section 2.3.3.

3) Subcritical flow condition

$Fr < 1$:

A $Fr < 1$ is subcritical flow, defined as the condition where the background flow is moving slower than a gravity wave speed defined by the depth d. When $Fr < 1$, then the term $\frac{dd}{dx}$ has a negative linear relationship with $\frac{dd_o}{dx}$. This relationship implies that as the height of the obstruction increases, the depth of the flow decreases. As the flow reaches the crest of the obstruction, where $\frac{dd_o}{dx} = 0$, the Fr must be ≤ 1, otherwise the subcritical flow condition over the entire fluid is violated. In pure subcritical flow throughout the entire domain, $Fr \neq 1$ at the crest.

The same analysis can performed on the subcritical flow as with the supercritical flow in the case where $Fr = 1$ at the crest. Again, the second term on the left-hand side of equation (2.24) is 0 when $Fr = 1$, the flow is subcritical ahead of the crest, and $\frac{d^2 d_o}{dx^2}$ does not equal 0 at the crest. As before, the sign of $\frac{dd}{dx}$ can either change from negative to positive or stay negative across the crest. For the same reason as supercritical flow, $\frac{dd}{dx}$ must remain the same sign and the fluid should transition from a subcritical to a supercritical flow across the crest. When this occurs, a hydraulic jump can form in the downstream flow from the obstruction to transition back to subcritical flow (Long 1954). No upstream jump occurs.

2.3.2 Expression for all solutions when Fr = 1 at crest

As mentioned before, when Fr = 1 at the crest and no other information is provided, there is no unique solution. However, there does exist an equation which describes the relationship between the upstream Fr value and the height of the obstruction crest H_m, given that the $Fr = 1$ at the crest. This equation has been obtained in work by Houghton and Kasahara (1968) and is equivalent to the line BAD in figure 2.3. Physically, this line is significant to the derivation at hand because it demarcates the

conditions for being unblocked (super- or subcritical flow) from partially blocked (development of an upstream bore). The reason that this line separates the two flows can be interpreted from earlier discussions of super- and subcritical flow. In the case where the fluid transitions from super- to subcritical flow ahead of the crest, and unstable state develops. The significance of this behavior will be explained in the current section, but for now can be explained as a condition suitable for the development of a bore in the form of an upstream hydraulic jump.

The solution for this line is mathematically obtained in the following manner: Start by integrating the time-independent equations of motions, equations (2.21) and (2.22), along the flow in the x direction. The results are:

$$\frac{1}{2}u^2 + g(d_o + d) = C_1, \tag{2.25}$$

and

$$ud = C_2. \tag{2.26}$$

Solve for constants (C_1, C_2) by prescribing the initial conditions (u_o, h_o, $d_o = 0$, $\eta = 0$):

$$\frac{1}{2}u_o^2 + gh_o = C_1, \tag{2.27}$$

$$u_o h_o = C_2. \tag{2.28}$$

Next, set (2.28) equal to (2.26) and (2.25) equal to (2.27):

$$\frac{1}{2}u_o^2 + gh_o = \frac{1}{2}u^2 + g(d_o + d),$$

$$u_o h_o = ud \Rightarrow d = \frac{u_o h_o}{u},$$

and combine the two equations to get:

$$\frac{1}{2}u^3 + gu(d_o - \frac{1}{2g}u_o^2 - h_o) + gu_o h_o = 0.$$

At this point, it will be convenient to introduce parameters that will be used in the analysis:

$$Fr_o = \frac{u_o}{\sqrt{gh_o}}, \tag{2.29}$$

$$H_o = \frac{d_o}{h_o}, \tag{2.30}$$

$$V_o = \frac{u}{u_o}, \tag{2.31}$$

where H_o, Fr_o and V_o are the non-dimensional height, Froude #, and non-dimensional velocity in the upstream flow. It will be beneficial to rewrite this equation as just a function of Fr_o and H_o. Rewriting the intermediary equation mentioned above in terms of the parameters (2.29), (2.30), and (2.31):

$$\frac{1}{2}V_o^3 Fr_o^2 + V_o(H_o - \frac{1}{2}Fr_o^2 - 1) + 1 = 0. \tag{2.32}$$

There exists a solution at the crest for where H = H_m and Fr reaches 1. Based on Houghton and Kasahara (1968), $V_m = Fr_o^{-\frac{2}{3}}$ is the corresponding normalized velocity for this condition. Solving equation (2.32) with V_m yields

$$-\frac{3}{2}Fr_o^{\frac{2}{3}} + \frac{1}{2}Fr_o^2 + 1 = H_m. \tag{2.33}$$

Equation (2.33) is the curve for BAD in a Fr-H space, as in Figure (2.3). Cur-

rently, the equations discussed in this derivation can only explain the flow behavior for when it is purely sub- or supercritical, and identifying where the flow regime changes. While the analysis explains that jumps must develop in order for the fluid to reach a steady state, these equations do not identify the properties of the upstream jumps. For this case, jump conditions will be developed for the purpose of describing the jump properties.

2.3.3 Jump conditions

The following portion of the derivation will define curves AE and BC as found in figure 2.3. The solutions for the following curves will be described as functions of only Fr_o and H_o. To identify the jump conditions, consider a situation where a discontinuity exists between super- and subcritical flow upstream of the crest of the obstacle d_m. All gravity waves generated in the supercritical flow are advected downstream, while gravity waves in the subcritical flow are able to move upstream and downstream. Along the interface from supercritical towards subcritical flow, the depth of the fluid rapidly increases and forms a jump leading to nonlinear steeping where the tangents along the interface will become oriented more vertically (Kundu 2008). For the purposes of clarity, this jump will be exclusively referred to as a bore in the sections that follow the derivations. The schematic for this situation is diagrammed in figure (2.2).

The nonlinear steepening is initially unstable. The condition for reaching a quasi-steady state is considered in Long (1954). According to equation (2.23), the smaller the Fr, the more negative is the relationship between $\frac{dd}{dx}$ and $\frac{dd_o}{dx}$. The consequence of the fluid depth decreasing quicker implies the Fr at the crest shall be larger. It is assumed that at some point during the bore evolution, the Fr at the crest will reach the sonic condition. The sonic condition therefore assumed to be reached when the deepening of the subcritical flow behind the bore increases the Fr at the crest of the obstruction to 1. A critical condition at the crest and at the jump implies that gravity

waves generated in the subcritical flow are unable to propagate upstream the jump, while gravity waves propagating downstream will continue past the crest and into the supercritical flow.

In order to diagnose the quasi-steady state flow, the conditions over the crest of the obstruction, the subcritical regime, and the speed of the jump all must be known. The following table summarizes the knowns and unknowns:

Known	Unknown
h_o	u_1
$d_o(x)$	h_1
u_o	c_1
	d_c
	u_c

where u_1 and h_1 are the speed and depth of the flow within the subcritical regime behind the bore, u_c and d_c are the speed and depth at the crest of the obstruction, and c_1 is the speed of the bore. The following analysis will construct 5 equations suitable to solve for these 5 unknowns in a frame of reference moving with the bore moving upstream and behind the bore to the crest. The fluid motion in this reference frame ahead of and behind the bore can be represented as

$$v_o = u_o - \zeta, \tag{2.34}$$

$$v_1 = u_1 - \zeta, \tag{2.35}$$

where ζ is the speed of the reference frame moving with the bore. For convenience, equations (2.34) and (2.35), will be rewritten in accordance with Baines (1995) as:

$$v_o = u_o + c_1, \tag{2.36}$$

$$v_1 = u_1 + c_1, \tag{2.37}$$

where c_1 is the magnitude of the bore speed moving in the opposite direction as the upstream flow. Rewriting equation (2.28), the mass continuity equation for the first jump condition is

$$v_o h_o = v_1 h_1, \tag{2.38}$$

or as it is represented in Baines (1995)

$$(u_o + c_1)h_o = (u_1 + c_1)h_1, \tag{2.39}$$

The second jump condition also applies mass continuity to the fluid contained within the subcritical regime up to the crest of the obstruction. This equation states that

$$u_1 h_1 = u_c d_c, \tag{2.40}$$

Because of the quasi-steady state condition, Houghton and Kasahara (1968); Long (1954) indicate that the fluid must be sonic at the crest of the obstruction. Therefore, the flow speed at the crest u_c is equal to the shallow water gravity wave speed, leading to the third equation:

$$u_c = \sqrt{g d_c}. \tag{2.41}$$

To derive the fourth jump condition, a steady-state, mass flux form of the equation of motion in the x direction in a reference frame with the motion of the bore is constructed by 1) eliminating the time derivatives; 2) multiplying equation (2.14) by

v and equation (2.16) by ρ; 3) Then adding these two products together. The result is

$$\frac{\partial \rho v^2}{\partial x} + \frac{\partial \rho vw}{\partial z} + \frac{\partial p}{\partial x} = 0. \tag{2.42}$$

If mass and momentum are conserved quantities, then integrating the equation of motion over the entire volume in question will remain a conserved quantity as well, even across the jump. The mathematical representation of this concept is

$$\int_V \left(\frac{\partial \rho v^2}{\partial x} + \frac{\partial \rho vw}{\partial z} + \frac{\partial p}{\partial x} \right) dV = 0. \tag{2.43}$$

The volume under consideration has an extent of Δx, Δy, and Δz. To start, there are no fluxes along the y-direction because the 2D flow is in the x-z direction. Instead, assume that Δy is of unit length. Equation (2.43), using Divergence theorem (Stoker 1957), can be rewritten as the flux of these quantities across the surface of the volume. Consequently, these constraints leave only four sides under consideration:

$$\int_V \left(\frac{\partial \rho v^2}{\partial x} + \frac{\partial p}{\partial x} \right) dV + \int_V \left(\frac{\partial \rho vw}{\partial z} \right) dV = \int_S (\rho v^2 + p)\hat{i} \cdot \hat{n} dS + \int_S (\rho vw)\hat{k} \cdot \hat{n} dS.$$

Side 1 ($n = -\hat{i}$):

$$= \int_S (\rho v^2 + p)\hat{i} \cdot (-\hat{i}) dS + \int_S (\rho vw) \cancelto{0}{\hat{k} \cdot (-\hat{i})} dS = -\int_0^{h_1} (\rho v^2 + p) dz,$$

where $dS = dydz$, and $dy = 1$. Integrating over a depth h_1, this leads to

$$-(\rho v_o^2 h_o + \frac{1}{2}\rho g h_o^2 + p_o h_1). \tag{2.44}$$

Now the same approach is done for the opposite side:

Side 3 ($n = \hat{i}$):

$$= \int_S (\rho v^2 + p)\hat{i}\cdot\hat{i}dS + \int_S (\rho v w)\hat{k}\cdot\hat{i}^{0}dS = \int_0^{h_1} (\rho v^2 + p)dz.$$

Integrating over a depth h_1, this leads to

$$\rho v_1^2 h_1 + p_o h_1 + \frac{1}{2}\rho g h_1^2. \tag{2.45}$$

At the top of the volume

Side 4 ($n = \hat{k}$):

$$= \int_S (\rho v^2 + p)\hat{i}\cdot\hat{k}^{0}dS + \int_S (\rho v w)\hat{k}\cdot\hat{k}dS = \int_{a_o}^{a_1} (\rho v w)dx,$$

where a_o, a_1 constrain the control volume in the x-direction moving with the bore. This integral is simply 0 because there is no vertical flux of motion across the top of the interface. Similarly, there is no vertical flux across side 2 because there is no vertical motion along the surface ahead of the obstruction. Therefore

Side 2 ($n = -\hat{k}$):

$$-\int_{a_o}^{a_1} (\rho v w)dx = 0. \tag{2.46}$$

Side 4 ($n = \hat{k}$):

$$\int_{a_o}^{a_1} (\rho v w)dx = 0. \tag{2.47}$$

Together equations (2.44),(2.45),(2.46),and (2.47) become the momentum principle applied across the jump, written as

$$\rho v_o^2 h_o + \frac{1}{2}\rho g h_o^2 = \rho v_1^2 h_1 + \frac{1}{2}\rho g h_1^2. \tag{2.48}$$

Solving equation (2.38) for v_1 and plugging it into equation (2.48), the result is

$$v_o^2 = \frac{1}{2} g h_1 \left(1 + \frac{h_1}{h_o}\right), \tag{2.49}$$

or as in Baines (1995)

$$(u_o + c_1)^2 = \frac{1}{2} g h_1 \left(1 + \frac{h_1}{h_o}\right). \tag{2.50}$$

The fifth and final condition is based on Bernoulli's principle. The flow from the subcritical regime behind the jump to the crest of the obstruction is governed by equations (2.21) and (2.22). Assuming a steady state and integrating over x results in

$$\frac{1}{2} u_c^2 + g(d_c + d_m) = \frac{1}{2} u_1^2 + g h_1. \tag{2.51}$$

In summary, the five equations for the five unknowns are

$$(u_o + c_1) h_o = (u_1 + c_1) h_1, \tag{2.52}$$

$$u_1 h_1 = u_c d_c, \tag{2.53}$$

$$u_c = \sqrt{g d_c}, \tag{2.54}$$

$$(u_o + c_1)^2 = \frac{1}{2} g h_1 \left(1 + \frac{h_1}{h_o}\right), \tag{2.55}$$

$$\frac{1}{2} u_c^2 + g(d_c + d_m) = \frac{1}{2} u_1^2 + g h_1. \tag{2.56}$$

These set of equations are sufficient to solve the quasi-steady state bore solutions for when a bore is not moving relative to the obstruction (curve AE) and when the flow over the obstruction is 0 (curve BC).

Curve AE

One set of solutions exist for a bore which is not propagating upstream. This solution occurs along the curve AE in figure 2.3, which implies that the density current and the

bore are moving at the same speed. To solve for curve AE, the bore speed is set equal to 0 (i.e. $c_1 = 0$), and equations (2.52), (2.53), (2.54), (2.55), and (2.56) are solved. The set of equations are solved by first manipulating equation (2.55) to be equal to h_l/h_o, defined as the bore strength. By solving the quadratic equation and rewriting it in terms of Fr_o, the result is

$$\frac{h_1}{h_o} = \frac{1}{2}(-1 + \sqrt{1 + 8Fr_o^2}). \tag{2.57}$$

Equation (2.57) is a relationship between the bore strength and the Froude number upstream Fr_o. Along with the other equations (2.52), (2.53), (2.54), (2.56), and (2.57), the solution for the system of linear equations to obtain the curve for AE is

$$H_o = \frac{1 + (1 + 8Fr_o^2)^{\frac{3}{2}}}{16Fr_o^2} - \frac{1}{4} - \frac{3}{2}Fr_o^{\frac{2}{3}}. \tag{2.58}$$

Curve BC

Curve BC defines the boundary between partially and completely blocked flow. Along the curve, the wind within the subcritical regime u_1 is equal to 0. The implications of the subcritical regime flow equaling 0 is that the flow over the obstruction is 0 ($u_c = 0$). Additionally, because there is no fluid traveling over the obstruction, the depth of the fluid over the obstruction d_c is 0. Using this information, the jump conditions are:

$$c_1 = u_o \left(\frac{h_1}{h_o} - 1 \right)^{-1}, \tag{2.59}$$

$$u_1 h_1 = u_c d_c = 0, \tag{2.60}$$

$$u_c = \sqrt{ghd_c} = 0, \tag{2.61}$$

$$H_o = \frac{h_1}{h_o}. \tag{2.62}$$

Since the bore strength $\frac{h_1}{h_o}$ will always be greater than 1, equation (2.59) implies that the bore speed is also positive and in the direction moving upstream from the obstruction. The equation for BC is obtained by solving these equations in terms of Fr_o and H_o:

$$Fr_o = (H_o - 1)\left[\frac{(1+H_o)}{2H_o}\right]^{\frac{1}{2}}. \tag{2.63}$$

2.4 Two-Layer Hydraulic theory

A two layer model employs a second layer that lies above the first layer adjacent to the surface. Baines (1995) investigated the differences between a one-layer model and two-layer model. Baines (1995) demonstrated that when the total depth of both fluids is significantly larger than the first layer, the two-layer model can be approximated by a one layer model with g replaced by reduced gravity g'. A diagram of the two-layer flow is in figure 2.4. The i in this system represents a system of layers starting at the surface and numbering upwards along the z direction. Within the domain, the depth of the total fluid is the addition of the two layers

$$D(x,t) = d_1(x,t) + d_2(x,t), \tag{2.64}$$

and within the disturbed flow

$$d_1(x,t) = h_{1o} + \eta(x,t) - d_o(x). \tag{2.65}$$

It is assumed that each layer within the system is irrotational and incompressible, such that

$$\mathbf{u}_i = \nabla\phi_i, \tag{2.66}$$

where ϕ is the velocity potential for a layer i. Following the same logic as the one-layer system, the x component of the equation of motion can be rewritten in the following manner:

$$\frac{\partial}{\partial x}\left[\frac{\partial \phi_i}{\partial t}+\frac{1}{2}u_i^2+\frac{p_i}{\rho_i}\right]=0, \qquad i=1,2. \tag{2.67}$$

Integrating equation (2.67) with respect to x gives:

$$\frac{\partial \phi_i}{\partial t}+\frac{1}{2}u_i^2+\frac{p_i}{\rho_i}=C*. \tag{2.68}$$

$C*$ can be found by evaluating the equation (2.68) far upstream in the undisturbed flow which is in a steady state (i.e $\frac{\partial \phi_i}{\partial t}=0$) along the interface $z=h_o+\eta$, where η is the displacement from h_o. Since the flow is hydrostatic, then the pressure p_i at the interface is equal to

$$p_i(z=h_o+\eta)=p_o-\rho_i g\eta. \tag{2.69}$$

Further, assuming that $u_i(z=h_o+\eta)=u_{io}$, then the quantity $C*$ is

$$\frac{1}{2}u_{io}^2+\frac{p_o}{\rho_i}-g\eta=C*. \tag{2.70}$$

Then rearranging equation (2.68) for p_i and substituting $C*$ in to equation (2.70) gives:

$$p_i(z)=p_o-\rho_i\left(\frac{\partial \phi_i}{\partial t}+\frac{1}{2}(u_i^2-u_{io}^2)+g\eta\right). \tag{2.71}$$

In order to couple the two layers, it is assumed that pressure is continuous across the interface. Applying the pressure continuity condition to equation (2.71) yields

$$\frac{\partial \phi_1}{\partial t} + \frac{1}{2}(u_1^2 - u_{1o})^2 + g\eta\left(1 - \frac{\rho_2}{\rho_1}\right) = \frac{\rho_2}{\rho_1}\left(\frac{\partial \phi_2}{\partial t} + \frac{1}{2}(u_2^2 - u_{2o}^2)\right). \tag{2.72}$$

As mentioned before, previous work (Baines 1984) has demonstrated that when the depth of the total fluid given in (2.64) is an order of magnitude larger than the depth of the inversion fluid (i.e $\frac{d_1}{D} << 1$), the obstruction has little effect on modifying the upper fluid. This holds true as long as the depth of the obstruction is small relative to the depth of the total fluid (i.e $\frac{d_o}{D} << 1$). The result of a deep upper layer is that $\frac{\partial \phi_2}{\partial t}$ and the difference $u_2^2 - u_{2o}^2$ are negligible. Therefore, equation (2.72) can be rewritten such that it is nearly identical to the one-layer fluid system:

$$\frac{\partial \phi_1}{\partial t} + \frac{1}{2}(u_{1o}^2 - u_1)^2 + g'\eta = 0, \tag{2.73}$$

but with g' replacing the g:

$$g' = \left(1 - \frac{\rho_2}{\rho_1}\right) g. \tag{2.74}$$

Because the first layer is assumed to be denser than the second layer, it will be convenient to rewrite ρ_2 in equation (2.74) as $\rho_1 + \Delta\rho$, which leads to

$$g' = -\frac{\Delta\rho}{\rho_1} g. \tag{2.75}$$

It will be shown later on that the relationship between ρ and the potential temperature θ can be used here to modify equation (2.75) into

$$g' = \frac{\Delta\theta}{\theta_1} g, \tag{2.76}$$

where $\Delta\theta$ is the difference between the θ of the top fluid and the bottom fluid. This is valid when the atmosphere is incompressible or nearly incompressible (Boussinesq

flow).

2.5 Discussion

The behavior captured within these equations is that of a fluid flowing over an obstruction, such as the flow of stable air over a density current. Using observational data, these equations work will be utilized to diagnose and predict when a bore should form (Koch et al. 1991; Koch and Clark 1999; Koch et al. 2008a,b). There are some assumptions that, under typical conditions of the nocturnal environment, do not represent the complexity of bore processes in the atmosphere. For example, the atmosphere is a multi-layer system where the fluids contain vorticity. The vorticity doesn't appear to play a significant role in determining the development of a bore, as studies have demonstrated good agreement with observations (Koch and Clark 1999; Koch et al. 2008b,a; Coleman and Knupp 2011; Haghi et al. 2017b). However, the presence of vorticity is at the center of gravity wave maintenance (Scorer 1949; Lindzen and Tung 1976a; Koch and Clark 1999). This issue will be addressed in the following derivation using linear wave theory.

As mentioned before, the 2-layer model approximation is a reasonably good approximation, but it does not capture the range of complexity observed in the nocturnal environment over the Great Plains. Therefore, the height and speed of a bore will assuringly include errors in the magnitude. Most likely these errors will be due to the stratification and shear contained within the layer above the inversion (Crook and Miller 1984; Crook 1988).

Moreover, this variation of hydraulic theory is unable to diagnose the structure and development of a bore head during its evolution (Kundu 2008). Once the bore head has formed, observations during PECAN demonstrate that the bore head can rarefy during its demise, as observed during PECAN (figure 2.5). This evolution

is also not predicted by hydraulic theory. The evolution has been addressed with nonlinear wave theory and has shown to provide good agreement (Christie et al. 1978, 1979; Christie 1989; Zimmerman and Rees 2004). Unfortunately, this study does not address the nonlinear maintenance of waves within the nocturnal boundary layer. Instead, there is a reliance on linear wave theory to capture the first-order behavior of gravity waves, such as their wavelengths and height of maximum vertical motion. This approach prescribes wave ducts presumed to be capable of trapping these waves. In the following section, the linear wave theory will be derived.

While previously mentioned studies have shown that a rigid obstruction constraint in hydraulic theory still provides good agreement with observations, modeling studies and laboratory studies have shown that the relationship between the density current and the bore are not so simple (Rottman and Simpson 1989; White and Helfrich 2012). For example, Rottman and Simpson (1989) used laboratory results to demonstrate under what conditions did the bore response behave more like a density current. Rottman and Simpson (1989) additionally outlined conditions where the density current and the bore appeared to remain attached, similar to work by Haase and Smith (1989). Using an analytical numerical model, White and Helfrich (2012) showed that including dissipation between the density current and the environmental fluid provides a better constraint for the density current speed. Moreover, they detail the amplification of waves within the subcritical regime by discussing the transfer of energy from the density current to the bore.

With the following exceptions in mind, the following research uses this theory judiciously. Further discussions of its usability are found in chapter 4 and 5.

2.6 Linear Wave Theory

Once a bore has developed, the previously derived variation of hydraulic theory fails to provide information about the maintenance of gravity waves that evolve from the subcritical region of the bore. The maintenance is important for understanding why gravity waves associated with bores are observed for long periods of time within the nocturnal environment (Crook 1988). Research has described the maintenance of gravity waves by prescribing a wave duct adjacent to the surface based on a profile of the Scorer parameter (Koch and Clark 1999; Goler and Reeder 2004; Martin and Johnson 2008; Koch et al. 2008b,a; Coleman et al. 2009; Coleman and Knupp 2011). Given a horizontal wavenumber for a trapped gravity wave and the Scorer parameter, the corresponding vertical wavenumber for the trapped gravity wave can be derived. The vertical wavenumber is a coefficient in the TGE. Solving the TGE will lead to solutions for $\bar{w}(z)$. This derivation will follow the derivations outlined in Gossard and Hooke (1975) and Baines (1995).

2.6.1 Setup

Equations of motion and continuity

The derivation of the TGE begins by applying the assumptions to the equations of motion and the continuity equation, equations (2.1), (2.2), and (2.4), for an inviscid flow:

$$\frac{Du}{Dt} = -\frac{1}{\rho}\frac{\partial p}{\partial x}, \tag{2.77}$$

$$\frac{Dw}{Dt} = -g - \frac{1}{\rho}\frac{\partial p}{\partial z}, \tag{2.78}$$

$$\frac{1}{\rho}\frac{D\rho}{Dt} + \nabla \cdot \mathbf{u} = 0. \tag{2.79}$$

The y-component has not been included; as with hydraulic theory, the structure of trapped gravity waves will assume to be 2-dimensional, in a x-z plane.

Incorporating the thermal heat equation

The equations (2.77), (2.78), and (2.79) above are insufficient to uniquely solve the TGE, given that they contain four variables u, w, p and ρ. Therefore, a fourth equation must be introduced. Consider that the flow under examination is isentropic, where the specific heat γ is considered constant. First shown by Sadi Carnot and summarized in Batchelor (1967); and Kundu (2008), the equation of state can be written as:

$$\frac{p}{\rho^{\gamma}} = C^*, \tag{2.80}$$

where C^* is a constant. This is a form of the thermal heat equation. If the thermal heat equation (2.80) is transformed by taking the natural log of both sides, followed by taking the total derivative of its natural log form, then an equation for the conservation of thermal energy is

$$\frac{Dp}{Dt} = c_s^2 \frac{D\rho}{Dt}, \tag{2.81}$$

where c_s is the speed of sound defined as:

$$c_s^2 = \gamma RT.$$

2.6.2 Flow assumptions

The following are assumptions about the flow appropriate for linearized gravity waves in the lower portion of the troposphere (Baines 1995):

1. The Boussinesq approximation is valid.

2. The variables can be decomposed into a base state that is a function of only z and a perturbation quantity that is a function of x, z, and t.

3. The background state is considered hydrostatic.

Validating the Boussinesq approximation

The Boussinesq approximation conserves perturbations of density in the buoyancy term (multiplied by g) while neglecting the perturbation quantities in the inertia terms (Baines 1995; Kundu 2008). This approximation is appropriate when the vertical dimensions are an order of magnitude smaller than any scale height and the perturbations in p and ρ (denoted with a prime) are an order of magnitude smaller than their background state counterparts (denoted by a subscript o) (Spiegel and Veronis 1960). To confirm that these condition have been met, the scale heights can be written for ρ and p as:

$$D(\rho) = \left[\frac{1}{\bar{\rho}}\frac{d\rho'}{dz}\right]^{-1} = 10{,}000 \text{ m} \tag{2.82}$$

$$D(p) = \left[\frac{1}{\bar{p}}\frac{dp'}{dz}\right]^{-1} = 10{,}000 \text{ m} \tag{2.83}$$

Given that our application of linear wave theory is restricted to the lowest few kilometers, it is clear that our order of magnitude requirement between the vertical dimension and the scale height is met. The comparison between the perturbation and base state quantities reveals that

$$\frac{|\rho'|}{|\rho_o|} = 10^{-2} \tag{2.84}$$

$$\frac{|p'|}{|p_o|} = 10^{-2} \tag{2.85}$$

Therefore it appears that a Boussinesq approximation is adequate.

Linearization of equations

The variables in the equations of motion and continuity can be linearized by representing them as the sum of a background and a perturbed state, where the background state is only a function of height and the perturbation quantities are a function of space and time:

$$u(x,z,t) = u_o(z) + u'(x,z,t), \tag{2.86}$$

$$w(x,z,t) = w_o(z) + w'(x,z,t), \tag{2.87}$$

$$p(x,z,t) = p_o(z) + p'(x,z,t), \tag{2.88}$$

$$\rho(x,z,t) = \rho_o(z) + \rho'(x,z,t). \tag{2.89}$$

The linearized equations are obtained by plugging equation (2.86), (2.87), (2.88), and (2.89) into the equations of motion, and eliminating: (i) any background flow components if they are inside a derivative in the x-direction or in the time derivative, (ii) w_o because it is assumed to be 0, and (iii) the product of two perturbation quantities is assumed to be an order of magnitude smaller than its base state.

2.6.3 Applying assumptions

This section applies assumptions to the equations(2.77), (2.78), (2.79) and (2.81). The complete mathematical manipulations are in appendix section 7.3.2.

U-equation of motion

The first step towards obtaining the linearized equations is multiplying the x-component of motion by $\frac{\rho}{\rho_o}$ and expanding ρ into a base-state and perturbation term.

The Boussinesq approximation is valid, therefore the base-state normalized density fluctuations are small in the inertia terms (Kundu 2008). The expression $(1+\frac{\rho'}{\rho_o})$ is approximately equal to 1 for the terms on the left-hand side. The next step is to expanded all terms into their base and perturbation states and apply the linearization. The result is

$$\boxed{\frac{\partial u'}{\partial t}+u_o\frac{\partial u'}{\partial x}+w'\frac{du_o}{dz}=-\frac{1}{\rho_o}\frac{\partial p'}{\partial x}}, \tag{2.90}$$

W-equation of motion

Following the same procedure as the x-component of motion, equation (2.78) is multiplied by $\frac{\rho}{\rho_o}$ and then ρ is expanded into a base state and perturbation term. Next, linearize the pressure term and use the hydrostatic approximation to eliminate the hydrostatic base state. Returning to the Boussinesq approximation, the expression $(1+\frac{\rho'}{\rho_o})$ in the inertial terms are approximated to be 1, while the perturbation density is kept in the buoyancy term. Lastly, u and w are expanded into their base and perturbation states and linearize. The result is:

$$\boxed{\frac{\partial w'}{\partial t}+u_o\frac{\partial w'}{\partial x}=-\frac{\rho'}{\rho_o}g-\frac{1}{\rho_o}\frac{\partial p'}{\partial z}}, \tag{2.91}$$

Thermal heat equation

For a Boussinesq flow, the fluid is nearly incompressible, implying that the flow adjusts nearly instantaneously ($c_s \to \infty$). In this case, the thermal heat equation is simply

$$\frac{D\rho}{Dt}=0$$

By expanding the thermal heat equation into its base and perturbation states and linearizing, the result is

$$\boxed{\frac{\partial \rho'}{\partial t} + u_o \frac{\partial \rho'}{\partial x} + w' \frac{d\rho_o}{dz} = 0}, \tag{2.92}$$

Continuity

The Boussinesq approximation, explicitly derived in Spiegel and Veronis (1960), demonstrates that the continuity equation is effectively the same as the continuity equation for an incompressible atmosphere, i.e.

$$\nabla \cdot \mathbf{u} = 0.$$

After expanding the continuity equation into the base and perturbation states, it is linearized to give

$$\boxed{\frac{\partial u'}{\partial x} + \frac{\partial w'}{\partial z} = 0}. \tag{2.93}$$

2.6.4 Deriving Taylor-Goldstein

The linearized equations provide 4 equations with 4 unknowns. The TGE is derived when these equations are linearly combined into one equation in terms of $\bar{w}(z)$, which is the structure function of the vertical motion. To begin, assume that a trapped gravity wave reaches a steady state, and therefore it is appropriate to neglect the time derivatives:

$$u_o \frac{\partial u'}{\partial x} + w' \frac{du_o}{dz} = -\frac{1}{\rho_o} \frac{\partial p'}{\partial x}, \tag{2.94}$$

$$u_o \frac{\partial w'}{\partial x} = -\frac{1}{\rho_o} \frac{\partial p'}{\partial z} - \frac{\rho'}{\rho_o} g, \tag{2.95}$$

$$u_o \frac{\partial \rho'}{\partial x} + w' \frac{d\rho_o}{dz} = 0, \tag{2.96}$$

$$\frac{\partial u'}{\partial x} + \frac{\partial w'}{\partial z} = 0. \tag{2.97}$$

Eliminate 3 of the 4 variables by taking $u_o \frac{\partial}{\partial x}$ of equation (2.95):

$$u_o^2 \frac{\partial^2 w'}{\partial x^2} + \frac{u_o}{\rho_o} \frac{\partial^2 p'}{\partial x \partial z} + u_o \frac{g}{\rho_o} \frac{\partial \rho'}{\partial x} = 0, \tag{2.98}$$

substitute equation(2.96) into equation (2.98):

$$u_o^2 \frac{\partial^2 w'}{\partial x^2} + \frac{u_o}{\rho_o} \frac{\partial^2 p'}{\partial x \partial z} - w' \frac{g}{\rho_o} \frac{d\rho_o}{dz} = 0, \tag{2.99}$$

and substitute equation (2.94) into equation (2.99):

$$u_o^2 \frac{\partial^2 w'}{\partial x^2} - u_o \frac{\partial}{\partial z} \left(u_o \frac{\partial u'}{\partial x} + w' \frac{du_o}{dz} \right) - w' \frac{g}{\rho_o} \frac{d\rho_o}{dz} = 0.$$

Incorporating the continuity equation (2.97), the result is

$$\boxed{u_o^2 \frac{\partial^2 w'}{\partial x^2} + u_o^2 \frac{\partial^2 w'}{\partial z^2} - u_o w' \frac{d^2 u_o}{dz^2} - w' \frac{g}{\rho_o} \frac{d\rho_o}{dz} = 0}. \tag{2.100}$$

Since soundings provide thermodynamic information based on temperature, it is convenient to define a relationship between the background potential temperature θ and density ρ. Start with the definition of θ_o and logarithmically differentiate. By taking into account that our atmosphere is considered nearly incompressible, the result is

$$\frac{1}{\theta_o} \frac{d\theta_o}{dz} = -\frac{1}{\rho_o} \frac{d\rho_o}{dz}. \tag{2.101}$$

By multiplying by g, this equation becomes the Brunt-*Väisälä* frequency, N^2, given as:

$$N^2 = \frac{g}{\theta_o}\frac{d\theta_o}{dz}. \tag{2.102}$$

This equation is a measure of the intrinsic frequency of the atmosphere due to vertical stratification.

Equation (2.100) is a homogeneous, linear second-order partial differential equation with variable coefficients having a dependence on z. Mathematically, this implies that it is possible for solutions of equation (2.100) to be wave-like in the x-direction, but not in the z-direction. Therefore, the trial solution for the perturbation in w' will take the form

$$w'(x,z) = \bar{w}(z)cos(kx). \tag{2.103}$$

This trial solution is also consistent with observations; gravity waves observed in the atmosphere have wave-like appearances in the x-direction. Plugging (2.101),(2.102), and (2.103) into equation (2.100) leads to the TGE

$$\boxed{\frac{d^2\bar{w}(z)}{dz^2} + m(z)\bar{w}(z) = 0}, \tag{2.104}$$

where

$$\boxed{m^2 = l(z)^2 - k^2 = \frac{N^2}{u_o^2} - \frac{\frac{d^2u_o}{dz^2}}{u_o} - k^2}. \tag{2.105}$$

1) m is the vertical wavenumber associated with a TGE solution;

2) l^2 is formally referred to as the Scorer parameter (Scorer 1949);

3) k is the horizontal wavenumber associated with a TGE solution.

2.6.5 Solving the Taylor Goldstein Equation

The Scorer parameter in equation (2.105) includes two components that are both functions of the background environment as a function of height. The first term is referred to as the stability term and is a function of the Brunt-*Väisälä* frequency. The second term is referred to as the curvature term because it includes the mathematical curvature of the horizontal wind with height. The observed profile of the Scorer parameter can change from positive to negative values with height (Koch et al. 2008b; Lindzen and Tung 1976a). Unfortunately analytical wave solutions of more than a couple layers become mathematically intensive. Thus, solutions can not be easily interpreted without numerical models. For this reason, the following solutions for trapped waves using the TGE are applied to a two-layer approximation of the atmosphere. The first layer is adjacent to the surface and associated with a profile of positive Scorer which is capped by an infinitely deep second layer associated with a profile of negative Scorer parameter. This approach follows the work of Baines 1995, as illustrated in figure 2.6.

To solve the TGE, the variable coefficients must be approximated to a constant value. When the coefficients are constant, solutions for the TGE can be obtained for both real and imaginary solutions. Those solutions may contain exponential or sinusoidal solutions since the coefficients are no longer a function of z. The general solution for the real roots will be obtained for the depth of a wave duct which is characterized by the vertical wavenumber m. The general solution for the imaginary roots will be obtained in a similar manner to solutions for real roots, but to describe the wave motion above the wave duct. These solutions will be patched together at the top of the wave duct. The piece-wise function for $\bar{w}(z)$ provides the structure function for equation (2.103) and therefore a solution for w'. Through the continuity equation (2.93), a solution for u' can be obtained. To begin, solutions for the TGE are assumed

of the form:

$$\bar{w}(z) = e^{irz}. \tag{2.106}$$

Substituting equation (2.106) into the equation (2.104), the roots for the TGE are:

$$r = \pm m = \pm\sqrt{l^2 - k^2}. \tag{2.107}$$

Solutions for real values of m

Real solutions are valid when l^2 is larger than the horizontal wavenumber k ($l^2 - k^2 > 0$). These solutions are assumed to be for the layer adjacent to the surface, as discussed earlier. The general solution for this first layer is as follows:

$$\bar{w}_r(z) = A_r e^{im_1 z} + B_r e^{-im_1 z}.$$

where m_1 is the magnitude of the positive root $\sqrt{l_1^2 - k^2}$, l_1^2 is the value of the Scorer parameter in the first layer assumed to be positive and A_r, B_r are constant coefficients of the general solution.

Boundary conditions Unique solutions for a given m require the application of boundary conditions at the ground and at the top of the wave duct. The first boundary condition that is imposed is the impermeability condition. At the ground, $w(0) = 0$, which leads to

$$-A_r = B_r. \tag{2.108}$$

The second boundary condition is a geometric constraint: the maximum in the vertical motion associated with a trapped wave occurs at a height h_{duct}. Therefore, A_r must equal

$$A_r = \frac{w_{max}}{e^{im_1(h_{duct})} - e^{-im_1(h_{duct})}}. \tag{2.109}$$

Applying (2.108) and (2.109) to the general solution, $\bar{w}(z)$ is determined to be

$$\bar{w}_r(z) = \frac{w_{max}}{e^{im_1(h_{duct})} - e^{-im_1(h_{duct})}}(e^{im_1 z} - e^{-im_1 z}). \tag{2.110}$$

The exponentials can be decomposed into sines and cosines, which take the form

$$\boxed{\bar{w}_r(z) = \frac{w_{max}}{sin(m_1 h_{duct})} sin(m_1 z)}. \tag{2.111}$$

Equation (2.111) is the solution for the TGE that describe linear waves with real vertical wavenumbers.

Solutions for when m is imaginary

Next, a solution for complex roots can also be obtained for solutions of m where l^2 is smaller than the horizontal wavenumber (when $\sqrt{l^2 - k^2} < 0$). By doing so ,the general solution is:

$$\bar{w}_i(z) = A_i e^{m_2 z} + B_i e^{-m_2 z},$$

where m_2 magnitude of the imaginary vertical wavenumber $\sqrt{l_2^2 - k^2} < 0$, and l_2 is the Scorer parameter in the second layer, and A_i and B_i are constant coefficients for the imaginary solution of the TGE.

Boundary conditions To obtain solutions for when m is imaginary, the profile of $\bar{w}(z)$ is assumed to exponentially decay above the duct h_{duct}. This assumption requires that $\bar{w} = 0$ as $z = \infty$, and that there is no downward propagating wave energy (Baines 1995):

$$\bar{w}_i(\infty) = A_i e^{m_2 \infty} + B_i \cancelto{0}{e^{-m_2 \infty}} = 0.$$

The first term will grow inexorably unless

$$A_i = 0. \tag{2.112}$$

This requirement is referred to as the finiteness condition. The last condition requires that solutions for the real part of the TGE matches solutions to the imaginary equations at $z = h_{duct}$, the height of the duct (i.e. equation (2.111) when $z = h_{duct}$). In this case

$$\bar{w}_r(z) = w_{max},$$

and

$$B_i = \frac{w_{max}}{e^{-m_2 h_{duct}}}. \tag{2.113}$$

Applying equation (2.112) and (2.113), the solution for TGE when the roots are imaginary is:

$$\bar{w}_i(z) = \frac{w_{max}}{e^{-m_2 h_{duct}}} e^{-m_2 z}.$$

Simplifying the equation for the exponentially decaying layer, the solution is:

$$\boxed{\bar{w}_i(z) = w_{max} e^{-m_2 (z - h_{duct})}}. \tag{2.114}$$

Equation (2.114) is the solution for imaginary part of the TGE that describe linear waves with imaginary vertical wavenumbers.

2.6.6 Compiling w'

A unique solution for w', given a unique m_1 and m_2 is as follows:

When $0 < z < h_{duct}$:

$$w'(x,z) = \bar{w}_r(z)cos(kx) = \frac{w_{max}}{sin(m_1 h_{duct})}sin(m_1 z)cos(kx), \tag{2.115}$$

When $z > h_{duct}$:

$$w'(x,z) = \bar{w}_i(z)cos(kx) = w_{max}e^{-m_2(z-h_{duct})}cos(kx). \tag{2.116}$$

When the vertical wavelength of a trapped wave is constrained to 4 times the height of the wave duct, implying that $sin(mh_{duct}) = 1$ for either m_1 or m_2, the piecewise equations are nearly identical to Baines (1995).

2.6.7 Solving for u'

u' for m_1 layer

Once the linear solution for w' is obtained, the result can be used in the continuity equation to solve for u'. A relationship between u'_{max} and w'_{max} provides an opportunity to calculate the anticipated maximum vertical motion at the top of the wave duct, given surface observations. This relationship is assisted with the impedance relationship. For more information about this process, see section 3.3.2.

Solutions for u' provide a unique solution for u. Provided u and w, and assuming a wave with vertical wavenumber m_1 is considered to be in a steady state, it is possible to trace trajectories for a parcel moving through a wave. This process will lead to a calculation of the maximum parcel displacement for a given parcel. For more information, see section 3.4.3.

To obtain u', substitute w' into the continuity equation

$$\frac{\partial u'}{\partial x} + \frac{\partial w'}{\partial z} = 0 \Rightarrow$$

$$\frac{\partial u'}{\partial x} = -m_1 \frac{w_{max}}{sin(m_1 h_{duct})} cos(kx) cos(m_1 z),$$

and integrate along x to solve for u'; the solution is

$$u'(x,z) = -\frac{m_1}{k} \frac{w_{max}}{sin(m_1 h_{duct})} cos(m_1 z) sin(kx) + C.$$

It is assumed that at the origin $x = 0$, $u'(0,z) = 0$. [1] Constraining u' leads to a solution for for C:

$$u'(0,z) = -\frac{m_1}{k} \frac{w_{max}}{sin(m_1 h_{duct})} cos(m_1 z) \cancelto{0}{sin(k0)} + C = 0 \Rightarrow$$

$$C = 0$$

Therefore the derived solution for u' for the m_1 layer is:

$$\boxed{u'(x,z) = -\frac{m_1}{k} \frac{w_{max}}{sin(m_1 h_{duct})} cos(m_1 z) sin(kx)}. \tag{2.117}$$

u' in m_2 layer

Following the same method for u' in the m_2 layer, substitute w' into the continuity equation

$$\frac{\partial u'}{\partial x} + \frac{\partial w'}{\partial z} = 0 \Rightarrow$$

[1] For u' to be "wavey" in the x-direction, there must be some location where $u'(x_o, z) = 0$. However, the choice of location is arbitrary as long as the coordinate system does not change.

$$\frac{\partial u'}{\partial x} = m_2 * w_{max} e^{-m_2(z-h_{duct})} cos(kx),$$

and integrate along x to solve for u'. The resulting solution is

$$u'(x,z) = \frac{m_2}{k} w_{max} e^{-m_2(z-h_{duct})} sin(kx) + C.$$

At $x = 0$, $u'(0,z) = 0$. Constraining u' leads to a solution for for C:

$$u'(0,z) = \frac{m_2}{k} \frac{w_{max}}{sin(m_1 h_{duct})} cos(m_1 z) \cancelto{0}{sin(k0)} + C = 0 \Rightarrow$$

$$C = 0.$$

Therefore the derived solution for u' for the m_2 layer is:

$$\boxed{u'(x,z) = \frac{m_2}{k} w_{max} e^{-m_2(z-h_{duct})} sin(kx)}. \tag{2.118}$$

2.6.8 Relationship between w_{max} and u_{max}

Based on the equations of motion for gravity waves in this variant of the linear wave theory, the continuity equation can be used to derive an equation for u'_{max}. Assuming that $w' = 0$ at the surface and integrating over a quarter of a wavelength, the maximum u_{max} is

$$u_{max} = -\frac{m_1}{k} \frac{w_{max}}{sin(m_1 h_{duct})}. \tag{2.119}$$

2.7 Discussion

The previous section established a relationship between u'_{max} and w'_{max} produced by a linear gravity wave that is trapped in a wave duct adjacent to the surface. This relationship makes it possible to take observations of surface winds and, with the impedance equation, relate the surface winds to the expected maximum vertical motion produced by a trapped wave. The process for obtaining u'_{max} from surface data will be discussed more extensively in section 3. Because previous research has used this variation of linear wave theory to describe wave ducts (Koch and Clark 1999; Goler and Reeder 2004; Martin and Johnson 2008; Koch et al. 2008b,a; Coleman et al. 2009; Coleman and Knupp 2011), the current work will also use linear wave theory applied to observations as well. Furthermore, the agreement between theory and observations will be studied to draw conclusions about what mechanisms are maintaining a wave duct.

While part of this research, in accordance with other past work, will diagnose observed trapped gravity waves, the application of linear wave theory as a prognostic tool to predict the expected vertical displacements of parcels within a bore and subsequent gravity wave train is relatively new. For this purpose, part of this research is aimed at justifying the usefulness of linear wave theory to estimate parcel displacements. This will be discussed in more detail within section 3. The data collected throughout the PECAN project is best suited to meet these objectives because of frequent before and after bore-passage soundings along with vertical profilers that intercepted multiple bores.

When a bore has pulled away from its parent density current, an evolution commonly takes place, where gravity waves in the subcritical regime become highly nonlinear, such that the nonlinear steepening is matched by the dispersive effects (Christie 1989). The version of linear wave theory described herein fails to capture this evolution. This failure is an apparent drawback to the linear wave theory approach because

studies by Koch et al. (2008a,b) and Coleman and Knupp (2011) have shown that this evolution is often observed in the nocturnal boundary layer environment. Fortunately, Zimmerman and Rees (2004) demonstrated that the Scorer parameter derived from linear wave theory still does a remarkably good job of defining the horizontal and vertical wavelengths of nonlinear waves. For this reason, this study presented herein is interested in understanding how well the linear wave theory captures the observed displacements. It is expected that the linear wave theory under predicts the vertical motions within the nonlinear waves and, consequently, underestimates the vertical parcel displacements.

This current variation of linear wave theory is also not able to account for any vertical displacements experienced by the semi-permanent displacement of the bore. Unfortunately, many bores exhibit a clear semi-permanent displacement not explainable with linear wave theory. Recently, studies by Toms et al. (2017) and Mueller and Geerts (2017) have demonstrated that the first wave in the wave train can be shallower and does not appear to contain the semipermanent displacement of the subcritical regime in the bore. This wave is either expected to be a solitary wave traveling through the supercritical flow without a semipermanent displacement or a gravity wave exhibiting the least displacement. It seems reasonable to restrict predictions garnered with linear wave theory to the first observed gravity wave in the train of waves. However, this is not true for all bores, as they are also observed to evolve into solitons and amplitude ordered solitary wave trains (Christie 1989; Koch et al. 2008a,b; Coleman and Knupp 2011). The current research makes no proclamation that linear wave theory is always appropriate, and discusses when applications are questionable.

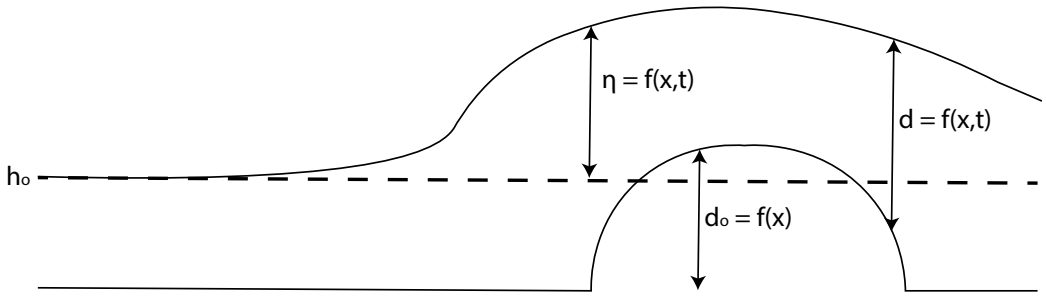

Figure 2.1: A diagram of flow passing over an obstruction of height d_o. The undisturbed flow height h_o is displaced by a depth η as it rises over the obstruction. Similar to diagram in (Baines 1995).

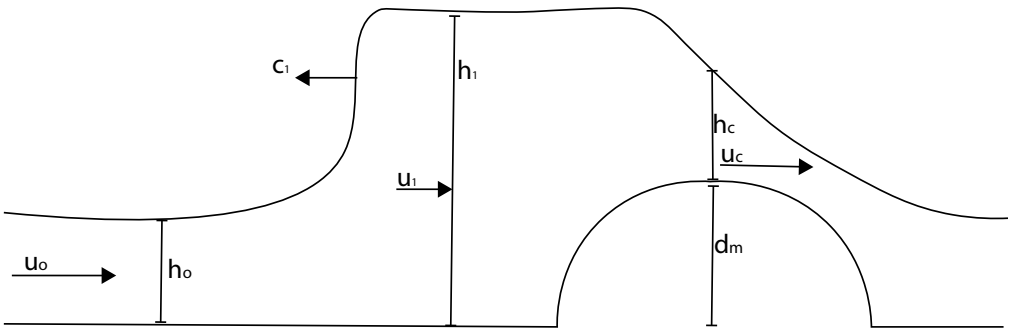

Figure 2.2: A diagram of a bore moving at a speed c_1 moving within a fluid layer of initial height h_o with a velocity u_o. The bore displaces the fluid layer to a height h_1 and degrades the fluid velocity to u_1. Some of the fluid passes over the obstruction at its crest of height h_m at a depth of d_c and velocity u_c. Similar to diagram in (Baines 1995).

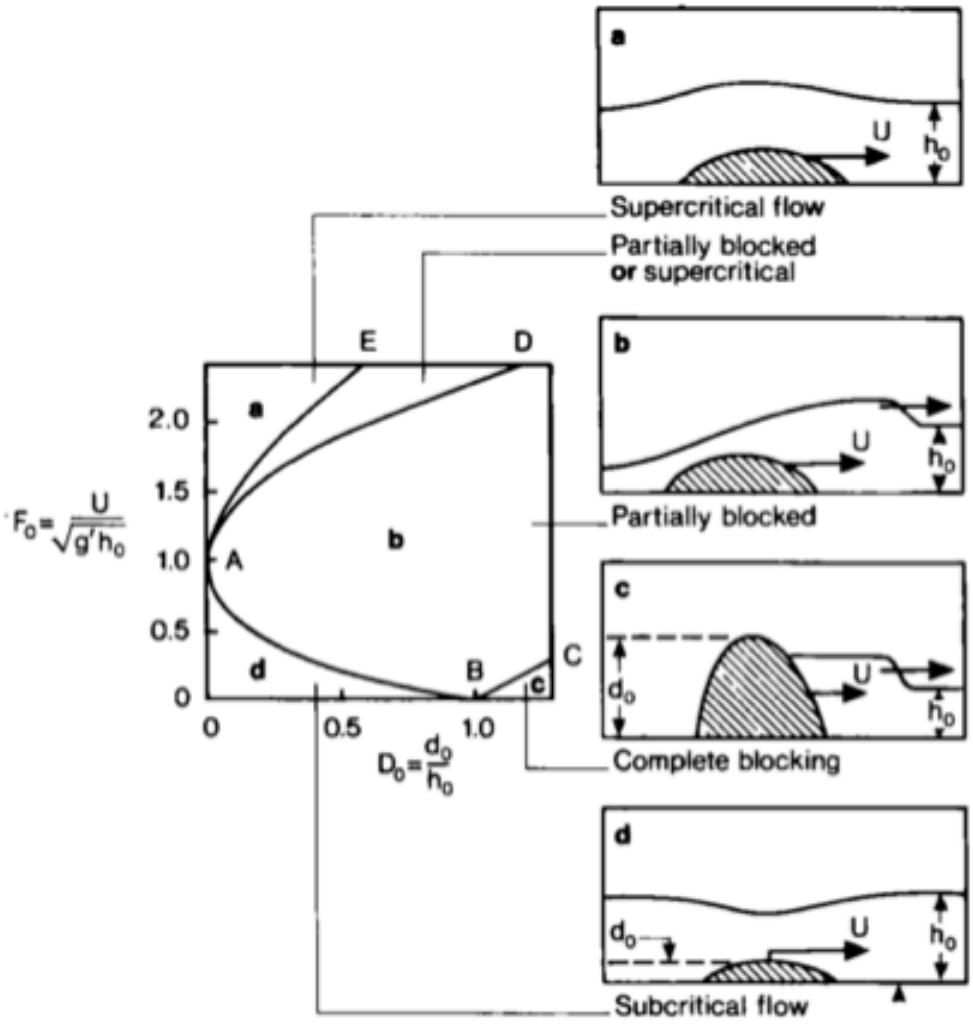

Figure 2.3: The flow regimes in a two-layer flow (approximated to a one-layer flow containing an upper layer of infinite depth) over a streamlined obstacle. Diagram lifted from Rottman and Simpson (1989) as adapted from Baines and Davies (1980).

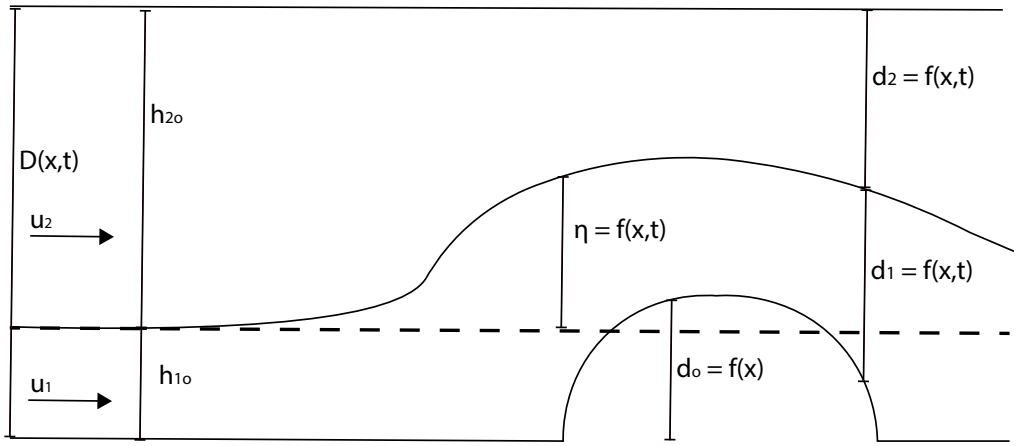

Figure 2.4: A diagram of a bore developing within a two layer flow with an of initial height h_{1o} with a velocity u_1. Similar to diagram in (Baines 1995).

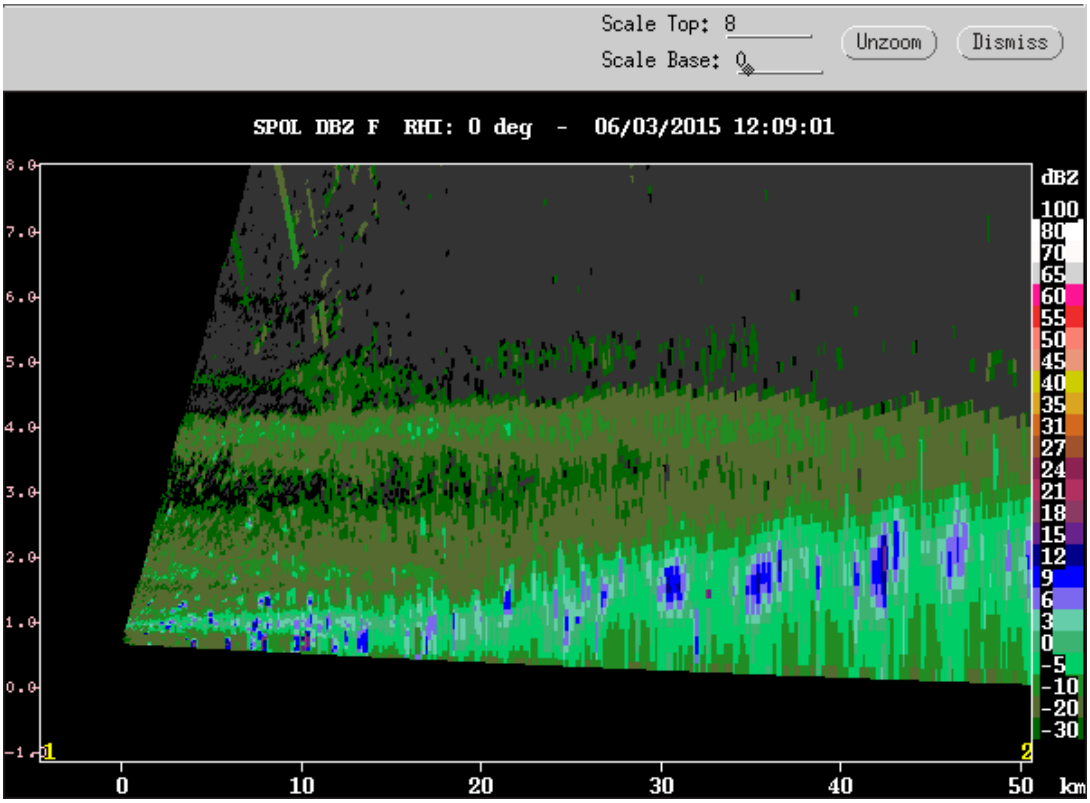

Figure 2.5: S-Pol reflectivity in RHI mode on June 3, 2016 at 1200 UTC. The reflectivity captures cloud development on what appears to be a rarefaction wave. This is similar to the evolutionary step conceptualized in figure 1.6 c.

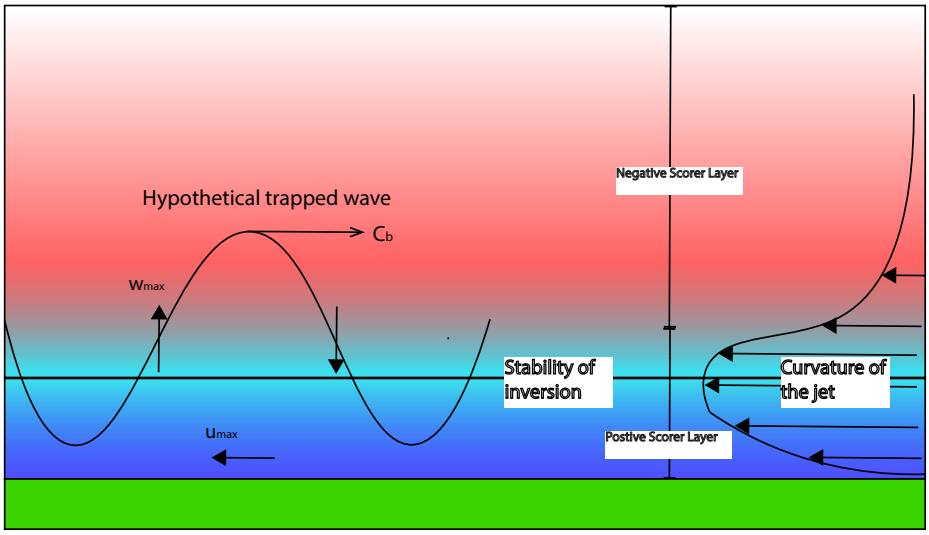

Figure 2.6: A diagram of a trapped wave according to solutions to the TGE following the work of (Baines 1995). The w_{max} and u_{max} are according to the perturbation winds expected within the trapped wave. C_b is the speed of the wave associated with the bore.

Chapter 3

Methods

The following chapter describes how the current study utilizes theoretical and empirical relationships to analyze observations of the nocturnal environment. The justification for these theoretical parameters have been described in section 2 and are summarized in Haghi et al. (2017b) and Haghi et al. (2017a).

3.1 Analyzing Radar Fine lines in IHOP_2002

Radar fine line (RFL) boundaries are lines of relative maxima observed in radar reflectivity. The radar fine lines analyzed in the current work are taken from the IHOP_2002 experiment (Weckwerth et al. 2004) and the PECAN field project (Geerts et al. 2016). Both experiments were conducted over the Great Plains (Fig. 3.1). The origin of these boundaries is explored using the following instruments:

1. Radar mosaics (available at http://catalog.eol.ucar.edu/ihop/) displayed at 15 min intervals from the operational S-band WSR-88D radar network (Hardy and Gage 1990) and the National Center for Atmospheric Research's S-PolKa radar (Keeler et al. 2000). S-Band radar operates at a wavelength of 1.5-7.5 cm. S-Pol provides generally good returns of reflectivity for precipitation hydrometeors at a low attenuation relative to other frequencies (Doviak and Zrnić 1984);

2. The Automated Surface Observing Systems (ASOS) stations provide T, RH, p, wind speed and direction at 1 min intervals. (ASOS Program Office Staff

1998) and the Oklahoma Mesonet stations provide T, T_d, p, 10 m wind speed and direction at 5 min intervals (Brock et al. 1995).;

3. Radiosonde soundings launched by the Atmospheric Radiation Measurement (ARM) Program (Stokes and Schwartz 1994) at 3 hour intervals during 26 May to 25 June at the ARM central facility (Lamont, OK) and during 26 May to 15 June at four auxiliary sites (Hillsboro KS; Morris, OK; Purcell, OK; and Vici, OK). The sampling frequency during a soundings ascent is around 1/2 Hz. The soundings include wind speed, wind direction, T, P, and T_d; all variables are a function of height;

4. NCAR's 915 MHz, 33-cm MAPR (Cohn et al. 2001) which provided 5 minute averaged observations of radar backscatter, and horizontal and vertical winds at 60 m vertical resolution up to ~5 km AGL. MAPR provides simultaneous measurements of u,v,and w for a single radar volume by reducing the volume needed to scan. MAPR uses a Spaced Antenna technique where a single transmitter sends a signal that is received by multiple antennas. Since a single volume is sampled, MAPR better meets the assumptions of temporal and spatial uniformity than Doppler beam swinging systems that sample multiple volumes.

The process of identifying and tracking of RFLs is illustrated in figure 3.2. First, boundaries were first identified in the radar mosaic as a RFLs (Fig. 3.2a). Such RFLs are often attributed to backscattering of the radar signal by insects (especially when insects are concentrated in convergence zones; Wilson et al. 1994), cloud condensation, or strong spatial gradients in refractive indices due to variations in moisture or temperature (Doviak and Zrnić 1984). Since these convergence zones exist near or within the leading edge of density currents, bores, heat bursts and frontal boundaries, the RFLs were utilized to identify the presence of a boundary. Second, once identified, their positions were marked on a political map at 15-minute intervals (Fig. 3.2b).

Third, an areal map of the RFL positions as a function of time were created for the night (Fig. 3.2c). This process provides information on the date, time, location, and duration of an event, which was used to determine the RFL speed and direction.

Next, surface observations along the path of the boundaries were used to categorize each RFLs as: undular bores, non-undular bores, density currents, heat bursts, retrogressing drylines, cold fronts, and stationary fronts. Specifically, changes in surface temperature, moisture, pressure, and winds were matched to the changes in surface observations discussed to accompany these phenomena in previous studies. Each categorization includes a classification as a measure of confidence. An event meeting (i) all requirements (in table 3.1) was deemed "well-determined," (ii) less than all the requirements was deemed "adequately determined," (iii) the use of radar images only was deemed "poorly determined, and (iv) no clear categorization was deemed undetermined. If the RFL was undetermined, the phenomenon was descriptively named based on its behavior and/or appearance.

The categorizations are listed in Table 3.1, along with the citations from previously work relevant to the characterizations. Convectively generated boundaries, aside from heat bursts, were categorized according to their progression in a commonly observed chain of events (e.g. Knupp 2006) as in Fig. 1.6. For clarity, an undular bore was defined in surface observations as a pronounced and sustained rise in the surface pressure, a rise or no change in the temperature and wind oscillations coincident with pressure oscillations (Koch et al. 1991). A solitary wave has similar characteristics, yet no sustained pressure rise (Christie et al. 1979; Christie 1989).

MAPR observations at Homestead (Fig. 3.1) provide useful information about the vertical structure of events. First, observing the vertical displacements of scattering layers in the signal-to-noise ratio (SNR) revealed whether layers are vertically displaced for at least two hours (indicative of a bore; Carbone et al. 1990 and Knupp 2006). Second, MAPR provides vertical motions. When an event experiences

stronger upward and weaker downward motions, this implies semi-permanent lifting. In most cases, the Homestead surface observations or Oklahoma Mesonet sites, in close proximity to MAPR, provided the supplementary surface data to categorize the event. For examples of bores in surface data and vertical profilers, see Tepper (1950), Koch et al. (2008b,a), Tanamachi et al. (2008), or Coleman and Knupp (2011).

3.2 Application of Hydraulic theory to atmospheric bores

3.2.1 Determining the flow regime

Bores generated from the intrusion of a convective outflow (i.e., density current) into a stable layer have been studied in an idealized framework by adapting hydraulic theory to the atmosphere, derived in section 2. Following Koch et al. (1991), density currents were approximated as obstructions in hydraulic theory in a two-dimensional, two-layer inviscid flow. As described in section 2.4, horizontal length scales of the disturbances were assumed to be much larger than the vertical length scale so that the hydrostatic approximation was assumed to be valid everywhere but at the leading edge of the jump (Baines 1995). Furthermore, the depth of the troposphere was assumed to be nearly an order of magnitude larger than the average depth of a stable surface inversion. According to Baines (1995); Rottman and Simpson (1989), this previously stated condition is sufficient to approximate the depth of the troposphere as infinitely deep. The two layer hydraulic model is similar to previous investigations using a single-layer model (Long 1954; Houghton and Kasahara 1968; Baines 1984; Rottman and Simpson (1989)), except that a form of reduced gravity was used (reduced gravity is described in section 2). As a result, the flow regime in a two-parameter space is given by Fr_o and H_o:

$$Fr_o = \frac{U_{inv} - C_{dc}}{\sqrt{g\frac{\Delta\theta}{\theta_{vw\_inv}}h_o}}, \tag{3.1}$$

$$H_o = \frac{d_o}{h_o}, \tag{3.2}$$

where

$$d_o = \frac{\theta_{vw}\Delta p}{\rho_w g[\frac{p_c}{p_w}\theta_{vw} - \theta_{vc}]}. \tag{3.3}$$

Fr_o is the upstream Froude number (the ratio of the density current-relative flow speed $U_{inv} - C_{dc}$ to the environmental gravity wave speed $\sqrt{g\frac{\Delta\theta}{\theta_{vw\_inv}}h_o}$, C_{dc} is the speed of the density current, H_o is the non-dimensional height (the ratio of the density current depth d_o to the surface inversion layer depth h_o), U_{inv} is the component of the average ground-relative environmental wind in the inversion layer directed parallel to the density current motion, g is the acceleration due to gravity, $\Delta\theta$ is the change in potential temperature across the inversion, θ_{vw_inv} is the mean virtual potential temperature of the inversion layer, Δp is the positive change in surface pressure across the density current front, ρ_w, p_w and θ_{vw} are the environmental surface density, pressure, and virtual potential temperature in the environment, and p_c and $\theta_v c$ are respectively the density current surface pressure and virtual potential temperature (Koch et al. (1991); Knupp (2006)). In calculating d_o, Δp was assumed to be the result of hydrostatic changes due to the density current and θ_{vc} was constant through the density current fluid. Surface observations were utilized to derive these quantities. There are errors implicitly contained in the calculation of a density current depth because a constant potential temperature profile was assumed to well describe the profile of temperature through the depth of a density current. Moreover, other sources of error in the density current depth came from ignoring the presence of stratification above the density current (Liu and Moncrieff 2000), changes in surface pressure due to the lifting of stable air over the density current, and environmental shear (Liu and Moncrieff 1996). Only

a dense vertical profiler network in space and time would have reduced these sources of errors.

The pair of Fr_o and H_o, as derived in section 2 indicate one of four flow regimes. When the flow is supercritical (regime a in Fig. 2.3 or subcritical (regime d in Fig. 2.3), a density current will not generate a bore. When the flow is partially or completely blocked (regime b or c in Fig. 2.3), a semi-permanent deepening of the inversion layer occurs ahead of the density current. The bore attains a height determined by Fr_o and H_o and, without considering the loss of energy due to wave radiation or turbulence, continues to expand horizontally for as long as the environmental flow remains partially or completely blocked (Carbone et al. 1990; Wakimoto and Kingsmill 1995; Koch and Clark 1999). Hydraulic theory was used herein to determine which flow regimes were likely present on any night during IHOP_2002.

3.2.2 μ parameter

If the flow regime is partially blocked, the μ parameter defines whether the bore that develops will either pull away from the density current or remain in some version of a bore/density current hybrid (Haase and Smith 1989; Rottman and Simpson (1989); Blake et al. 2017; Haghi et al. 2017b). A bore/density current hybrid can be identified in surface observations when a temperature trends towards colder values with the passage of the density current, but with oscillations in the temperature that are coincident with oscillations in the pressure(see figure 5.7). Haase and Smith (1989) evaluated this behavior with the μ parameter:

$$\mu = \frac{C_o}{C_{dc}}, \tag{3.4}$$

where $C_o = \frac{2Nh_o}{\pi}$, and N is the $Brunt - V\ddot{a}is\ddot{a}l\ddot{a}$ frequency, given by

$$N = \sqrt{\frac{g}{\theta_v}\frac{\partial \theta_v}{\partial z}}, \tag{3.5}$$

where θ_v is the virtual potential temperature. Following Haase and Smith (1989), $\mu > 0.7$ was considered to be a favorable condition for a bore to pull away from the density current. If $\mu < 0.7$, then the bore was assumed to be unable to pull away and some hybrid form of a density current/bore forms. From a forecaster perspective, if the bore never pulls away from the density current, the semi-permanent lifting will be masked by the hydrostatic pressure changes assumed to be associated with the density current. Therefore the μ parameter can help identify when a bore is generating lift along a density current. However, treatment of the hybrid bore/density current is precarious because the concept is relatively unaddressed in the literature. For example, it is known that both a bore and a density current provide lift for parcels in the environmental fluid (Koch and Clark 1999), but there is no understanding on the efficacy of using the μ parameter as a nowcasting tool. Because this study is the first known attempt to use the μ parameter for prognostic purposes, the following work will only track the value of μ as it passes over surface observations and comment on its agreement.

3.2.3 Determining bore strength

Fr_o and H_o provide the necessary parameters to iteratively solve for the bore strength ($\frac{h_1}{h_o}$) and, subsequently, the bore speed and height. The three equations that constrain the bore strength, defined as the height of the bore to the height of the inversion, are presented in Rottman and Simpson (1989) and as restated in the following form:

$$\frac{C}{(g' h_o)^{\frac{1}{2}}} = \left[\frac{1}{2}\frac{h_1}{h_o}\left(1 + \frac{h_1}{h_o}\right)\right]^{\frac{1}{2}}, \tag{3.6}$$

$$\frac{h_1}{h_o} = \frac{1}{2}\frac{u_1^2}{g'h_o} + \frac{3}{2}\left[\frac{h_1}{h_o}\frac{u_1}{(g'h_o)^{\frac{1}{2}}}\right]^{\frac{2}{3}}, \tag{3.7}$$

$$\frac{u_1}{g'h_o}^{\frac{1}{2}} = F_o - \left(1 - \frac{h_o}{h_1}\frac{C}{g'h_o}\right)^{\frac{1}{2}}. \tag{3.8}$$

According to Rottman and Simpson (1989), u_1 is the speed (relative to the density current) of the fluid downstream of the bore, g' is reduced gravity, and C is the speed of the bore in a reference frame where the upstream fluid is at rest, and C_b is defined as the ground-relative bore speed, given as $C_b = C - U_{inv}$.

3.2.4 Theoretical bore speed

Given the bore strength and h_o, bore height, h_1, is simply:

$$h_1 = h_o * (bore\ strength). \tag{3.9}$$

With h_1, a unique solution for the ground-relative bore speed can be calculated with the following two formulas, given by Rottman and Simpson (1989):

$$\text{If } \frac{h_1}{h_o} < 2 : \text{solve for C with (3.6) and plug into } C_b = C - U_{inv}, \tag{3.10}$$

$$\text{If } \frac{h_1}{h_o} > 2 : (\frac{C}{g'h_o})^{\frac{1}{2}} = 1.19(\frac{h_1}{h_o})^{\frac{1}{2}} - U_{inv}, \tag{3.11}$$

Where U_{inv} must have the opposite sign as C_b since the bore is propagating against the flow. Equation (3.10) has been determined by Rottman and Simpson (1989) to be appropriate for a bore with its bore strength is less than 2, because very little mixing is observed. Mixing along the bore interface has been shown to reduce the hydrostatic pressure and, therefore, the speed. Rottman and Simpson (1989) noted that bores with a bore strength greater than 2 are more affected by the mixing and, therefore, adhere more to equation (3.11). This equation is adapted from Wood and Simpson (1984) for

density currents of a height h_1.

3.3 Application of Linear Wave Theory

3.3.1 Conditions necessary for trapped wave

While hydraulic theory has been used to determine when the inversion fluid becomes blocked (partially or completely) and the depth of the bore response (Knupp 2006; Koch et al. 2008b,a), hydraulic theory does not provide insight on how a bore interacts with surroundings that contain varying shear and stratification. Rottman and Simpson (1989) avoids this complication by restricting stratification to an infinitely thin layer between two neutral, quiescent fluids which does not allow vertical wave propagation. Therefore, based on this current interpretation of hydraulic theory, it is unclear when the atmosphere allows (or restricts) the vertically propagation of waves. However, linear wave theory can be used to describe when gravity waves are trapped in a wave duct (Baines 1995). In the case of an atmospheric bore, the bore consists of a wave packet, a spectrum of gravity waves each characterized by a horizontal and vertical wavelength. Untrapped waves should quickly diminish in amplitude with time from imperfect reflection within a duct (Scorer 1949; Lindzen and Tung 1976a; and Lindzen and Rosenthal 1976b).

The TGE is appropriate for determining the structure of vertical motions in a wave (derived in section 2.6):

$$w'' - m^2(z)w = 0, \tag{3.12}$$

$$m^2 = l^2 - k^2 = \frac{N^2}{(U - C_b)^2} - \frac{\frac{\partial^2 U}{\partial z^2}}{U - C_b} - k^2, \tag{3.13}$$

where w is the vertical velocity, m is the vertical wavenumber, l^2 is the Scorer parameter, k is the horizontal wavenumber, U is the horizontal wind normal to the orientation of the bore, and N is the $Brunt - V\ddot{a}is\ddot{a}l\ddot{a}$ Frequency. As mentioned in section 2, the

literature describes the first term of ((3.13)) as the "stability term," since N contains information about the atmospheric stratification, and the second term as the "curvature term," since the second derivative of the horizontal wind pertains to the curvature of the vertical profile of the wind. Henceforth, any mention of curvature will be in reference to the second derivative of the horizontal wind with respect to height.

The vertical profile of l^2 is utilizedin to determine the presence of a wave duct and what waves, if any, are trappable (Knupp 2006; Koch et al. 2008a). To evaluate (3.13), the analysis employ two methods that define a single value for a positive l_1^2 and negative l_2^2 layer:

$l_1^2(l_2^2)$ is the observed maximum (minimum) l_2 value in the positive (negative) layer;

$l_1^2(l_2^2)$ is the mean value of the positive (negative) l_2 layer.

According to Baines (1995), a trapped wave mode will exist if

$$l_1 > k > l_2, \tag{3.14}$$

and

$$z_1(l_1^2 - l_2^2)^{\frac{1}{2}} > \frac{\pi}{2}, \tag{3.15}$$

where k is the positive horizontal wavenumber and z_1 is the transition height between the positive and negative vertical wavenumbers. To determine trapped wave modes, it assumed: (i) all trapped wave modes propagate in the layer of positive Scorer parameter values bounded by the ground and z_1, and (ii) that waves exponentially decay through the negative Scorer parameter layer bounded between z_1 and the top of the atmosphere. If equation (3.14) and (3.15) are satisfied, the vertical wavelength m_1 is defined such that:

$$m_1^{2*} = \frac{\frac{\pi}{2}}{z_1}. \tag{3.16}$$

In accordance with Lindzen and Tung (1976a), the $*$ here defines a specific m_1^{2*} that represents the vertical wavenumber associated with the mode $n = 0$. This mode is hypothesized to be the least attenuated by dissipative processes and thereby the most dominant mode.

Combining equations (3.13), (3.14) and (3.16), a trapped wave mode exists for a unique k of the form:

$$k = \sqrt{l_1^2 - m_1^{2*}}, \tag{3.17}$$

Following this methodology, two horizontal wavenumbers k_{max} and k_{mean} are obtained.

The pairs of m and k uniquely solve (3.12). As in Baines (1995), ρ and U are assumed continuous across z_1 so that w and $\frac{\partial w}{\partial z}$ are continuous across z_1 as well. The solution for the normalized w vertical profile is then (derived in section 2.6:

$$w(z) = \sin m_1^* z, \qquad 0 < z < z_1, \tag{3.18}$$

$$= \sin m_1^* z_1 e^{-m_2(z-z_1)}. \quad z > z_1. \tag{3.19}$$

This analysis ignores the consequence of multiple layers where the Scorer parameter changes sign. This will be discussed in section 4.4.

Discussion

Outlined above are the two methods for determining the representative values of the Scorer parameter for a two-layer linear wave theory approximation. The methods were chosen because they encompass a range of reasonable solutions. These range of solutions are hypothesized to encompass the likely range of horizontal wavelengths observed in the atmosphere. Unfortunately, there exist no observational study which has prescribed the Scorer values for a two-layer system. Therefore, this work is the

first observational study to do so.

The first method used to find k_{max} should describe the smallest trappable horizontal wavelength. According to Baines (1995), the range provided by the maximum and minimum l_1 and l_2 will will correlate with the largest horizontal wavenumber. Since the horiontal wavenumber is inversely proportional to the horizontal wavelength, a small horizontal wavenumber implies that large horizontal wavelength. There should be some skepticism for how well this prescribes the observed horizontal wavelength. Specifically, the maximum and minimum l^2 often occurs over a small portion of the total depth of the positive and negative layers prescribed in the two-layer model. Therefore, it is not unreasonable to expect this trapped wave to be infrequently observed. Yet, it should set the lower bound for likely observed horizontal wavelengths.

The second method uses a mean value for the positive and negative Scorer layers. The mean values should provide a larger horizontal wavelength which is trappable in the wave duct. It is suspected that this sets the upper bound for trapped waves because longer horizontal wavelengths, given the same vertical wavelength, are more prone to leakage (Durran et al. 2015). These two methods are by no means without arguable problems. However, based on a choice of k, section 4 will demonstrate that this range defined by these two values qualitatively agrees with observations.

3.3.2 Deriving the maximum vertical motion

A trapped wave will be described as an internal gravity wave able to be maintained within a wave duct for least two cycles (Lindzen and Tung 1976a). These waves are assumed to be associated with a long-lived bore. For this methodology, solving equation (3.18) with (3.19), with methods described in section 3.3.1, provides a normalize profile of the vertical motion.

The theoretical magnitude of the vertical motion within the trapped waves is derived in section 2.6.8. In order to calcualte the maximum value of vertical motion from

observations, the impedance relationship can be used. In the impedance relationship, the observed perturbation of u' can be determined by relating it to the perturbation in pressure p' (Gossard and Hooke 1975):

$$u' = \frac{m}{\omega \rho_s} p', \tag{3.20}$$

where ω is the intrinsic frequency of the wave and ρ_s is the surface density. It is seen that maximum and minimum perturbations in pressure are directly proportional to maximum and minimum values in the horizontal wind. Therefore, identifying the perturbation u' wind in the direction of the wave collocated with the maximum p' is equal to the max perturbation in u'. The same can be done for the minimum u' wind perturbation.

Using equation (3.20) to determine u'_{max} and u'_{min} substituting it into equation (2.118), an equation for the vertical motion is

$$w_{max} = -[u'(p_{min}) - u'(p_{max})] * \frac{k}{2m_1}, \tag{3.21}$$

where $u'(p_{max})$ are the wind speeds in the direction of the bore at the maximum wave pressure, and m_1 is the vertical wave number in the positive Scorer layer adjacent to the surface.

3.4 Forecast tool for predicting bore lift

The current section is an outline of a method to analyze lifting by a bore. The method requires a fine line is observed in radar reflectivity and, in the case that a RFL is a density current, uses theretical parameteres to determine if a bore shall form. If a bore is to form, the properties of the bore are calculated from hydraulic theory. Based off of hydraulic and linear wave theory, parcel over a specified depth are hypothetically

displaced vertically according to two methods.

3.4.1 Predicting the presence of a bore

1. Identifying the boundary

For a forecaster examining images of radar reflectivity, the identification of a boundary begins with the presence of a discernible RFL in reflectivity or in visible satellite. The method for identifying the origin of a fine line is outlined in section 3.1. These fine lines may be associated with a bore, density current (Wilson and Roberts (2006), Haghi et al. 2017b), heat burst 4, cold front (Koch et al. 1991) or other boundary.

Once the boundary has been identified and surface observations have been collected that capture changes to surface temperature, pressure, moisture, and wind associated with the target boundary, then a characterization can be made (the characterizations are explained in table 3.1). If the boundary is believed to be a density current or bore, the impedance relation (Gossard and Hooke 1975) can be used to gauge if the surface observations are indeed indicative of a gravity wave. Using surface observations and loops of radar images, the vector difference between the surface wind vector associated with the maximum and minimum pressure (presumed to be the pressure at the gravity wave crest and the pressure ahead of the gravity wave, respectively) can be compared with the movement of the boundary (Gossard and Hooke 1975). If there is good agreement, then, according to impedance relation, the boundary is a gravity wave phenomenon. This process is demonstrated in section 5.

If the observations indicate the presence of a density current as in section 3.2.1, the next step is to use a time series of the temperature, dewpoint, pressure, wind speed and wind direction to characterize the depth and speed of the density current (Koch et al. 1991). Soundings are useful for characterizing the depth and strength of the environmental nocturnal inversion, but usually not available when the nocturnal

inversion develops since the operational National Weather Service vertical soundings for temperature, dewpoint and wind are only taken at 00 and 12 UTC. In this situation, it is advised that estimates of these parameters can be taken from model forecast soundings.

2. Calculating the flow regime and bore properties

Assuming the properties of the density current and the inversion are determinable, the flow regime can be calculated using the same method in section 3.2.1. If the flow regime is partially blocked, then theoretically a bore should form. According to the μ parameter, the bore that develops will either pull away from the density current or remain in some version of a bore/density current hybrid (Haase and Smith 1989; Rottman and Simpson (1989); Blake et al. 2017). In times where there is a hybrid bore/density current (Haase and Smith 1989; Rottman and Simpson 1989), the surface temperature may exhibit an oscillatory pattern associated with the surface pressure. This hybrid case occurs when the density current sheds the head and the cold air of the density current head is trapped within a gravity wave circulation behind the bore (Rottman and Simpson 1989; Helfrich and White 2010).

Once the blocking and μ are determined, then the bore strength and bore speed can be calculated, described within section 3.2.3 and 3.2.4. Given a bore height assuming it has reached a steady state, a two layer-lifting method can be applied to calculate the parcel displacement through the bore.

3.4.2 Technique 1: Lifting according to hydraulic theory

The first method to determine lift is an adaptation of hydraulic theory. Based on impermeability, there can be no lift at the surface. Lift increases linearly from 0 at the surface until it reaches the top of the inversion (the linear lift is a simplification and is not assumed to be a perfect representation of the atmosphere). The depth of the

max lifting will be the difference between the height of the bore and the height of the inversion layer, $h_1 - h_o$. Above the inversion, the displacement will remain a constant $h_1 - h_o$ up to 5km. However, this displacement above the bore is not considered to be permanent (although Parsons et al. 2017 indicate that the semi-permanent lift above the duct can last on the order of a couple of hours). Instead, the lift is assumed to be the most accurate at the top of the wave crests. This approach is the first time this methodology will be applied in a case study and it is illustrated in figure 3.3.

It is assumed that the method accuracy shall decrease as the bore pulls away from its parent density current and evolves into a group of gravity waves or as a soliton. The applicability of hydraulic theory over the entire life cycle of the bore is not addressed in this work, although observations seem to suggest that the semi-permanent displacement can maintain itself for long periods of time (section 4). The shortcomings of this technique will be discussed in 5.

3.4.3 Technique 2: Lifting according to linear wave theory

The second method is determined from linear wave theory. As the density current height and speed change, the partial or complete blocking may cease. When the blocking ceases, the bore depth will begin to subside and return the environmental inversion height. However, hydraulic theory does not explain why waves that evolve from a bore are observed to last for long periods of time without the presence of a density current. If there is a suitable wave duct for trapping some of the wave modes associated with the bore, then trapped waves will maintain their shape even as the blocked fluid spreads out and settles back to the environmental height. The displacement by a parcel passing through a trapped wave will be evaluated with the second lifting technique. This method uniquely solves the wind profile for a 2D cross section of a theoretically trapped wave. Theoretical parcel trajectories are obtained within this 2D cross section and the depth of largest displacement is calculated from

the trajectories. The trajectory analysis is described in the next section.

Trajectory analysis

To obtain trajectories, equation (3.21) provides the maximum expected value of w' within the wave. This method is described in section 3.3.1. Using the value for w_{max} in equation (3.21) and uniquely solving equations (3.18), (3.19), (2.118), and (2.119), then a field for u and w can be determined. With the perturbation quantities known, the full equation for u and w are calculated using the following:

$$u = u_o(z) + u'(x,z), \tag{3.22}$$

$$w = w'(x,z), \tag{3.23}$$

where $u_o(z)$ is the environmental horizontal wind determined from sounding data. If a parcel at a height z and a location x is followed in time, then the maximum displacement the parcel experiences can be calculated along its path. This displacement is calculated with the following equations (Reap 1972):

$$x(x,z,t) = x(t-1) + u(x(t-1), z(t-1)) * \Delta t, \tag{3.24}$$

$$z(x,z,t) = z(t-1) + w(x(t-1), z(t-1)) * \Delta t, \tag{3.25}$$

where Δt is the time step of integration. For our calculations, the time step was 1 second, which provides enough temporal resolution for a parcel that performs one oscillation on the order of 100 seconds. The displacement is determined by finding the maximum height of the displaced parcel, then subtracting it from its initial height.

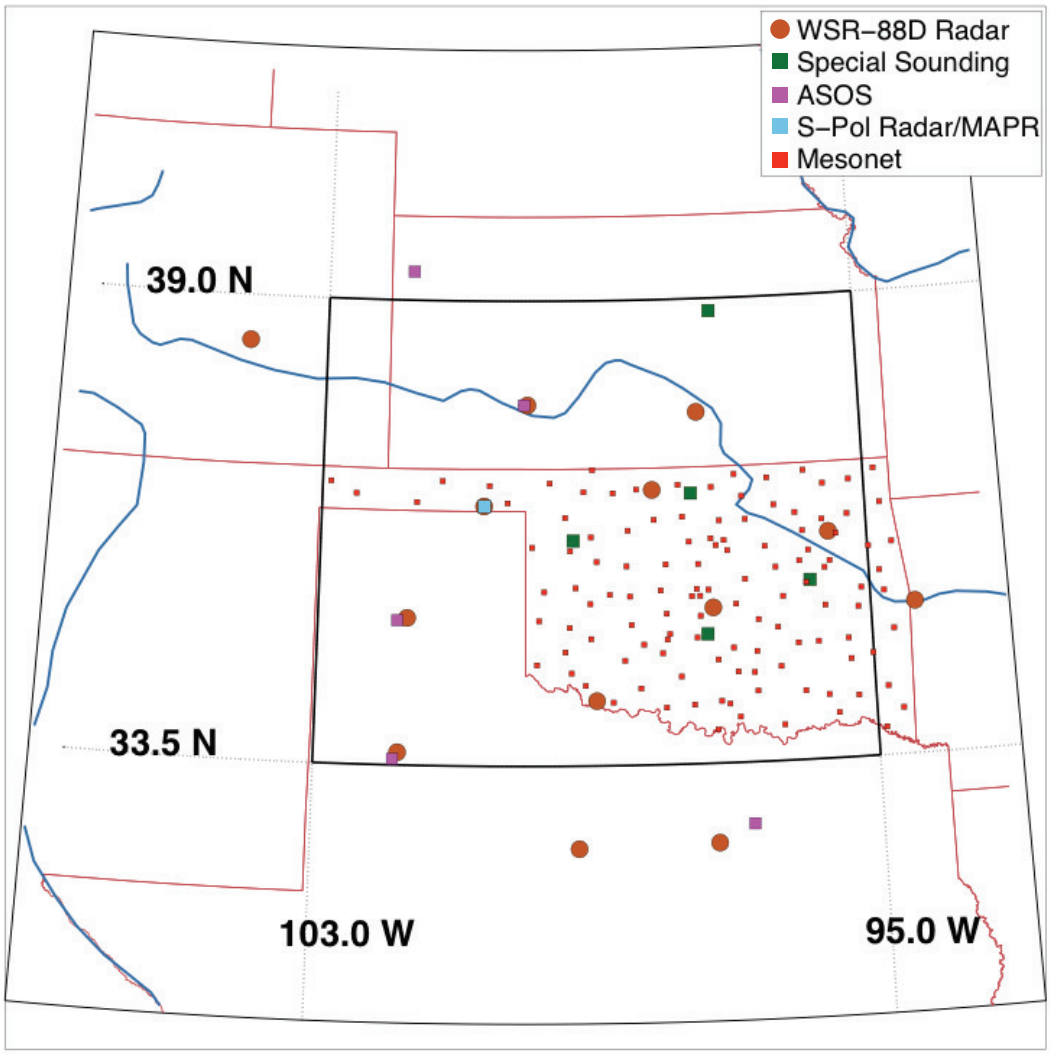

Figure 3.1: Map of the IHOP_2002 experimental domain showing the lat-lon extent, state boundaries and key observation sites. The measurement facilities utilized in this study are the WSR-88D Radar network, ARM special sounding sites, NWS ASOS, the S-POL radar at Homestead accompanied by the MAPR profiler, and the Oklahoma Mesonet, color-coded in the legend. Blue lines indicate rivers.

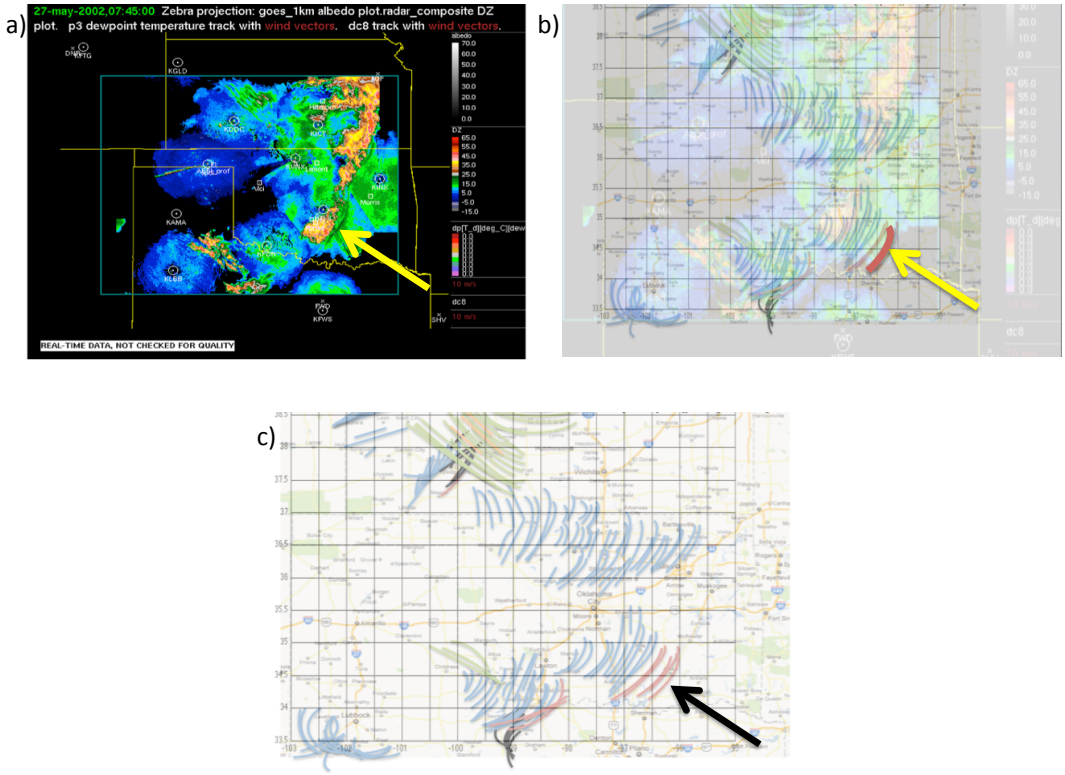

Figure 3.2: An example of the RFL marking method for 27th May, 2002; a) a composite radar image, the yellow arrow indicates the RFL of interest; b) the composite radar image superimposed over a political map of the IHOP_2002 domain, with the transparency increased. The red arch marks the location of the RFL of interest; and c) the RFL map for the May 27th, 2002 after all of the RFLs for the night have been analyzed and marked on the map. The color couplets (blue/red; green/black; orange/purple) indicate when fine lines become multiple fine lines and different color couplets are used to assist the eye of the reader when distinguishing overlapping RFLs.

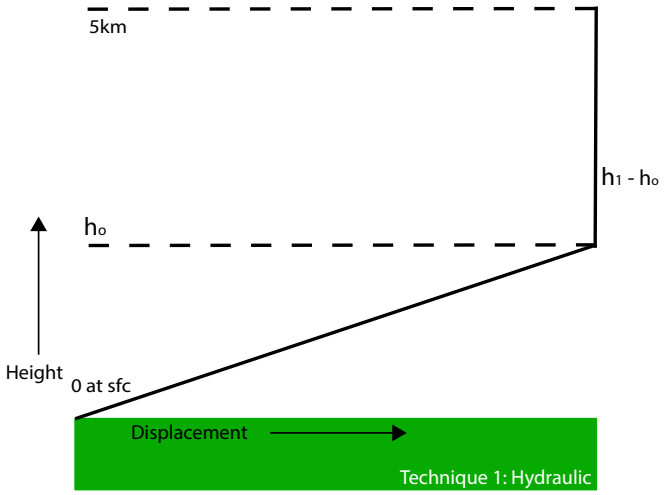

Figure 3.3: Technique 1 for bore lifting using hydraulic theory. The displacement represents the height of the parcel at a given level z above the ground by which it will be displaced. The displacement is 0 at the surface and is applied up to 5km above the ground.

Table 3.1: Definitions for characterizing observed boundaries on radar and in surface observations. SFL and MFL stand for single and multiple fine lines, respectively.

	RFL appearance -	**ΔP** (mb/30mins)	**ΔT** (^{o}C/30mins)	**ΔT_d** (^{o}C/30mins)	**Wind direction** -	**Citations** -	**Comments** -
Convectively Generated							
Density current	*SFL*	≥ 0.5	≤ 0.5	–	*one wind shift with initial pressure rise*		
Undular bore	*MFL*	≥ 0.5	≥ 0	–	*oscillates with pressure*	*Koch et al.* 1991	*semi – permanent pressure rise*
Non-undular bore	*SFL*	≥ 0.5	≥ 0	–	one wind shift with pressure rise		
Solitary wave	*SFL/MFL*	≥ 0.5	≥ 0	–	*oscillates with pressure*		*no permanent pressure rise*
Heat burst	*SFL*	≤ 0.1	≥ 1.0	–	*one wind shift with pressure fall*	*Bernie and Johnson* 1994	
Synoptic							
Retrogressing dryline	*SFL*	≥ 0	≤ 0	$\leq 1.0-2.0$	*veering winds with passage*	*Ziegler and Hane* 1993	*Used synoptic maps*
Cold front	*SFL*	*see comment*	$<< 0$	< 0	*wind shift with pressure rise*		*Used synoptic maps; Pressure min. at passage*
Stationary front	*SFL*	–	–	–	–	*AMS glossary*	*Used synoptic maps*
Other Boundaries							
Gravity Wave	*SFL/MFL*	*see comment*	0	–	–		*oscillations in pressure*
Undetermined							
Warming event	*SFL*	–	≥ 0	–	–		*no clear source*
Fine line*	*SFL*	–	–	–	–		*no clear source motion perpendicular to wave fronts*
Undular waves*	*MFL*	–	–	–	–		*adheres to no categorization*
No categorization							

Chapter 4

Systematic Study

4.1 Introduction

The work and figures presented herein are extracted from (Haghi et al. 2017b). This chapter presents an analysis of atmospheric bores and other convergent boundaries observed from 15 May to 25 June 2002 within a 16-06 LST (22-12 UTC) time window using data collected during International H_20 project (IHOP_2002) over the Southern Great Plains of the United States ((Weckwerth et al. 2004)). The main objectives of this chapter is to 1) demonstrate the frequency and behavior of observed bores, 2) compare the observations with a statistical model employing a variation of hydraulic theory, and 3) explain the direction and longevity of bores through an application of linear wave theory.

Previously, case studies provisionally identify fine lines in radar reflectivity as bores whose dynamic and thermodynamic structure is then studied with surface observations and pre-bore environmental soundings (e.g., Locatelli et al. 1998; Knupp 2006; Koch et al. 2008b,Koch et al. 2008a; Tanamachi et al. 2008; Coleman and Knupp 2011; Marsham et al. 2011). These case studies of bores generally found good agreement with predictions from hydraulic and linear wave theory. However, it is difficult to draw generalizations from case studies and such an approach does not provide information on the frequency of such events. The research in this chapter moves beyond the individual case study approach and systematically examines the relationship

between multiple convectively generated outflows, bores and their nocturnal environment.

As in Wilson and Roberts (2006), bores are initially identified in the RFLs and subsequently by analyzing surface wind data from IHOP_2002 for oscillations in the wind.[1] The present study builds upon Wilson and Roberts (2006) with the inclusion of surface thermodynamic meteorological measurements to describe bore evolutions that are unobservable by radar and wind measurements alone. This improvement to the Wilson and Roberts (2006) method also assisted with the identification of a non-undular bore (see table 3.1), which refers to bores that display a prominent single rise in pressure and one wind shift with little indication of a secondary fluctuation. By this definition, rarefaction waves are also included (White and Helfrich 2012). This approach uses the methods outlined in section 3 to characterize the observe 152 RFLs.

4.2 Overview of Observed RFLs

The results of the systematic study provide evidence that the nocturnal environment is often favorable for generating a bore or solitary wave. Of the 152 categorized boundaries, 65 are considered a bore ($\sim$43%) initiated by a density current or cold front (Fig. 4.1, 62 density currents; 3 cold fronts). There is a reasonable amount of confidence that the bores were correctly identified since 44 of the 65 bores were classified as well-determined, 8 were adequately determined and only 13 bores were poorly determined. Moreover, atmospheric bores and solitary waves made up 62 of the 98 convectively generated boundaries ($\sim$63%); a category that also included 28 density currents and 8 heat bursts.

For the 57 well-determined convectively generated boundaries, 44 density currents generated a bore ($\sim$77%), 5 density currents did not ($\sim$9%), and 8 were heat

[1] Wilson and Roberts (2006) also used surface winds to discriminate elevated from surface-based boundaries that initiate convection

bursts ($\sim$14%, Fig. 4.2). Thus, density currents initiate a bore-like response in the environment 90% of the time ($\frac{44}{44+5} \times 100 \sim 90\%$). Given the inability to classify some RFLs with higher confidence, the exact percentages should be treated with some caution. However, these results indicate that density currents commonly trigger bores in the nocturnal environment and those bores account for a significant fraction of the total number of RFLs ($\sim$43%) observed over the IHOP_2002 domain.

The finding that bores are common in the nocturnal environment is qualitatively consistent with the conclusions of Wilson and Roberts (2006). An important distinction between the two systematic studies is that 16 of the 39 well-determined bores identified in this study (not including solitary waves) are non-undular bores which were undetected in Wilson and Roberts (2006). The reason for this difference is attributed to use of thermodynamic surface data to supplement radar reflectivity and surface winds. In Wilson and Roberts (2006) definition of a bore, these non-undular bores would fall outside of the classification and were potentially grouped into the gust front category. Thus, its likely that Wilson and Roberts (2006) underestimated the number of bores, which may impact how gust front-driven convection is framed in their study.

Bores were observed on 23 of the 32 ($\sim$70%) days when convection occurred in the domain (Fig. 4.3). 14 of the 32 days with bores ($\sim$61%) occurred on nights with a synoptic boundary present. Over the entire IHOP_2002 campaign, bores were present on 23 of the 42 ($\sim$55%) days. During the convectively active period of May 15-20th, 24 bore events occurred, while only 2 density currents did not generate a bore ($\frac{24}{24+2} \times 100 = \sim 92\%$). The ratio of generated bores to total density currents during this active period is also the one of the highest during the campaign. These percentages may be an underestimation, since not all density currents or bores were readily apparent in the radar reflectivity images and bores may have been generated once density currents moved out of the IHOP_2002 domain. It is noted that the number

of observed frontal boundaries and bores diminish during the campaign (Fig. 4.3). The times series contain a relative maxima with a periodicity of ∼8-10 days. The time-scale is likely due to the timing of synoptically active periods, which provide a mechanism for nocturnal convection and thus density currents that generate bores (Weckwerth and Parsons 2006).

It noteworthy that most of the bores did not evolve into a solitary wave. This may be a symptom of how solitary waves and bores are defined within this study (for reference, see table 3.1). However, the definition is fluid. For example, (Koch et al. 2008b,a) recognizes a soliton (a group of solitary waves) as an amplitude-ordered bore, an intermediary between the presented definition of a bore and a solitary wave. This analysis would count the amplitude ordered bores as an undular bore even though it exhibits the behavior of both an undular bore and a solitary wave. Meanwhile, the use of a finite domain implies that some solitary waves may have been characterized as a bore because the evolution to a solitary wave took place outside the domain. The true nature of this evolution from a bore to an amplitude-ordered solitary wave is left to later numerical simulations studies.

4.3 Preferred times for a blocked flow regime

In this section, the characteristic flow regime is estimated for the entire IHOP_2002 campaign, including days when convection did not occur. The purpose is to gauge how often the environment is predisposed to develop a bore if perturbed with a density current. Using the non-dimensional parameters (Fr_o and H_o) as done in previous case studies (Koch et al. 1991; Koch and Clark 1999; Kingsmill and Andrew Crook 2003; Knupp 2006; Koch et al. 2008b, Koch et al. 2008a), the flow regime is calculated, but within a bootstrap resampled statistical model. A bootstrap is appropriate for capturing the "true" distribution, since the number of density currents observed are

low (26 events). This statistical approach moves beyond case studies that rely on local measurements at a fixed site or aircraft measurements.

The values for h_o, U_{inv}, and $\Delta\theta_{vw\_inv}$ are determined from the 5 special ARM sounding sites for the sounding taken at 2100, 000, 300, and 600 LST. The quality check eliminated soundings with missing data of temperature, moisture or wind below the surface inversion. Unfortunately, a large portion of environmental soundings has missing data (out of a possible 440 special soundings for 2100, 000, 300, and 600 LST, there were only 188 usable soundings left [55, 51, 39, and 43, at the respective sounding times]). The density current properties were calculated from the radar observations as described in section 3 and from estimates of the height of a density current, d_o, based on surface observations (described in Koch et al. 1991). Surface observations were available to calculate d_o for 26 of the 49 observed density currents with 21 of the 26 are observations from density currents that generated a bore.

The following is a description of the resampling technique used to construct Fr_o and H_o (Fig. 4.4). 1) Three density current parameters (d_o, C_{dc}, and orientation/direction of movement) are resampled independently, constructing "artificial" density currents. This independent resampling reduces the oversampling the same density current. An unavoidable consequence is the independent resampling increases in the spread of the final distribution of the flow regime. 2) The three environmental conditions, h_o, $\Delta\theta$, and U_{inv}, are resampled dependently. A dependent resampling is appropriate, since the pool of soundings is likely representative of the true environmental variability during the campaign.

A total of 100,000 replications were performed for each bootstrap resampling. The 100,000 replications were found by starting with 1,000 replications and increased the number until the variation in the final solution is minimal (Efron and Tibshirani 1993 pg. 50-51). Using the 100,000 replications, smoothed 2D density estimate of the Fr_o and H_o pairs were created. The result is similar to a topographic mapping, but

instead displays the frequency of occurrence per unit area. The results of the analysis are plotted on an adapted Rottman and Simpson (1989) diagram of the flow regimes as a function of time for 2100, 000, 300, and 600 LST (Fig. 4.5). The contours encompass the percentage total number of resampled pairs as a function of density. The 1% densest points in the 2D density estimate are interpretable as the most likely response produced in the environment. Changes in the 2D density estimate suggest that the flow regime adjusts to the evolution of the environmental conditions during the night.

The most likely response for every resampled time lies in the partially blocked flow (Fig. 4.5). The resamplings imply that convective outflows in the nocturnal environment are often predisposed to producing bores. This result echoes the observational findings in section 4.2 that density currents commonly initiate a bore response (Fig. 4.1). From 000-600 LST, the distribution transitions to a strong, unimodal distribution, centered at Fr_o of 1 and H_o of 1-1.5 within the partially blocked regime. The distribution contracts with time around the densest points, where the densest points fall in the partially blocking regime. As the distribution contracts with time, the bore strength settles near 2 (dashed lines, Fig. 4.5). According to Rottman and Simpson (1989), this bore strength should produce laminar bores (i.e. non-turbulent). Unfortunately, the IHOP_2002 data set lacked an extensive vertical profiling network well suited to examine the evolving structure of bores. Hence, investigation of the issue of laminar versus turbulent bores is beyond the scope of the present study.

To determine what aspect of the environment may be controlling the changes in the distribution, changes to the inversion properties and wind speed in the observed environment are investigated. The average strength and the height of the inversion increases two fold from 2100 to 600 LST (100-200m; 2.65-5.50 K), while the average strength of the horizontal wind in the inversion increased by only 7% from 21 to 600 LST (5.06-5.41 ms^{-1}). The inversion height is in the denominator of Fr_o (3.1) and H_o

(3.2) so as the inversion depth increases, both the Fr_o and H_o diminish; specifically, H_o should approach or pass unity. The net affect of the deepening inversion is to move the peak of the 2D density estimate towards a partially blocked flow regime (Fig. 4.5). Therefore, it is argued that the likelihood of generating bores increases through the night due to the strengthening and deepening of the inversion, while the mean flow associated with the NLLJ in the inversion layer generally play a lesser role. There are a few effects of the nocturnal environment that are not accounted for in this approach: the strengthening inversion will diminish the height and change the shape of the density current (Liu and Moncrieff 2000) and the environmental shear will amplify the leading edge of the density current (Liu and Moncrieff 1996). For this reason, it is not clear if the density current depth, and thus H_o, increases or decreases during the night.

The bootstrap resampled distributions of hydraulic theory are compared to the observed times of when density currents and bores appear within the radar reflectivity mosaic. For this analysis, the initial and final observed times of the RFLs are used and their duration is calculated. It is assumed that all of the events begin as a density current, implying the first observation of a RFL is, in general, associated with a density current. The final observed time of a RFL is assumed to be associated with the characterized state described in section 3.1. Additionally, the mean initial and final times, along with the duration are bootstrap resampled. These bootstrap resamplings are plotted alongside the observed times to assist the interpretation of statistical separation.

In figure 4.6a, the observations (black dots) of density currents that do not generate a bore overlap in time with density currents that do generated a bore (Fig. 4.6a). Physically, this result implies that a time threshold for bore formation was not observed. However, 75% of the density current bootstrapped means fall outside of the 1% whisker for undular bores (Fig. 4.6a), implying that density currents were more

likely to generate a bore as the night progressed. The tendency to generate a bore as the night progressed is consistent with the bootstrap of the mean final observed time, where only 1% of the bootstrapped means for undular bores overlap with density currents (Fig. 4.6b). While both bores and solitary waves, on average, appear to exist within a similar window of time, solitary waves were observed (black dots) exclusively later in the night (100+ LST), and bores were observed much earlier (2100+ LST). This result may be due to the development of more favorable environmental conditions or it may simply reflect the evolution of the bore life cycle as described in Christie (1989).

Bores tended to last 2 hours longer than density currents on average (Fig. 4.6c) with a high amount of certainty (70% of the undular bore resampled means do not overlap with density currents). From this longevity, it is hypothesized that the bores lifetime is at least partially explainable due to wave trapping.

4.4 Vertical Shear and Wave Trapping

In the atmosphere, bores degrade into a packet of waves that either are trapped within a wave duct or vertically propagate away. For this reason, bores are treated as a packet of infinite wave modes who's longevity is dependent on the presence of a viable wave duct. One favorable condition for trapping is a highly sheared layer containing a critical level (Lindzen and Tung 1976a), where the wind vector at some height is equal to the bore motion vector. Previous studies point to the vertical shear above the NLLJ for trapping of waves (e.g., Crook 1986; Koch et al. 1991; Koch et al. 2008a). Another condition is the vertical advection of vorticity by the vertical wave motion. The vertical advection of vorticity is synonymous with curvature in eqn. 5 (Crook 1988).

The examination of wave trapping begins by measuring the difference between

the shear vectors within the NLLJ (derived from radiosonde data taken at the 5 ARM sites at 2100, 000, 300, and 600 LST) and the direction of bore motion. Multiple layers of vertical shear through the lower troposphere are investigated, but just two of the depths with the smallest difference are presented. These two shear vectors extend from the height of the wind maximum in the NLLJ upward to either 1.5 km or 2.5 km AGL. A simple comparison of the direction of the NLLJ with the direction of the bores is avoided because theory (Shapiro et al. 2016) and the observations have peaks in u and v at different heights and therefore the relationship may not be so simple.

The angular difference between the movement of bores and the two aforementioned shear vectors are shown in Fig. 4.7. The direction of the bore movement is slightly rotated counterclockwise to the bulk shear vector extending from the NLLJ maximum to 1.5 km and slightly clockwise to the bulk shear vector extending to 2.5km. The alignment between the bore motion and the vectors increases with time. It is possible that the bores are aligning with a bulk shear vector who's depth lies between these layers. Alignment with a specific height is plausible given that there is great variation in the direction and speed of the wind above the wind maximum of the NLLJ (Shapiro et al. 2016). The general tendency towards alignment of the direction of the bore movement and the shear vectors with time suggest that the NLLJ plays a role in wave trapping.

The role of the NLLJ in wave trapping is further investigated through analyzing possible wave ducts ahead of observed bores using linear wave theory (described in 3.2). Data is utilized from the same 5 ARM sounding sites to calculate the environmental Scorer parameter. This analysis identifies a wave duct as: a layer of positive Scorer parameter adjacent to the surface topped by a layer of negative Scorer parameter (l_2^2); a critical level embedded within a sheared layer where the Richardson # is less than $\frac{1}{4}$ ((Lindzen and Tung 1976a)). A vertical profile of the normalized vertical motion is derived by solving for equation (3.12) and comparing it to observations of

bores that passed over MAPR.

Vertical profiles of temperature, moisture and winds, taken from soundings located within ~100 km of 13 bore events are utilized to diagnose the wave trapping mechanism. It is conceded that the environmental conditions in the analyzed soundings may not represent the true pre-bore environment. Repeating this analysis on data taken from Plains Elevated Convection at Night (PECAN) will be very beneficial because pre- and post-bore soundings were launched within close proximity to bore passage. For brevity, only one of the 13 case studies is presented, but this case study exhibits commonalities between nearly all analyzed environments.

The case study involves a 4 June 2002 bore (also analyzed by Koch et al. 2008b). The 6 LST sounding at Vici, OK is used for this analysis. In Fig. 4.8a, the profile of the Scorer parameter is displayed as a function of direction to illustrate how trapping varies with bore orientation. Wave trapping appears unfavorable for a bore traveling from 30-150 degrees, where the Scorer parameter exhibits a layer of negative values adjacent to the ground topped by a layer of positive values (Fig. 4.8b). Critical levels may be present for a wave coming from 150-290 degrees. While analysis of the Richardson # and the bore-relative flow appears to suggest a critical layer could be present (not shown), no wave traveled in this direction around 6 LST. For a wave traveling from 290-30 degrees, it appears that there is a positive Scorer layer below a large negative layer (Fig. 4.8a), providing a favorable pattern for wave trapping.

The 4 June bore is observed to move from 330 degrees, consistent with a favorable profile of the Scorer parameter. The bore is aligned with a curvature term that is large and negative at low levels (due to the denominator, the bore-relative winds, being negative), but positive above 1000m. Comparing the magnitude of the first and second term of the Scorer parameter (Fig. 4.8a), variations in the Scorer (Fig. 4.8b) are dominated by the curvature term. By attributing changes in the curvature (Fig. 4.8b) to changes in the Scorer parameter, then the top of the wave duct is due to the

inflection point above the nose of the NLLJ.

Next, the difference between the observed and predicted vertical motion profiles and the horizontal wavelengths is examined. Comparison between the predicted normalized vertical profile of *w* (Fig. 4.9d) and the *w* observations from MAPR (Fig. 4.10) shows good agreement. The height of the maximum *w* from MAPR and the predicted height of the maximum w are both close to 1000m. Additionally, the observed horizontal wavelength (calculated from the translation speed of the bore and period of the disturbance from MAPR vertical wind) is around 10km, falling within the range of theorized wavelengths (5036m and 13805m, Fig. 4.10). Based on this analysis of linear wave theory, this wave is expected to be trapped due to curvature.

If it is hypothesized that the curvature is not the mechanism of wave trapping, but a critical level (LT76), then only 2 of the 13 cases are explainable. Instead, 9 out of the 13 appear trapped according to this linear wave analysis where the curvature term dominates the profile of the Scorer parameter. The last 2 of the 13 cases do not appear to be trapped according to these two methods. This result is consistent with other studies highlighted in Koch et al. (1991). The maximum vertical motion is located near the transition from positive to negative Scorer parameter, and observations (Fig. 4.10) compare well with this finding. Therefore, it is concluded that the curvature above the maximum wind in the NLLJ is generally not correlated with a critical layer as in Lindzen and Tung (1976a), but often contains the positive curvature necessary for wave trapping in the nocturnal environment of the Southern Great Plains.

It is conceded that this linear wave theory requires trapped waves to exponentially decay within an infinitely deep second negative Scorer layer, which is not consistent with observed Scorer profiles. Therefore, this adaptation of linear theory cannot alone explain complete trapping. Interestingly, vertical motions extending above the analyzed negative Scorer parameter layer are observed (although the vertical motions from the MAPR data are limited to areas that surpass a threshold for signal to noise

ratio). This vertical motions is hypothesized to be in part to the insufficient trapping of waves within the wave duct adjacent to the ground, allowing vertical motions to extend upward into the lower troposphere. This behavior has been observed by Blake et al. 2017. Because these waves that emerge from bores appear to last quite a long time, it is presumed that a more complex interaction of wave trapping is taking place which is unexplained by this current method. Additionally, observations may contain nonlinear motions that are not represented in the linear analysis. For example, solitary waves are one form of nonlinear waves that may evolve form a bore (Knupp 2006; Koch et al. 2008b,a). This nonlinear theory shall be explored in a model framework within future studies.

4.5 Figures

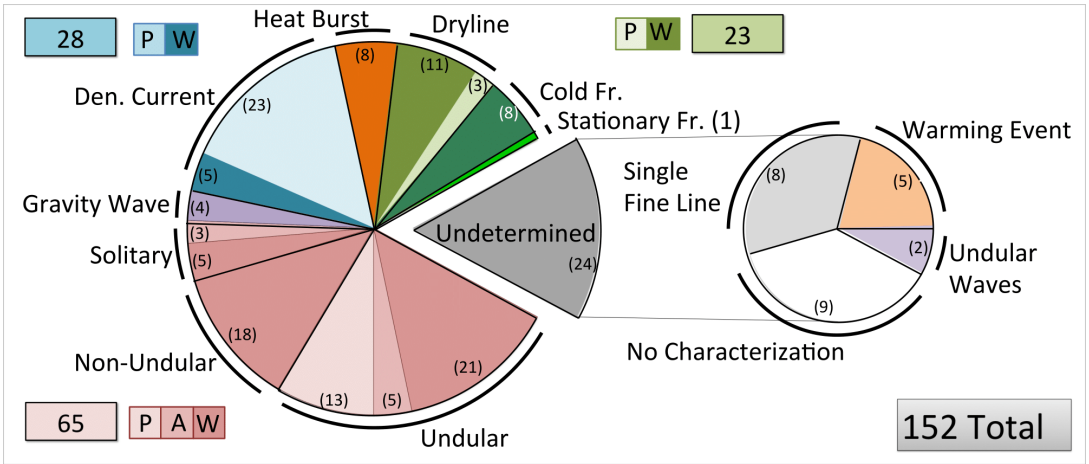

Figure 4.1: A Pie chart depicting the distribution of characterized RFLs during IHOP_2002. The shade of red represent atmospheric bores, the purple are gravity waves, the blue shades are density currents, the orange are heat bursts, and the green shades are frontal surface boundaries. Within the bore, density current, and dry-line shades are tints to indicate well-determined (W), adequately determined (A) and poorly determined (P) events. Undetermined cases are broken into a secondary pie chart, where orange is warming events, white is no characterization, grey is a single fine lines, and the purple are undular waves. (refer to the Appendix for clarification on characterizations).

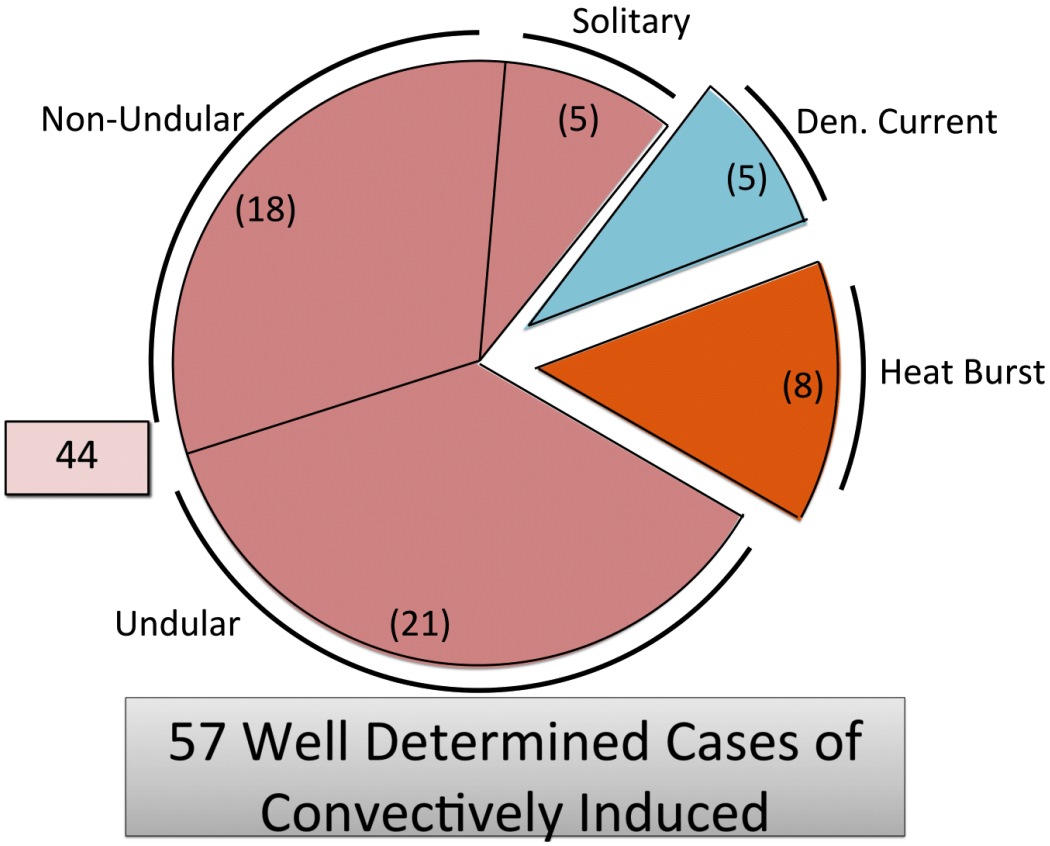

Figure 4.2: A pie chart depicting the distribution of convectively induced RFLs for cases of well- determined only. Colors coding is identical to figure 5.

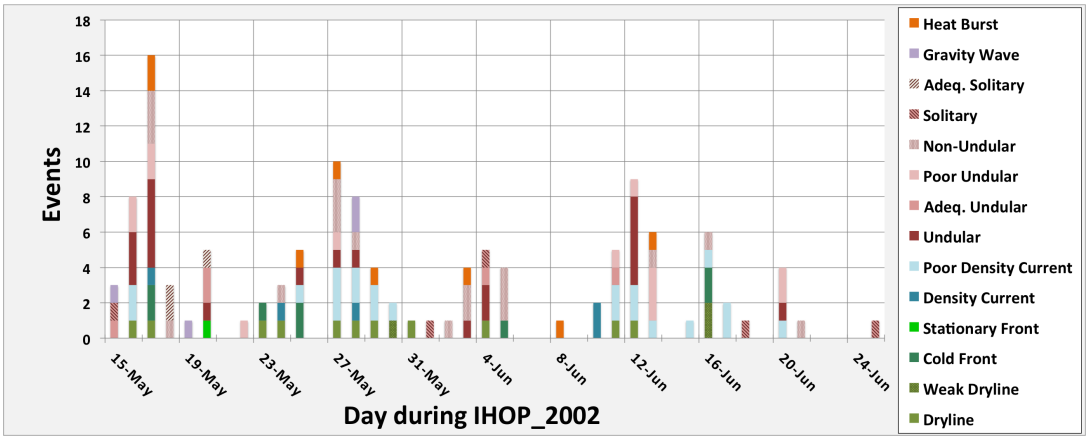

Figure 4.3: Bar graph of characterized phenomena during IHOP_2002 by day; the color-coding follows Fig. 5. Undetermined cases are not included.

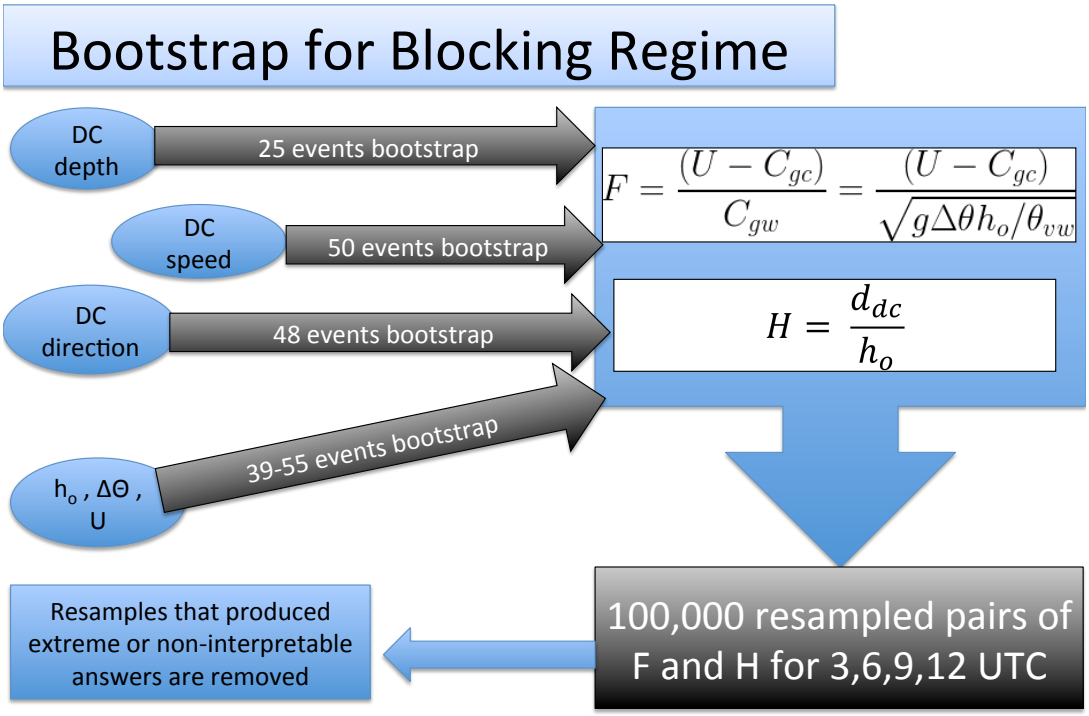

Figure 4.4: Flow chart illustrating the bootstrap resampling process utilized for estimating the 2D density estimate of flow-regime responses (Figure 9). 4 different bootstraps of the density current and environmental conditions are performed (top left) and used to calculate the Fr and H values (top right). The 100,000 resampled pairs are passed through a quality check to remove non-realistic values (bottom left).

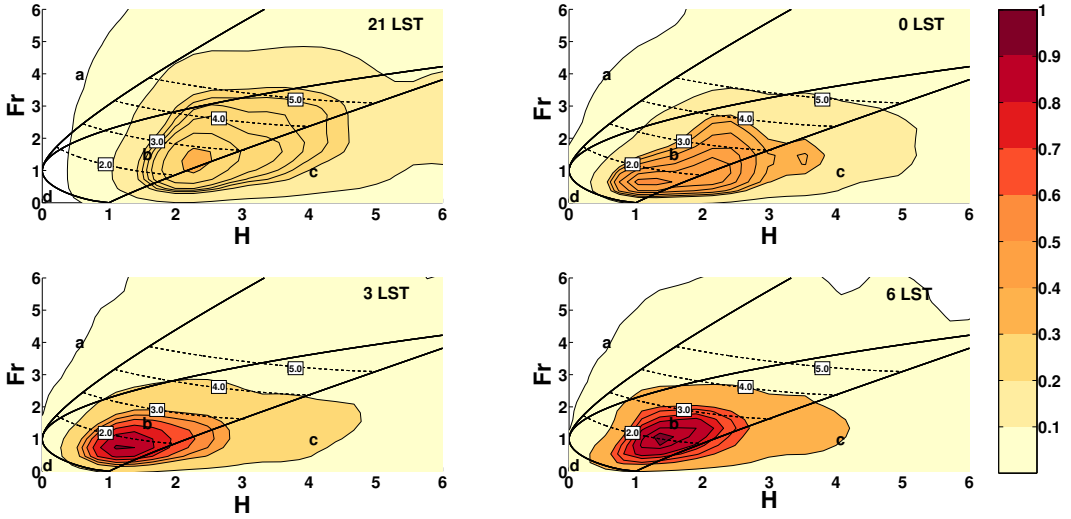

Figure 4.5: Contours of the 95th, 50th, 25th, 20th, 15th, 10th and 5th percentile of the densest points in the 2D density estimate as a function of time. Color-fills are the magnitude of the 2D density estimate normalized by the densest value among all 4 panels (analogous to a measure for the likelihood of observing a regime relative to the most likely regime at any point during the night), dashed lines represent bore strength; a) 21 LST, b) 0 LST, c) 3 LST and d) 6 LST. Modeled after Rottman and Simpson (1989).

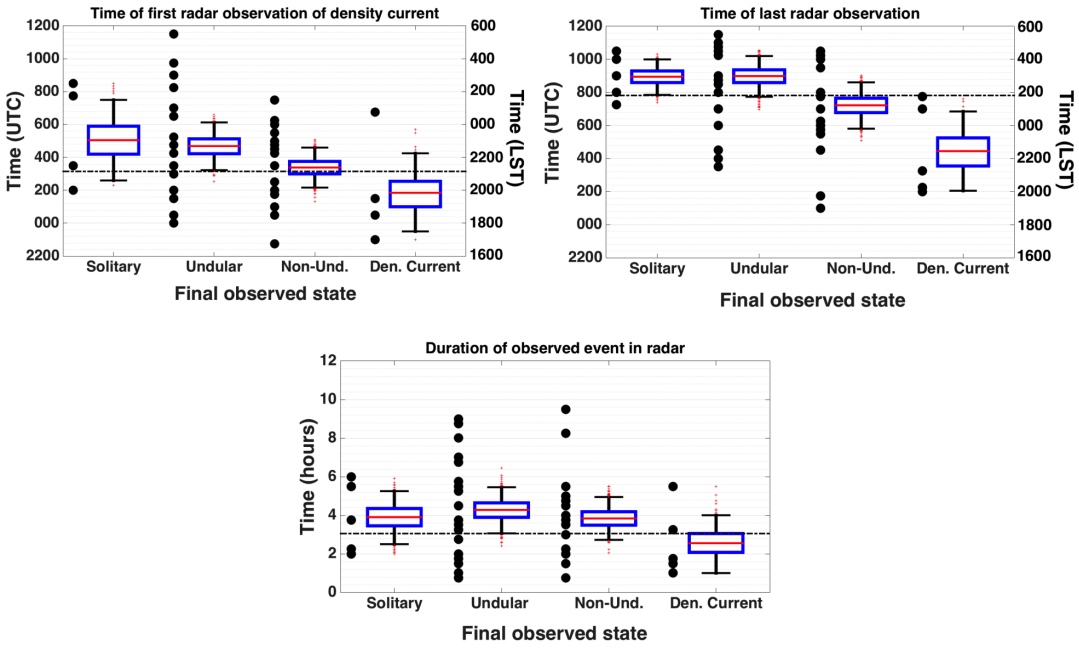

Figure 4.6: Boxplots of the resampled means for the: a)initial observance b) final observance (UTC and LST), and c) duration (hours) of RFLs during IHOP_2002 according to their final observed state: solitary waves, undular bores, non-undular bores and density currents. Black dots represent observed data; black dotted line represents the value associated with the 1st percentile whisker for undular bores.

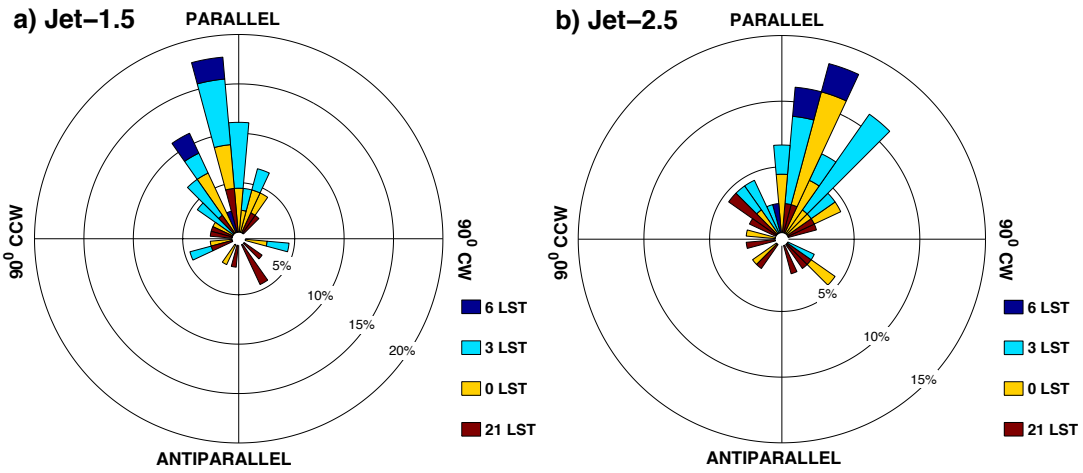

Figure 4.7: The angular difference between an observed bore direction and the direction of the environmental bulk shear vector contained between the height at the max NNLJ wind and a) 1.5km and b) 2.5km. The values are calculated from both the initial and final observed bore directions. In this plot, the 00 direction implies that the wind shear vector in that layer is aligned parallel and with the direction of movement of the bore, while a counterclockwise CCW (clockwise CW) implies the shear vector is 900 to rotated the left (right) of the bore motion. Contours are in percent of total for bulk shear; 45 cases for each.

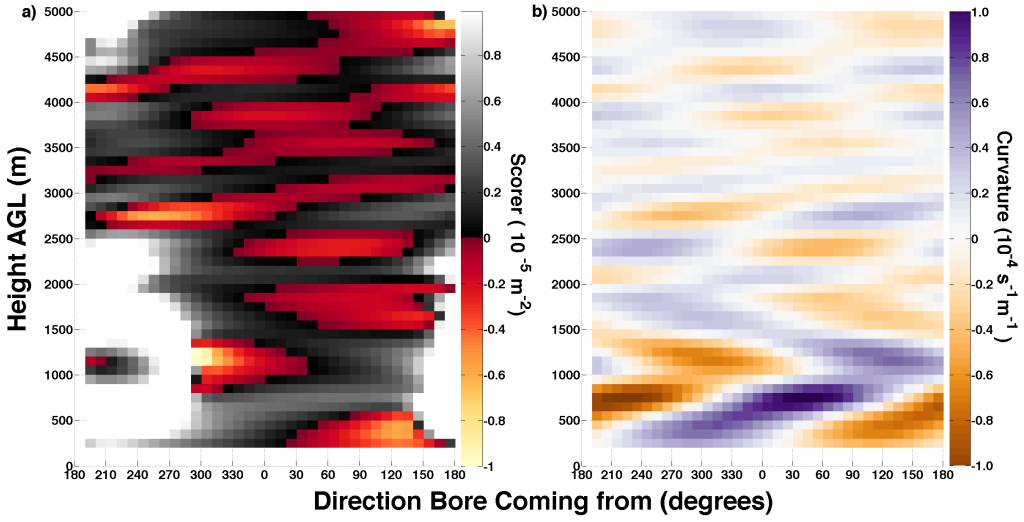

Figure 4.8: Analysis of a pre-bore environment from Vici, OK at 6 LST for a bore traveling from 334 at 10.8 m/s: a) Scorer parameter as a function of direction; b) curvature of the wind as a function of direction.

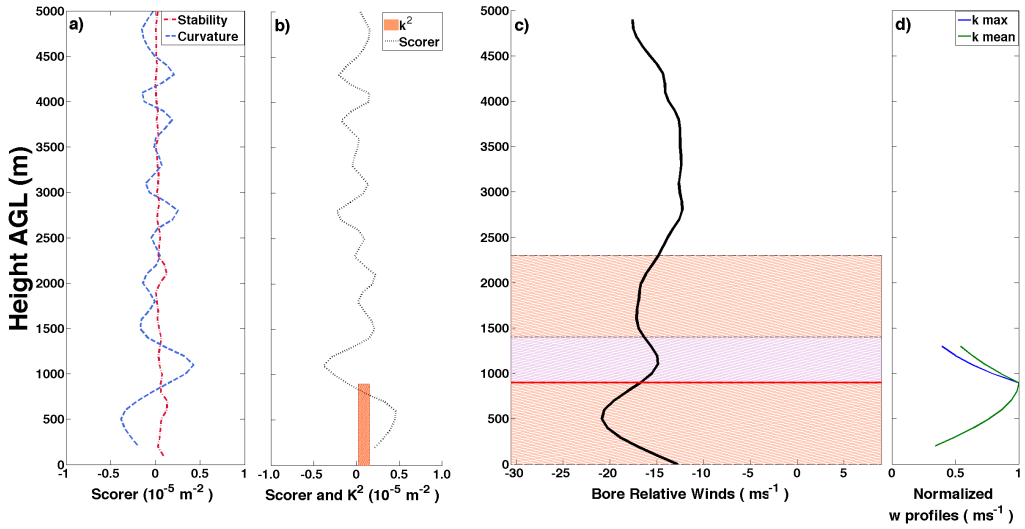

Figure 4.9: Analysis of the same bore from fig. 12 for the: a) stability and curvature terms of the Scorer parameter in the direction of the bore; b) Scorer parameter in the direction of the bore and the possible k2 range (indicated by the hatched orange box, defining a range of horizontal wavelengths for trapped modes between 5022m and 13606m); c) bore-relative winds with positive and negative Scorer parameter layers superimposed for the lowest 3 layers (orange hatch is positive layers and blue hatch is negative layers of the observed environment). Note: the bottom two layers are used to prescribe the two-layer solutions of the TGE, where the observed negative Scorer layer is assumed infinitely deep in the two-layer solution; d) normalized vertical wind profile for a trapped wave.

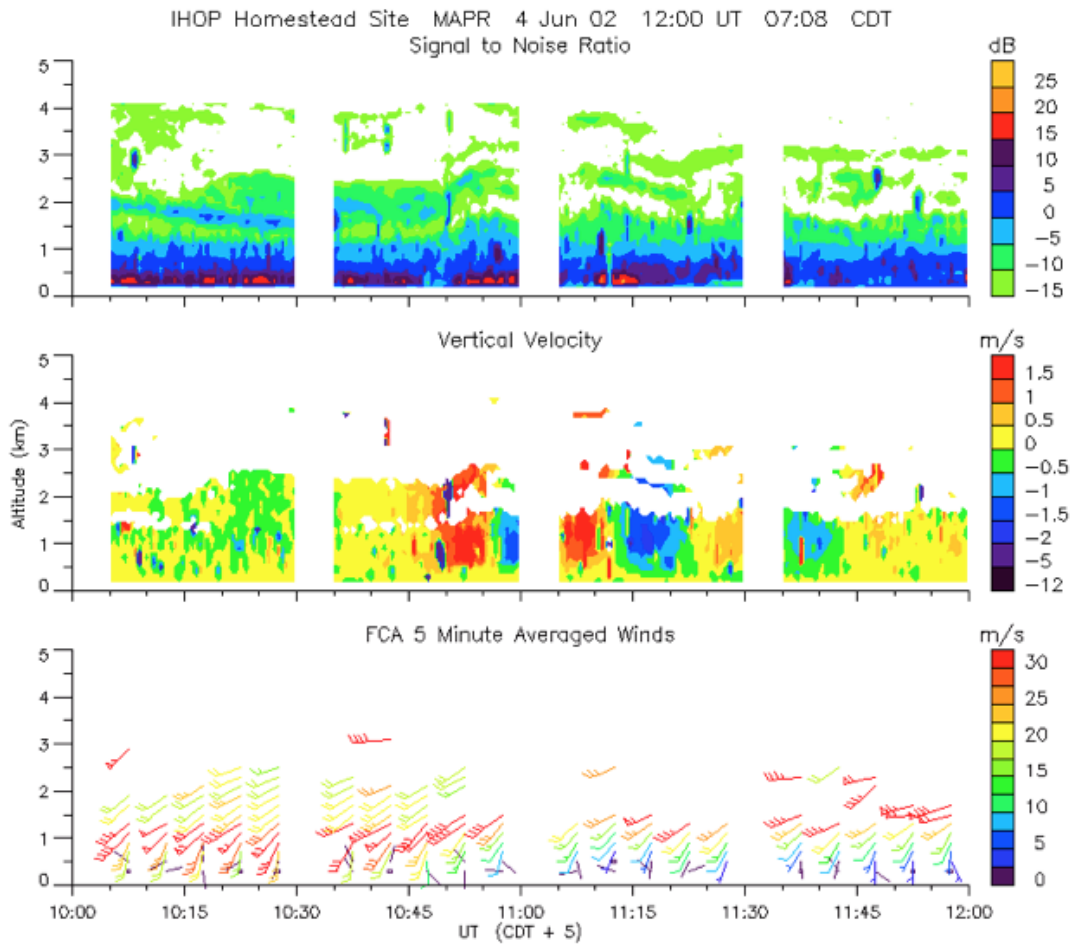

Figure 4.10: Multiple Antenna Profiler (MAPR) for one of the two June 4th, 2002 bores. The top panel is a time lapse of the signal-to-noise ratio, middle panel is the time lapse of the vertical velocity, and the bottom panel is the time lapse of the horizontal wind vector as a function of height. All panels are from 10-12 UTC.

Chapter 5

Bore Lifting

5.1 Introduction

The following work is an application of the method outlined in 3 to detect bores in the nocturnal environment, as shown in figure 5.1. The method begins with 1) evaluating fine lines in radar reflectivity characterized as a convective outflow and 2) applying derived hydraulic theory. If theory predicts a bore is indeed expected to form, 3) the μ parameter should indicate if a bore will pull away from its parent density current. Hydraulic theory also prescribes how deep the bore response should be and how fast this bore should be moving through the environment. Last, 4) two techniques are applied to sounding data to predict how high a bore will displace environmental parcels: a) lifting expected when a bore develops along a density current and b) lifting of a parcel based on its dwell time through the linear wave circulations. To be clear, this second lifting method is not being applied to the gravity waves observed behind the first wave of the bore, as (Toms et al. 2017) noted that the profile of the Scorer parameter, a component of the linear wave analysis, changes once the first wave of a train of waves associated with a bore disturbs the environment. The techniques in this study are intended to be heuristic and will be refined in later studies.

While IHOP_2002 is an appropriate dataset for characterizing the behavior of atmospheric bores in the nocturnal environment of the Great Plains, PECAN is a exceptional dataset for analyzing the pre- and post-bore environments. According to

Geerts et al. (2016) one of the PECAN goals was to examine "how the mesoscale environment modulates the initiation, structure, propagation, and evolution of bores, solitons, and other trapped wave disturbances, and sought to determine the inherent role of these systems in the maintenance of nocturnal MCSs. PECAN aimed to detect and understand bores propagating away from their parent cold pool and those that remain an integral part of MCSs." Our study aligns well with these goals.

To perform the analysis, the following work will use data from stationary surface facilities, called Fixed PECAN Integrated Sounding Arrays (FPISA)s, soundings before and after the passage of a bore and the Kansas mesonet (information about equipment used at the Kansas mesonet can be found at mesonet.k-state.edu/). Each FPISA includes a surface station with instruments to measure surface pressure, temperature, moisture and winds. Additionally, each FPISA includes a vertical profiler such as a 915 MHz wind profiler. 915 MHz wind profilers are LAP3000 (Radian/Vaisala) profilers operating in Doppler beam swinging mode (Cohn et al. 2001). Raw data is given in 30 second intervals, with a scanning pattern characterized by sampling at an elevation angle of 60^o for 4 scans followed by one vertically pointing scan and repeating. Only vertically-pointing scans are used in our analysis, implying a temporal resolution of 2.5 minutes. The vertical winds are derived from the backscattered signal.

Data during PECAN was collected from June 1- July 15, 2015, mainly in the Central Plains and was based in Hays, KS (Geerts et al. 2016). This study investigates one of the longest-lived bores during PECAN occurred on 3 June, 2015. It was generated from a well-organized MCS that moved across Nebraska. This case study is instructive in that a part of the bore initiated convection. The behavior of the bore varied along the bore front, from a hybrid density current/bore with convection firing along its front to a soliton with no convection. While there was no active bore mission on this night and thus no mobile intercepts of the bore with pre- and post-bore soundings

for this night, there are soundings ahead of the bore before it passes over 4 different sounding sites.

5.2 Case Study: June 3rd , 2015 Bore

5.2.1 Description

The synoptic conditions for 3 June at 00 UTC consisted of a weak ridge aloft at 500 mb extending from southern New Mexico northeastward into Kansas. This resulted in 20-25 kt westerly flow over the Rocky Mountains and into the Central Plains. Stronger westerly flow was noted at 250 mb (figure 5.2 a) with 30-40 kt winds over the target region (figure 5.2 b). To the west of the target region in the lee of the Rocky Mountains, a surface low pressure and trough extended northeastward into the Dakotas (figure 5.2 c and d). A moisture gradient existed across the PECAN domain, where dry conditions near Dodge City moistened towards the Missouri/Kansas border. With a surface low pressure centered over Colorado, the upslope winds aided convective initiation in the late afternoon along the range in Wyoming (figure 5.2 c and d). Values of surface-based CAPE 3000 J/kg extended over a large corridor with very little surface-based CIN (figure 5.2 d).

The target MCS organized and by 100 UTC it had a mesoscale outflow visible on radar. Along the convective outflow is an enhanced area of reflectivity > 40 dBZ. By 500 UTC, this MCS reached the northwest edge of the PECAN domain and passed over the FP4 site in Minden, NE (figure 5.3 a). There was a single fine line leading the convection, not visible in the MRMS reflectivity. Behind the MCS outflow was a group of convective cells bubbling up to the west in the Nebraska panhandle (figure 5.3 a). At 700 UTC, these group of convective cells organized into a secondary MCS in south central Nebraska (figure 5.3 b). By 900 UTC, the convective outflow of the target MCS exhibits the appearance of gravity waves along its extent (figure 5.3 c)

traveling southward across southern Nebraska toward the Kansas border. An example is provided in figure 5.4 at 900 UTC that highlights the radar fine lines in the PECAN radar mosaic. It is possible that, at this point, the convective outflow has generated a bore and the gravity waves observed in radar reflectivity are indeed along the extend of the subcritical regime of the bore.

Between 900 and 1100 UTC, the MCS convective outflow moved ahead of the main convection, coincident with a drop in the reflectivity within the core of the convective complex. However, around 1000 UTC, convective cells began to redevelop along the convective outflow and were becoming more numerous by 1100 UTC. (red circled area in (figure 5.3 d). These convective cells appear to be correlated with a train of fine lines that may be part of the target bore. By 1300 UTC, the target MCS was maintained along this line of wave-like features and the second MCS was catching up with the target MCS (figure 5.3 e). A line of convection was favorably interacting with the southeastward-moving secondary convective outflow. By 1300 UTC, it was highly likely that the convective outflow had generated a bore based on the longevity (Haghi et al. 2017b). The bore remained intact throughout the morning and is captured in visible satellite imagery at 1545 UTC in figure 5.5. The second MCS had merged with the original MCS and ongoing convection was still aligned with the waves along the convective outflow of the first MCS (figure 5.3 f).

Looking at the event in its entirety, the convective outflow appears to have multiple modes along its leading edge and convection seem to be confined to an area on the east side of the outflow. This point is demonstrated in isopleths of the fine line front as it moved through the domain (figure 5.6). To the east, the convective outflow is co-located with the most active portions of the MCS, transitioning to a convective outflow that appears to have moved away from the core of the convection and evolved into a gravity wave-like appearance. While new convection did fired along the wave fronts, it was at locations closer to the ongoing convection. Based on the synoptic charts,

the convective cells seem to be correlated with the position of the deep moisture. To the west, no new convection was generated, but instead there was a very clear train of waves.

5.2.2 Applying the Methodology

The convective outflow persisted long enough for the system to pass over the surface observations at FP4 in Minden, NE (orange diamond labeled "1" in figure 5.5), along with a 915 MHz wind profiler. At $\sim$ 500 UTC, a sounding, launched from FP4 just ahead of the approaching convective outflow, sampled the pre-storm environment. As the first MCS moved towards the ESE, it also crossed the Kansas mesonet site at Washington, KS (orange circle labeled "2" in figure 5.5). Only these two locations (FP4 Minden, NE and Washington, KS) observed the convective outflow associated with the first MCS. The second convective outflow was observed at most surface observations stations, but this convective outflow was in the disturbed environment of the first convective outflow and bore. Because this is the first attempt to apply theory to observations, the second convective outflow is excluded from the analysis. However, the calculations of theoretical parameters using the second MCS convective outflow can be found in appendix 7.4, table 3.1 and 7.2. The data processing techniques are discussed in detail in the methods section 3.

5.2.3 Hydraulic Theory

First, the impedance relationship, equation (3.20), as described in Gossard and Hooke (1975) is applied to the surface data at FP4 Minden, NE to gauge if the observed phenomenon moves according to a gravity wave. As described in Gossard and Hooke (1975), the impedance relationship is independent of height, so surface measurements offer valuable information about the structure of the wave aloft. Using FP4 surface

data, the direction of movement on radar agrees well with the expected direction of propagation (figure 5.7 b).

Using the direction derived from the impedance relationship, the flow regime is calculated with Fr_o from (3.1) and H_o from (3.2) using surface observations in the PECAN domain to diagnose if the density current should generate a bore (an example is seen in figure 5.7 a). Values of θ_{vw}, θ_{vc}, P_w, and P_c are obtained from surface data at FP4. After calculating ρ_w, the theoretical height of the density current is determined with (3.3). To evaluate the inversion, a sounding launched from FP4 Minden, NE at $\sim$ 500 UTC (446 UTC) is used for the following properties: h_o, U_{inv}, $\theta_{vw_{inv}}$, and $\Delta\theta$. A description of the method for calculating these values is in section 3.2.

From these observations, Fr_o and H_o are calculated, and the result is plotted in figure (5.7 c). The flow regime at FP4 lies along the line separating supercritical flow from partially blocked flow. Additionally, the Fr_o and H_o uniquely prescribe a bore strength. The bore strength ($\frac{h_1}{h_o} = 3.35$) also implies that the bore will behave like a density current (Rottman and Simpson 1989) because the turbulent effects become more important as the height of the bore increases. The response observed by (Rottman and Simpson 1989) is akin to a hybrid density current/bore. They are called "C bores" by (Rottman and Simpson 1989) and are akin to the gravity current/gravity current wave given by Haase and Smith (1989). The results from the flow diagram can be compared with the value for μ calculated with (equation (3.4)). The μ value is 0.68, implying that the response could be either a bore or a density current/bore hybrid. The μ value agrees well with the response from hydraulic theory.

Comparison of theoretical bore values with the 915 MHz profiler at FP4 in Minden, NE (figure 5.8) demonstrates visible differences. First, the bore height in the observations (1000-1200 m) is noticeably shallower than the theoretical (1700 m). There may be a multitude of reason for this discrepancy. For example, a density current head will become flattened in high stratification (Liu and Moncrieff 2000). To

test this hypothesis, the value for N was averaged over the inversion. the $N = 0.03s^{-1}$ in the surface inversion over FP4 (Minden, NE) is larger than the strong stratification case $N = 0.016s^{-1}$ in Liu and Moncrieff (2000). Based on stratification alone, a reduction in the density current would lead to a reduction in the bore head through reducing H_o. However, the study (Liu and Moncrieff 2000) assumes a neutral layer above the inversion layer. Neutral layers above the surface inversion are often not the case in the nocturnal environment. At FP4 Minden, NE, the layer above the surface inversion was moderately stratified up to 700 mb Because bores are in fact gravity wave features, stratification above the inversion could provide a mechanism for some wave radiation. Additionally, it is assumed that the density current profile of potential temperature is invariant. While it is commonly understood that an constant potential temperature profile is unrealistic, it provides a simple estimation of the height from surface data only. As a result, the estimation of the density current height incurred errors. Also, the observed density current speed (15 ms^{-1}) is faster than the predicted density current speed (12 ms^{-1}). It is possible that this difference is attributable to the strong stratification within the inversion layer, which may increase the speed of a density current as noted in Liu and Moncrieff (2000).

One other hypothesis for why the observations of the bore height are not as deep as predicted by hydraulic theory may be due to the bore not being in a quasi-steady state. As noted in section 2.3.3, for a bore to reach its quasi-steady state, the Fr of the fluid passing over the head of the density current must reach unity. Only then are the predictions of hydraulic theory valid. It is possible that the bore may have still been in its incipient stages and therefore would deepen as time went on. Due to limited observations this determination is not possible.

The μ parameter and the flow regime calculated from surface data collected at FP4 Minden, NE ($\mu = 0.68$) were accurate in predicting that the convective outflow would be a hybrid bore/density current. Interestingly, if we used the speed of the density

current from observations, the denominator in μ would increase, and the value of μ would be less. Likewise, using the density current speed from observations would increase the Fr_o and place the flow squarely in the zone where a density current/bore hybrid case should form. Therefore it is plausible that the value of μ was smaller than theoretically calculated. Either way for this case, it does not change the interpretation. The μ parameter agrees well with 915 MHz observations of SNR and vertical velocity, suggesting a bore head with waves proceeding along the back of the density current (figure 5.8).

The same density current was sampled later at a Kansas mesonet station in Washington, KS around 900 UTC, roughly along the same radial from FP4 Minden, NE. A sample of the surface data as the density current passed Washington is in figure 5.9. Theoretical values are found in table 5.1. The density current height appears to be overestimated (an estimated height of 2000 m), similar to FP4 Minden, NE. Note that this overestimation may be due to reasons previously stated. Hydraulic theory based on Fr_o and H_o imply that the flow is near complete blockage. It is difficult to confirm how much of the flow was indeed blocked without vertical profiler data.

The μ parameter ($\mu = 0.52$) implies that the response should appear like a density current/bore hybrid. In the surface observations (figure 5.9), an oscillation of the temperature with time is coincident with an oscillation in the wind speed, where positive wind speeds changes are in phase with positive temperature changes. One possibility for this explanation is larger wind speeds from the NLLJ being mixed down to the surface along with warm air at the top of the inversion. We attribute this to the bore circulation and not the density current circulation because the flow regime has been determined to be a near complete block. However, with the μ parameter < 0.7, it is possible that the bore and the density current have not separated, which is a point of emphasis because this phenomenon is mostly ignored using conventional hydraulic theory. Studies such as Helfrich and White (2010) have attempted to observe the

relationship between a density current and a developing bore within the confines of a numerical model. Their results show that the interface between the density current and the bore will often become muddled and their fluids will mix as the bore develops. Because PECAN did in fact measure bores as they evolved, analysis of their evolution similar to Helfrich and White (2010) may prove valuable. For example, observations of a bore in its forming stage are non-existent.

The flow regime and the μ parameter at Washington, KS provided conflicting results. According to hydraulic theory, a completely blocked bore should pull away from their parent density current because no fluid is making it over the head. However, the μ parameter implies that the bore should remain a bore/density current hybrid, more akin to the flow regime diagnosis at FP4 Minden, NE. One reason for this discrepancy is the properties of the inversion were diagnosed with the FP4 Minden, NE sounding because no soundings were launched from the Washington, KS mesonet. It is reasonable to believe that the inversion will have strengthened and deepened before the density current arrived at Washington, KS. The overestimated density current height and underestimated inversion height could shift the flow regime to be more akin with FP4 Minden, NE. Therefore it is imperative that future studies examine the sensitivity of soundings to spatial and temporal deviations from where and when it is launched.

5.2.4 Linear wave theory

Once the bore pulled away from the density current, it is assumed that there is a time where the displaced fluid subsides and the bore has either evolved into a group of solitary waves or gravity waves within the inversion. Zimmerman and Rees (2004) analyzed how well linear wave theory prescribes the observed wavelength of nonlinear waves. The finding suggest that linear wave theory does determine the properties of the wave duct well, even though nonlinear theory suggests this should be ampli-

tude dependent. Therefore, it is in our interest to test how well linear wave theory reproduces the vertical displacements observed. It is expected that linear wave theory should under-predict the displacement, but by how much? The explanation for defining a given k, m and w_{max} is outlined in section 3.3.1.

The bore extended across the entire state of Kansas figure 5.6. Observations from FP5 Brewster, KS and Dodge City, KS show the evolution from an undular bore that becomes a packet of solitary waves, often referred to as a soliton, by the time it reaches Dodge City (Koch et al. 2008b,a). Using the profile of the Scorer parameter in equation (3.13) from the 600 UTC FP5 Brewster, KS and 1200 UTC Dodge City, KS soundings, and applying our method in section 3.3.1 to solve TGE equation (3.12), there are two unique sets of k and m believed to encompass the observed k and m values.

In the case of FP5 Brewster, KS, the mean l^2 method described in 3.3.1 fails to identify a trappable wave, but the max l^2 method identifies a horizontal wavelength of 5300 m and a vertical wavelength of 2000 m. When compared with with the S-Pol reflectivity (6 km, figure 5.10) and FP5 Brewster, KS 915 MHz profiler (6 km, assuming a wave speed of 9.68 ms-1, 5.11 a), there is qualitatively good agreement. While there is no way to compare the theoretical wavelength calculated from Dodge City, KS with observations, it is noted that their max l^2 method has a horizontal wavelength of 3700 m and a vertical wavelength of 2800 m, while the mean l^2 method has a horizontal wavelength of 17000 m and a vertical wavelength of 2800 m. The observed value of a 6 km horizontal wavelength falls well within our k_{max} and k_{mean} predicted for FP5 Brewster, KS and Dodge City, KS. The height of the vertical motion predicted by our method for FP5 Brewster ($\sim 500m$) aligns well with one of the observed vertical motion maxima (figure 5.11 b). However, there are multiple vertical maxima within the leading wave. Because our method for prescribing a wave duct includes assuming that the layer above the wave duct is negative and infinitely deep, it

can not explain the complexity of vertical motion observed above the first max. Likewise, Toms et al. (2017); Mueller and Geerts (2017) recognized that vertical profile of the Scorer parameter can change when the first wave disturbs the environment. Because there are no soundings available after the first wave passes through, nor would there be in a real forecast situation, the subsequent waves are left to be analyzed in later studies. Therefore, it appears that the linear theory does a good job with the wavelengths observed, aligned with Zimmerman and Rees (2004), but is too simple to explain all of the complexity.

5.2.5 Layer-Lifting Technique

The following section will examine both the hydraulic and the linear wave theory techniques of parcel displacement. Both of these methods are discussed in section 3. The first technique based on hydraulic theory was applied to the sounding at FP4 Minden, NE. As mentioned before, the first technique is assumed to be valid when the bore has initially reached a quasi-steady state with its parent density current. Determining if the bore is in a quasi-steady state requires identifying Fr at the top of the density current. Based on wind profiler data alone, distinguishing between the density current and the incipient bore is difficult. Additionally, there is no current observational study that does identify a bore in a quasi-steady state. A future study should design an investigation to determine if the hydraulic technique for bore lifting performs better when the $Fr = 1$ at the crest of the density current.

The hydraulic technique predicts that the bore will lift air at the top of the inversion by nearly 1200 m. As expected, observations suggest that the air at the top of the inversion was lifted by 800 meters. Therefore, it is expected that the lifting by hydraulic theory overestimates the destabilization occurring due to the bore.

The second technique, as discussed in the previous section, is applied to the 600 UTC FP5 Brewster, KS and 1200 UTC Dodge City, KS soundings. Following the

technique describe in section 3.4.3, trajectories are calculated for a parcel traveling through linear waves. The maximum displacement expected at FP5 Brewster, KS and Dodge City, KS is around 25 m and 100 m, respectively. Clearly, the displacement by linear waves is too small, almost an order smaller than the observed displacements in the FP5 915 MHz wind profiler. This result is not unexpected. As in Zimmerman and Rees (2004), the amplitude of nonlinear waves is poorly represented by the linear wave theory. Therefore, this method alone does not provide much insight to a forecaster.

Modified soundings

The displacements for both methods were applied to their respective soundings and these post-bore soundings were superimposed on their respective pre-bore soundings, shown in figure 5.13. The first technique based on hydraulic theory was applied to the FP4 Minden, NE sounding. The calculated post-bore sounding profile is saturated from 900 mb up to 600 mb. Additionally, it appears a large area of saturated air is close to its LFC. Observations of convective initiation indicate that just to the south of Washington, KS the bore initiated convection behind the leading edge (figure 5.3 e, left-most red circle). Additionally, soundings at Topeka, KS also show a very deep layer of moisture. In fact, the sounding for Topeka, KS was also lifted in a similar manner, but using the second convective outflow from the trailing MCS. This second density current is not evaluated here in this work, but placed in the appendix in section 7.4 for reference.

The soundings from the second technique are also plotted in figure 5.13 b and c. First, it is clear that the displacement by the linear waves is inconsequential. There is very little change to the profile. Second, just as a note, FP5 Brewster, KS and Dodge City, KS soundings show a very stable and dry boundary layer, with the dryness extending throughout the profiles. Therefore, it may be very difficult to convect any

parcels given even a strong displacement.

Profiles of stability parameters

Three parameters of instability are plotted in figure 5.14 from the FP4 Minden, NE sounding at 5 UTC. These parameters include the profiles of CAPE, CIN and the distance a parcel must vertically travel to reach its LFC after being displaced. This last instability parameter is called LFC-LPL (LFC minus the lifted parcel level, or the height to which a parcel was displaced). There are three profiles provided in figure 5.14: the undisturbed environment, the disturbed environment based on theory, and the environment disturbed based on observed lift in the 915 MHz wind profiler at FP4 Minden, NE. In figure 5.14 a, the the CAPE increases by about 1000 J/kg in the lower 2000 m. Of most note is the CAPE increases from nearly 0 to 3500-4000 J/kg in the layer between 2000-3000 (3500 J/kg using the disturbed profile based on observations and 4000 J/kg based on the theoretical lift). At that same height, the CIN is nearly reduced to 0. In fact, the entire profile of CIN drops to nearly 0 everywhere. Parcels between 2000-3500 m are displaced to their LFC, indicating that convection should have ensued with the passage of the bore. Observations from the 915 MHz profiler indicate an elevated return of SNR from 2500 to 3500 (figure 5.8), possibly indicating the presence of convection. However, based on the SNR alone, it does not appear that the suspected convection penetrated deep into the troposphere. Comparisons with radar reflectivity while the bore crossed over the FP4 Minden, NE also indicate that convective cells were not penetrating deep into the troposphere. It is believed that this discrepancy may have to do with the overly simplified approach to lifting the parcel. For example, the lift above the bore is qualitatively consistent with predictions from the first method, but it does not account for the larger and subsequent descents occurring behind the head of the bore, observed in the vertical motions in figure 5.8. Therefore it is plausible that larger subsidence behind the bore head reduced displaced

parcel heights. Then, either the parcels did not reach their LFC according technique 1 or other processes, such as mixing, diminished the temperature or moisture of the parcels.

The same type of CAPE, CIN, and LFC-LPL profiles are also constructed for the 6 UTC FP5 Brewster, KS and 1200 UTC Dodge City, KS soundings. Both methods do not modify the instability parameters to a significant degree; qualitatively they are the same. This again is not unexpected based on the small magnitudes of lift predicted

Some things of note. These changes to the instability parameters are similar to the profiles observed by Coleman and Knupp (2011). The benefit of this work to Coleman and Knupp (2011) is the vertical profile of CAPE, CIN, and LFC-LPL are plotted, while Coleman and Knupp (2011) only diagnosed the surface parcels. Since the parcels near 2000-3500 m had a significant increase in their CAPE profile, gauging the instability parameters for parcels as a function of height gives insight to forecasters that surface-based analyses do not provide. It is important to gauge the impact of the density current in lifting, as Koch and Clark (1999) noted that bores may destabilize the air and subsequently convection along a trailing density current. Based on radar observations, it did not seem that this type of behavior was observed. Instead, it seemed that there were elevated single cells that developed along the waves of the bore and these cells would then be ingested into the larger MCS. It is unclear if this is akin to the process called discrete propagation described in Fovell et al. (2006), but it is mentioned for the point of future comparison.

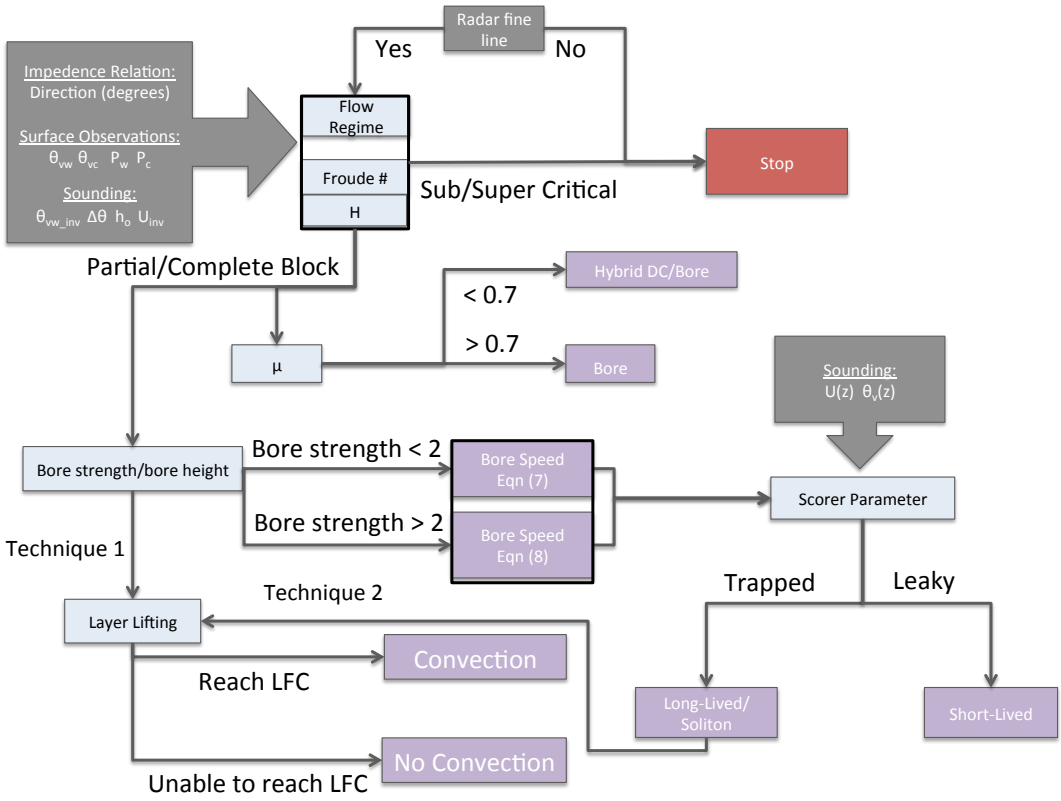

Figure 5.1: A flowchart depicting the methodology for determining if a bore will form and applying two different techniques to predict if convection will occur.

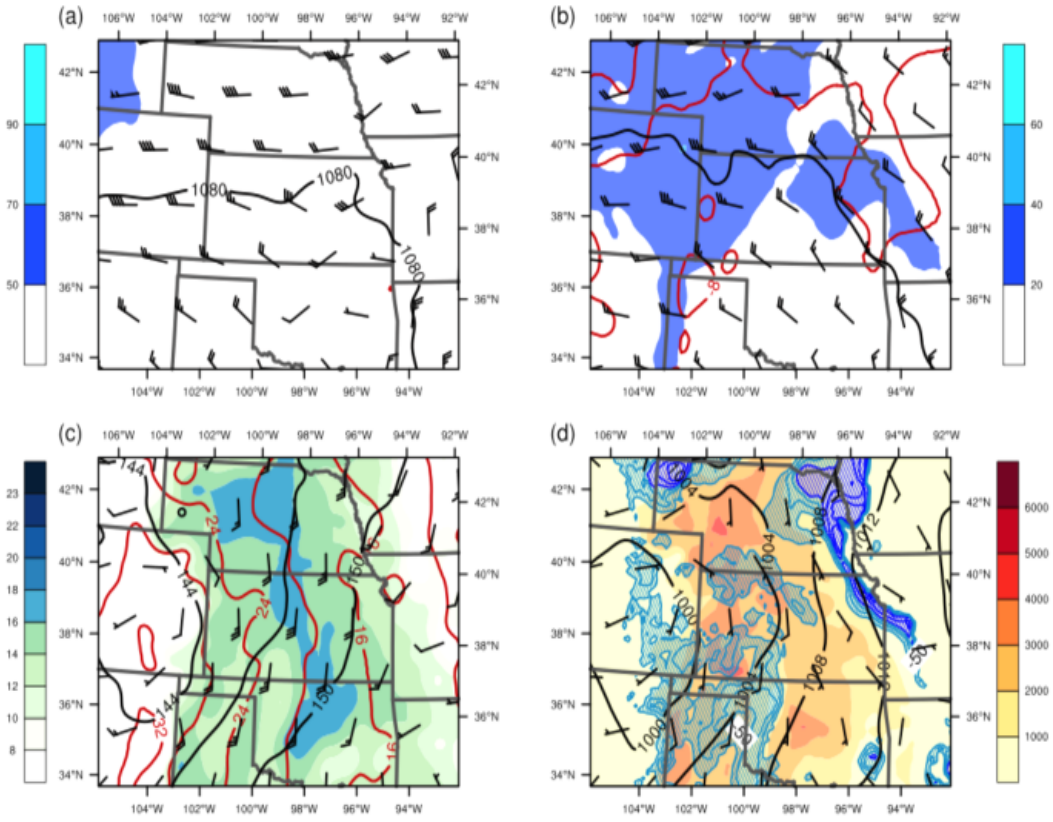

Figure 5.2: Synoptic maps of 3 June, 2015 MCS event centered over the PECAN domain: a) 250mb chart of wind vectors with wind magnitude contour-filled, both in knots, and isoheights contoured in decameters; b) 500mb chart of winds and isoheights same as 250mb along with temperature in degrees celsius contoured in red; c) 850mb chart of wind vectors in knots, temperature contoured in red, and mixing ratio in g/kg contour-filled; d) surface wind vectors, pressure contoured in millibars, surface-based CAPE in J/kg contour-filled, and surface-based CIN in J/kg hashed.

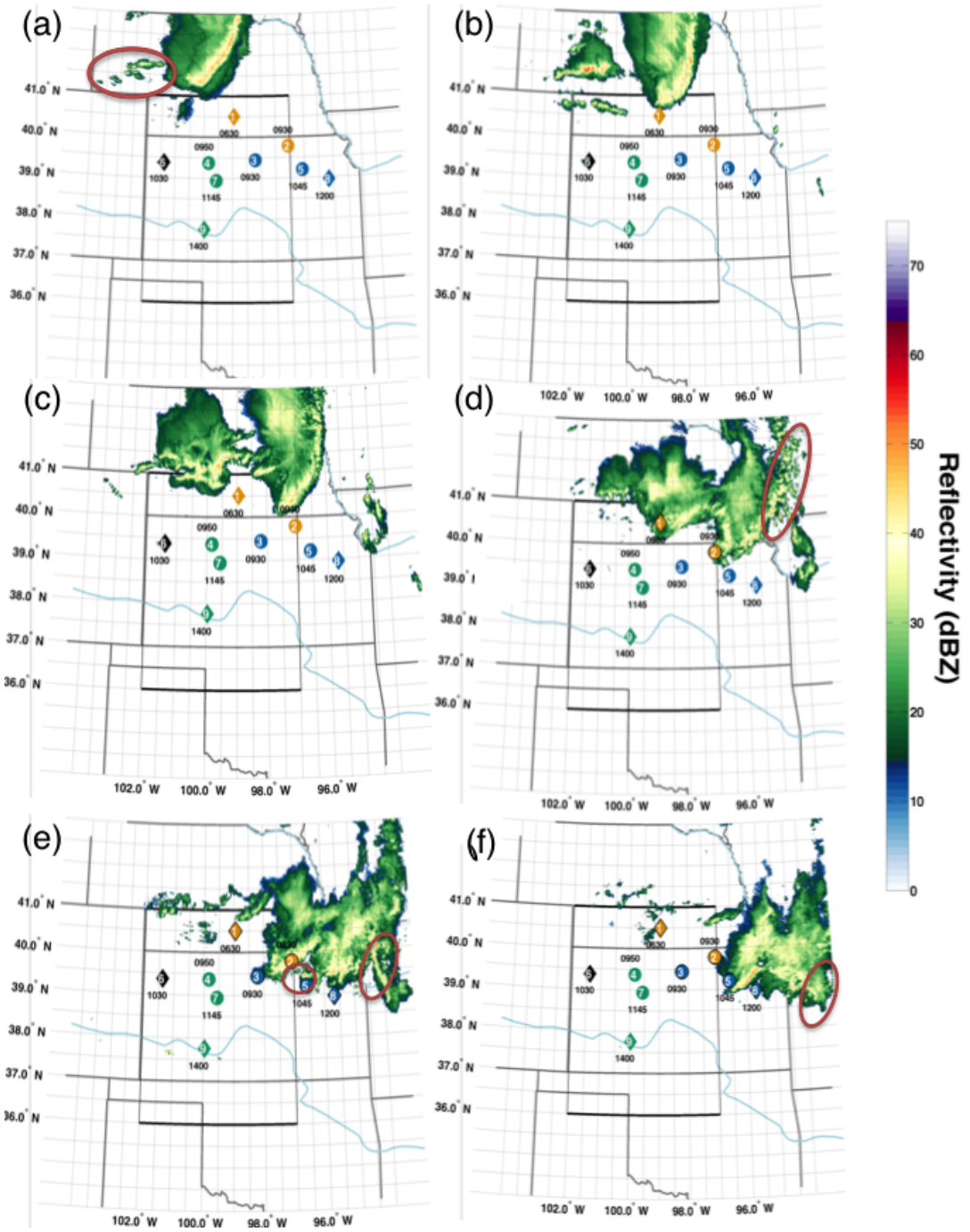

Figure 5.3: MRMS Radar reflectivity data for 3 June 2015. Red circles indicate convection initiation along convective outflow; a)-f) are at 500, 700, 900, 1100, 1300, 1500 UTC, respectively. The orange (blue) symbols are locations for the surface observations of the target (secondary) density current, the green symbols demonstrate the evolution of the target bore into a soliton, and the black symbol is where observations of the target bore without its density current. Diamond shapes indicate sites with vertical profilers.

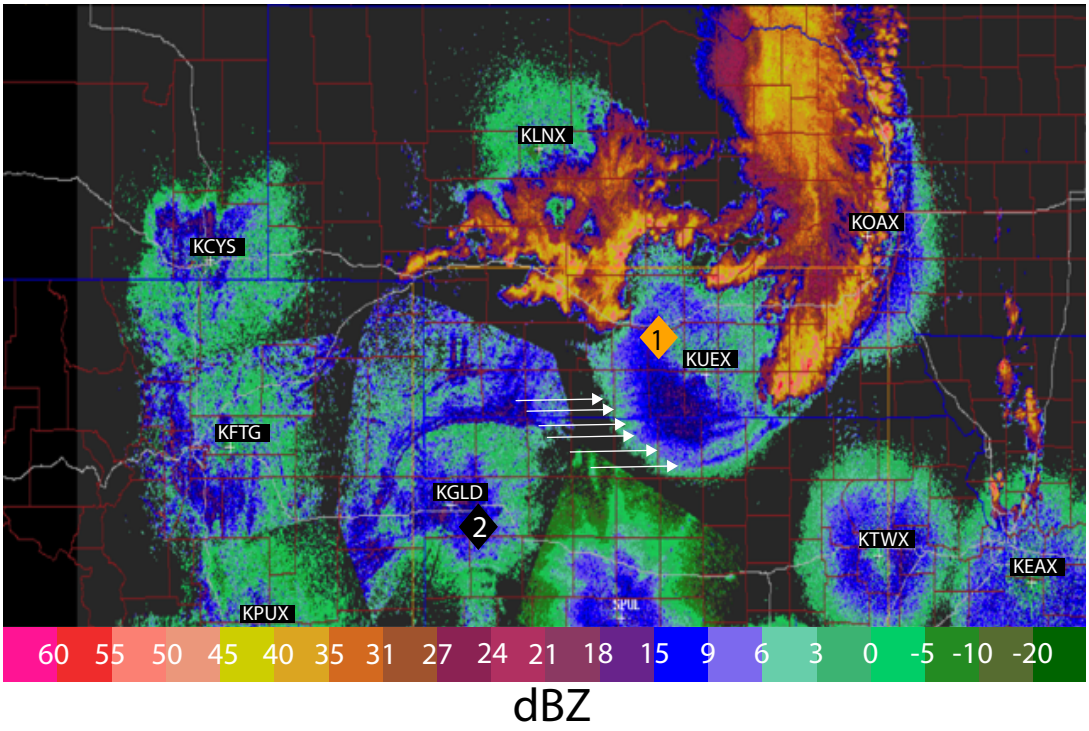

Figure 5.4: Radar mosaic of reflectivity extracted from the PECAN field catalog at 912 UTC. The train of parallel radar fine lines (identified with white arrows) are indicative of a gravity wave train are visible around the leading edge of the MCS. This is often indicative of a bore or a density current with a train of gravity waves along its extent.

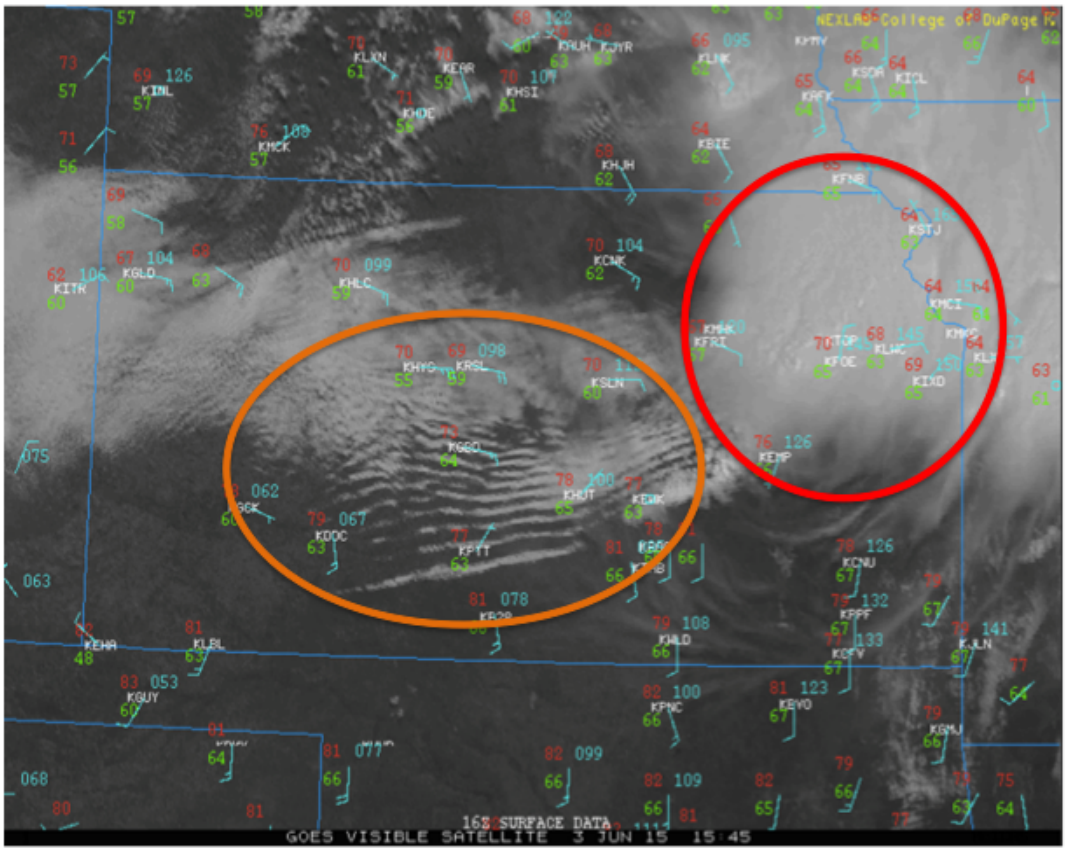

Figure 5.5: A visible satellite imagery on the morning of 3 June 2015 at 1545 UTC of the undular bore emanating from the first MCS moving southward through Kansas.

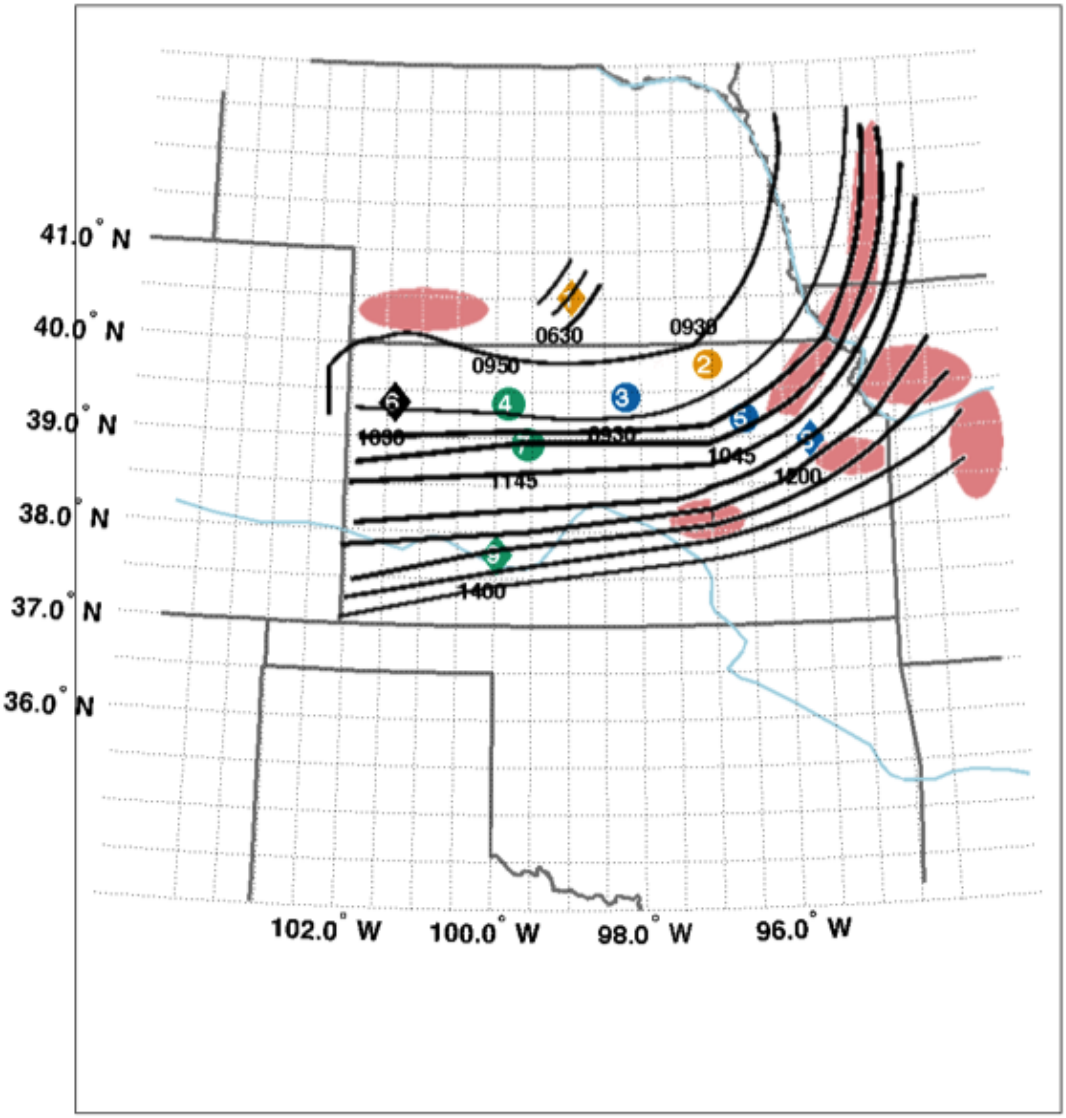

Figure 5.6: Isopleth's of the bore front as it moved southward through the the central plains and into the Missouri River Valley. Red filled circles indicate locations of convection along the bore front.

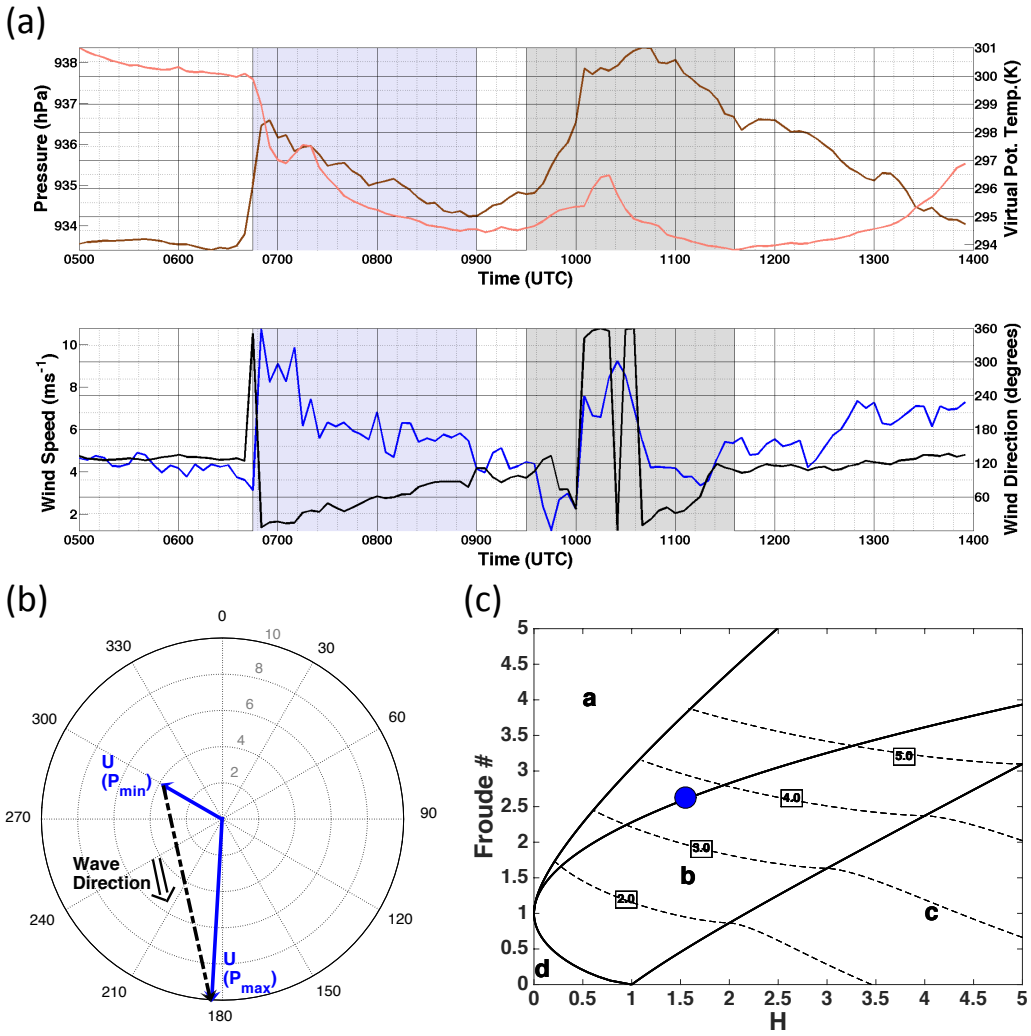

Figure 5.7: FP4 Minden, NE a) thermodynamic surface observations from FP4 in Minden, NE: Reddish line is virtual potential temperature, brown line is pressure, dynamic surface observations from FP4: blue line is wind speed, black line is wind direction, Grey shaded area indicates the time a bore passed the surface mesonet and blue shaded area indicates the time a density current passed the surface mesonet; b) wind rose illustrating the procedure to determine the wave direction using the impedance relationship; c) flow-regime diagram.

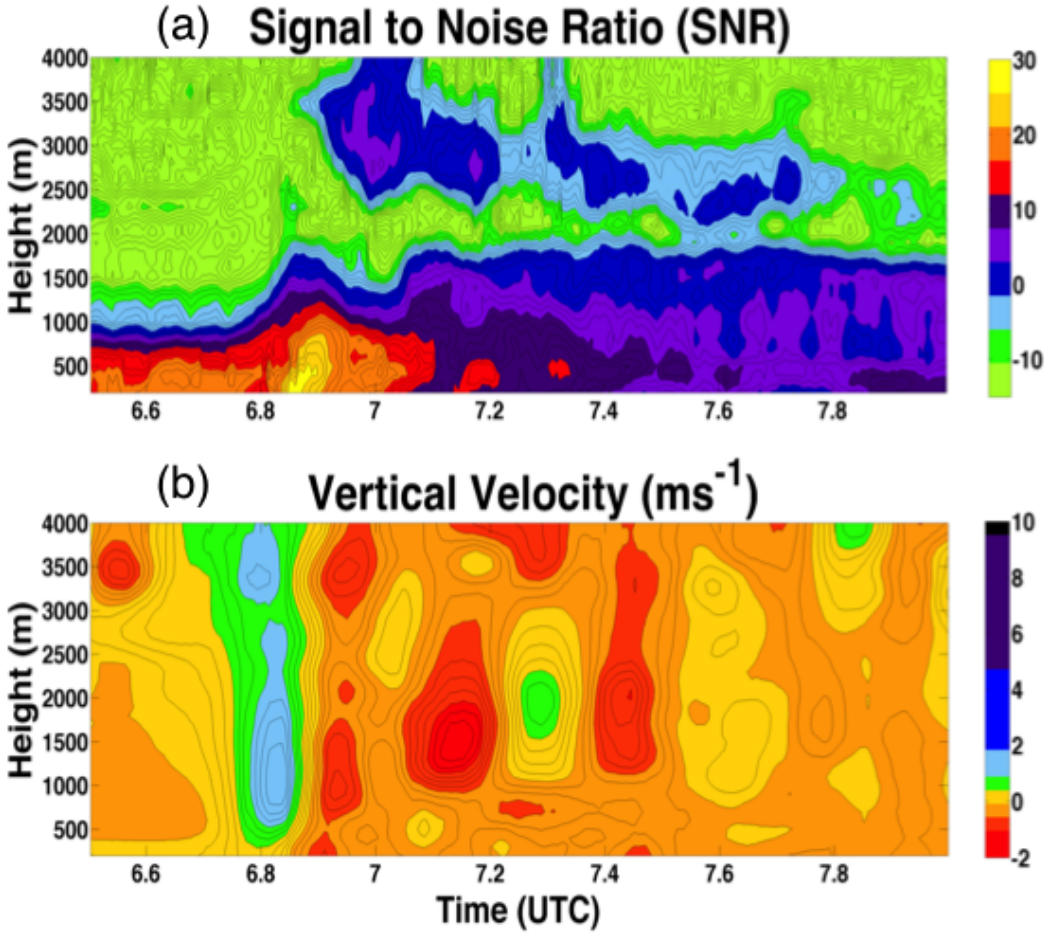

Figure 5.8: FP4 Minden, NE 915 MHz wind profiler as a function of height and time: a) SNR contour-filled in dB; b) vertical velocity, smoothed over a moving 5 min average in time.

	$Washington, KS$	$Minden, NE$		
	DC 1	DC 1		
density current				
$\theta_{vw}(K)$	296.0	294.2		
$\theta_{vc}(K)$	293.0	289.5		
$P_w(hPa)$	961.0	933.5		
$P_c(hPa)$	964.0	935.0		
$\rho_w(kgm^{-3})$	1.131	1.107		
$d_o(m)$	2040	790		
Obs. $C_{dc}(ms^{-1})$	–	15		
Thy. $C_{dc}(ms^{-1})$	15.6	11.2		
Obs. $C_b(1)(ms^{-1})$	14	–		
Obs. boreheight(m)	–	1200		
FP4 sounding :	$h_o = 500m$	$\Delta\theta(K) = 10$	$\theta_{vw\ inv}(K) = 311$	$U_c(ms^{-1}) = 16.6$
H	4.0	1.6		
Fr	2.6	2.3		
μ	0.52	0.72		
Thy. $C_b(ms^{-1})$	14	9.7		
borestrength	4.4	3.4		
boreheight(m)	2200	1700		
Topeka sounding :	$h_o = 640m$	$\Delta\theta(K) = 7$	$\theta_{vw\ inv}(K) = 308$	$U_c(ms^{-1}) = 24.8$
H	3.2	1.4		
Fr	3.3	3.0		
μ	0.49	0.64		
Thy. $C_b(ms^{-1})$	-7.6	-4.5		
borestrength	4.9	4.3		
boreheight(m)	3100	2500		
Dodge City sounding :	$h_o = 850m$	$\Delta\theta(K) = 14$	$\theta_{vw\ inv}(K) = 309$	$U_c(ms^{-1}) = 25.6$
H	2.4	1.1		
Fr	2.1	1.9		
μ	0.80	1.0		
Thy. $C_b(ms^{-1})$	-17	-13		
borestrength	3.45	2.8		
boreheight(m)	2900	2300		

Table 5.1: Table of surface observations and calculated hydraulic parameters from FP4 Minden, NE and the Kansas mesonet station in Washington, KS. Like-colors in the same column offer comparisons between observations and theory. Calculations of the hydraulic theory parameters and μ are presented in section 3.

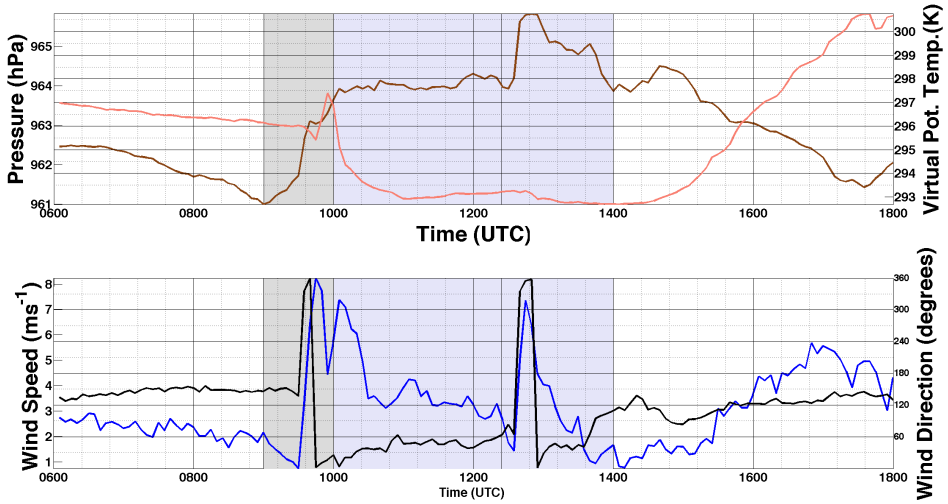

Figure 5.9: Washington, KS: a)thermodynamic surface observations. Reddish line is virtual potential temperature, brown line is pressure, dynamic surface observations: blue line is wind speed, black line is wind direction, Grey shaded area indicates the time a bore passed the surface mesonet and blue shaded area indicates the time the density current passed the surface mesonet. Solid line within blue shaded area separates the surface traces of the target density current and the secondary density current.

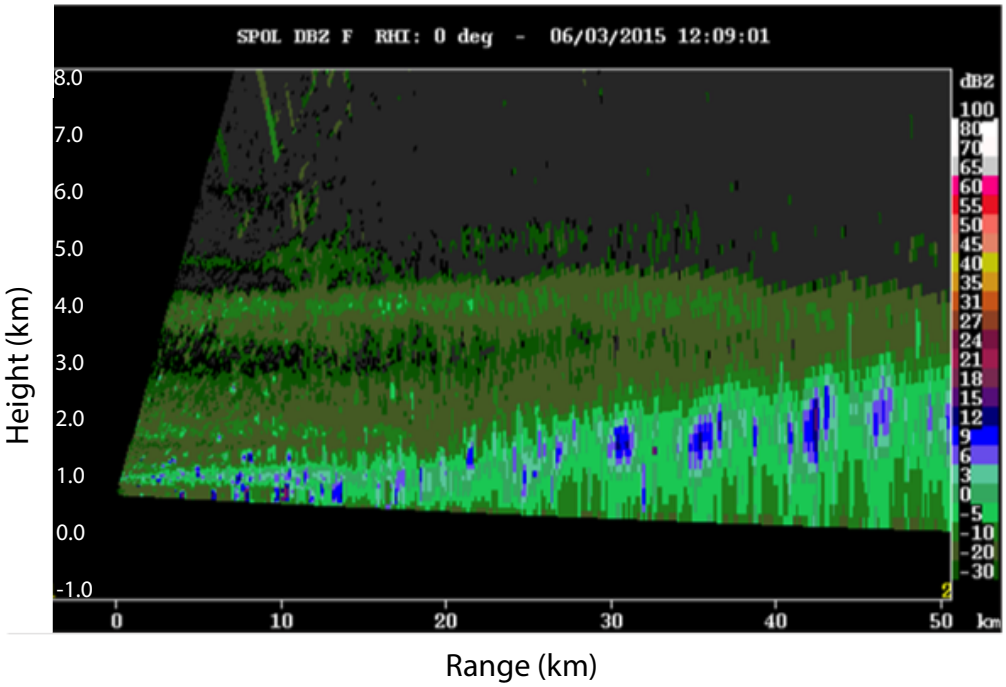

Figure 5.10: S-Pol RHI Scan of reflectivity factor through bore on 3 June 2015 at 1209 UTC. The RHI is looking due North.

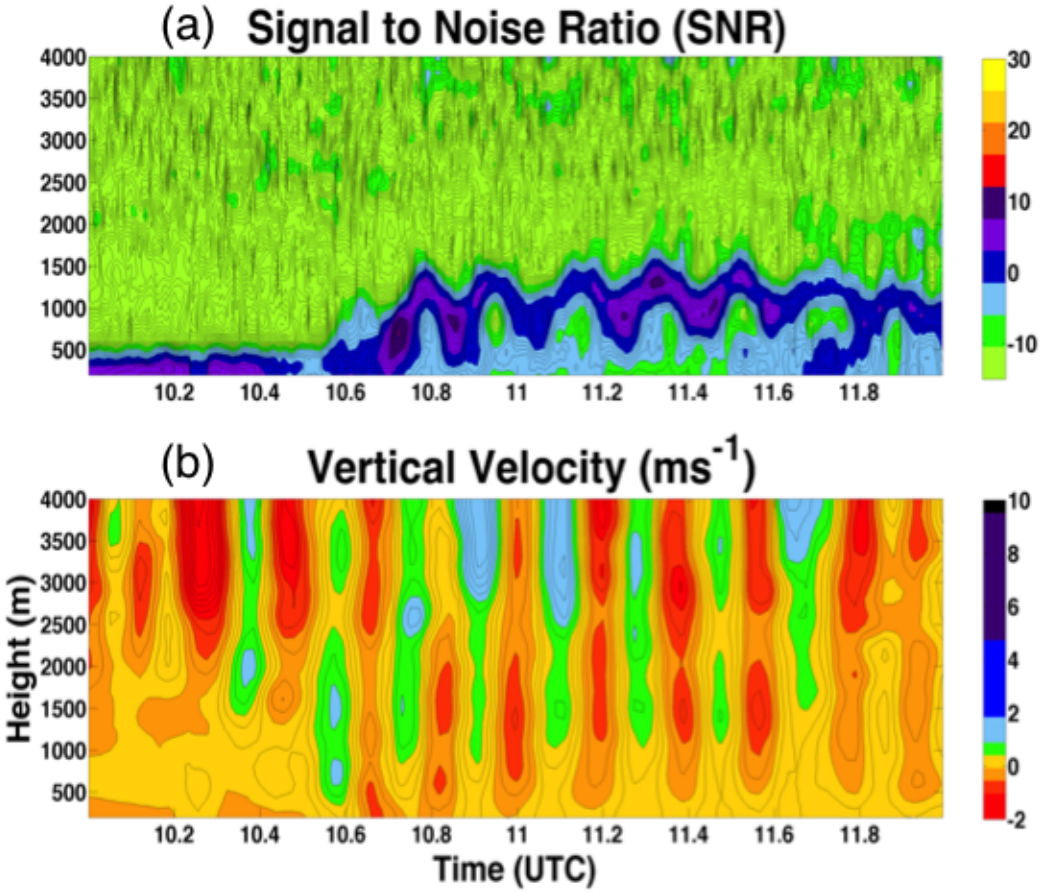

Figure 5.11: Same as figure 9, but at FP5 Brewster, KS.

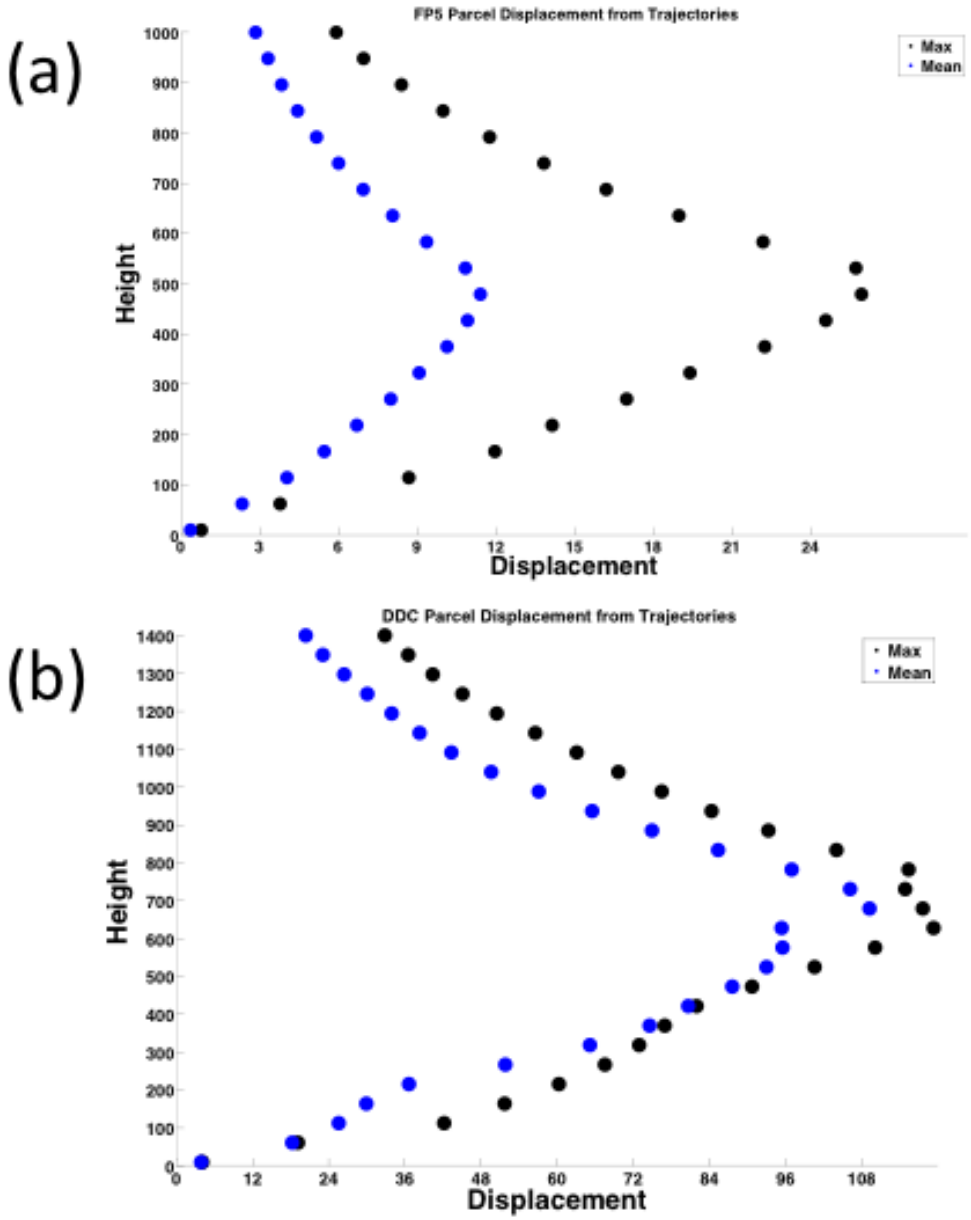

Figure 5.12: Measured displacements for parcels using technique 2. Displacements are made using FP5 Brewster, KS and Dodge City, KS soundings.

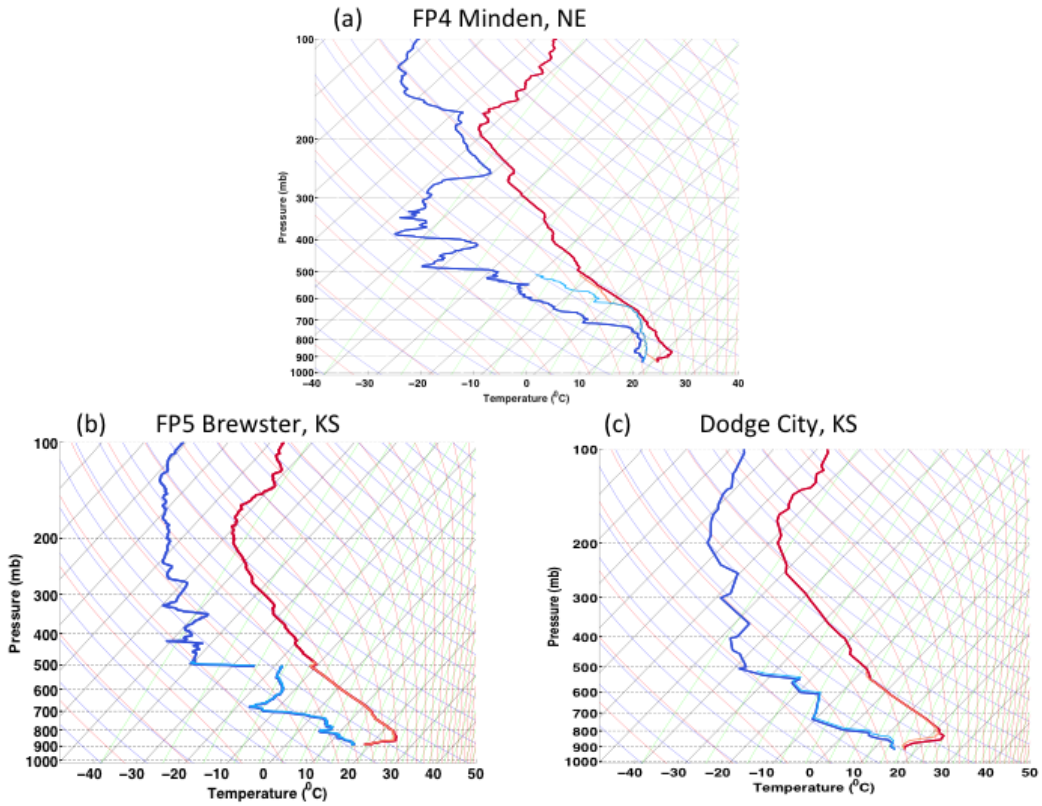

Figure 5.13: Modified soundings using the two layer-lifting techniques: a) FP4 Minden, NE 5 UTC using first technique; b) FP5 Brewster, KS 600 UTC using second technique; c) Dodge City, KS 1200 UTC using second technique. The lighter red and blue lines indicate the temperature and dewpoint profile after the parcels have been displaced.

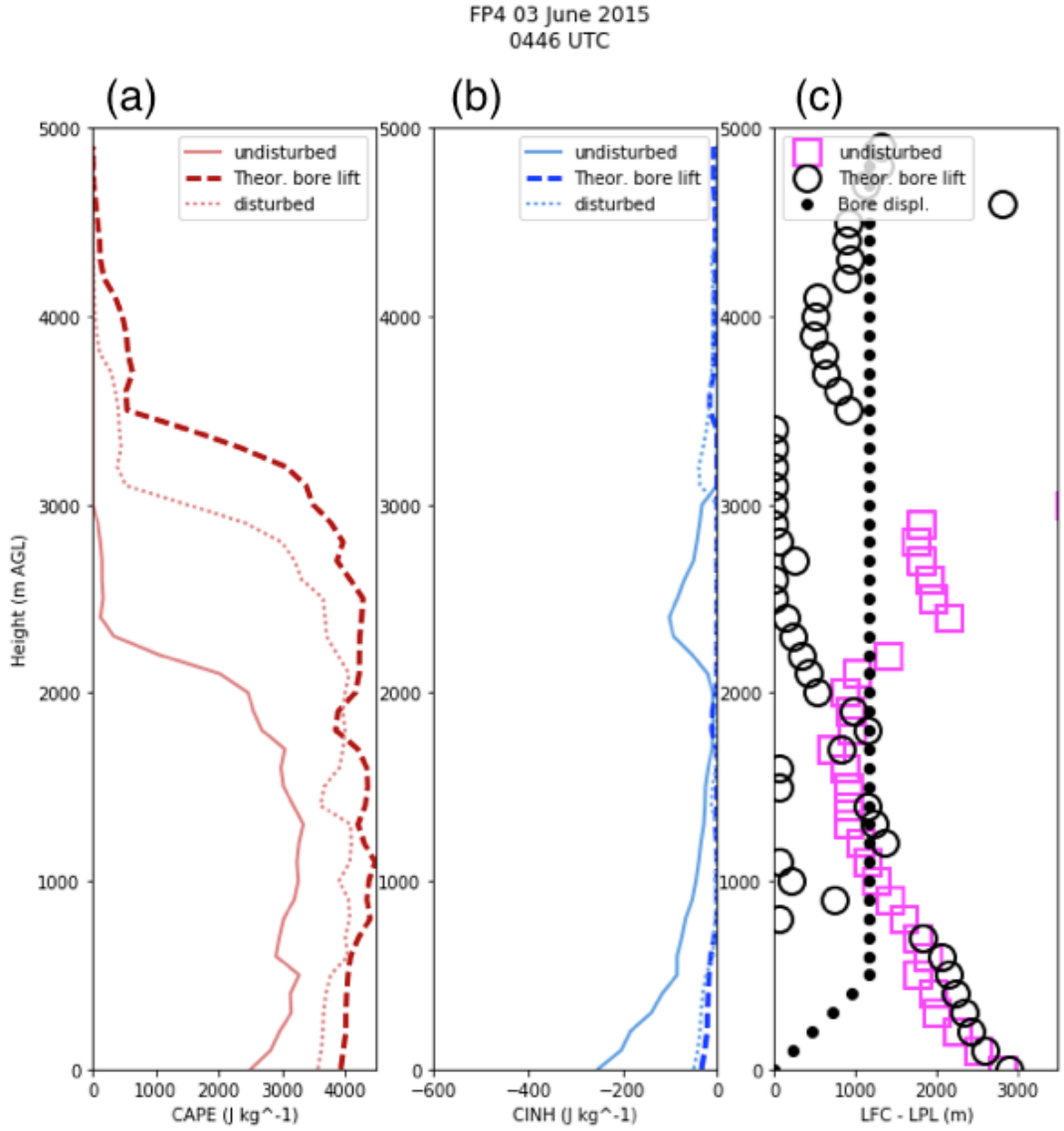

Figure 5.14: Profiles for CAPE, CIN, and LFC-LPL at FP4 Minden, NE using the expected displacement with theory and applying the first technique of parcel displacement. Undisturbed soundings (solid) are the pre-bore soundings, theoretical bore lift (dashed) are the soundings after technique 1 has been applied according to the calculate lift from theory, and disturbed (dotted line) is the lift observed in the 915 MHz wind profiler at Minden, NE. Bore displacement (black solid dot) is the bore displacement function based off of technique 1.

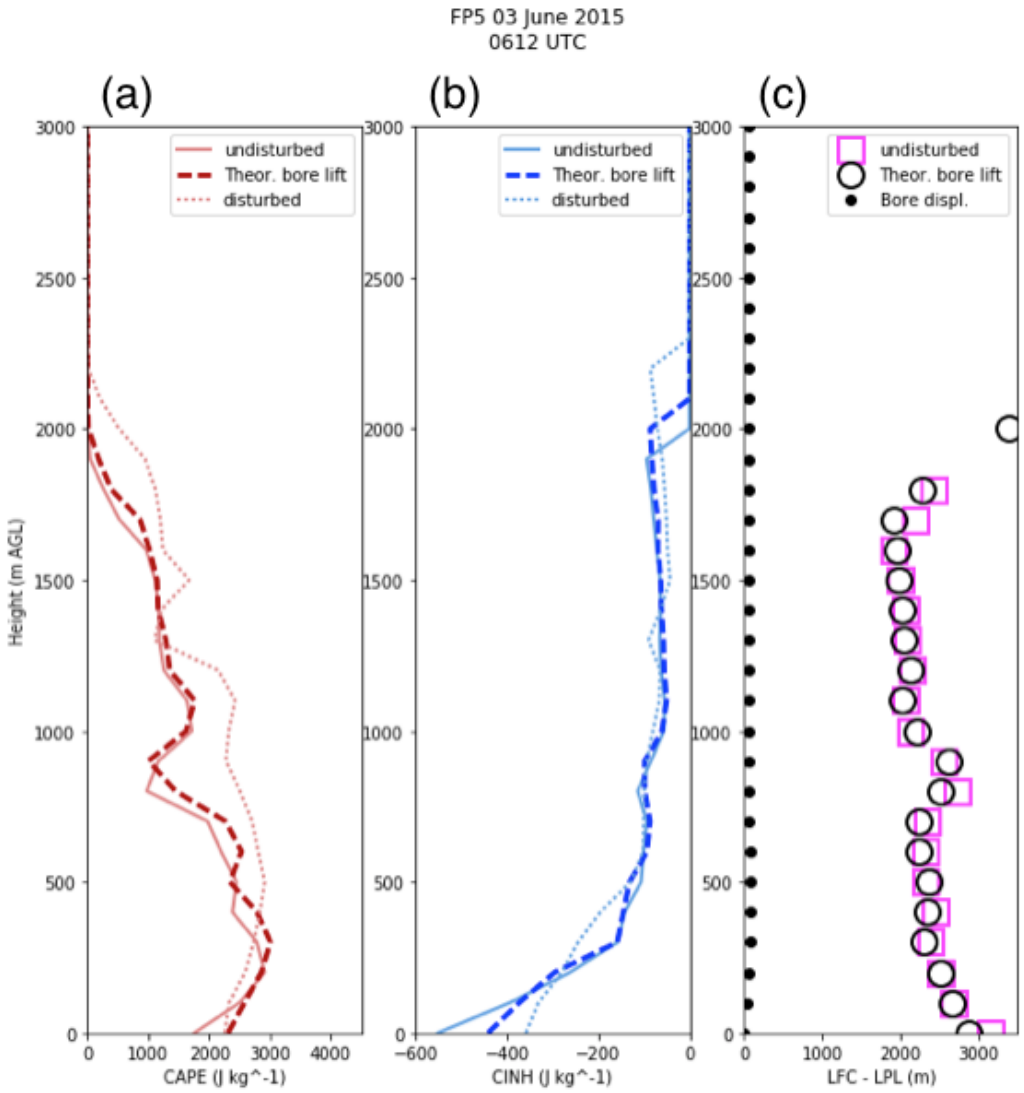

Figure 5.15: Same as 5.14, but at FP5 Brewster, KS, using technique 2, and with disturbed soundings calculated from the 915 MHz profiler at Brewster, KS.

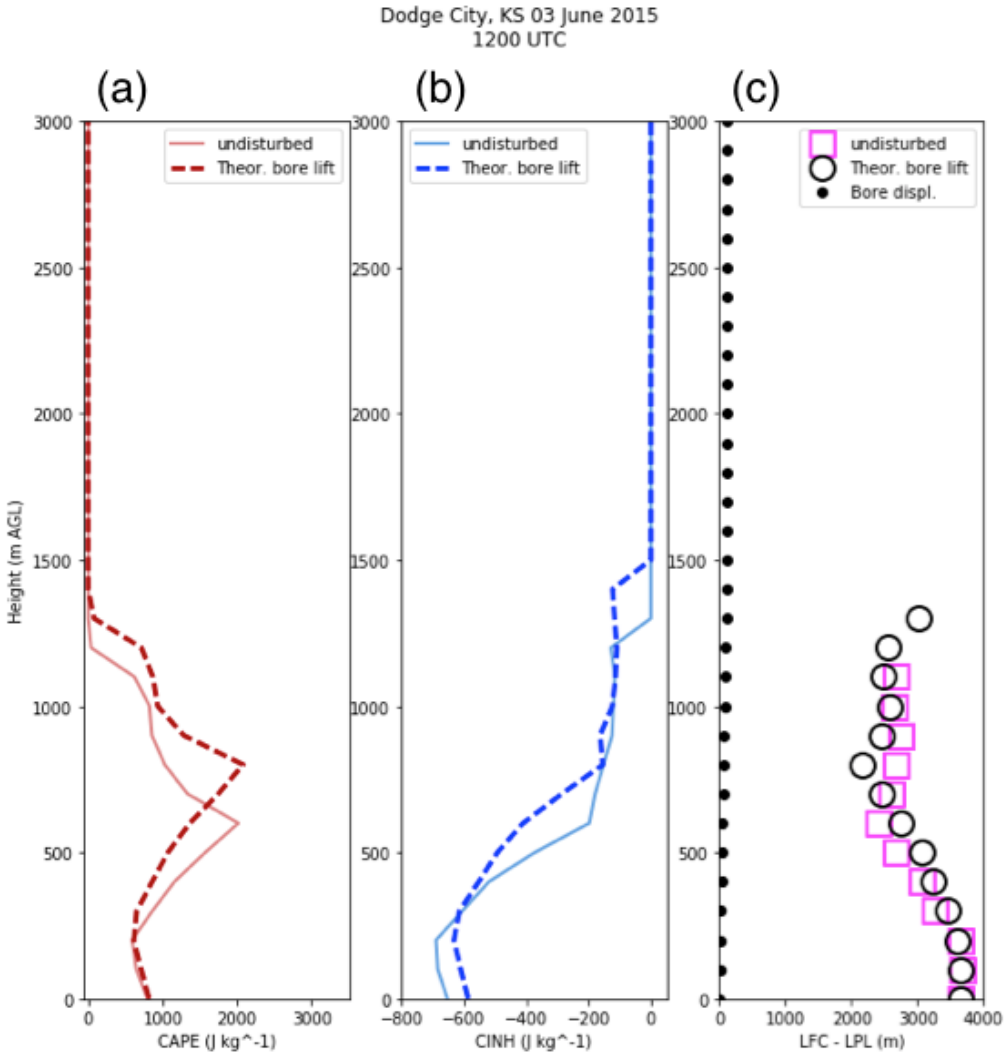

Figure 5.16: Same as 5.15, but at Dodge City, KS and there is no disturbed profile available.

Chapter 6

Conclusions

6.0.1 Systematic study

Radar and surface measurements taken during IHOP_2002 were utilized in tandem to show that convective outflows intrude into the Southern Great Plains stable nocturnal boundary layer and frequently generate atmospheric bores ($\sim$43% of all observed radar fine lines attributed to a bore). This finding is supported by the presented application of hydraulic theory and suggests the dominant flow regime is a partially blocked flow. Observations indicate a likely time to observe bores occurs during 2200-200 LST (400-800 UTC), coincident with the strongest signal for a partially blocked flow. The height and strength of the inversion are the most influential factors for developing an atmospheric bore and the curvature of the NLLJ is found to be a critical determinant for maintaining long-lived bores. As the night progresses, the direction of atmospheric bores generally align with the direction of the shear vector defined by the height of maximum wind in NLLJ to 1.5km and height of maximum wind in NLLJ to 2.5km. As in Koch et al. (1991), the transition of the Scorer parameter from positive to negative values occurs above the wind maximum of the NLLJ, near or at the inflection point in the wind profile associated with the curvature. The preferential direction of bore movement indicates that the effectiveness of the waveguide varies with orientation due to variations in the curvature term. The 13 cases analyzed support this theory. Based on this analysis, an argument can be made for

bores having a preferential direction containing the most maintainable wave modes.

The systematic study also raises questions regarding the dynamics of atmospheric bores. Past studies (Baines 1995; Lindzen and Tung 1976a) suggest that most wave ducts are "leaky" and most, but not all, wave energy is trapped within the wave duct. Because a convective outflow is often a 3D response, the variation around a density current may impact how the environment traps gravity waves generated in a bore. The question is of great importance to understanding what portion of a bore, if any, will maintain itself as it travels away from its parent density current. Also, leaky wave energy may have play a secondary role in convective maintenance. Leaking wave energy will displace parcels above a bore and destabilize these parcels. If this is occurring near an ongoing convective updraft, constructive interference between the ongoing updraft and the leaking wave energy could provide more unstable parcels for convection.

6.0.2 Method for predicting bore displacements

On June 3rd, radar and satellite imagery demonstrated a disparity in convective initiation: near the MCS, convective cells bubbled along the eastern extent of the visible waves associated with bore, while along the same bore to the west there was no convection. A methodology is developed for forecasters utilizing only surface data and soundings to gauge the displacement of parcels by a bore. This work utilizes hydraulic and linear wave theory as the foundation for prediction, the first application of theory for prognostic purposes. Therefore, the focus on surface data and soundings is intended to utilize observations that are available to forecasters, whether they be real time or extracted from forecast models. While the use of vertical profilers would significantly enhance a forecaster's ability to diagnose bore-initiated convection, they are scarce in situ. Therefore, this work contains the most applicable method for forecasting bore and subsequent convective initiation.

Using hydraulic theory, the estimation of the density current height, the bore strength and the bore height are all overestimated. First, this may be due to estimations of the density current height based on the assumption that the potential temperature through the depth of the density current is constant, while in reality there is variation. Second, stratification within the inversion layer and above has a dampening effect on the height of the density current (Liu and Moncrieff 2000). Third, hydraulic theory also does not capture the shear present within the inversion layer. This is a weakness of hydraulic theory. However, the μ parameter correctly identifies whether the bore would outrun the density current or become a hybrid bore/density current according to the surface data at two weather stations.

When a bore pulls away from its density current and evolves into a train of gravity or solitary waves, it is proposed that they are diagnosable using linear wave theory. Based on this hypothesis, linear wave solutions of the TGE are constructed assuming that the atmosphere behaves like a two-layer system of a positive Scorer parameter layer adjacent to the surface topped by an infinitely deep negative Scorer parameter layer. The simple model does quite well at constraining the expected horizontal and vertical wavelength and the height of the vertical motion. These results are echoed by the 13 cases of the systematic study and other work (Zimmerman and Rees 2004; Blake et al. 2017). However, the two-layer model is not sophisticated enough to capture the multiple oscillations in the Scorer parameter diagnosed from a sounding, and these variations are hypothesized to contribute to the multiple observed maxima in the vertical motion sampled by the 915 MHz wind profiler at FP5 Brewster, KS. Future research exploring the complexity of a real environment to explain the untrapped wave modes would significantly improve the usefulness of this tool.

Two techniques are proposed in a heuristic approach to gauge how well the methods predict bore-lift. The first technique, based on hydraulic theory, appears to overpredict the lift. This overprediction is expected, as our theoretical bore height was

too large compared with the 915 MHz wind profiler observations taken at FP4 Minden, NE. The second technique based on linear wave theory severely underpredicts the vertical motion and parcel displacement inside of a trapped gravity wave. The underprediction is not a shock as observations from the 915 MHz wind profiler at FP5 Brewster, KS illustrate that these waves could have been highly nonlinear (Koch et al. 2008b,a; Coleman and Knupp 2011). While the second method also did not predict that convection would occur, it was evident that the stability over both Dodge City and FP5 was too large to initiate deep convection. So the techniques identified the correct answer. However, there is reason to be skeptical that these two techniques would perform as well in an environment with more subtle differences between a bore that will or will not initiate convection.

Nevertheless, this work demonstrates that under favorable conditions, a bore is capable of lifting parcels to their LFC, according to hydraulic theory. Profiles of CAPE, CIN, and the LFC-LPL demonstrate that parcels should have reached their LFC between 2000 m to 3500 m. Observations from the 915 MHz wind profiler at FP4 Minden, NE corroborate these findings. Yet, it does not appear that the convection grows upscale. Based on the very favorable profiles of CAPE and CIN, this result seem to suggest that initiation of convection by a bore are aided by other mechanism(s). These findings seem to at least partially explain why Wilson and Roberts (2006) found that out of all of the observed bores (21), most remained benign (only 3 initiated convection that grew upscale). More often, bores seem to play a role in convective initiation through the collision with other boundaries (Purdom 1976; Wilson and Schreiber 1986; Carbone et al. 1990; Koch et al. 1991; Wakimoto and Kingsmill 1995; Kingsmill and Andrew Crook 2003). This result may be due to the constructive interference of vertical circulations between the two boundaries. These findings would benefit from research that quantifies how much unstable air must be displaced in order for convective cells to organize and grow upscale. This is a weakness of this

study. In fact, even with a perfect prediction of bore lift, it is not clear that this tool is sufficient to provide the forecaster reliable information for dissemination. Luckily, an abundance of data to clarify these questions about bore-initiated convection is available from the PECAN field project.

6.0.3 General insight

The work presented in this dissertation is a collection of research aimed at understanding how to contextualize the role of atmospheric bores within the life cycle of a convective system and their implication on initiating and maintaining convection. Furthermore, this research has illuminated why understanding the role of bores in nocturnal convection is congruent with reproducing and predicting nocturnal rainfall over the Great Plains. This work is no way provides all the answers. However, based on this work, there are some implications to be made.

1. **How often does a density current generate a bore over the Southern Great Plains?** The nocturnal environment over the Great Plains is inherently predisposed to generate bores. At first it was astonishing that a large number of bores, generated by convective outflows, were observed during the IHOP_2002 field campaign. However, these results are consistent with hydraulic theory, which also indicates that the interaction between the density current and the nocturnal stable boundary layer should fall in the partially blocked flow-favorable for bore development.

2. **How long are these bores maintained by the nocturnal environment?** The systematic study found that these bores have a longer lifetime than density currents by two hours on average (bore are observed in radar for 4.5 hours on average). Their longevity is most likely linked to the favorable wave ducts produced by the curvature of the NLLJ. Although the data analyzed is from a single field

campaign, the proposed mechanisms for generation and maintenance of bores are governed by the general dynamics and thermodynamics of the summertime Great Plains nocturnal environment: a stable surface boundary layer, the presence of a southerly NLLJ, and the ongoing production of density currents from mesoscale convective systems.

Yet, the results during IHOP_2002 do not seem to be an anomaly. PECAN radar mosaics captured over 170 radar fine lines during the PECAN campaign. From first-hand experience of analyzing radar fine lines, bores appeared just as prevalent in PECAN as in IHOP_2002. Based on the work herein, there is a good deal of reason to redo a systematic study on bores observed during PECAN. First of all, a strength of PECAN was the pre- and post-bore soundings launched by mobile and fixed PISAs. The benefit of this strategy is evident in the work just presented. For a bore event with pre- and post-bore soundings, comparing these bore-lifting techniques to observed displacements could prove invaluable. Second, the bores were sampled across their fronts. One fallout from IHOP_2002 and from first-hand experience in PECAN, the atmosphere produces a range of bore responses. Not only is the production of a bore quite different form one to another, but their lifetimes seem to be not predetermined. Some bore fail to become trapped waves and dissipate, some bores evolve into a single solitary wave or a train of solitary waves. Some bores last a couple hours while some travel state lengths over the course of a night. It is quite possible that the explanations for these varying bore responses in similar environments are due to the morphology of density currents and how these bores interact with the environmental winds. PECAN offers the most unique dataset to date for answering some of these questions while building upon the observations of IHOP_2002.

3. **Can theory by applied to a density current as a prognostic tool for bore generation?** The results in this work and from other works (Koch et al. 2008a,b; Coleman and Knupp 2011) suggest that hydraulic theory is very appropriate for determining generation of a bore. Moreover, it appears that the empirical μ parameter also provides useful information for when a bore should pull away. Although not discussed in the section 5, the μ parameter also compared well between observations and other analyzed surface stations. This work is found in table 7.4 and 7.2.

4. **Does the theory predict how much the air is vertically displaced?** The first attempt appears to give mixed, but promising results. While hydraulic theory does appear to perform better than linear gravity wave theory in capturing the displacements observed, hydraulic theory is unable to diagnose the speed and height of solitary waves. Also, the first technique based on hydraulic theory is constructed specifically to match results from FP4 Minden, NE and it is unclear how well it would continue to perform under different environmental conditions. For example, if the atmosphere above the surface inversion was strongly stratified or if there were multiple layers of varying stratification, the lifting profile could appear significantly different. If the method was improved to incorporate this herein discussed complexity, then its applicability would be wider. The second technique based on linear wave theory is simply not robust enough to capture the nonlinear interactions of solitary waves.

5. **Can the theory help distinguish between environments that are and are not conducive for a bore to generate convection?** While the methods did seem to diagnose the environment correctly, it appeared that the environment was dry to the west and moist to the east. Would these techniques be able to distinguish between two environments with very subtle differences? As implied before, it

is hypothesized that the percent of correct forecasts would diminish.

6.0.4 Future Work

Comparing findings of IHOP_2002 with PECAN

The finding that bores are ubiquitous in the summer of 2002 over the Southern Great Plains is believed to not be happenstance. As mentioned before, first-hand experience in the PECAN field and with the data suggests that this PECAN also produced atmospheric bores with a high frequency. Yet, observations of bores during PECAN and IHOP_2002 are remarkably different in a couple of ways. For example, vertical motions from a bore observed during PECAN are as high as 9 ms^{-1}, while vertical motions observed in IHOP_2002 never exceeded 4 or 5 $ms^{-}1$. Also, from what can be recalled, it was the first time a large rarefaction wave was observed with vertical profilers. And the variation in bore responses during PECAN seemed to be much larger than during IHOP_2002. This difference may be because mobile profiles were able to target bores, where this mobility was absent during IHOP_2002. Was there a fundamental difference between the PECAN and IHOP_2002 environment? A detailed systematic study of bores observed during PECAN would be a step towards answering these questions.

Bores role in nocturnal convection

From a dynamics standpoint, a convective outflow will experience unfavorable changes to the pressure gradient force driving its propagation unless a bore displaces fluid upward and away from the leading edge of the outflow. A consequence of this semi-permanent lift is induced upward motions. Moreover, this work illustrates that the vertical motions extend well above the shallow nocturnal boundary layer and through the lower troposphere. This lifting will act to erode any convective inhibition

within the storm inflow and may release convective instability initiating or maintaining deep convection (Coleman and Knupp 2011). Whether bores enhance the precipitation and contribute to the nocturnal maximum in rainfall over this region is a subject for future research. Idealized simulations of convection in stable environments (e.g., Parker 2008; Schumacher 2009; French and Parker 2010) and simulations of specific events (e.g., Blake et al. 2017) suggest that bores can play a role in maintaining deep convection. Moreover, this work has provided a solid foundation for pursuing the role of bores in nocturnal convection. The PECAN project (Geerts et al. 2016) will certainly prove valuable in exploring this topic.

Part of understanding the role of bores in nocturnal convection is addressed within this work. This first-time heuristic approach did provide promise that hydraulic theory provides guidance to forecast the destabilization by a bore. However, the technique based on linear wave theory suggests that the gravity waves are nonlinear. At this stage, more case studies must be performed and more sophisticated approaches must be developed.

Developing a framework for convective initiation and maintenance by a bore is important for organized convective system's structure, movement, and changes in intensity. As in Parker (2008); French and Parker (2010), the shear balance described in Rotunno et al. (1988) between the density current and the environmental shear changes so that the balance is now between the bore and the environment. Moreover, if a bore is driving convection, as seen in Parker (2008), the speed of the storm adjusts to the speed of the bore. Similarly, in French and Parker (2010), the shear above the jet favorably contributed to this RKW balance in layer with high theta-e air. Based on our study, bores trapped within a surface layer are positively correlated to the curvature above the nose of the jet. Therefore, it seems reasonable to investigate that a bore may often displace unstable parcels that eventually are ingested by an organized system. In the context of eastward-drifting clusters of convection from the

Rockies that organize and develop a convective outflow, the changes to propagation direction and speed, as seen in 1.2, may be better explained. Finally, bores may create new elevated convective cells, as seen in the case study from section 5 and become ingested into the main complex. This phenomenon appears to happen often in very destabilized environments and must change the intensity and longevity of the system. Understanding these feedbacks is necessary for creating a unified framework for nocturnal convective systems.

Improving the application of theory

Another future research goal is bridging the gap between bore theory and the expected response in the environment. For example, two-layer hydraulic theory, as in Rottman and Simpson (1989), correctly identifies whether a bore response will develop, but assumes a neutral second layer. In some instances, the theory characterizes the resulting bore response qualitatively well (Koch et al. 2008b,a) while numerical simulations that account for the environmental cold pool interaction have demonstrated a larger variation in bore responses, especially ones that evolve into solitons (Klemp et al. 1997; Helfrich and White 2010; White and Helfrich 2012).

One place for improvement would be applying nonlinear solutions for solitary waves to the atmosphere and reproduce the displacements. Numerous studies has been done using nonlinear theory according to Benjamin-Davies-Ono and Kortweig-De Vries solutions for nonlinear flow (Christie 1989; Zimmerman and Rees 2004; Helfrich and White 2010; White and Helfrich 2012). For example, Zimmerman and Rees (2004) produced solutions of solitary based on profiles of stability, shear and the Richardson # alone. Could this approach be applied to the atmosphere? If it could, more accurate depictions of the amplitude would give better information about the parcel displacements.

Still unaddressed by linear wave theory is the leakage of wave energy out of the

surface wave duct and into the environment aloft. It is unclear how this leaking wave energy interacts with other layers of varying Scorer parameter since real environments are incredibly complex and physically difficult to interpret, but a multi-layer model would be beneficial for addressing this issue. Some simple approaches to understanding how and when wave energy will leak out of a duct has been addressed by Durran et al. (2015) for waves trapped by the tropopause. It is possible that their solutions can be applied to a surface duct in a similar manner.

A crucial unaddressed issue by theory is the evolution of a bore from inception to its assumed steady state and the evolution of a bore front into a packet of waves. While a bore develops, the interaction between the density current and the environmental inversion is likely to be extremely important. This is highlighted by White and Helfrich (2012) that uses numerical simulations to produce a density current intruding a stable layer and, by varying parameters used in hydraulic theory, simulate the evolution of rarefaction waves, solitary waves, undular bores and density currents that generated no bore. Unfortunately there are no observational studies that illustrate these kinds of evolutions. PECAN does offer some promise, but the evolution may happen too quick to be captured with vertical profilers spaced 10s to 100s of kilometers away from one another. Similarly, there is only one observational study on the evolution of a density current into a solitary wave (Knupp 2006). Once again, PECAN is the best dataset to date for studying this phenomenon. A good future study for solving this problem would be using data assimilation on a case study from PECAN and following the evolution in the solutions.

6.0.5 Broader goals

The work herein and the future work discussed is one facet of a much larger set of scientific goals:

(i) Fostering interdisciplinary collaboration This presented work has attempted

to bridge the gap between theory and observations. Currently ongoing within the OUMAP (OU Multi-scale data Assimilation and Predictability Laboratory) group are data assimilation studies using PECAN data to simulate observed bores and compare the results with theoretical models. Their work is in part based on the research presented within. These cross-disciplinary studies have fostered collaborations and improved to the quality of research. This kind of cooperation is a principal component of present day ingenuity.

(ii) Improving communication between research and operations The scientific questions addressed herein are questions important to operational forecasters. For example, will this MCS produce a bore that initiates another MCS, or assists this ongoing MCS to last beyond the solutions of forecast models? Can the expected change in convective potential be characterized in a way that it is consumable by the public? Continuing to engage in research that can eventually be disseminated to the public by forecasters is a goal that has tangible positive impacts on the public response: saving lives and protecting investments.

(iii) Improving forecast models The work presented aims to improve the physical understanding of atmospheric bores in the nocturnal environment while providing tools that have prognostic capabilities. Some beneficial improvements to models could come from a parameterization of bores based on theory. This is important for climate models and long-range forecasts that currently rely on parameterizations to represent convection over a coase spatial grid. Even short-term forecast models could benefit from an algorithm designed to target convective outflows and diagnose their potential to developing bore-initiated convection. From experience with 1 km grid-spaced models, vertical motions will be attenuated for some shorter trapped waves because of the insufficient vertical grid spacing. If this algorithm is developed and tested within a forecast model, then future studies comment on the improvements to representations of the nocturnal maximum, modeled storm structure, etc.

(iv) Education This vein of research provides a marry of dynamics, numerical models, and forecast improvement. Because it is difficult to be proficient in all aspects, bores offers students, faculty, and operations this unique opportunity to collaborate and teach one another. Teaching and engaging other professionals with different skill sets provide individuals with a more robust set of tools. In the evolving field of engineering, having a wide range of skill sets is necessary to tackle more complex problems with far reaching implications.

References

Alexander, M. J., J. H. Richter, and B. R. Sutherland, : Generation and Trapping of Gravity Waves from Convection with Comparison to Parameterization.

Arritt, R. W., T. D. Rink, M. Segal, D. P. Todey, C. A. Clark, M. J. Mitchell, and K. M. Labas, 1997: The Great Plains Low-Level Jet during the Warm Season of 1993. *Monthly Weather Review*, **125** (9), 2176–2192. doi:10.1175/1520-0493(1997)125<2176:TGPLLJ>2.0.CO;2.

Augustine, J. A. and K. W. Howard, 1991: Mesoscale Convective Complexes over the United States during 1986 and 1987. *Monthly Weather Review*, **119** (7), 1575–1589. doi:10.1175/1520-0493(1991)119<1575:MCCOTU>2.0.CO;2.

Baines, P. G., 1984: A unified description of two-layer flow over topography. *Journal of Fluid Mechanics*, **146** (-1), 127 pp. doi:10.1017/S0022112084001798.

Baines, P. G., 1995: *Topographic effects in stratified flows.* Cambridge University Press, 482 pp.

Baines, Â. and Â. Davies, 1980: Laboratory studies of topographic effects in rotating and/or stratified fluids. *In WMO Orographic Effects in Planetary Flows p 233-299 (SEE N80-33811 24-42).*

Batchelor, G., 1967: *Introduction to fluid dynamics.* Cambridge University Press, 615 pp.

Benjamin, T. B., 1968: Gravity currents and related phenomena. *J . Fluid Mech*, **31** (2), 209–248.

Blackadar, A. K., 1957: Boundary layer wind maxima and their significance for the growth of nocturnal inversions. *Bulletin of the American Meteorological Society*, **38**, 283–290.

Blake, B., D. B. Parsons, K. Haghi, and S. Castleberry, 2017: The structure, evolutions, and dynamics of a nocturnal convective system simulated using the WRF-ARW model. *Monthly Weather Review*, **in review.**

Bleeker, W. and M. J. Andre, 1951: On the diurnal variation of precipitation, particularly over central U.S.A., and its relation to large-scale orographic circulation systems. *Quarterly Journal of the Royal Meteorological Society*, **77** (332), 260–271. doi:10.1002/qj.49707733211.

Bonner, W. D., 1968: Climatology of the low level jet. *Monthly Weather Review*, **96** (12), 833–850. doi:10.1175/1520-0493(1968)096<0833:COTLLJ>2.0.CO;2.

Brock, F. V., K. C. Crawford, R. L. Elliott, G. W. Cuperus, S. J. Stadler, H. L. Johnson, and M. D. Eilts, 1995: The Oklahoma Mesonet: a technical overview. *Journal of Atmospheric and Oceanic Technology*, **12** (1), 5–19. doi:10.1175/1520-0426(1995)012<0005:TOMATO>2.0.CO;2.

Bryan, G. H. and R. Rotunno, 2014a: Gravity currents in confined channels with environmental shear. *Journal of the Atmospheric Sciences*, **71** (3), 1121–1142. doi:10.1175/JAS-D-13-0157.1.

—— and ——, 2014b: The optimal state for gravity currents in shear. *Journal of the Atmospheric Sciences*, **71** (1), 448–468. doi:10.1175/JAS-D-13-0156.1.

Carbone, R. E. and J. D. Tuttle, 2008: Rainfall occurrence in the U.S. warm season: the diurnal cycle. *Journal of Climate*, **21** (16), 4132–4146. doi:10.1175/2008JCLI2275.1.

——, J. W. Conway, N. A. Crook, and M. W. Moncrieff, 1990: The generation and propagation of a nocturnal squall line. Part I: observations and implications for mesoscale predictability. *Monthly Weather Review*, **118** (1), 26–49. doi:10.1175/1520-0493(1990)118<0026:TGAPOA>2.0.CO;2.

——, J. D. Tuttle, D. A. Ahijevych, and S. B. Trier, 2002: Inferences of predictability associated with warm season precipitation episodes. *Journal of the Atmospheric Sciences*, **59** (13), 2033–2056. doi:10.1175/1520-0469(2002)059<2033:IOPAWW>2.0.CO;2.

Christie, D. R., 1989: Long nonlinear waves in the lower atmosphere. *Journal of the Atmospheric Sciences*, **46** (11), 1462–1491. doi:10.1175/1520-0469(1989)046<1462:LNWITL>2.0.CO;2.

——, K. J. Muirhead, and A. L. Hales, 1978: On Solitary Waves in the Atmosphere. *Journal of the Atmospheric Sciences*, **35** (5), 805–825. doi:10.1175/1520-0469(1978)035<0805:OSWITA>2.0.CO;2.

——, ——, and ——, 1979: Intrusive density flows in the lower troposphere: A source of atmospheric solitons. *Journal of Geophysical Research*, **84** (C8), 4959 pp. doi:10.1029/JC084iC08p04959.

Clark, A. J., W. A. Gallus, and T.-C. Chen, 2007: Comparison of the Diurnal Precipitation Cycle in Convection-Resolving and Non-Convection-Resolving Mesoscale Models. *Monthly Weather Review*, **135** (10), 3456–3473. doi:10.1175/MWR3467.1.

Clarke, R. H., 1972: The morning glory: an atmospheric hydraulic jump. *Journal of Applied Meteorology*, **11** (2), 304–311. doi:10.1175/1520-0450(1972)011<0304:TMGAAH>2.0.CO;2.

——, 1984: Colliding sea-breezes and the creation of internal atmospheric bore waves: two-dimensional numerical studies. *Australian Meteorological Magazine*, **32** (December), 207–226.

——, R. K. Smith, and D. G. Reid, 1981: The Morning Glory of the Gulf of Carpentaria: An Atmospheric Undular Bore. *Monthly Weather Review*, **109** (8), 1726–1750. doi:10.1175/1520-0493(1981)109<1726:TMGOTG>2.0.CO;2.

Clark, T. L. and W. R. Peltier, 1984: Critical level reflection and the resonant growth of nonlinear mountain waves. *Journal of the Atmospheric Sciences*, **41** (21), 3122–3134. doi:10.1175/1520-0469(1984)041<3122:CLRATR>2.0.CO;2.

Cohn, S. A., W. O. J. Brown, C. L. Martin, M. E. Susedik, G. D. Maclean, and D. B. Parsons, 2001: Clear air boundary layer spaced antenna wind measurement with the Multiple Antenna Profiler (MAPR). *Annales Geophysicae*, **19** (8), 845–854. doi:10.5194/angeo-19-845-2001.

Coleman, T. A. and K. R. Knupp, 2011: Radiometer and profiler analysis of the effects of a bore and a solitary wave on the stability of the nocturnal boundary layer. *Monthly Weather Review*, **139** (1), 211–223. doi:10.1175/2010MWR3376.1.

——, ——, and D. Herzmann, 2009: The spectacular undular bore in Iowa on 2 October 2007. *Monthly Weather Review*, **137** (1), 495–503. doi:10.1175/2008MWR2518.1.

Cotton, W. R., R. L. George, P. J. Wetzel, and R. L. McAnelly, 1983: A long-lived mesoscale convective complex. Part I: the mountainâĂŞgenerated component. *Monthly Weather Review*, **111** (10), 1893–1918. doi:10.1175/1520-0493(1983)111<1893:ALLMCC>2.0.CO;2.

Craig Goff, R., 1976: Vertical Structure of Thunderstorm Outflows. *Monthly Weather Review*, **104** (11), 1429–1440. doi:10.1175/1520-0493(1976)104<1429:VSOTO>2.0.CO;2.

Crook, N. A., 1986: The effect of ambient stratification and moisture on the motion of atmospheric undular bores. *Journal of the Atmospheric Sciences*, **43** (2), 171–181. doi:10.1175/1520-0469(1986)043<0171:TEOASA>2.0.CO;2.

——, 1988: Trapping of low-level internal gravity waves. *Journal of the Atmospheric Sciences*, **45** (10), 1533–1541. doi:10.1175/1520-0469(1988)045<1533:TOLLIG>2.0.CO;2.

Crook, N. A. and M. J. Miller, 1984: A numerical and analytical study of atmospheric undular bores. *Quarterly Journal of the Royal Meteorological Society*, **111** (467), 225–242. doi:10.1002/qj.49711146710.

Cummins, P. F., L. Armi, P. F. Cummins, and L. Armi, 2010: Upstream Internal Jumps in Stratified Sill Flow: Observations of Formation, Evolution, and Release. *Journal of Physical Oceanography*, **40** (6), 1419–1426. doi:10.1175/2010JPO4435.1.

Dai, A., 2001: Global Precipitation and Thunderstorm Frequencies. Part II: Diurnal Variations. *Journal of Climate*, **14** (6), 1112–1128. doi:10.1175/1520-0442(2001)014<1112:GPATFP>2.0.CO;2.

——, F. Giorgi, and K. E. Trenberth, 1999: Observed and model-simulated diurnal cycles of precipitation over the contiguous United States. *Journal of Geophysical Research*, **104** (D6), 6377 pp. doi:10.1029/98JD02720.

Davies, H. C., 1979: Phase-lagged wave-CISK. *Quarterly Journal of the Royal Meteorological Society*, **105** (444), 325–353. doi:10.1002/qj.49710544402.

Davis, C. A., K. W. Manning, R. E. Carbone, S. B. Trier, and J. D. Tuttle, 2003: Coherence of warm-season continental rainfall in numerical weather prediction models. *Monthly Weather Review*, **131** (11), 2667–2679. doi:10.1175/1520-0493(2003)131<2667:COWCRI>2.0.CO;2.

Doviak, R. J. and D. S. Zrnić, 1984: *Doppler Radar and Weather Observations.* Dover Publications, Inc., 562 pp.

Durran, D. R., M. O. G. Hills, and P. N. Blossey, 2015: The Dissipation of Trapped Lee Waves. Part I: Leakage of Inviscid Waves into the Stratosphere. *Journal of atmospheric science*, **72** (April), 1569–1584. doi:10.1175/JAS-D-14-0238.1.

Easterling, D. R. and P. J. Robinson, 1985: The Diurnal variation of thunderstorm activity in the United States. *Journal of Climate and Applied Meteorology*, **24** (10), 1048–1058. doi:10.1175/1520-0450(1985)024<1048:TDVOTA>2.0.CO;2.

Efron, B. and R. J. Tibshirani, 1993: *An introduction to the bootstrap.* Chapman and Hall/CRC, 436 pp.

Emanuel, K. A., 1983: Inertial Instability and Mesoscale Convective Systems. part II. Symmetric CISK in a Baroclinic Flow.

Epifanio, C. C., D. R. Durran, C. C. Epifanio, and D. R. Durran, 2001: Three-dimensional effects in high-drag-state flows over long ridges. *Journal of the Atmospheric Sciences*, **58** (9), 1051–1065. doi:10.1175/1520-0469(2001)058<1051:TDEIHD>2.0.CO;2.

Farquharson, J. S., 1939: The diurnal variation of wind over tropical Africa. *Quarterly Journal of the Royal Meteorological Society*, **65** (280), 165–184. doi:10.1002/qj.49706528004.

Fovell, R. G., 2002: Upstream influence of numerically simulated squall-line storms. *Quarterly Journal of the Royal Meteorological Society*, **128** (581), 893–912. doi:10.1256/0035900021643737.

——, G. L. Mullendore, and S.-H. Kim, 2006: Discrete propagation in numerically simulated nocturnal squall lines. *Monthly Weather Review*, **134** (12), 3735–3752.

French, A. J. and M. D. Parker, 2010: The response of simulated nocturnal convective systems to a developing low-level jet. *Journal of the Atmospheric Sciences*, **67** (10), 3384–3408. doi:10.1175/2010JAS3329.1.

Fritsch, J. M., R. J. Kane, and C. R. Chelius, 1986: The Contribution of mesoscale convective weather systems to the warm-season precipitation in the United States. *Journal of Climate and Applied Meteorology*, **25** (10), 1333–1345. doi:10.1175/1520-0450(1986)025<1333:TCOMCW>2.0.CO;2.

Geerts, B., and Coauthors, 2016: The 2015 Plains Elevated Convection At Night (PECAN) field project. *Bulletin of the American Meteorological Society*, BAMS–D–15–00257.1. doi:10.1175/BAMS-D-15-00257.1.

Goler, R. A. and M. J. Reeder, 2004: The Generation of the Morning Glory. *Journal of the Atmospheric Sciences*, **61** (12), 1360–1376. doi:10.1175/1520-0469(2004)061<1360:TGOTMG>2.0.CO;2.

Gossard, E. E. and W. H. Hooke, 1975: *Waves in the atmosphere*. Elsevier, 456 pp.

Haase, S. P. and R. K. Smith, 1989: The numerical simulation of atmospheric gravity currents. Part II. Environments with stable layers. *Geophysical & Astrophysical Fluid Dynamics*, **46** (1-2), 35–51. doi:10.1080/03091928908208903.

Haghi, K., D. Imy, D. B. Parsons, and S. E. Koch, 2017a: A theory-based approach to forecasting bore-initiated convection in the nocturnal environment. *Weather and Forecasting*.

——, D. B. Parsons, and A. Shapiro, 2017b: Bores observed during IHOP_2002: the relationship of bores to the nocturnal environment. *Monthly Weather Review*, **in review.**

Hane, C. E., J. D. Watts, D. L. Andra, J. A. Haynes, E. Berry, R. M. Rabin, and F. H. Carr, 2003: The evolution of morning convective systems over the U.S. Great Plains during the warm season. Part I: the forecast problem. *Weather and Forecasting*, **18** (6), 1286–1294. doi:10.1175/1520-0434(2003)018<1286:TEOMCS>2.0.CO;2.

Hardy, K. and K. S. Gage, 1990: The history of radar studies of the clear atmosphere. *Radar in Meteorology: Battan Memorial and 40th Anniversary Radar Meteorology Conference* 806.

Heideman, K. F. and J. M. Fritsch, 1988: Forcing Mechanisms and Other Characteristics of Significant Summertime Precipitation. *Weather and Forecasting*, **3** (2), 115–130. doi:10.1175/1520-0434(1988)003<0115:FMAOCO>2.0.CO;2.

Helfrich, K. R. and B. L. White, 2010: Nonlinear Processes in Geophysics A model for large-amplitude internal solitary waves with trapped cores. *Nonlin. Processes Geophys*, **17**, 303–318. doi:10.5194/npg-17-303-2010.

He, M.-Y., H.-B. Liu, B. Wang, D.-L. Zhang, M.-Y. He, H.-B. Liu, B. Wang, and D.-L. Zhang, 2016: A Modeling Study of a Low-Level Jet along the Yun-Gui Plateau in South China. *Journal of Applied Meteorology and Climatology*, **55** (1), 41–60. doi:10.1175/JAMC-D-15-0067.1.

Higgins, R. W., and Coauthors, 1997: Influence of the Great Plains Low-Level Jet on Summertime Precipitation and Moisture Transport over the Central United States. *Journal of Climate*, **10** (3), 481–507. doi:10.1175/1520-0442(1997)010<0481:IOTGPL>2.0.CO;2.

Holton, J. R., 1967: The diurnal boundary layer wind oscillation above sloping terrain. *Tellus*, **19** (2), 199–205. doi:10.1111/j.2153-3490.1967.tb01473.x.

Holtslag, A. A. M., and Coauthors, 2013: Stable atmospheric boundary layers and diurnal cycles: challenges for weather and climate models. *Bulletin of the American Meteorological Society*, **94** (11), 1691–1706. doi:10.1175/BAMS-D-11-00187.1.

Houghton, D. D. and A. Kasahara, 1968: Nonlinear shallow fluid flow over an isolated ridge. *Communications on Pure and Applied Mathematics*, **21** (1), 1–23. doi:10.1002/cpa.3160210103.

Houze, R. A., 2004: Mesoscale convective systems. *Reviews of Geophysics*, **42** (4), RG4003 pp. doi:10.1029/2004RG000150.

Jiang, X., N. C. Lau, and S. A. Klein, 2006: Role of eastward propagating convection systems in the diurnal cycle and seasonal mean of summertime rainfall over the U.S. Great Plains. *Geophysical Research Letters*, **33** (19), 1–6. doi:10.1029/2006GL027022.

——, N.-C. Lau, I. M. Held, and J. J. Ploshay, 2007: Mechanisms of the Great Plains Low-Level Jet as Simulated in an AGCM. *Journal of the Atmospheric Sciences*, **64** (2), 532–547. doi:10.1175/JAS3847.1.

Keeler, R., J. Lutz, and J. Vivekanandan, 2000: S-Pol: NCAR's polarimetric Doppler research radar. *IGARSS 2000. IEEE 2000 International Geoscience and Remote Sensing Symposium. Taking the Pulse of the Planet: The Role of Remote Sensing in Managing the Environment. Proceedings (Cat. No.00CH37120).* Vol. 4 1570–1573. [Available online at http://ieeexplore.ieee.org/lpdocs/epic03/wrapper.htm?arnumber=857275.]

Kincer, J. B., 1916: Daytime and nighttime precipitation and their economic significance. *Monthly Weather Review*, **44** (11), 628–633. doi:10.1175/1520-0493(1916)44<628:DANPAT>2.0.CO;2.

Kingsmill, D. E. and N. Andrew Crook, 2003: An observational study of atmospheric bore formation from colliding density currents. *Monthly Weather Review*, **131** (12), 2985–3002. doi:10.1175/1520-0493(2003)131<2985:AOSOAB>2.0.CO;2.

Klemp, J. B., R. Rotunno, and W. C. Skamarock, 1997: On the propagation of internal bores. *Journal of Fluid Mechanics*, **331**, 81–106. doi:10.1017/S0022112096003710.

Knupp, K., 2006: Observational analysis of a gust front to bore to solitary wave transition within an evolving nocturnal boundary layer.

Kobbé, G., 1899: The Tidal âĂIJBoreâĂİ at Moncton. *Scientific American*, **81** (23), 356–356. doi:10.1038/scientificamerican12021899-356.

Koch, S. E. and W. L. Clark, 1999: A nonclassical cold front observed during COPS-91: frontal structure and the process of severe storm initiation. *Journal of the Atmospheric Sciences*, **56** (16), 2862–2890. doi:10.1175/1520-0469(1999)056<2862:ANCFOD>2.0.CO;2.

——, P. B. Dorian, R. Ferrare, S. H. Melfi, W. C. Skillman, and D. Whiteman, 1991: Structure of an internal bore and dissipating gravity current as revealed by Raman lidar. *Monthly Weather Review*, **119** (4), 857–887. doi:10.1175/1520-0493(1991)119<0857:SOAIBA>2.0.CO;2.

——, C. Flamant, J. W. Wilson, B. M. Gentry, and B. D. Jamison, 2008a: An atmospheric soliton observed with Doppler radar, differential absorption lidar, and a molecular Doppler lidar. *Journal of Atmospheric and Oceanic Technology*, **25** (8), 1267–1287. doi:10.1175/2007JTECHA951.1.

——, W. Feltz, F. Fabry, M. Pagowski, B. Geerts, K. M. Bedka, D. O. Miller, and J. W. Wilson, 2008b: Turbulent mixing processes in atmospheric bores and solitary waves deduced from profiling systems and numerical simulation. *Monthly Weather Review*, **136** (4), 1373–1400. doi:10.1175/2007MWR2252.1.

Kundu, P., 2008: *Fluid mechanics*, fourth ed. Elsevier, 872 pp.

Laing, A. G. and J. M. Fritsch, 1993a: Mesoscale Convective Complexes in Africa. *Monthly Weather Review*, **121** (8), 2254–2263. doi:10.1175/1520-0493(1993)121<2254:MCCIA>2.0.CO;2.

Laing, A. G. and J. M. Fritsch, 1993b: Mesoscale Convective Complexes over the Indian Monsoon Region. *Journal of Climate*, **6** (5), 911–919. doi:10.1175/1520-0442(1993)006<0911:MCCOTI>2.0.CO;2.

Laing, A. G. and J. Michael Fritsch, 1997: The global population of mesoscale convective complexes. *Quarterly Journal of the Royal Meteorological Society*, **123** (538), 389–405. doi:10.1002/qj.49712353807.

Lamb, S. H., 1932: *Hydrodynamics*, sixth edit ed. Dover Publications, Inc.

Lane., T. P. and T. L. Clark, 2002: Gravity waves generated by the dry convective boundary layer: Two-dimensional scale selection and boundary-layer feedback. *Quarterly Journal of the Royal Meteorological Society*, **128** (583), 1543–1570. doi:10.1002/qj.200212858308.

Lighthill, M. J., 1978: *Waves in fluids.* Cambridge University Press, 504 pp.

Lindzen, R. S. and K.-K. Tung, 1976a: Banded convective activity and ducted gravity waves. *Monthly Weather Review*, **104** (12), 1602–1617. doi:10.1175/1520-0493(1976)104<1602:BCAADG>2.0.CO;2.

Lindzen, R. S. and A. J. Rosenthal, 1976b: On the instability of Helmholtz velocity profiles in stably stratified fluids when a lower boundary is present. *Journal of Geophysical Research*, **81** (9), 1561–1571. doi:10.1029/JC081i009p01561.

Liu, C. and M. W. Moncrieff, 1996: A numerical study of the effects of ambient flow and shear On density currents. *Monthly Weather Review*, **124** (10), 2282–2303. doi:10.1175/1520-0493(1996)124<2282:ANSOTE>2.0.CO;2.

—— and ——, 2000: Simulated density currents in idealized stratified environments. *Monthly Weather Review*, **128** (5), 1420–1437. doi:10.1175/1520-0493(2000)128<1420:SDCIIS>2.0.CO;2.

Li, Y. and R. B. Smith, 2010: The Detection and Significance of Diurnal Pressure and Potential Vorticity Anomalies East of the Rockies. *Journal of the Atmospheric Sciences*, **67** (9), 2734–2751. doi:10.1175/2010JAS3423.1.

Locatelli, J. D., M. T. Stoelinga, P. V. Hobbs, and J. Johnson, 1998: Structure and evolution of an undular bore on the High Plains and its effects on migrating birds. *Bulletin of the American Meteorological Society*, **79** (6), 1043–1060. doi:10.1175/1520-0477(1998)079<1043:SAEOAU>2.0.CO;2.

Long, R. R., 1954: Some aspects of the flow of stratified fluids: II. Experiments with a two-fluid system. *Tellus A*, **6** (2). doi:10.3402/tellusa.v6i2.8731.

Lynch, D. K., 1982: Tidal Bores. *Scientific American*, **247** (4), 146–156. doi:10.1038/scientificamerican1082-146.

Maddox, R. A., 1980: Meoscale Convective Complexes. *Bulletin of the American Meteorological Society*, **61** (11), 1374–1387. doi:10.1175/1520-0477(1980)061<1374:MCC>2.0.CO;2.

——, 1983: Large-Scale Meteorological Conditions Associated with Midlatitude, Mesoscale Convective Complexes. *Monthly Weather Review*, **111** (7), 1475–1493. doi:10.1175/1520-0493(1983)111<1475:LSMCAW>2.0.CO;2.

Mapes, B. E., 1993: Gregarious Tropical Convection. *Journal of the Atmospheric Sciences*, **50** (13), 2026–2037. doi:10.1175/1520-0469(1993)050<2026:GTC>2.0.CO;2.

Marsham, J. H., S. B. Trier, T. M. Weckwerth, and J. W. Wilson, 2011: Observations of elevated convection initiation leading to a surface-based squall line during 13 June IHOP_2002. *Monthly Weather Review*, **139** (1), 247–271. doi:10.1175/2010MWR3422.1.

Martin, E. R. and R. H. Johnson, 2008: An Observational and modeling study of an atmospheric internal bore during NAME 2004. *Monthly Weather Review*, **136** (11), 4150–4167. doi:10.1175/2008MWR2486.1.

Miller, D. and J. M. Fritsch, 1991: Mesoscale Convective Complexes in the Western Pacific Region. *Monthly Weather Review*, **119** (12), 2978–2992. doi:10.1175/1520-0493(1991)119<2978:MCCITW>2.0.CO;2.

Mueller, D. and B. Geerts, 2017: Evolution and vertical structure of the 20 June 2015 bore observed during PECAN. *Monthly Weather Review*, **in review.**

Nagpal, O. P., 1979: The sources of atmospheric gravity waves. *Contemporary Physics*, **20** (6), 593–609. doi:10.1080/00107517908210928.

Nehrkorn, T., 1986: Wave-CISK in a Baroclinic Basic State. *Journal of the Atmospheric Sciences*, **43** (23), 2773–2791. doi:10.1175/1520-0469(1986)043<2773:WCIABB>2.0.CO;2.

Parish, T. R., L. D. Oolman, T. R. Parish, and L. D. Oolman, 2010: On the Role of Sloping Terrain in the Forcing of the Great Plains Low-Level Jet. *Journal of the Atmospheric Sciences*, **67** (8), 2690–2699. doi:10.1175/2010JAS3368.1.

Parker, M. D., 2008: Response of simulated squall lines to low-level cooling. *Journal of the Atmospheric Sciences*, **65** (4), 1323–1341. doi:10.1175/2007JAS2507.1.

Parsons, D., K. Haghi, K. Halbert, and E. Blake, 2017: An examination of the potential role of atmospheric bores in the initiation and maintenance of nocturnal convection over the Southern Great Plains. *Monthly Weather Review.*

Pedlosky, J., 1987: *Geophysical Fluid Dynamics*, second ed. Springer, 710 pp.

Peregrine, D. H., 1965: Calculations of the development of an undular bore. *J . Fluid Mech*, **25** (2), 321–330. doi:10.1017/S0022112066001678.

Prandtl, L., 1952: *Essentials of fluid mechanics.* New York: Hafner.

Pritchard, M. S., M. W. Moncrieff, and R. C. J. Somerville, 2011: Orogenic Propagating Precipitation Systems over the United States in a Global Climate Model with Embedded Explicit Convection. *Journal of the Atmospheric Sciences*, **68** (8), 1821–1840. doi:10.1175/2011JAS3699.1.

Purdom, J. F. W., 1976: Some Uses of High-Resolution GOES Imagery in the Mesoscale Forecasting of Convection and Its Behavior. *Monthly Weather Review*, **104** (12), 1474–1483. doi:10.1175/1520-0493(1976)104<1474:SUOHRG>2.0.CO;2.

Rayleigh, L., 1914: On the theory of long waves and bores. *Proceedings of the Royal Society of London. Series A: Mathematical and Physical Sciences*, **90** (619), 324–328. doi:10.1098/rspa.1914.0055.

Raymond, D. J., 1983: Wave-CISK in Mass Flux Form. *Journal of the Atmospheric Sciences*, **40** (10), 2561–2574. doi:10.1175/1520-0469(1983)040<2561:WCIMFF>2.0.CO;2.

——, 1984: A Wave-CISK Model of Squall Lines. *Journal of the Atmospheric Sciences*, **41** (12), 1946–1958. doi:10.1175/1520-0469(1984)041<1946:AWCMOS>2.0.CO;2.

Reap, R. M., 1972: An Operational Three-Dimensional Trajectory Model. *Journal of Applied Meteorology*, **11** (8), 1193–1202. doi:10.1175/1520-0450(1972)011<1193:AOTDTM>2.0.CO;2.

Rottman, J. W. and J. E. Simpson, 1989: The formation of internal bores in the atmosphere: A laboratory model. *Quarterly Journal of the Royal Meteorological Society*, **115** (488), 941–963. doi:10.1002/qj.49711548809.

Rotunno, R., J. B. Klemp, and M. L. Weisman, 1988: A theory for strong, long-lived squall lines. *Journal of the Atmospheric Sciences*, **45** (3), 463–485. doi:10.1175/1520-0469(1988)045<0463:ATFSLL>2.0.CO;2.

Schumacher, R. S., 2009: Mechanisms for quasi-stationary behavior in simulated heavy-rain-producing convective systems. *Journal of the Atmospheric Sciences*, **66** (6), 1543–1568. doi:10.1175/2008JAS2856.1.

Scorer, R. S., 1949: Theory of waves in the lee of mountains. *Quarterly Journal of the Royal Meteorological Society*, **75** (323), 41–56. doi:10.1002/qj.49707532308.

Shapiro, A., E. Fedorovich, S. Rahimi, A. Shapiro, E. Fedorovich, and S. Rahimi, 2016: A unified theory for the Great Plains nocturnal low-level jet. *Journal of the Atmospheric Sciences*, **73** (8), 3037–3057. doi:10.1175/JAS-D-15-0307.1.

Simpson, J., 1997: *Gravity currents in the environment and the laboratory*, second ed. Cambridge University Press, 244 pp.

Smith, R. K., 1988: Travelling waves and bores in the lower atmosphere: the âĂŸmorning glory' and related phenomena. *Earth-Science Reviews*, **25** (4), 267–290. doi:10.1016/0012-8252(88)90069-4.

——, M. J. Coughlan, and J.-L. Lopez, 1986: Southerly Nocturnal Wind Surges and Bores in Northeastern Australia. *Monthly Weather Review*, **114** (8), 1501–1518. doi:10.1175/1520-0493(1986)114<1501:SNWSAB>2.0.CO;2.

Spiegel, E. A. and G. Veronis, 1960: On the Boussinesq Approximation for a Compressible Fluid. *The Astrophysical Journal*, **131**, 442 pp. doi:10.1086/146849.

Stensrud, D. J., 1996: Importance of low-level jets to climate: a review. *Journal of Climate*, **9** (8), 1698–1711. doi:10.1175/1520-0442(1996)009<1698:IOLLJT>2.0.CO;2.

——, and Coauthors, 2009: Convective-Scale Warn-on-Forecast System. *Bulletin of the American Meteorological Society*, **90** (10), 1487–1499. doi:10.1175/2009BAMS2795.1.

Stoker, J. J., 1957: *Water waves*, volume iv ed. Interscience Publisher, Inc., 567 pp.

Stokes, G. M. and S. E. Schwartz, 1994: The Atmospheric Radiation Measurement (ARM) Program: programmatic background and design of the cloud and radiation test bed. *Bulletin of the American Meteorological Society*, **75** (7), 1201–1221. doi:10.1175/1520-0477(1994)075<1201:TARMPP>2.0.CO;2.

Surcel, M., M. Berenguer, I. Zawadzki, M. Surcel, M. Berenguer, and I. Zawadzki, 2010: The Diurnal Cycle of Precipitation from Continental Radar Mosaics and Numerical Weather Prediction Models. Part I: Methodology and Seasonal Comparison. *Monthly Weather Review*, **138** (8), 3084–3106. doi:10.1175/2010MWR3125.1.

Tanamachi, R. L., W. F. Feltz, and M. Xue, 2008: Observations and numerical simulation of upper boundary layer rapid drying and moistening events during the International H 2 O Project (IHOP_2002). *Monthly Weather Review*, **136** (8), 3106–3120. doi:10.1175/2008MWR2204.1.

Tepper, M., 1950: A propsed mechanism of squall lines: the pressure jump line. *Journal of Meteorology*, **7** (1), 21–29. doi:10.1175/1520-0469(1950)007<0021:APMOSL>2.0.CO;2.

Toms, B. A., J. M. Tomaszewski, D. D. Turner, S. E. Koch, B. A. Toms, J. M. Tomaszewski, D. D. Turner, and S. E. Koch, 2017: Analysis of a Lower Tropospheric Gravity Wave Train Using Direct and Remote Sensing Measurement Systems. *Monthly Weather Review*, MWR–D–16–0216.1. doi:10.1175/MWR-D-16-0216.1.

Toth, J. J. and R. H. Johnson, 1985: Summer Surface Flow Characteristics over Northeast Colorado. *Monthly Weather Review*, **113** (9), 1458–1469. doi:10.1175/1520-0493(1985)113<1458:SSFCON>2.0.CO;2.

Trier, S. B. and D. B. Parsons, 1993: Evolution of Environmental Conditions Preceding the Development of a Nocturnal Mesoscale Convective Complex. *Monthly Weather Review*, **121** (4), 1078–1098. doi:10.1175/1520-0493(1993)121<1078:EOECPT>2.0.CO;2.

Trier, S. B., C. A. Davis, and D. A. Ahijevych, 2010: Environmental Controls on the Simulated Diurnal Cycle of Warm-Season Precipitation in the Continental United States. *Journal of the Atmospheric Sciences*, **67** (4), 1066–1090. doi:10.1175/2009JAS3247.1.

Tripoli, G. J. and W. R. Cotton, 1989: Numerical Study of an Observed Orogenic Mesoscale Convective System. Part 2: Analysis of Governing Dynamics. *Monthly Weather Review*, **117** (2), 305–328. doi:10.1175/1520-0493(1989)117<0305:NSOAOO>2.0.CO;2.

Tutig, V., 1992: Trapped lee waves : a special analytical solution. *Meteorology and Atmospheric Physics*, **50**, 189–195.

Tuttle, J. D. and C. A. Davis, 2006: Corridors of Warm Season Precipitation in the Central United States. *Monthly Weather Review*, **134** (9), 2297–2317. doi:10.1175/MWR3188.1.

Vera, C., and Coauthors, 2006: The South American Low-Level Jet Experiment. *Bulletin of the American Meteorological Society*, **87** (1), 63–77. doi:10.1175/BAMS-87-1-63.

Wakimoto, R. M. and D. E. Kingsmill, 1995: Structure of an atmospheric undular bore generated from colliding boundaries during CaPE. *Monthly Weather Review*, **123** (5), 1374–1393. doi:10.1175/1520-0493(1995)123<1374:SOAAUB>2.0.CO;2.

Wallace, J. M., 1975: Diurnal Variations in Precipitation and Thunderstorm Frequency over the Conterminous United States. *Monthly Weather Review*, **103** (5), 406–419. doi:10.1175/1520-0493(1975)103<0406:DVIPAT>2.0.CO;2.

Weckwerth, T. M. and D. B. Parsons, 2006: A review of convection initiation and motivation for IHOP_2002. *Monthly Weather Review*, **134** (1), 5–22. doi:10.1175/MWR3067.1.

——, and Coauthors, 2004: An overview of the International H 2 O Project (IHOP_2002) and some preliminary highlights. *Bulletin of the American Meteorological Society*, **85** (2), 253–277. doi:10.1175/BAMS-85-2-253.

Weisman, M. L. and R. Rotunno, 2004: âĂIJA theory for strong long-lived squall linesâĂİ revisited. *Journal of the Atmospheric Sciences*, **61** (4), 361–382. doi:10.1175/1520-0469(2004)061<0361:ATFSLS>2.0.CO;2.

Wetzel, P. J., W. R. Cotton, and R. L. McAnelly, 1983: A long-lived mesoscale convective complex. Part II: evolution and structure of the mature complex. *Monthly Weather Review*, **111** (10), 1919–1937. doi:10.1175/1520-0493(1983)111<1919:ALLMCC>2.0.CO;2.

White, B. L. and K. R. Helfrich, 2012: A general description of a gravity current front propagating in a two-layer stratified fluid. *Journal of Fluid Mechanics*, **711**, 545–575. doi:10.1017/jfm.2012.409.

Wilson, J. W. and W. E. Schreiber, 1986: Initiation of convective storms at radar-observed boundary-layer convergence lines. *Monthly Weather Review*, **114** (12), 2516–2536. doi:10.1175/1520-0493(1986)114<2516:IOCSAR>2.0.CO;2.

—— and R. D. Roberts, 2006: Summary of convective storm initiation and evolution during IHOP: observational and modeling perspective. *Monthly Weather Review*, **134** (1), 23–47. doi:10.1175/MWR3069.1.

——, T. M. Weckwerth, J. Vivekanandan, R. M. Wakimoto, and R. W. Russell, 1994: Boundary Layer Clear-Air Radar Echoes: Origin of Echoes and Accuracy of Derived Winds. *Journal of Atmospheric and Oceanic Technology*, **11** (5), 1184–1206. doi:10.1175/1520-0426(1994)011<1184:BLCARE>2.0.CO;2.

Wolyn, P. G. and T. B. Mckee, 1994: The Mountain-Plains Circulation East of a 2-km-High NorthâĂŞSouth Barrier. *Monthly Weather Review*, **122** (7), 1490–1508. doi:10.1175/1520-0493(1994)122<1490:TMPCEO>2.0.CO;2.

Wood, I. R. and J. E. Simpson, 1984: Jumps in layered miscible fluids. *Journal of Fluid Mechanics*, **140** (-1), 329 pp. doi:10.1017/S0022112084000628.

Xu, Q. and J. H. Clark, 1984: Wave CISK and Mesoscale Convective Systems. *Journal of the Atmospheric Sciences*, **41** (13), 2089–2107. doi:10.1175/1520-0469(1984)041<2089:WCAMCS>2.0.CO;2.

Zimmerman, W. B. and J. M. Rees, 2004: Long solitary internal waves in stable stratifications. *Nonlinear Processes in Geophysics*, **11** (2), 165–180. doi:10.5194/npg-11-165-2004.

Chapter 7

Appendix

7.1 Abbreviations

1. CAPE- Convective Available Potential Energy. An integral of buoyant energy over the depth of the troposphere for a given parcel. Buoyancy is measured according to the American Meteorological Society Glossary as:

$$CAPE = \int_{p_n}^{p_f} (\alpha_p - \alpha_c) dp,$$

where α_p is the specific volume of a parcel, α_c is the specific volume of the surrounding environment, p_f is the pressure at the level of free convection and p_n is the pressure at a level of neutral buoyancy.

2. CIN-Convective INhibition. The integral of negative buoyant energy, opposite of CAPE.

3. dBZ-decibels relative to Z, where Z is the reflectivity factor.

4. Fr- Froude number. A ratio of the flow speed to the intrinsic long period gravity wave speed determined by equation (3.1), (Rottman and Simpson 1989).

5. H-Non-dimensional height. A ratio of the obstruction height (density current depth) to the depth of the inversion layer (Rottman and Simpson 1989). It is used in hydraulic theory and referenced in equation (3.2)

6. LFC- Level of Free Convection. The height to which a parcel must rise in order to remain buoyant relative to its environment until it reaches the equilibrium level. The equilibrium level is the height at which the parcel is no longer buoyant relative to its environment.

7. LPL- Lifted parcel level. The height of a theoretical parcel.

8. k- the horizontal wavenumber used in linear wave theory.

9. m-the vertical wavenumber used in linear wave theory. It is defined as:

$$m = \sqrt{l^2 - k^2}.$$

10. MRMS-Multi-Radar/Multi-Sensor system. It is a post-processing algorithm that eliminates many real-time radar problems (e.g. ground clutter, second trip). It integrates multiple available observations (e.g. surface and upper-air observations) and makes a mosaic using multiple radars. For a more detailed description, visit http://www.nssl.noaa.gov/projects/mrms/ .

11. μ-μ parameter- a ratio of the infinitesimal amplitude long waves to the speed of a density current (Haase and Smith 1989). See 3 for a mathematical representation.

    .

12. SNR-Signal to noise ratio. The ratio of peak power to noise power (Doviak and Zrnić 1984), defined as:

13. theta-e -Equivalent potential temperature. Defined as the temperature a parcel would possess at a reference level (typically 1000 mb) if all moisture condensed and fell out of the parcel. For a mathematical depiction of theta-e, visit http://glossary.ametsoc.org/wiki/Equivalent_potential_temperature .

$$SNR = \frac{[I^2(0) + Q^2(0)]erf^2[aB_6\tau/2]}{kT_{sy}B_n},$$

where

$$SNR = B_6 = 1.04/\tau,$$

and I and Q are in-phase and quadrature component, respectively,τ is the pulse width, T_{sy} is the radio noise level in terms of a system temperature N/kB_n, k is Boltzmann's constant and erf is the error function:

$$erf(x) = \frac{2}{\sqrt{\pi}} \int_0^x e^{-t^2} dt$$

7.2 Hydraulic Theory

7.2.1 Setup

Pressure equation

$$0 - gz - \frac{1}{\rho}\frac{dp}{dz} \Rightarrow dp = -\rho g dz,$$

$$\int_{p(x,z)}^{p_o} dp = -\int_z^{h_o+\eta} \rho g dz \Rightarrow p_o - p(x,z) = -\rho g(h_o + \eta) + \rho g z,$$

$$p(x,z,t) = p_o + \rho g(\eta + h_o - z)$$

Differentiated U equation of motion

$$\frac{\partial p}{dx} = \frac{\partial(p_o + \rho g(\eta + h_o - z))}{\partial x} = \cancelto{0}{\frac{\partial p_o}{\partial x}} + g\rho\frac{\partial \eta}{\partial x} + \cancelto{0}{g\rho\frac{\partial h_o}{\partial x}} - \cancelto{0}{g\rho\frac{dz}{dx}} = g\rho\frac{\partial \eta}{\partial x} \Rightarrow$$

$$\frac{\partial u}{\partial t} + u\frac{\partial u}{\partial x} = -g\frac{\partial \eta}{\partial x}.$$

Integrating Continuity Equation

$$\int_{d_o}^{\eta+h_o} (\nabla \cdot \mathbf{u}) dz = \int_{d_o}^{\eta+h_o} \left(\frac{\partial u}{\partial x} + \frac{\partial w}{\partial z} \right) dz = \int_{d_o}^{\eta+h_o} \frac{\partial u}{\partial x} dz + \int_{d_o}^{\eta+h_o} \frac{\partial w}{\partial z} dz$$

In the case where continuity is integrated over z, but there is a partial derivative with respect to x in the integrand along with boundaries of integration that are also function of x, the integration requires use of Leibniz rule:

$$\frac{\partial}{\partial x} \left(\int_{a(x)}^{b(x)} f(x,z) dz \right) = f(x,b(x)) \cdot \frac{\partial}{\partial x} b(x) - f(x,a(x)) \cdot \frac{\partial}{\partial x} a(x) + \int_{a(x)}^{b(x)} \frac{\partial}{\partial x} f(x,z) dz$$

Rearranging Leibniz rule (2.18), the u-equation of motion can be rewritten (2.17) as:

$$\int_{d_o}^{\eta+h_o} \frac{\partial u}{\partial x} dz + \int_{d_o}^{\eta+h_o} \frac{\partial w}{\partial z} dz$$

$$= \frac{\partial}{\partial x} \left(\int_{d_o}^{\eta+h_o} u dz \right) - u(x, \eta + h_o) \cdot \frac{\partial (\eta + h_o)}{\partial x} + u(x, d_o) \cdot \frac{\partial}{\partial x}(d_o) + \int_{d_o}^{\eta+h_o} \frac{\partial w}{\partial z} dz$$

$$= \frac{\partial}{\partial x} (u(\eta + h_o) - u(d_o)) - u \left(\frac{\partial (\eta)}{\partial x} + \cancelto{0}{\frac{\partial (h_o)}{\partial x}} \right) + u\frac{\partial d_o}{\partial x} + \int_{d_o}^{\eta+h_o} dw$$

$$= \frac{\partial}{\partial x}(ud) - u\frac{\partial \eta}{\partial x} + u\frac{\partial d_o}{\partial x} + w(\eta + h_o) - w(d_o)$$

Making use of the definitions of w (2.9) and (2.10), the result is:

$$= \frac{\partial}{\partial x}(ud) - u\frac{\partial \eta}{\partial x} + u\cancelto{0}{\frac{\partial d_o}{\partial x}} + \frac{D\eta}{Dt} - u\cancelto{0}{\frac{\partial d_o}{\partial x}}$$

$$= \frac{\partial}{\partial x}(ud) - \cancelto{0}{u\frac{\partial \eta}{\partial x}} + \frac{\partial \eta}{\partial t} + \cancelto{0}{u\frac{\partial \eta}{\partial x}}$$

$$= \frac{\partial \eta}{\partial t} + \frac{\partial}{\partial x}(ud).$$

7.2.2 Evaluating the flow over an obstruction

Super- and Sub-critical condition

Beginning with the equations of motion:

$$u\frac{du}{dx} + g\frac{d\eta}{dx} = 0,$$

$$\frac{d}{dx}(ud) = 0.$$

If these steady state versions of (2.20) and (2.23) are combined:

$$u\frac{du}{dx} + g\frac{d\eta}{dx} = u\frac{du}{dx} + g\frac{d(d_o + d - h_o)}{dx} = u\frac{du}{dx} + g\frac{dd_o}{dx} + g\frac{dd}{dx} + g\cancelto{0}{\frac{dh_o}{dx}} = 0 \Rightarrow$$

$$u\frac{du}{dx} + g\frac{dd_o}{dx} + g\frac{dd}{dx} = 0,$$

and

$$\frac{d}{dx}(ud) = u\frac{dd}{dx} + d\frac{du}{dx} \Rightarrow -\frac{u}{d}\frac{dd}{dx} = \frac{du}{dx}.$$

the result is:

$$u\frac{du}{dx}+g\frac{dd_o}{dx}+g\frac{dd}{dx}=u(-\frac{u}{d}\frac{dd}{dx})+g\frac{dd_o}{dx}+g\frac{dd}{dx}=(-\frac{u^2}{d}+g)\frac{dd}{dx}+g\frac{dd_o}{dx}\Rightarrow$$

$$(\frac{u^2}{dg}-1)\frac{dd}{dx}=\frac{dd_o}{dx} \tag{7.1}$$

Regime change when Fr = 1

Differentiate equation (2.23) with respect to x:

$$\frac{d}{dx}\left[(\frac{u^2}{dg}-1)\frac{dd}{dx}=\frac{dd_o}{dx}\right]\Rightarrow$$

$$\left(\frac{1}{dg}\frac{du^2}{dx}+\frac{u^2}{g}\frac{dd^{-1}}{dx}\right)\frac{dd}{dx}+\left(\frac{u^2}{dg}-1\right)\frac{d^2d}{dx^2}=\frac{d^2d_o}{dx^2}\Rightarrow$$

$$\left(\frac{2u}{dg}\frac{du}{dx}-\frac{u^2}{d^2g}\frac{dd}{dx}\right)\frac{dd}{dx}+\left(\frac{u^2}{dg}-1\right)\frac{d^2d}{dx^2}=\frac{d^2d_o}{dx^2}.$$

Now differentiate equation (2.20) with respect to x:

$$\frac{d}{dx}(ud)=0\Rightarrow$$

$$d\frac{du}{dx}+u\frac{dd}{dx}=0\Rightarrow$$

$$\frac{du}{dx}=-\frac{u}{d}\frac{dd}{dx}.$$

Combining these two equations, the result is:

$$\left(\frac{2u}{dg}(-\frac{u}{d}\frac{dd}{dx})-\frac{u^2}{d^2g}\frac{dd}{dx}\right)\frac{dd}{dx}+\left(\frac{u^2}{dg}-1\right)\frac{d^2d}{dx^2}=\frac{d^2d_o}{dx^2}\Rightarrow$$

$$\left(-\frac{2u^2}{d^2g}\frac{dd}{dx}-\frac{u^2}{d^2g}\frac{dd}{dx}\right)\frac{dd}{dx}+\left(\frac{u^2}{dg}-1\right)\frac{d^2d}{dx^2}=\frac{d^2d_o}{dx^2}\Rightarrow$$

$$-\frac{3u^2}{d^2g}\left(\frac{dd}{dx}\right)^2+\left(\frac{u^2}{dg}-1\right)\frac{d^2d}{dx^2}=\frac{d^2d_o}{dx^2}.$$

Curve BAD

This solution is defined by integrating the time-independent equations of motion along the flow in the x direction:

$$\Rightarrow u\frac{du}{dx}+g\frac{d\eta}{dx}=\frac{1}{2}\frac{du^2}{dx}+\frac{d(g\eta)}{dx}=\frac{d(\frac{1}{2}u^2+g\eta)}{dx}=0$$

$$\int\frac{d(\frac{1}{2}u^2+g\eta)}{dx}dx=\int d(\frac{1}{2}u^2+g\eta)\Rightarrow$$

$$\int d(\frac{1}{2}u^2+g[d+d_o-h_o])\Rightarrow$$

$$\int d(\frac{1}{2}u^2+g[d+d_o-h_o])\Rightarrow$$

$$\frac{1}{2}(u^2)+g(d_o+d)=C_1 \tag{7.2}$$

and

$$\Rightarrow \int \frac{d(uh)}{dx} dx = \int d(uh) \Rightarrow$$

$$uh = C_2 \tag{7.3}$$

The constants (C_1, C_2) can be solved for by prescribing the initial conditions (u_o, h_o, $d_o = 0$, $\eta = 0$):

$$\frac{1}{2}(u^2_{u=u_o}) + g(\cancelto{0}{d_o} + d_{d=h_o})$$

$$= \frac{1}{2}(u_o^2) + g(h_o) = C_1 \tag{7.4}$$

Similarly:

$$u_{u=u_o} d_{d=h_o} = C_2 \Rightarrow$$

$$u_o h_o = C_2. \tag{7.5}$$

Next, set (2.28) equal to (2.26) and (2.25) equal to (2.27):

$$\frac{1}{2}(u_o^2) + g(h_o) = \frac{1}{2}(u^2) + g(d_o + d)$$

$$u_o h_o = ud \Rightarrow d = \frac{u_o h_o}{u}$$

and combine the two equations:

$$\frac{1}{2}u_o^2 + gh_o = \frac{1}{2}u^2 + g(d_o + d) = \frac{1}{2}u^2 + gd_o + g\frac{u_o h_o}{u} \Rightarrow$$

$$\frac{1}{2}u_o^2 + gh_o - \frac{1}{2}u^2 - gd_o - g\frac{u_o h_o}{u} = 0 \Rightarrow$$

multiply by u:

$$\frac{1}{2}u_o^2 u + gh_o u - \frac{1}{2}u^3 - gd_o u - gu_o h_o = 0$$

combine gu terms:

$$gu(\frac{1}{2g}u_o^2 + h_o - d_o) - \frac{1}{2}u^3 gu_o h_o = 0$$

and multiply by -1:

$$\underbrace{\boxed{\tfrac{1}{2}u^3}}_{(1)} + \underbrace{\boxed{gu(d_o - \tfrac{1}{2g}u_o^2 - h_o)}}_{(2)} + \underbrace{\boxed{gu_o h_o}}_{(3)} = 0$$

At this point, it will be convenient for us to introduce parameters that will be used in the analysis:

$$Fr_o = \frac{u_o}{\sqrt{gh_o}}, H_o = \frac{d_o}{h_o}, V_o = \frac{u}{u_o}.$$

Starting with the third term form the equation above:

$$gu_o h_o = \frac{u_o^3}{u_o^2} gh_o = \frac{1}{Fr_o^2}u_o^3$$

Second term:

$$gu(d_o - \frac{1}{2g}u_o^2 - h_o) = \frac{guh_o}{u_o^2}(\frac{u_o^2 d_o}{h_o} - \frac{1}{2}\frac{u_o^4}{gh_o} - u_o^2) = \frac{u}{Fr_o^2}(\frac{u_o^2 d_o}{h_o} - \frac{1}{2}Fr_o^2 u_o^2 - u_o^2)$$

$$= \frac{u}{Fr_o^2}(u_o^2 H_o - \frac{1}{2}Fr_o^2 u_o^2 - u_o^2) = \frac{uu_o^2}{Fr_o^2}(H_o - \frac{1}{2}Fr_o^2 - 1) = \frac{V_o u_o^3}{Fr_o^2}(H_o - \frac{1}{2}Fr_o^2 - 1)$$

First Term:

$$\frac{1}{2}u^3 = \frac{1}{2}\frac{u^3 u_o^3}{u_o^3} = \frac{1}{2}V_o^3 u_o^3$$

Putting them all back together and dividing by $\frac{u_o^3}{Fr_o^2}$:

$$\frac{1}{2}V_o^3 u_o^3 + \frac{V_o u_o^3}{Fr_o^2}(H_o - \frac{1}{2}Fr_o^2 - 1) + \frac{1}{Fr_o^2}u_o^3 = \frac{1}{2}\frac{V_o^3 \cancel{u_o^3} Fr_o^2}{\cancel{u_o^3}} + \frac{V_o \cancel{u_o^3} \cancel{Fr_o^2}}{\cancel{u_o^3}\cancel{Fr_o^2}}(H_o - \frac{1}{2}Fr_o^2 - 1) + \frac{\cancel{u_o^3}\cancel{Fr_o^2}}{\cancel{u_o^3}\cancel{Fr_o^2}}^{1} =$$

$$\frac{1}{2}V_o^3 Fr_o^2 + V_o(H_o - \frac{1}{2}Fr_o^2 - 1) + 1 = 0 \tag{7.6}$$

Now that there is an equation in terms of Fr_o, H_o and V_o, the curve representing the condition where H = H_m can be solved. This value correlates to the largest ratio between the obstruction and the initial height of the fluid where the flow will be either supercritical or subcritical throughout. Based on Houghton and Kasahara (1968), $V_m = Fr_o^{-\frac{2}{3}}$ is the corresponding normalized velocity for H_m. Using this to solve for H_m and the curve for BAD:

$$\frac{1}{2}V_o^3 Fr_o^2 + V_o(H_o - \frac{1}{2}Fr_o^2 - 1) + 1 = \frac{1}{2}\cancel{Fr_o^{-\frac{6}{3}}Fr_o^2}^{1} + Fr_o^{-\frac{2}{3}}(H_m - \frac{1}{2}Fr_o^2 - 1) + 1$$

$$= \frac{1}{2} + Fr_o^{-\frac{2}{3}}H_m - \frac{1}{2}Fr_o^2 Fr_o^{-\frac{2}{3}} - Fr_o^{-\frac{2}{3}} + 1 \Rightarrow -\frac{1}{2} + \frac{1}{2}Fr_o^2 Fr_o^{-\frac{2}{3}} + Fr_o^{-\frac{2}{3}} - 1 = Fr_o^{-\frac{2}{3}}H_m \Rightarrow$$

$$-\frac{3}{2}Fr_o^{\frac{2}{3}} - \frac{1}{2}Fr_o^2 + 1 = H_m \tag{7.7}$$

7.2.3 Jump Conditions

fourth condition

To derive the fourth equation, start in a framework centered around the jump and not accelerating relative to the frame of reference, where v_o and v_1 are the fluid speed ahead of and behind the bore within this frame of reference. Next, incorporate (2.14) into (2.4) by multiplying (2.4) by v and multiplying ρ by (2.14), then adding them together (reminder that ρ is considered constant throughout the fluid):

$$\rho \nabla \cdot v = \rho \frac{\partial v}{\partial x} + \rho \frac{\partial w}{\partial z} = 0 \Rightarrow \ mult.\ by\ v \ \Rightarrow$$

$$v\rho \frac{\partial v}{\partial x} + v\rho \frac{\partial w}{\partial z} = 0$$

Multiply (2.14) by ρ and add to above equation:

$$v\rho \frac{\partial v}{\partial x} + v\rho \frac{\partial w}{\partial z} + \rho v \frac{\partial v}{\partial x} + \rho \frac{1}{\rho} \frac{\partial p}{\partial x} = 0.$$

Since u is independent of z and ρ is constant with height, then:

$$\frac{\partial \rho v^2}{\partial x} + \frac{\partial \rho v w}{\partial z} + \frac{\partial p}{\partial x} = 0 \tag{7.8}$$

If mass and momentum are conserved quantities, then integrating the equation of motion over the entire volume in question will remain a conserved quantity as well, even across the jump. If this jump is assumed to have reached a steady state, then equation (2.42) may be integrated over the volume:

$$\int_V (\frac{\partial \rho v^2}{\partial x} + \frac{\partial \rho v w}{\partial z} + \frac{\partial p}{\partial x}) dV = 0$$

Taking advantage of Divergence theorem to rewrite the integration as the flux of the quantities across the surface of the volume:

$$\int_V (\frac{\partial \rho v^2}{\partial x} + \frac{\partial p}{\partial x})dV + \int_V (\frac{\partial \rho vw}{\partial z})dV = \int_S (\rho v^2 + p)\hat{i} \cdot \hat{n} dS + \int_S (\rho vw)\hat{k} \cdot \hat{n} dS$$

The volume under consideration has an extent of Δx, Δy, and Δz. To start, there are no fluxes along the y-direction because the 2D flow is in the x-z direction. Instead, assume that Δy is of unit length. Equation (2.43), using Divergence theorem (Stoker 1957), can be rewritten as the flux of these quantities across the surface of the volume. Consequently, these constraints leave only four sides under consideration:

Side 1 ($n = -\hat{i}$):

$$= \int_S (\rho v^2 + p)\hat{i} \cdot -\hat{i} dS + \int_S (\rho vw)\cancelto{0}{\hat{k} \cdot -\hat{i}} dS = -\int_0^{h_1} (\rho v^2 + p)dz$$

Insert (2.13) into p:

$$= -\int_0^{h_1} (\rho v^2 + p_o + \rho g(\eta + h_o - z))dz$$

This integral must be separated into two integrals to account for the volume above the free surface:

$$= -\int_0^{h_o} (\rho v^2 + p_o + \rho g(\eta + h_o - z))dz - \int_{h_o}^{h_1} (\rho \cancelto{v=0}{v^2} + p_o + \cancelto{\rho=0}{\rho g(\eta + h_o - z)})dz$$

assign $v = v_o$ for v wind in fluid layer, since it is in the undisturbed fluid ahead of the jump:

$$= -(\rho v_o^2 z + p_o z + \rho g(\eta z + h_o z - \frac{1}{2}z^2))]_0^{h_o} - p_o z]_{h_o}^{h_1}$$

$$= -(\rho v_o^2 h_o + p_o h_o + \rho g(\cancel{\eta h_o}^{z=h_o \Rightarrow \eta = 0} + h_o^2 - \frac{1}{2}h_o^2)) - (p_o(h_1 - h_o))$$

$$= -(\rho v_o^2 h_o + \cancel{p_o h_o} + \frac{1}{2}\rho g h_o^2)) + \cancel{p_o h_o} - p_o h_1$$

$$= -(\rho v_o^2 h_o + \frac{1}{2}\rho g h_o^2 + p_o h_1) \tag{7.9}$$

Now lets do the same for the opposite side:

Side 3 ($n = \hat{i}$):

$$= \int_S (\rho v^2 + p)\hat{i}\cdot\hat{i}dS + \int_S (\rho v w)\hat{k}\cdot\hat{i}^{0}dS = \int_0^{h_1}(\rho v^2 + p)dz$$

Insert (2.13) into p:

$$= \int_0^{h_1}(\rho v^2 + p_o + \rho g(\eta + h_o - z))dz$$

$$= \rho v^2 z + p_o z + \rho g(\eta z + h_o z - \frac{1}{2}z^2)]_o^{h_1}$$

η on the 3rd side equals $h_1 - h_o$ and $u = u_1$:

$$= \rho v_1^2 h_1 + p_o h_1 + \rho g((h_1 - \cancel{h_o})h_1 + \cancel{h_o h_1} - \frac{1}{2}h_1^2)$$

$$= \rho v_1^2 h_1 + p_o h_1 + \frac{1}{2}\rho g h_1^2 \tag{7.10}$$

Lets take a look at the top of the volume:

Side 4 ($n = \hat{k}$):

$$= \int_S (\rho v^2 + p)\hat{i}\cdot\hat{k}^{0}dS + \int_S (\rho v w)\hat{k}\cdot\hat{k}dS = \int_{a_o}^{a_1}(\rho v w)dx$$

This integral is simply 0 because no vertical flux across the top. Therefore if continuity across the surface holds true, there can be no vertical motion along side 4. This integral is set to 0. Similarly, the same is done for Side 2, since it is along the surface where $d_o = 0$. Therefore:

Side 2 ($n = -\hat{k}$):

$$-\int_{a_o}^{a_1} (\rho v w) dx = 0 \tag{7.11}$$

Side 4 ($n = \hat{k}$):

$$\int_{a_o}^{a_1} (\rho v w) dx = 0 \tag{7.12}$$

Now that all 4 sides have been evaluated, the combined results for ((2.44),(2.45),(2.46),(2.47)) are:

$$\int_V (\frac{\partial \rho v^2}{\partial x} + \frac{\partial \rho v w}{\partial z} + \frac{\partial p}{\partial x}) dV = -(\rho v_o^2 h_o + \frac{1}{2}\rho g h_o^2 + \cancel{p_o h_1}) + \rho v_1^2 h_1 + \cancel{p_o h_1} + \frac{1}{2}\rho g h_1^2$$

$$\rho v_o^2 h_o + \frac{1}{2}\rho g h_o^2 = \rho v_1^2 h_1 + \frac{1}{2}\rho g h_1^2 \tag{7.13}$$

Solving equation (2.38) for v_o and plugging it into equation (2.48), the result is

$$\rho v_o^2 h_o + \frac{1}{2}\rho g h_o^2 = \rho v_o^2 h_1 + \frac{1}{2}\rho g h_1^2 \Rightarrow \rho v_o^2 h_o + \frac{1}{2}\rho g h_o^2 = \rho (\frac{v_o h_o}{h_1})^2 h_1 + \frac{1}{2}\rho g h_1^2 \Rightarrow$$

$$\rho v_o^2 h_o + \frac{1}{2}\rho g h_o^2 = \rho (\frac{v_o h_o}{h_1})^2 h_1 + \frac{1}{2}\rho g h_1^2 \Rightarrow \rho v_o^2 h_o - \rho (\frac{v_o h_o}{h_1})^2 h_1 = \frac{1}{2}\rho g (h_1^2 - h_o^2) \Rightarrow$$

$$\rho v_o^2(h_o - \frac{h_o^2 h_1}{h_1^2}) = \frac{1}{2}\rho g(h_1^2 - h_o^2) \Rightarrow v_o^2 = \frac{1}{2}g\frac{h_1^2 - h_o^2}{(h_o - \frac{h_o^2 h_1}{h_1^2})} \Rightarrow$$

$$v_o^2 = \frac{1}{2}g\frac{h_1^2 - h_o^2}{(h_o - \frac{h_o^2}{h_1})} = \frac{1}{2}g\frac{h_1}{h_o}\frac{h_1^2 - h_o^2}{(h_1 - h_o)} = \frac{1}{2}g\frac{h_1}{h_o}\frac{\cancel{(h_1 - h_o)}(h_1 + h_o)}{\cancel{(h_1 - h_o)}} \Rightarrow$$

$$v_o^2 = \frac{1}{2}gh_1(1 + \frac{h_1}{h_o}),$$

Or equally

$$(u_o + c_1)^2 = \frac{1}{2}gh_1(1 + \frac{h_1}{h_o}). \tag{7.14}$$

fifth condition

Our final condition is based on Bernoulli's principle. The flow from the subcritical regime behind the jump to the crest of the obstruction is governed by (2.19). If it is assumed to be a steady state and integrate over x:

$$u\frac{du}{dx} + g\frac{d\eta}{dx} = \frac{d}{dx}(\frac{1}{2}u^2 + g\eta) \Rightarrow$$

$$\int_{a_1}^{a_c} \frac{d}{dx}(\frac{1}{2}u^2 + g\eta)dx = \int_{a_1}^{a_c} \partial(\frac{1}{2}u^2 + g\eta) = (\frac{1}{2}u^2 + g\eta)]_{a_1}^{a_c} \Rightarrow$$

$$= \frac{1}{2}(u_c^2 - u_1^2) + g(d_c + d_m - h_1) \Rightarrow$$

$$\frac{1}{2}u_c^2 + g(d_c + d_m) = \frac{1}{2}u_1^2 + gh_1, \tag{7.15}$$

7.2.4 Curve AE

Bore strength equation

To start, equation (2.55) is manipulated so a solution for h_l/h_o can be obtained:

$$(u_o + \cancel{c_1}^{0})^2 = \frac{1}{2}gh_1(1+\frac{h_1}{h_o}) \Rightarrow$$

$$u_o^2 = \frac{1}{2}gh_1(1+\frac{h_1}{h_o}) = \frac{1}{2}gh_1 + \frac{1}{2}g\frac{h_1^2}{h_o} \Rightarrow$$

$$\frac{1}{2}g\frac{h_1^2}{h_o} + \frac{1}{2}gh_1 - u_o^2 = 0$$

Solving the quadratic equation

$$h_1 = \frac{-\frac{1}{2}g \pm \sqrt{\frac{g^2}{4} - 4(\frac{1}{2}\frac{g}{h_o})(-u_o^2)}}{\frac{g}{h_o}}$$

Since the subcritical flow height h_1 must be positive, real solutions of h_1 are considered, implying:

$$h_1 = \frac{-\frac{1}{2}g + \sqrt{\frac{g^2}{4} - 4(\frac{1}{2}\frac{g}{h_o})(-u_o^2)}}{\frac{g}{h_o}}$$

$$= \frac{h_o}{g}(-\frac{1}{2}g + \sqrt{\frac{g^2}{4} + 2\frac{g}{h_o}u_o^2})$$

$$= \frac{h_o}{g}(-\frac{1}{2}g + \frac{g}{2}\sqrt{1 + 8\frac{u_o^2}{gh_o}})$$

$$= \frac{h_o}{2}(-1 + \sqrt{1 + 8\frac{u_o^2}{gh_o}})$$

Since $F_o^2 = \frac{u_o^2}{gh_o}$, then:

$$= \frac{h_o}{2}(-1+\sqrt{1+8F_o^2}) \Rightarrow$$

$$\frac{h_1}{h_o} = \frac{1}{2}(-1+\sqrt{1+8F_o^2}) \tag{7.16}$$

Find the equation AE

To get the full equation for curve AE, divide equation (2.56) by h_0 and recognize that $\frac{d_m}{h_o} = H_o$:

$$\frac{1}{2}\frac{u_c^2}{h_o} + g\frac{(d_c+d_m)}{h_o} = \frac{1}{2}\frac{u_1^2}{h_o} + g\frac{h_1}{h_o} \Rightarrow$$

$$\frac{1}{2}\frac{u_c^2}{h_o} + gH_o + g\frac{d_c}{h_o} = \frac{1}{2}\frac{u_1^2}{h_o} + g\frac{h_1}{h_o}.$$

Next, bring in the sonic condition, equation (2.53) to equate $u_c^2 = gd_c$ and divide by g:

$$\frac{1}{2}\frac{gd_c}{h_o} + g\frac{d_c}{h_o} + gH_o = \frac{1}{2}\frac{u_1^2}{h_o} + g\frac{h_1}{h_o} \Rightarrow$$

$$gH_o = \frac{1}{2}\frac{u_1^2}{h_o} + g\frac{h_1}{h_o} - \frac{1}{2}\frac{gd_c}{h_o} - g\frac{d_c}{h_o} \Rightarrow$$

$$H_o = \underbrace{\boxed{\tfrac{1}{2}\tfrac{u_1^2}{gh_o}}}_{(1)} + \underbrace{\boxed{\tfrac{h_1}{h_o}}}_{(2)} - \underbrace{\boxed{\tfrac{3}{2}\tfrac{d_c}{h_o}}}_{(3)}$$

The objective will be express each of the three parts of H_o in terms of Fr_o only.

The first term, $\frac{1}{2}\frac{u_1^2}{gh_o}$, can be rewritten as a function of the bore strength $\frac{h_1}{h_o}$ and Fr_o using the mass conservation equation (2.52) across the jump at rest:

$$\frac{1}{2}\frac{u_1^2}{gh_o} = \frac{1}{2}\frac{u_o^2 h_o^2}{gh_o h_1^2} = \frac{1}{2}\frac{Fr_o^2 h_o^2}{h_1^2} = \frac{1}{2}\frac{h_o^2}{h_1^2}Fr_o^2.$$

Using equation (2.57), this first term can be represented as a function of just Fr_o:

$$\frac{2Fr_o^2}{(-1+\sqrt{1+8F_o^2})^2}.$$

The second term simply is the bore strength, and can be rewritten using (2.57) as

$$\frac{1}{2}(-1+\sqrt{1+8F_o^2}).$$

The third term substitutes the sonic condition in equation (2.54) into d_c and then relates the mass flux across the top of the obstruction, equation (2.53) to the mass flux entering the bore (2.52). The result is

$$\frac{d_c^3}{h_o^3} = \frac{u_c^2 d_c^2}{gh_o^3} = \frac{u_o^2 h_o^2}{gh_o^3},$$

and using the fact that $\frac{u_1^2}{gh_o} = Fr_o^2$, then the result for the third term is

$$Fr_o^{\frac{2}{3}} = \frac{d_c}{h_o}.$$

Now substituting these new expressions back into the three terms, the solution for the equation describing a bore not moving relative to the obstruction is

$$H_o = \frac{2Fr_o^2}{(-1+\sqrt{1+8F_o^2})^2} + \frac{1}{2}(-1+\sqrt{1+8F_o^2}) - \frac{3}{2}Fr_o^{\frac{2}{3}}.$$

It can be shown that this equation is equivalent to the equation in Baines (1995):

$$H_o = \frac{1+(1+8Fr_o^2)^{\frac{3}{2}}}{16Fr_o^2} - \frac{1}{4} - \frac{3}{2}Fr_o^{\frac{2}{3}}. \tag{7.17}$$

7.2.5 Curve BC

Curve BC defines the boundary between partially and completely blocked flow. Along the curve, the wind within the subcritical regime u_1 is 0. The implications of the subcritical regime flow equaling 0 is that the flow over the obstruction is 0. Using this information, jump conditions can be rewritten as:

$$(u_o + c_1)h_o = (\cancelto{0}{u_1} + c_1)h_1 = c_1 h_1 \Rightarrow$$

$$u_o h_o = c_1(h_1 - h_o) = c_1 h_o(\frac{h_1}{h_o} - 1) \Rightarrow u_o = c_1(\frac{h_1}{h_o} - 1) \Rightarrow$$

$$c_1 = u_o(\frac{h_1}{h_o} - 1)^{-1} \tag{7.18}$$

$$u_1 h_1 = u_c d_c = 0 \tag{7.19}$$

$$u_c = \sqrt{g d_c} = 0 \tag{7.20}$$

$$\frac{1}{2}\cancelto{0}{u_c^2} + g(\cancelto{0}{d_c} + d_m) = \frac{1}{2}\cancelto{0}{u_1^2} + g h_1 \Rightarrow g d_m = g h_1 \Rightarrow$$

$$d_m = h_1$$

diving by h_o and recognize that $\frac{d_m}{h_o} = H_o$:

$$H_o = \frac{h_1}{h_o} \tag{7.21}$$

Using equation (2.62) and plugging it into equation (2.55):

$$(u_o + c_1)^2 = \frac{1}{2} g h_1 (1 + \frac{h_1}{h_o}) = \frac{1}{2} g h_1 (1 + H_o) \Rightarrow$$

Divide by gh_o:

$$\frac{(u_o + c_1)^2}{g h_o} = \frac{1}{2} \frac{h_1}{h_o} (1 + H_o) = \frac{1}{2} H_o (1 + H_o)$$

Expand $(u_o + c_1)^2$ Plug in (2.59):

$$\frac{(u_o + c_1)^2}{g h_o} = \frac{1}{g h_o} (u_o^2 + 2 u_o c_1 + c_1^2) = \frac{1}{g h_o} \left(u_o^2 + 2 u_o \frac{u_o}{H_o - 1} + (\frac{u_o}{H_o - 1})^2 \right) = \frac{1}{2} H_o (1 + H_o)$$

Simplifying, the equation for curve BC is

$$= \frac{u_o^2}{g h_o} \left(1 + \frac{2}{H_o - 1} + \frac{1}{(H_o - 1)^2} \right) = F_o^2 \left(1 + \frac{2}{H_o - 1} + \frac{1}{(H_o - 1)^2} \right) =$$

$$\frac{F_o^2}{(H_o - 1)^2} \left[(H_o - 1)^2 + 2(H_o - 1) + 1 \right] = \frac{1}{2} H_o (1 + H_o) =$$

$$\frac{F_o^2}{(H_o - 1)^2} [(H_o - 1) + 1]^2 = \frac{F_o^2}{(H_o - 1)^2} H_o^2 = \frac{1}{2} H_o (1 + H_o) \Rightarrow$$

$$F_o^2 = \frac{(H_o - 1)^2 (1 + H_o)}{2 H_o} \Rightarrow$$

$$F_o = (H_o - 1) [\frac{(1 + H_o)}{2 H_o}]^{\frac{1}{2}}. \tag{7.22}$$

7.2.6 Two-Layer Hydraulic Theory

Two-layer Equation of Motion

In order to couple the two layer flow, it is assumed that pressure is continuous across the interface. Applying this assumption to equation (2.71), the solutions is

$$\cancel{p_{1o}} - \rho_1 \left(\frac{\partial \phi_1}{\partial t} + \frac{1}{2}(u_1^2 - u_{1o}^2) + g\eta) \right) = \cancel{p_{1o}} - \rho_2 \left(\frac{\partial \phi_2}{\partial t} + \frac{1}{2}(u_2^2 - u_{2o}^2) + g\eta \right) \Rightarrow$$

$$\frac{\partial \phi_1}{\partial t} + \frac{1}{2}(u_1^2 - u_{1o}^2) + g\eta = \frac{\rho_2}{\rho_1} \left(\frac{\partial \phi_2}{\partial t} + \frac{1}{2}(u_2^2 - u_{2o}^2) + g\eta \right) \Rightarrow$$

$$\frac{\partial \phi_1}{\partial t} + \frac{1}{2}(u_{1o}^2 - u_1^2) + g\eta \left(1 - \frac{\rho_2}{\rho_1} \right) = \frac{\rho_2}{\rho_1} \left(\frac{\partial \phi_2}{\partial t} + \frac{1}{2}(u_2^2 - u_{2o}^2) \right) \Rightarrow$$

$$\frac{\partial \phi_1}{\partial t} + \frac{1}{2}(u_1^2 - u_{1o}^2) + g\eta \left(1 - \frac{\rho_2}{\rho_1} \right) = \frac{\rho_2}{\rho_1} \left(\frac{\partial \phi_2}{\partial t} + \frac{1}{2}(u_2^2 - u_{2o}^2) \right).$$

Reduced Gravity

If the assumption that the first layer is denser than the second layer is used, it will be convenient to rewrite equation (2.74) as:

$$g' = \left(1 - \frac{\rho_2}{\rho_1} \right) g = \left(1 - \frac{\rho_1 + \Delta\rho}{\rho_1} \right) g = \left(1 - 1 - \frac{\Delta\rho}{\rho_1} \right) g \Rightarrow$$

$$g' = -\frac{\Delta\rho}{\rho_1} g. \tag{7.23}$$

In an incompressible atmosphere, it can be shown that (2.75) is equivalent to

$$g' = \frac{\Delta\theta}{\theta_1} g. \tag{7.24}$$

This relationship is explained later in the linear wave theory.

7.3 Linear Wave Theory

7.3.1 Equation of state

Consider that the flow is isentropic where the specific heat γ is considered constant. First shown by Sadi Carnot and summarized in Batchelor (1967); Kundu (2008), the equation of state can be written as:

$$\frac{p}{\rho^\gamma} = C*. \tag{7.25}$$

Where $C*$ is a constant. By taking the natural log of equation (7.25)

$$\ln \frac{p}{\rho^\gamma} = \ln C* \Rightarrow$$

$$\ln p - \gamma \ln \rho = \ln C* \Rightarrow$$

and taking the total derivative, then the equation of state can be expressed as:

$$\frac{D\ln p}{Dt} - \gamma \frac{D\ln \rho}{Dt} = \frac{D\ln C*}{Dt} = 0 \Rightarrow$$

$$\frac{1}{p}\frac{Dp}{Dt} - \frac{\gamma}{\rho}\frac{D\rho}{Dt} = 0 \Rightarrow$$

$$\frac{Dp}{Dt} = \frac{\gamma p}{\rho}\frac{D\rho}{Dt} \Rightarrow$$

$$\frac{Dp}{Dt} = \gamma RT\frac{D\rho}{Dt} \Rightarrow$$

$$\frac{Dp}{Dt} = c_s^2 \frac{D\rho}{Dt},$$

where c_s is the speed of sound defined as:

$$c_s^2 = \gamma RT.$$

7.3.2 Linearization of equations

The following are assumptions about the flow appropriate for linearized gravity waves in the lower portion of the troposphere (Baines 1995):

1. The background state is considered hydrostatic.
2. The Boussinesq approximation is valid.
3. The variables can be decomposed into a base state that is a function of only z and a perturbation quantity that is a function of x, z, and t.

U-component:

$$\frac{Du}{Dt} = -\frac{1}{\rho}\frac{\partial p}{\partial x} + \nu \nabla^2 u = \frac{\partial u}{\partial t} + u\frac{\partial u}{\partial x} + w\frac{\partial u}{\partial z} = -\frac{1}{\rho}\frac{\partial p}{\partial x}.$$

Multiply by $\frac{\rho}{\rho_o}$ and expand ρ into a base state and perturbation term:

$$\left(\frac{\rho_o + \rho'}{\rho_o}\right)\left[\frac{\partial u}{\partial t} + \frac{\partial u}{\partial x} + w\frac{\partial u}{\partial z}\right] = -\frac{1}{\rho_o}\frac{\partial p}{\partial x} \Rightarrow$$

$$\left(1 + \frac{\rho'}{\rho_o}\right)\left[\frac{\partial u}{\partial t} + \frac{\partial u}{\partial x} + w\frac{\partial u}{\partial z}\right] = -\frac{1}{\rho_o}\frac{\partial p}{\partial x}.$$

In this case where the Boussinesq approximation is valid, the base state-normalized density fluctuations are small in the inertia terms (Kundu 2008). For this reason,

$(1+\frac{\rho'}{\rho_o})$ is approximated well by 1 for the terms on the left-hand side. Next, linearize the rest of the terms:

$$\frac{\partial u_o}{\partial t}+\frac{\partial u'}{\partial t}+(u_o+u')\frac{\partial(u_o+u')}{\partial x}+(w_o+w')\frac{\partial(u_o+u')}{\partial z}=-\frac{1}{\rho_o}\frac{\partial p_o}{\partial x}+-\frac{1}{\rho_o}\frac{\partial p'}{\partial x}$$

Eliminate base-state terms that are 0 or constant in x or t:

$$\cancelto{0}{\frac{\partial u_o}{\partial t}}+\frac{\partial u'}{\partial t}+(u_o+u')\frac{\partial(\cancelto{0}{u_o}+u')}{\partial x}+(\cancelto{0}{w_o}+w')\frac{\partial(u_o+u')}{\partial z}$$
$$=-\frac{1}{\rho_o}\cancelto{0}{\frac{\partial p_o}{\partial x}}+-\frac{1}{\rho_o}\frac{\partial p'}{\partial x}$$

Approximate terms with more than one perturbation quantity to 0:

$$\frac{\partial u'}{\partial t}+(u_o+\cancelto{0}{u'\cdot'})\frac{\partial u'}{\partial x}+w'\frac{\partial(u_o+\cancelto{0}{u'\cdot'})}{\partial z}=-\frac{1}{\rho_o}\frac{\partial p'}{\partial x}$$

The linearized u-component of the equation of motion is therefore:

$$\boxed{\frac{\partial u'}{\partial t}+u_o\frac{\partial u'}{\partial x}+w'\frac{du_o}{dz}=-\frac{1}{\rho_o}\frac{\partial p'}{\partial x}} \tag{7.26}$$

W-component:

$$\frac{Dw}{Dt}=-g-\frac{1}{\rho}\frac{\partial p}{\partial z}=$$

$$\frac{\partial w}{\partial t}+u\frac{\partial w}{\partial x}+w\frac{\partial w}{\partial z}=-g-\frac{1}{\rho}\frac{\partial p}{\partial z}$$

Follow the same formula as the u-component, multiply by $\frac{\rho}{\rho_o}$ and expand ρ into a base state and perturbation term:

$$\left(\frac{\rho_o+\rho'}{\rho}\right)\left[\frac{\partial w}{\partial t}+u\frac{\partial w}{\partial x}+w\frac{\partial w}{\partial z}\right]=-\frac{(\rho_o+\rho')}{\rho_o}g-\frac{1}{\rho_o}\frac{\partial p}{\partial z}\Rightarrow$$

$$\left(1+\frac{\rho'}{\rho}\right)\left[\frac{\partial w}{\partial t}+u\frac{\partial w}{\partial x}+w\frac{\partial w}{\partial z}\right]=-(1+\frac{\rho'}{\rho})g-\frac{1}{\rho_o}\frac{\partial p}{\partial z}.$$

Next, linearize the pressure term and use the hydrostatic approximation to eliminate the hydrostatic base state:

$$\left(1+\frac{\rho'}{\rho}\right)\left[\frac{\partial w}{\partial t}+u\frac{\partial w}{\partial x}+w\frac{\partial w}{\partial z}\right]=-g-\frac{\rho'}{\rho_o}g-\frac{1}{\rho_o}\frac{\partial(p_o+p')}{\partial z}\Rightarrow$$

$$\left(1+\frac{\rho'}{\rho}\right)\left[\frac{\partial w}{\partial t}+u\frac{\partial w}{\partial x}+w\frac{\partial w}{\partial z}\right]=-g-\frac{\rho'}{\rho_o}g-\frac{1}{\cancel{\rho_o}}\cancel{\frac{\partial p_o}{\partial z}}^{-g}-\frac{1}{\rho_o}\frac{\partial p'}{\partial z}\Rightarrow$$

$$\left(1+\frac{\rho'}{\rho}\right)\left[\frac{\partial w}{\partial t}+u\frac{\partial w}{\partial x}+w\frac{\partial w}{\partial z}\right]=\cancel{-g}-\frac{\rho'}{\rho_o}g\cancel{+g}-\frac{1}{\rho_o}\frac{\partial p'}{\partial z}\Rightarrow$$

$$\left(1+\frac{\rho'}{\rho}\right)\left[\frac{\partial w}{\partial t}+u\frac{\partial w}{\partial x}+w\frac{\partial w}{\partial z}\right]=-\frac{\rho'}{\rho_o}g-\frac{1}{\rho_o}\frac{\partial p'}{\partial z}$$

Returning to the Boussinesq approximation, the $(1+\frac{\rho'}{\rho_o})$ in the inertial terms are approximated to be 1, while the perturbation density is kept in the buoyancy term as it is very important. Next, linearize u and w:

$$\frac{\partial(w_o+w')}{\partial t}+(u_o+u')\frac{\partial(w_o+w')}{\partial x}+(w_o+w')\frac{\partial(w_o+w')}{\partial z}=-\frac{\rho'}{\rho_o}g-\frac{1}{\rho_o}\frac{\partial p'}{\partial z}$$

Eliminate the base-states that are assumed to be 0 or their derivatives are assumed to be 0:

$$\frac{\partial(\cancel{w_o}^{0}+w')}{\partial t}+(u_o+u')\frac{\partial(\cancel{w_o}^{0}+w')}{\partial x}+(\cancel{w_o}^{0}+w')\frac{\partial(\cancel{w_o}^{0}+w')}{\partial z}=-\frac{\rho'}{\rho_o}g-\frac{1}{\rho_o}\frac{\partial p'}{\partial z}$$

Approximate terms with more than one perturbation quantity to 0:

$$\frac{\partial w'}{\partial t} + (u_o + \cancel{u'}^{\,'\cdot'})\frac{\partial w'}{\partial x} + w'\cancel{\frac{\partial w'}{\partial z}}^{\,'\cdot'} = -\frac{\rho'}{\rho_o}g - \frac{1}{\rho_o}\frac{\partial p'}{\partial z}$$

The linearized w-component of the equation of motion is:

$$\boxed{\frac{\partial w'}{\partial t} + u_o\frac{\partial w'}{\partial x} = -\frac{\rho'}{\rho_o}g - \frac{1}{\rho_o}\frac{\partial p'}{\partial z}}$$

Equation of state

$$\frac{Dp}{Dt} = c_s^2\frac{D\rho}{Dt},$$

For a Boussinesq flow, the fluid is nearly incompressible, implying that the flow adjusts nearly instantaneously ($c_s \to \infty$). In this case, the differentiated form of the equation of state is simply:

$$\frac{D\rho}{Dt} = 0$$

Linearizing:

$$\frac{D\rho}{Dt} = \frac{\partial\rho}{\partial t} + u\frac{\partial\rho}{\partial x} + w\frac{\partial\rho}{\partial z} = 0 \Rightarrow$$

$$\frac{\partial(\rho_o + \rho')}{\partial t} + (u_o + u')\frac{\partial(\rho_o + \rho')}{\partial x} + (w_o + w')\frac{\partial(\rho_o + \rho')}{\partial z} = 0 \Rightarrow$$

Where ρ_o is independent of t and x and w_o is 0:

$$\frac{\partial(\cancel{\rho_o}^{\,0} + \rho')}{\partial t} + (u_o + u')\frac{\partial(\cancel{\rho_o}^{\,0} + \rho')}{\partial x} + (\cancel{w_o}^{\,0} + w')\frac{\partial(\rho_o + \rho')}{\partial z} = 0 \Rightarrow$$

And primes multiplied by another prime are assumed 0:

$$\frac{\partial \rho'}{\partial t} + (u_o + \cancel{u'}^{\,'\cdot'})\frac{\partial \rho'}{\partial x} + w'\frac{\partial(\rho_o + \cancel{\rho'}^{\,'\cdot'})}{\partial z} = 0 \Rightarrow$$

which leads to the linearized form:

$$\boxed{\frac{\partial \rho'}{\partial t} + u_o\frac{\partial \rho'}{\partial x} + w'\frac{d\rho_o}{dz} = 0}.$$

Continuity equation:

$$\frac{1}{\rho}\frac{D\rho}{Dt} + \nabla\cdot\mathbf{u} = 0$$

The Boussinesq approximation, explicitly derived in Spiegel and Veronis (1960), demonstrates that the continuity equation is effectively the same as the continuity equation for an incompressible atmosphere:

$$\frac{1}{\cancel{\rho}}\frac{D\cancel{\rho}^{\,0}}{Dt} + \nabla\cdot\mathbf{u} \Rightarrow$$

$$\nabla\cdot\mathbf{u} = 0.$$

Linearizing the continuity equation and removing the base states or derivatives that are 0:

$$\nabla\cdot\mathbf{u} = \frac{\partial(u_o + u')}{\partial x} + \frac{\partial(w_o + w')}{\partial z} = 0 \Rightarrow$$

$$\frac{\partial(\cancel{u_o}^{\,0} + u')}{\partial x} + \frac{\partial(\cancel{w_o}^{\,0} + w')}{\partial z} = 0 \Rightarrow$$

$$\boxed{\frac{\partial u'}{\partial x} + \frac{\partial w'}{\partial z}} = 0. \tag{7.27}$$

This is the linearized form of continuity equation.

7.3.3 Deriving Taylor-Goldstein

To begin, assume that the waves reach a steady state. Then the time derivatives can be neglected:

$$u_o \frac{\partial u'}{\partial x} + w' \frac{du_o}{dz} = -\frac{1}{\rho_o} \frac{\partial p'}{\partial x} \tag{7.28}$$

$$u_o \frac{\partial w'}{\partial x} = -\frac{1}{\rho_o} \frac{\partial p'}{\partial z} - \frac{\rho'}{\rho_o} g \tag{7.29}$$

$$u_o \frac{\partial \rho'}{\partial x} + w' \frac{d\rho_o}{dz} = 0 \tag{7.30}$$

$$\frac{\partial u'}{\partial x} + \frac{\partial w'}{\partial z} = 0 \tag{7.31}$$

Then eliminate 3 of the 4 variables by taking $u_o \frac{\partial}{\partial x}$ of (7.29):

$$u_o^2 \frac{\partial^2 w'}{\partial x^2} + \frac{u_o}{\rho_o} \frac{\partial^2 p'}{\partial x \partial z} + u_o \frac{g}{\rho_o} \frac{\partial \rho'}{\partial x} = 0 \tag{7.32}$$

then substituting (7.30) into (7.32):

$$u_o^2 \frac{\partial^2 w'}{\partial x^2} + \frac{u_o}{\rho_o} \frac{\partial^2 p'}{\partial x \partial z} - w' \frac{g}{\rho_o} \boxed{\frac{d\rho_o}{dz}} = 0 \tag{7.33}$$

and plugging (7.28) into (7.33):

$$u_o^2 \frac{\partial^2 w'}{\partial x^2} + u_o \frac{\partial}{\partial z} \left(\boxed{\frac{1}{\rho} \frac{\partial p'}{\partial x}} \right) - w' \frac{g}{\rho_o} \frac{d\rho_o}{dz} = 0 \Rightarrow$$

$$u_o^2 \frac{\partial^2 w'}{\partial x^2} - u_o \frac{\partial}{\partial z} \left(\boxed{u_o \frac{\partial u'}{\partial x} + w' \frac{du_o}{dz}} \right) - w' \frac{g}{\rho_o} \frac{\partial \rho_o}{\partial z} = 0 \Rightarrow$$

And incorporating the continuity equation (7.31), the result is

$$u_o^2\frac{\partial^2 w'}{\partial x^2} - u_o\frac{\partial}{\partial z}\left[-u_o\frac{\partial w'}{\partial z} + w'\frac{du_o}{dz}\right] - w'\frac{g}{\rho_o}\frac{d\rho_o}{dz} = 0 \Rightarrow$$

$$u_o^2\frac{\partial^2 w'}{\partial x^2} + u_o^2\frac{\partial^2 w'}{\partial z^2} + \cancel{u_o\frac{\partial u_o}{\partial z}\frac{\partial w'}{\partial z}} - \cancel{u_o\frac{\partial w'}{\partial z}\frac{du_o}{dz}} - u_o w'\frac{d^2 u_o}{dz^2} - w'\frac{g}{\rho_o}\frac{d\rho_o}{dz} = 0 \Rightarrow$$

$$u_o^2\frac{\partial^2 w'}{\partial x^2} + u_o^2\frac{\partial^2 w'}{\partial z^2} - u_o w'\frac{d^2 u_o}{dz^2} - w'\frac{g}{\rho_o}\frac{d\rho_o}{dz} = 0 \tag{7.34}$$

Because soundings will provide thermodynamic information based on temperature, it is convenient to define a relationship between the background θ and ρ. Start with the definition of θ and logarithmically differentiate:

$$\theta_o = T_o(1000/P_o)^{\frac{R_d}{C_p}} \Rightarrow$$

$$\frac{1}{\theta_o}\frac{d\theta_o}{dz} = \frac{1}{T_o}\frac{dT_o}{dz} + \frac{-1}{P_o}\frac{dP_o}{dz}\frac{R_d}{C_p}.$$

Note that $\frac{R_d}{C_p} = 1-\gamma^{-1}$, where $\gamma = \frac{C_p}{C_v}$:

$$\frac{1}{\theta_o}\frac{d\theta_o}{dz} = \frac{1}{T_o}\frac{dT_o}{dz} + \frac{-1}{p_o}\frac{dp_o}{dz}(1-\gamma^{-1}) = \frac{1}{T_o}\frac{dT_o}{dz} + \frac{-1}{p_o}\frac{dp_o}{dz} + \frac{1}{\gamma}\frac{dp_o}{dz}.$$

Bringing in the logarithmically differentiated equation of state, a relationship between ρ and θ exists such that:

$$\frac{1}{\theta_o}\frac{d\theta_o}{dz} = \frac{1}{T_o}\frac{dT_o}{dz} + \frac{-1}{P_o}\frac{dP_o}{dz} + \frac{1}{\gamma}\frac{dP_o}{dz} = -\frac{1}{\rho_o}\frac{d\rho_o}{dz} + \frac{1}{\gamma}\frac{dP_o}{dz}$$

Since the last term is only important in a compressible atmosphere with sound waves,

the Boussinesq approximation can be used to neglect the last term:

$$\frac{1}{\theta_o}\frac{d\theta_o}{dz} = -\frac{1}{\rho_o}\frac{d\rho_o}{dz} \tag{7.35}$$

By multiplying by g, this equation becomes the Brunt-*Väisälä* frequency, N^2, given as:

$$N^2 = \frac{g}{\theta_o}\frac{d\theta_o}{dz}. \tag{7.36}$$

Let's assume that the variable w' is an equation of the form:

$$w'(x,z,t) = \bar{w}(z)cos(kx). \tag{7.37}$$

Plugging (2.101),(2.102), and (2.103) into equation (2.100) leads us to the Taylor-Goldstein equation (TGE):

$$u_o^2\frac{\partial^2 w'}{\partial x^2} + u_o^2\frac{\partial^2 w'}{\partial z^2} - u_o w'\frac{d^2 u_o}{dz^2} - w'N^2 = 0$$

$$u_o^2(-k)^2\bar{w}(z)cos(kx) + u_o^2\frac{\partial^2\bar{w}(z)}{\partial z^2}cos(kx) - u_o\frac{\partial^2 u_o}{\partial z^2}w(z)cos(kx) - N^2\bar{w}(z)cos(kx) = 0$$

Divide through by $cos(kx)u_o^2$:

$$-k^2\bar{w}(z) + \frac{d^2\bar{w}(z)}{dz^2} - \bar{w}(z)\frac{\frac{d^2 u_o}{dz^2}}{u_o} - \bar{w}(z)\frac{N^2}{u_o^2} = 0$$

Which leads to the Taylor Goldstein equation (TGE):

$$\frac{d^2\bar{w}(z)}{dz^2} + \bar{w}(z)\left(\frac{N^2}{u_o^2} - \frac{\frac{d^2 u_o}{dz^2}}{u_o} - k^2\right) = 0 \tag{7.38}$$

7.3.4 Solving TGE

To begin, solutions for the TGE are assumed of the form:

$$\bar{w}(z) = e^{irz}.$$

Plugging equation (2.107) into the equation (2.104):

$$\frac{\partial^2(e^{irz})}{\partial z^2} + (e^{irz})m^2 = (ir)^2 e^{irz} + e^{irz}m^2 = 0.$$

Divide by e^{imz}:

$$= -r^2 + m^2 \Rightarrow r^2 = m^2,$$

$$\boxed{r = \pm m = \sqrt{l^2 - k^2}}.$$

Solutions when m is real

The general solution for this first layer is as follows:

$$\bar{w}(z) = A_r e^{im_1 z} + B_r e^{-im_1 z}.$$

where m_1 is the magnitude of the positive root $\sqrt{l_1^2 - k^2}$ and l_1^2 is the value of the Scorer parameter in the first layer.

Boundary conditions

The first boundary condition that is imposed is the impermeability condition. At the surface, $w(0) = 0$.

$$\bar{w}(0) = A_r e^{im_1(0)} + B_r e^{-im_1(0)} = 0 \Rightarrow$$

$$= A_r + B_r = 0 \Rightarrow$$

$$-A_r = B_r. \tag{7.39}$$

The second boundary condition is a geometric constraint: the maximum in the vertical motion associated with a trapped wave occurs at a height h_{duct}:

$$\bar{w}(h_{duct}) = A_r e^{im_1(h_{duct})} - A_r e^{-im_1(h_{duct})} = w_{max} \Rightarrow$$

$$A_r(e^{im_1(h_{duct})} - e^{-im_1(h_{duct})}) = w_{max} \Rightarrow$$

$$A_r = \frac{w_{max}}{e^{im_1(h_{duct})} - e^{-im_1(h_{duct})}}. \tag{7.40}$$

applying (2.108) and (2.109) to the general solution, $\bar{w}(z)$ is determined to be:

$$\bar{w}(z) = \frac{w_{max}}{e^{im_1(h_{duct})} - e^{-im_1(h_{duct})}}(e^{im_1 z} - e^{-im_1 z}). \tag{7.41}$$

The exponentials can be decomposed into sines and cosines to get:

$$(e^{im_1 z} - e^{-im_1 z}) = cos(m_1 z) + isin(m_1 z) - cos(-m_1 z) - isin(-m_1 z)$$

Recognizing that $cos(-m_1 z) = cos(m_1 z)$ and $sin(-m_1 z) = -sin(m_1 z)$, then the equations are:

$$\cancel{cos(m_1 z)} + isin(m_1 z) - \cancel{cos(-m_1 z)} + isin(m_1 z) = 2isin(m_1 z)$$

$$\bar{w}(z) = \frac{w_{max}}{2i sin(m_1 h_{duct})} 2i sin(m_1 z) \Rightarrow$$

$$\boxed{\bar{w}(z) = \frac{w_{max}}{sin(m_1 h_{duct})} sin(mz)}. \tag{7.42}$$

Equation (2.111) is the solution for the vertical component of the TGE that describe linear waves with real vertical wavenumbers.

Solutions when m is imaginary

Next, find a solution for complex roots, where m_2 is a complex number (when $\sqrt{l^2 - k^2} < 0$). By doing so ,the general solution is:

$$\bar{w}(z) = A_i e^{m_2 z} + B_i e^{-m_2 z}.$$

Boundary conditions

One assumption made about a two-layer solution for the TGE is that the profile of the m exponentially decays above the duct h_{duct}. This requires that at $z = \infty, \bar{w} = 0$ and that there is no downward propagating wave energy (Baines 1995).

$$\bar{w}(\infty) = A_i e^{m_2 \infty} + B_i \cancelto{0}{e^{-m_2 \infty}}.$$

The first term will grow inexorably unless:

$$A_i = 0. \tag{7.43}$$

The second condition to be applied matches solutions of the real and imaginary equations at $z = h_{duct}$.

$$\bar{w}(h_{duct}) = B_i e^{-m_2 h_{duct}} = \frac{w_{max}}{\cancel{e^{im_1 h_{duct}} - e^{-im_1 h_{duct}}}} (\cancel{e^{im_1 h_{duct}} - e^{-im_1 h_{duct}}}) \Rightarrow$$

$$B_i = \frac{w_{max}}{e^{-m_2 h_{duct}}}. \tag{7.44}$$

Applying equation (2.112) and (2.113), the solution for the TGE when the roots are imaginary is:

$$\bar{w}(z) = \frac{w_{max}}{e^{-m_2 h_{duct}}} e^{-m_2 z}.$$

Simplifying the equation for the exponentially decaying layer, the solution is:

$$\bar{w}(z) = \frac{w_{max}}{e^{-m_2 h_{duct}}} e^{-m_2 z} = w_{max} e^{-m_2 z + m_2 h_{duct}} = w_{max} e^{-m_1 (z - h_{duct})} \Rightarrow$$

$$\boxed{\bar{w}(z) = w_{max} e^{-m_2 (z - h_{duct})}}. \tag{7.45}$$

Equation (2.114) is the solution for the vertical component of the TGE that describe linear waves with imaginary vertical wavenumbers.

7.3.5 Compiling w'

Now a piecewise solution can be constructed by solving for w':

When $0 > z > h_{duct}$:

$$\boxed{w'(x,z,t) = \bar{w}(z) cos(kx) = \frac{w_{max}}{sin(m_1 h_{duct})} sin(m_1 z) cos(kx)} \tag{7.46}$$

When $z < h_{duct}$:

$$\boxed{w'(x,z,t) = \bar{w}(z) cos(kx) = w_{max} e^{-m_2 (z - h_{duct})} cos(kx)} \tag{7.47}$$

7.3.6 Solving for u'

u' in m_1 layer

An advantage of this linear solutions for w' is that it can be used in the continuity equation to solve for u'. Plugging in w' into the continuity equation:

$$\frac{\partial u'}{\partial x} + \frac{\partial w'}{\partial z} = 0 \Rightarrow \frac{\partial u'}{\partial x} = -\frac{\partial w'}{\partial z} = -\frac{\partial [\frac{w_{max}}{sin(m_1 h_{duct})} sin(m_1 z) cos(kx)]}{\partial z}$$

$$\frac{\partial u'}{\partial x} = -m_1 \frac{w_{max}}{sin(m_1 h_{duct})} cos(kx) cos(m_1 z).$$

Integrating the equation with respect to x:

$$\int \frac{\partial u'}{\partial x} dx = \int -m_1 \frac{w_{max}}{sin(m_1 h_{duct})} cos(kx) cos(m_1 z) dx \Rightarrow$$

$$\int du' = \int -m_1 \frac{w_{max}}{sin(m_1 h_{duct})} cos(kx) cos(m_1 z) dx \Rightarrow$$

$$u'(x,z) = -\frac{m_1}{k} \frac{w_{max}}{sin(m_1 h_{duct})} cos(m_1 z) sin(kx) + C \Rightarrow$$

The initial condition u' is $u(0,z)' = 0$ will be applied to u' to solve for C:

$$u'(0,z) = -\frac{m_1}{k} \frac{w_{max}}{sin(m_1 h_{duct})} cos(m_1 z) \cancelto{0}{sin(k0)} + C = 0 \Rightarrow$$

$$C = 0$$

Therefore the derived solution for u' for the m_1 layer is:

$$\boxed{u'(x,z) = -\frac{m_1}{k}\frac{w_{max}}{sin(m_1 h_{duct})}cos(m_1 z)sin(kx)}. \tag{7.48}$$

u' in m_2 layer

Following the same method for u' in the m_2 layer, plug w' into the continuity equation:

$$\frac{\partial u'}{\partial x} + \frac{\partial w'}{\partial z} = 0 \Rightarrow \frac{\partial u'}{\partial x} = -\frac{\partial w'}{\partial z} = m_2 * w_{max} e^{-m_2(z-h_{duct})} cos(kx)$$

Integrating the equation with respect to x:

$$\int \frac{\partial u'}{\partial x} dx = \int m_2 * w_{max} e^{-m_2(z-h_{duct})} cos(kx) dx \Rightarrow$$

$$\int du' = \int m_2 * w_{max} e^{-m_2(z-h_{duct})} cos(kx) dx \Rightarrow$$

$$u'(x,z) = \frac{m_2}{k} w_{max} e^{-m_2(z-h_{duct})} sin(kx) + C \Rightarrow$$

Using the same initial condition, u' is $u(0,z)' = 0$:

$$u'(0,z) = \frac{m_2}{k} w_{max} e^{-m_2(z-h_{duct})} \cancelto{0}{sin(k0)} + C = 0 \Rightarrow$$

$$C = 0$$

Therefore the derived solution for u' for the m_2 layer is:

$$\boxed{u'(x,z) = \frac{m_2}{k} w_{max} e^{-m_2(z-h_{duct})} sin(kx)}. \tag{7.49}$$

7.3.7 finding u_{max}

If it is assumed that motions within gravity waves in the atmosphere are well described by linear wave theory, then the continuity equation (2.75) can be used to derive an equation for u' that describes the relationship between max perturbations in u' and max perturbation in w':

$$\frac{\partial u'}{\partial x} + \frac{\partial w'}{\partial z} = 0 \Rightarrow \frac{\partial u'}{\partial x} = -\frac{\partial w'}{\partial z} = -\frac{\partial [\frac{w_{max}}{sin(m_1 h_{duct})} sin(m_1 z) cos(kx)]}{\partial z}$$

$$\frac{\partial u'}{\partial x} = -m_1 \frac{w_{max}}{sin(m_1 h_{duct})} cos(kx) cos(nz)$$

If this equation is integrated with respect to x at the surface:

$$\int_0^{u_{max}} \frac{\partial u'}{\partial x} dx = \int_0^{x(u_{max}))} -m_1 \frac{w_{max}}{sin(m_1 h_{duct})} cos(kx) \cancelto{1 \; at \; surface}{cos(0)} dx \Rightarrow$$

$$\int_0^{u_{max}} du' = -m_1 \frac{w_{max}}{sin(m_1 h_{duct})} \int_0^{x(u_(max))} cos(kx) dx \Rightarrow$$

$$u_{max} = -\frac{m_1}{k} \frac{w_{max}}{sin(m_1 h_{duct})} sin(kx)]_0^{u_{max}} \Rightarrow$$

$$u_{max} = -\frac{m_1}{k} \frac{w_{max}}{sin(m_1 h_{duct})} [\cancelto{1}{sin(kx_{u_max})} - \cancelto{0}{sin(0)}] \Rightarrow$$

$$u_{max} = -\frac{m_1}{k} \frac{w_{max}}{sin(m_1 h_{duct})}, \tag{7.50}$$

where $sin(m_1 h_{duct}) = 1$ when evaluating waves whose maximum vertical motion is at a height a quarter of the vertical wavenumber.

7.4 Extraneous tables and figures

Table 7.1: Table of theoretical and observed values calculated with surface data, sounding data and 449 MHz wind profilers at FP4 and FP5. The purple shades of boxes indicate observed and theorized values that appear to agree well with one another. The green shaded boxes indicate when the μ parameter qualitatively agreed. Three soundings were used to calculate theoretical parameters. Using all three soundings was a heuristic approach to demonstrate that the closer the sounding is to an observation site, the better the observations agree with theory. DC1 and DC2 refer to the first density current associated with the target MCS and the second density current of the subsequent MCS that catches up with the target MCS later in the night. Next to the sounding sites are the parameters calculated from the soundings and used in the theory.

	$FP4$		$Ellis, KS$	$Topeka, KS$	$Salina, KS$
	DC 1	DC 1	DC 2	DC 2	DC 2
density current/bore					
$\theta_{vw}(K)$	300	300	300	300	
$\theta_{vc}(K)$	297	295.2	297.5	297.8	
$P_w(hPa)$	933.5	933.5	934.0	975.0	
$P_c(hPa)$	936.6	935.2	934.5	977.0	
$\rho_w(kgm^{-3})$	1.06	1.06	1.09	1.15	
$d_o(m)$	2197	897	446	1918	
Obs. $C_{dc}(ms^{-1})$	-14.98	-14.98	-8.66	-12.36	
Thy. $C_{dc}(ms^{-1})$	-16.06	-11.9	-6.45	-12.62	
Obs. $C_b(1)(ms^{-1})$	–	–	–	14.19	
Obs. $C_b(2)(ms^{-1})$	–	–	-10.68	–	
Obs. boreheight(m)	2000	2000	2500	–	
FP4 sounding :	$h_o = 500m$	$\Delta\theta(K) = 10$	$\theta_{vw\ inv}(K) = 311$	$U_c(ms^{-1}) = 16.58$	
H	4.38	1.79	0.89	3.84	
Fr	2.60	2.27	1.83	2.33	
μ	0.50	0.67	1.24	0.63	
Thy. $C_b(ms^{-1})$	10.80	2.27	7.75	13.12	
borestrength	4.35	3.35	2.6	3.95	
boreheight(m)	2125	1675	1325	1975	
Topeka sounding :	$h_o = 644m$	$\Delta\theta(K) = 7$	$\theta_{vw\ inv}(K) = 308$	$U_c(ms^{-1}) = 23.83$	
H	3.39	1.06	0.69	2.98	
Fr	3.32	1.93	2.53	3.04	
μ	0.47	0.64	1.18	0.60	
Thy. $C_b(ms^{-1})$	8.21	4.51	1.87	6.59	
borestrength	5.05	3.95	3.25	0.60	
boreheight(m)	3252	2544	2093	2930	
Dodge City sounding :	$h_o = 850m$	$\Delta\theta(K) = 14$	$\theta_{vw\ inv}(K) = 309$	$U_c(ms^{-1}) = 25.61$	
H	2.57	1.54	0.53	2.26	
Fr	2.14	1.97	1.65	1.97	
μ	0.77	1.04	1.92	0.98	
Thy. $C_b(ms^{-1})$	17.35	12.75	9.1	16.08	
borestrength	3.45	2.75	2.25	3.25	
boreheight(m)	2933	2338	1912	2763	

	Washington	*Mitchell*	*Hill City*	*Rocky Ford*
	DC 1	*DC* 2	*DC* 2	*DC* 2
density current				
$\theta_{vw}(K)$	296	297.0	299.2	296
$\theta_{vc}(K)$	293	293.5	297.5	293.5
$P_w(hPa)$	961.0	959.5	934.0	975.5
$P_c(hPa)$	964.0	961.5	934.5	977.5
$\rho_w(kgm^{-3})$	1.13	1.13	1.09	1.15
$d_o(m)$	2030	1300	750	1700
Obs. $C_{dc}(ms^{-1})$	15	13	9	12
Thy. $C_{dc}(ms^{-1})$	15.5	12.6	-6.44	12.5
Obs. $C_b(1)(ms^{-1})$	14	11	–	14
Obs. $C_b(2)(ms^{-1})$	–	–	10	–
Obs. boreheight(m)	2000	–	1600	–
FP4 sounding :	$h_o = 500m$	$\Delta\theta(K) = 10$	$\theta_{vw\ inv}(K) = 311$	$U_c(ms^{-1}) = 16.6$
H	4.1	2.60	1.6	3.4
Fr	2.6	2.3	1.8	2.3
μ	0.52	0.63	1.2	0.64
Thy. $C_b(ms^{-1})$	14.2	12.4	8.7	12.7
borestrength	4.3	3.8	2.6	3.9
boreheight(m)	2100	1900	1300	1900
Topeka sounding :	$h_o = 644m$	$\Delta\theta(K) = 7$	$\theta_{vw\ inv}(K) = 308$	$U_c(ms^{-1}) = 23.8$
H	3.2	2.0	1.2	2.6
Fr	3.3	3.1	2.5	3.0
μ	0.49	0.60	1.2	0.61
Thy. $C_b(ms^{-1})$	7.6	5.6	2.3	6.3
borestrength	4.9	4.2	2.6	4.5
boreheight(m)	310	2700	2100	2900
Dodge City sounding :	$h_o = 850m$	$\Delta\theta(K) = 14$	$\theta_{vw\ inv}(K) = 309$	$U_c(ms^{-1}) = 25.6$
H	2.4	1.5	0.89	2.0
Fr	2.1	2.0	1.7	2.0
μ	0.80	0.98	1.9	0.98
Thy. $C_b(ms^{-1})$	17.4	14.1	10.6	15.4
borestrength	3.45	2.95	2.6	3.15
boreheight(m)	2900	2500	1900	2700

Table 7.2: Same as 7.4, continued.

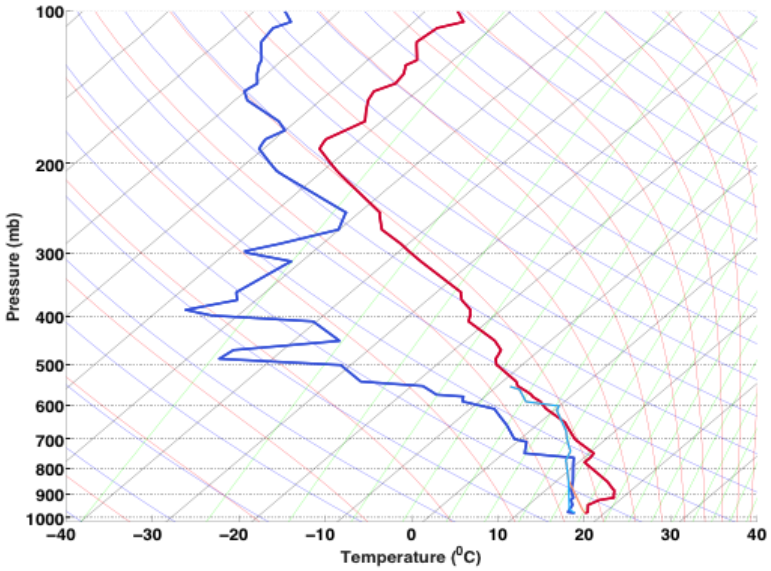

Figure 7.1: Modified sounding from Topeka, KS 1200 UTC using technique 1. The lighter blue and red lines indicate the displaced sounding while the darker red and blue lines indicate the original pre bore sounding.

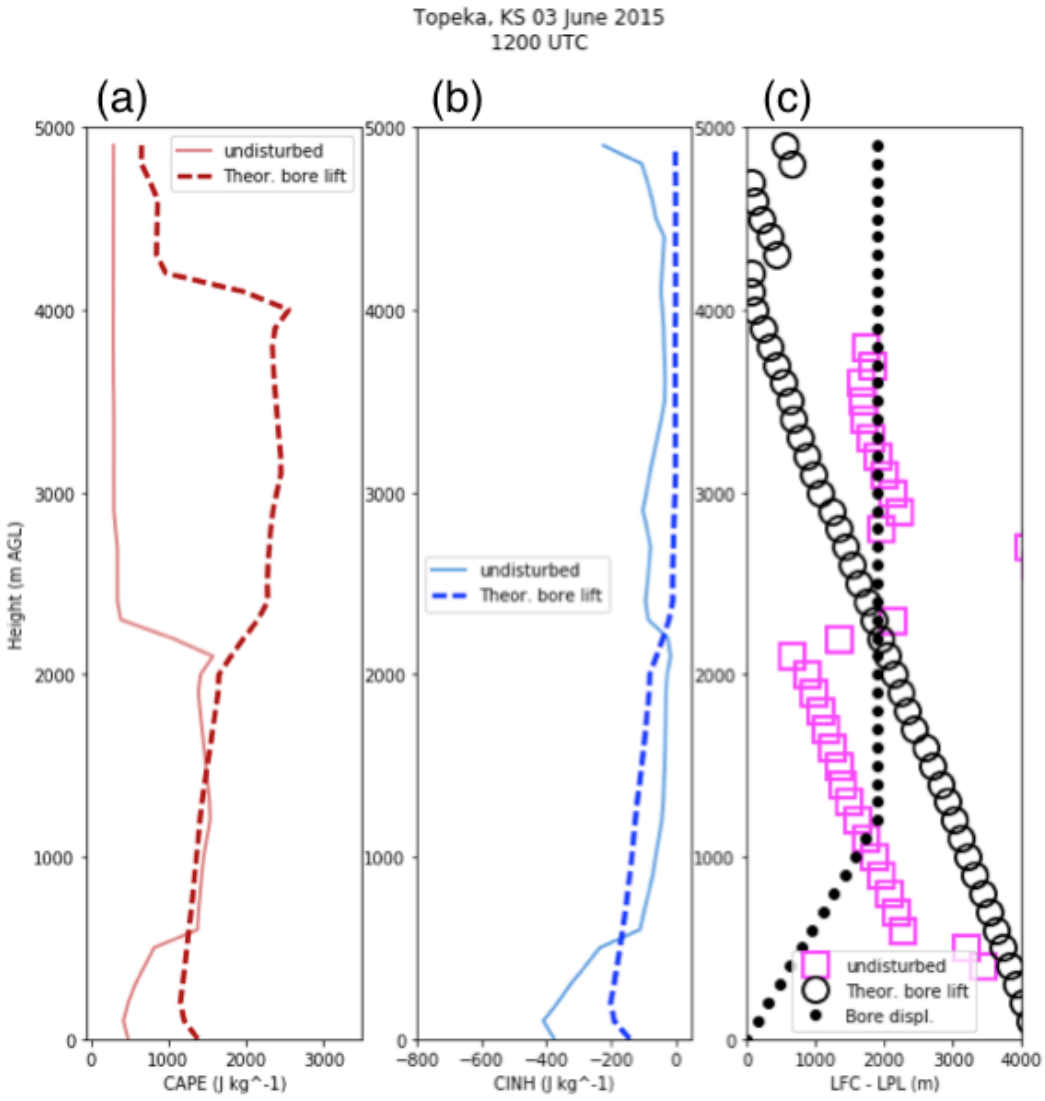

Figure 7.2: Profiles for CAPE, CIN, and LFC-LPL at Topeka, KS using the expected displacement with theory and applying the first technique of parcel displacement. Undisturbed soundings (solid) are the pre-bore soundings and theoretical bore lift (dashed). Bore displacement (black solid dot) is the bore displacement function based off of technique 1.